Investigation of surface-liquid-interaction on flat bugs (Aradidae), selected European true bugs (Heteroptera), and transfer of principles onto technical surfaces

Untersuchung der Oberflächen-Flüssigkeitsinteraktion von Rindenwanzen (Aradidae), ausgewählten europäischen Wanzen (Heteroptera), und Übertragung der Prinzipien auf technische Oberflächen

Von der Fakultät für Mathematik, Informatik und Naturwissenschaften der RWTH Aachen University zur Erlangung des akademischen Grades eines Doktors der Naturwissenschaften genehmigte Dissertation vorgelegt von

Diplom-Biologe

Florian Hischen

aus Hannover

Berichter: Universitätsprofessor Dr. Peter Bräunig

Universitätsprofessor Dr. Werner Baumgartner

Tag der mündlichen Prüfung: 13.10.2017

Diese Dissertation ist auf den Internetseiten der Universitätsbibliothek online verfügbar.

Abstract

The present work investigates surface-liquid-interactions that occur on neotropical flat bugs from the genus *Dysodius* (Aradidae) and selected European true bugs (Heteroptera). In case of *Dysodius* water- as well as oil-based interaction are researched. The former enabling the fascinating phenomenon called “adaptive camouflage” on these bugs, the latter concerning directional, passive fluid transport in the external scent efferent system (defense secretion system). European bugs are investigated with regard to comparable functionality of their scent efferent system only. Morphological studies are carried out by means of scanning- and transmission electron microscopy in order to extract fluid-interaction relevant body features. Chemical studies, like GC-MS and HPLC-MS, are used as means to figure chemical composition of surface waxes. Fluid-flow studies are carried out via high-speed video capturing, followed by custom algorithm analysis with the goal of understanding the surface-fluid-interaction dynamics. By means of laser ablation and casting, different materials (like steel and polymers) are provided with artificial fluid-transport channels, biomimetically abstracted from the bugs and their performance is analyzed by above mentioned techniques. In the end of this work a novel approach for the fabrication of thermal conductive all-metal replicas of biological samples is presented that will enable even more sophisticated investigation ways for phenomena like evaporation and condensation in the future.

Zusammenfassung

Die vorliegende Arbeit untersucht die Oberflächen-Flüssigkeits-Interaktion, die auf neotropischen Rindenwanzen der Gattung *Dysodius* (Aradidae) und ausgewählten europäischen Wanzen (Heteroptera) zu beobachten ist. Im Falle von Dysodius werden sowohl wasser-, wie auch öl-basierte Interaktionen untersucht. Erstere ermöglichen diesen Wanzen die faszienierende Fähigkeit der „adaptiven Tarnung“, letzere betreffen den Flüssigkeitstransport im sog. „external scent efferent system“. Europäische Vertreter werden nur in Hinblick auf dieses System untersucht. Morphologische Untersuchungen von Körpermerkmalen, die relevant für Flüssigkeitsinteraktion sind, werden mittels Raster- und Transelektronenmikroskopie durchgeführt. Analysemethoden wie GC-MS und HPLC-MS dienen der Entschlüsselung der chemischen Zusammensetzung von Öberflächenwachsen. Mittels Hochgeschwindigkeits-Videoaufnahmen wird das Flüssigkeitsverhalten aufgezeichnet, gefolgt von der Auswertung mit selbstgenerierten Algorithm, mit dem Ziel die Dynamik der Flüssigkeits-Oberflächen-Interaktion zu verstehen. Durch Lasergravur und Abformung werden verschiedene Materialen (wie Stahl und Polymere) mit einem künstlichen, bionisch inspiriertem Kanal nach Vorbild der Wanzen versehen und mit zuvor genannten Methoden in Hinblick auf Leistungsfähigkeit untersucht. Am Ende der Arbeit wird eine neuartige Methode zur Herstellung von temperaturleitenden Vollmetalrepliken biologischer Oberflächen vorgestellt, die künftig tiefergehende Untersuchungen von Phänomenen wie Verdunstung und Kondensation ermöglichen wird.

List of abbreviations

2PPL two-photon-polymerization

AS abdominal segment

BSTFA N,O-bis(trimethylsilyl)trifluoroacetamide

C/Ca capillary

Ca caput (head)

CAM computer-aided manufacturing

Cla clavus

Co corium

DAG dorsal abdominal gland

DC direct current

En endocuticula

Ep/Epi epicuticula

ESI electrospray ionization

Ev/Eva evaporium

Ex exocuticula

FFT fast-Fourier-transformation

GC gas chromatography

Gla glabrous area

HPLC High-performance liquid chromatography

HRC Hardness Rockwell, scale C

Hy hypodermis

IPT Institute for Production Technology

LED light emitting diode

Me membranous part of the wing

Me metal

Met metanotum

MS mass spectrometry

Ms microstructures

MTG metapleural scent gland system

O ostiole, or orifice

OCT optical coherence tomography

P/Pe peritreme

PC personal computer

PDMS poly(dimethylsiloxzane)

PET poly(ethylene terephthalate)

PMMA poly(methylmetacrylate)

Pro pronotum

PVD physical vapor deposition

Ro rostrum

Scu scutellum

Se setae

SEM scanning electron microscopy

SES scent efferent system

So hemelytra socket

STD standard deviation

TEM transmission electron microscopy

UV ultraviolet

Wg wax glands

Wi wings

For my family and friends.

Table of Contents

1. Introduction

Wherever one will look, interaction between the living world and fluids will be found. Apart from the obvious interaction of aquatic life in its surroundings, all land dwellers have to deal with it as well. From habitants of the most arid areas on this planet that seek to manage their fluid maintenance to those of the humid climates of rainforests and swamps, liquid handling is key to survival. And as various as the circumstances and demands for the different situations are, nature has come up with solutions to cope with the necessary.

But, liquid handling in nature obviously goes beyond the handling of simple water alone. Lifeforms sweat watery solutions in order to cool down, cover themselves with mucus, slimes, greases and hydrogel capsules to prevent water loss, produce and apply poisons and defense fluids in and on various body parts for hunting reasons or self-defense, make use of fluids to help their reproductive process or nurture the offspring and much more. In the end though it comes down to one thing: The interaction of a certain fluid with a certain part of (body-) surface. And this is a field that doesn`t concern nature alone.

Various fields in science and application are in need for individual solutions of liquid-surface-interaction and biomimetic findings have shown over and over again that nature in most cases already found the fitting answer to a specific problem. Wheather it is bottom-up (finding a solution in nature, abstract and understand it, apply it technically) or top-down (search for a specific technical problem that has been solved in a natural system), biomimetics can offer a good way to find the answer that is needed.

1.1 Motivation and Goal

This work tries to spotlight the fascinating world of liquid-surface-interaction that can be found in the order of bugs (Hemiptera, suborder Heteroptera), since these insects in many cases deal with several different ways of liquid handling in and on their bodies. The main motivation of this work was to discover the possibilities and ways bugs use to handle various liquids, with the goal to a) understand the underlying mechanisms and b) to abstract them onto technical surfaces and find applications and/or application possibilities.

2. State of the Art

The interaction of liquids and surfaces has always been of great interest for various fields of research. From the simple need for water repellent fabrics that protects one from rain yet being vapor permeable (e.g. Gohlke & Tanner, 1976) up to sophisticated surfaces and coatings for enhanced lubrication, needed to reduce friction in between movable parts to reduce wear (e.g. Kadiyala & Bijwe, 2013; Kovalchenko, Ajayi, Erdemir, Fenske, & Etsion, 2005), the understanding of the given liquid-surface-interaction is most crucial. More recently, also the field of micro-fluidics, with uprising applications like the lab-on-a-chip (e.g. Haeberle & Zengerle, 2007), has shown increasing interest not only for better understanding of basic physical principles, but also for solutions that allow the guidance of fluids in a controlled and predictable fashion (e.g. Mark, Haeberle, Roth, Von Stetten, & Zengerle, 2010; Wang et al., 2005).

History has shown, that nature has brought forth solutions for most complex problems – some already understood and applied, others discovered but not yet understood, and the majority probably undiscovered – therefore, giving the field of biomimetics growing relevance in the past decades. Prominent findings, for example the discovery of the lotus effect (e.g. Barthlott & Neinhuis, 1997; Marmur, 2004), fog harvesting inspired by beetles (e.g. White, Sarkar, & Kietzig, 2013), show only a glimpse of liquid surface interaction that can be found in nature and that in some cases lead to revolutionary applications. Hence, having a closer look on natures various "liquid-specialists" will provide even more insight toward this end – from expanding the understanding of basic principles to new fields of applications.

In nature, surface-liquid-interaction happens basically everywhere. Not only in aquatic environments is the phenomenon constantly present; practically all land living life on this planet is subdued to it too. Body surfaces interact with fluids all the time and everywhere. In many cases this interaction concerns water for example from rain or dew (e.g. Dickerson, Shankles, Madhavan, & Hu, 2012; Malik et al., 2015), or water based fluids and solutions (e.g. sweat) on the skin or shell of an animal (e.g. Nadel, Bullard, & Stolwijk, 1971; Schleger & Turner, 1965).

There are many examples that even go beyond simple passive interaction. Nature has come up with a variety of systems that allow active influence of body-surface fluids: Moisture harvesting lizards (Comanns, Effertz, Hischen, Staudt, Böhme, et al., 2011), dew catching spiders and beetles (e.g. Malik, Clement, Gethin, Krawszik, & Parker, 2014), or even camouflage based on getting wet or staying dry, like observed on the neotropical flat bug *Dysodius lunatus* (FABRICIUS, 1794, Silberglied & Aiello, 1980). Especially when we have a close look into the class of insects, the most common interaction is the repellence of water on

the surface. Due to a cuticle being surfaced by waxes and non-polar substances (e.g. Blomquist & Jackson, 1979), most insects are rendered with a hydrophobic surface and therefor water will form droplets, which then eventually roll off. This mechanism provides insects with an effective protection against rain and dew droplets that would otherwise render them immobile, or even block their tracheas and thus, rendering them unable to breath.

In contrary to described water interactions, there are oil/fat based fluid interactions on plants and animals as well. Here we talk in most cases about oily substances that are produced from the organisms themselves. Examples for such fluid can be found on nearly every higher lifeform and often the sole purpose for such fluids is the protection from drying out (for example fat secretion on human skin/hair; e.g. Keis, Huemmer, & Kamath, 2007; Robbins, 1988)), prevention of wetting (e.g. the uropygial glands of water birds; e.g. Farner, King, & Parkes, 1982; Florkin, Scheer, & Brush, 1978), or, like in the case of many insects, defensive secretions with the purpose of fending off and/or distracting predators. Especially the order of Hemiptera and the sub-order of Heteroptera are infamous for showing a wide selection of species that produce oily defense fluids in order to defend themselves (e.g. Aldrich, 1988; Gough, Hamilton, Games, & Staddon, 1985; Krall, Bartelt, Lewis, & Whitman, 1999).

This oil-surface-interaction, as well as the interesting behavior of wetting-induced camouflage (as earlier introduced for *Dysodius lunatus*), render the sub-order of Heteroptera a fascinating candidate for deeper investigation of described phenomena and are the reason behind the research presented in this work.

2.1 Bugs (Hemiptera: Heteroptera)

Within the class of Insecta, the order of Hemiptera (sub-order Heteroptera, also called “true bugs”) show a big diversity with so far over 40.000 species described worldwide. As true bugs inhabit almost all parts of the world, their mode of life, individual habitat and morphology hereby are as diverse as the number of species. One can find plant- and fungi-suckers, insect predators and parasitic species, in many cases showing morphological adaptions that either are reasoned by or contribute to their specific diet or habitat. (Freely adapted from Schuh & Slater, 1995)

The general morphology of Heteroptera is given in the following **Figure 1**.

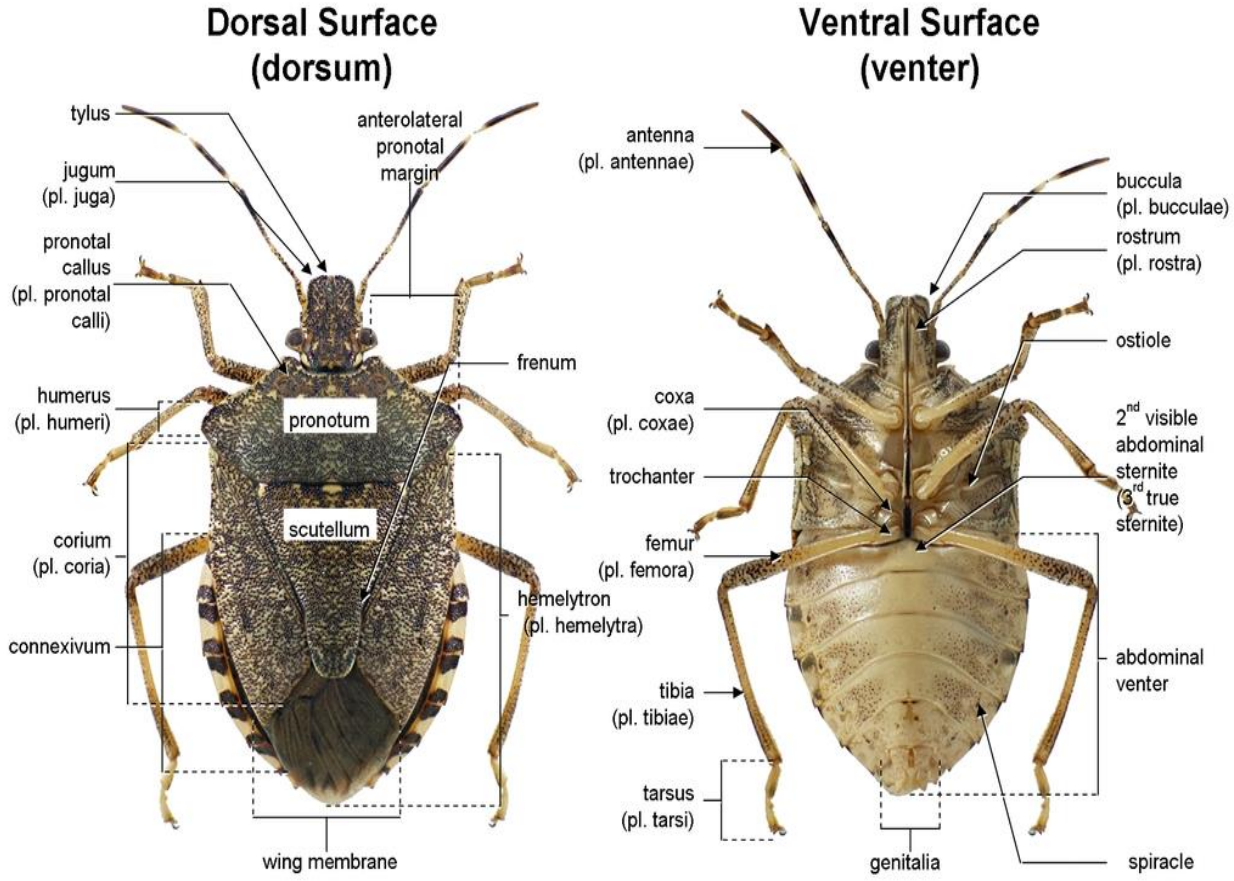

Figure 1: General morphology of Heteroptera. *Example bug here is Halyomorpha haly (Stål, 1855), the brown marmorated stink bug. Image from Paiero, Marshall, McPherson, & Ma, 2013.*

As shown in **Figure 1,** Heteroptera exhibit some general features that clearly distinct them from other Insecta at first glance. On the dorsal surface this would be the often armored looking pronotum and even

more so, the big, pronounced and triangularly shaped scutellum, which for example is an easy recognizable feature to distinguish bugs from beetles. One also sees the wings, in bugs called hemylytra. In resting state (as shown in the figure), only the front pair of wings is visible. They consist of the sclerotized part, the so called corium) and the membranous part. On the ventral side one can find two more very distinctive morphological features: The (often very long) rostrum (jabbing-sucking) and the ostiole, which is the orifice of the scent gland system that produces stinky, often even poisonous defense secretions.

Probably one of the best known examples for this kind of defense system in Europe, is the common green stink bug *Palomena prasina* (LINNAEUS, 1761, see also **Figure 55** and **Figure 69**) which produces sticky and intensively smelly defensive secretions from a scent glands located ventral between the second and third pair of legs. This, as well as most bug defense fluids, for the main part consist out of n-alkanes and n-alkenes, as well as aldehydes and ketones (Aldrich, 1988; Durak & Kalender, 2007). Such fluids often are guided through channel systems or capillaries, to reach areas of the cuticle where evaporation can take place most efficiently. The evaporating zones are usually characterized by micro-scale protrusions, wrinkles or microstructures that enlarge increase surface and allow for more effective evaporation of the active repellent substances in the defense fluid (e.g. in Kment & Davidová-Vilímová, 2010; Kment, Stys, & Vilímová, 2012). A well describe example for these, are the evaporative fields of *Graphosoma lineatum* (LINNAEUS, 1761) (Durak & Kalender, 2009). In their total, gland ositiole (or orifice), the fluid channel (peritreme) and evaporative field (evaporium) are called the (external) scent efferent system (SES). The relative position on the body is hereby various as later shown in discussed in chapter 4. Example images of different SES are shown in following **Figure 2**, in order to clarify the composition and nomenclature.

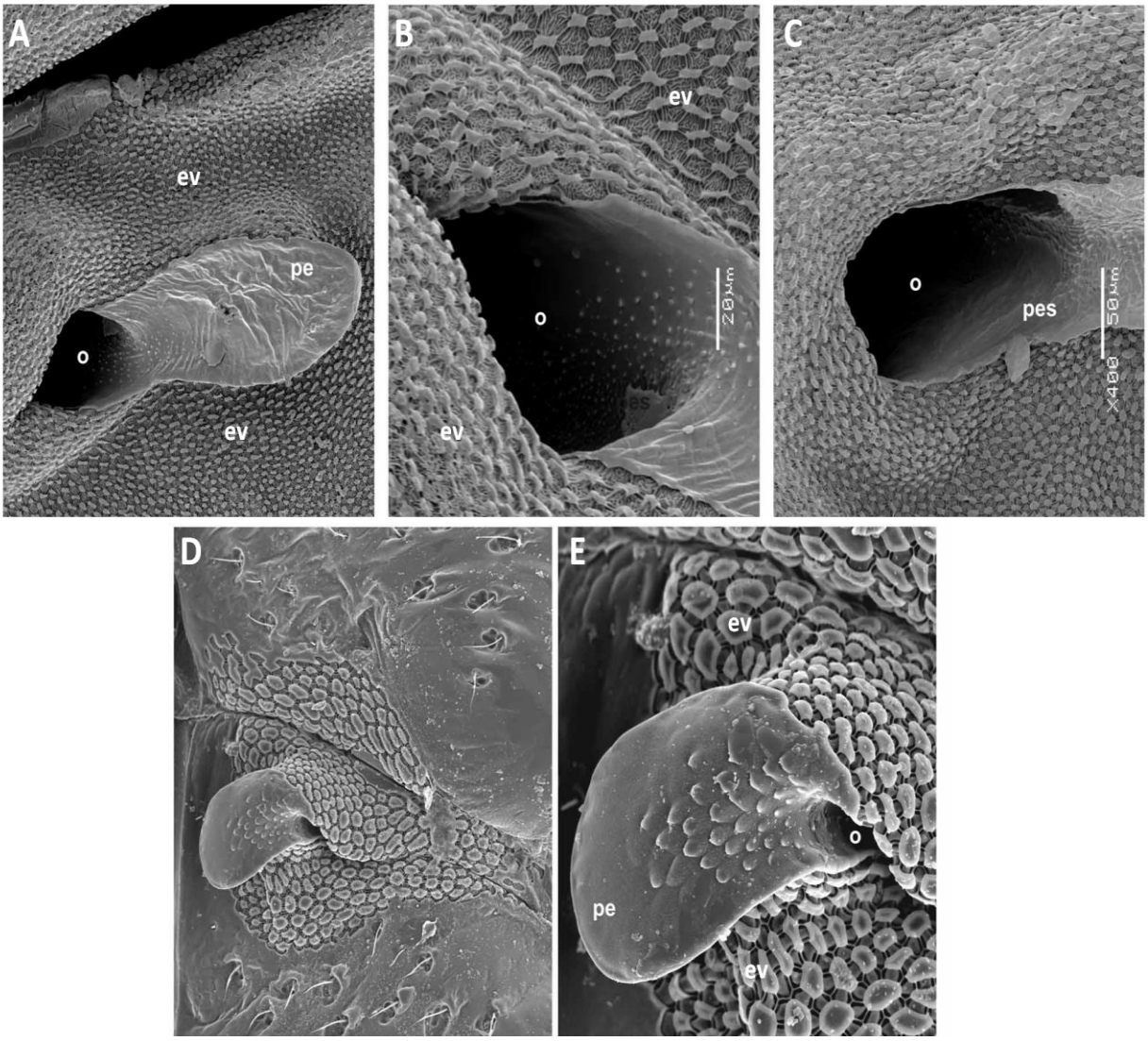

Figure 2: Example morphologies of external SES. A-C *SES of Ditomotarsus punctiventris (Spinola, 1852).* ***D-E*** *SES of Thaumastella aradoides (HORVÁTH,1896). Morphological features of the SES are marked by "o" (=ostiole, or orifice), "pe" (=peritreme) and "ev" (=evaporium). Images modified from Kment & Davidová-Vilímová, 2010.*

It has already been shown that one of the interesting elements of the defensive secrete system in true bugs is the peritreme, a channel guiding the fluid to above-mentioned evaporative zones. In (Plamadeala et al., 2017a) we showed that the micro-structured defense fluid channel of the neotropical flat bugs (Aradidae) *Dysodius lunatus* and *Dyosodius magnus* (HEISS, 1990; Heiss, 1990) can be used as an biomimetic inspiration towards the design of technical surfaces that transport oily fluids unidirectional. However, in case of *Dysodius*, the transport system functions is located dorsally on the abdomen, in form of a closed capillary, since its wings cover the channel structure on the bug itself (discussed in Chapter 4).

This work will try to uncover more aspects of the SES, since it clearly depicts a complicated and complex oil-surface-interaction regime. Considering this, special attention will be put towards the peritreme and the fact that unidirectional flow of defense oils so far only has been shown for *Dysodius*, but not for other species or families of Heteroptera. Detailed investigation of individual, morphological features of the SES of 11 species (including *Dysodius lunatus* and *D. magnus*) from a total of five different families and seven different subfamilies from various areas of the world are presented in Chapter 4 of this work. The findings revealed here had been used in an attempt to transfer the found principles and morphologies to transfer unidirectional liquid transport inspired by bugs onto technical surfaces. These findings will be presented in Chapter 5.

Dysodius has not solely been an inspiration for research towards its intrinsic oil handling abilities of the SES. Silberglied & Aiello (1980) presented an interesting work that dealt with the "camouflage of integumentary wetting in bark bugs", a behavior that we later dubbed "adaptive camouflage" (Hischen et al., 2017). This behavior depicts the second interesting liquid-handling regime that can be found on *Dysodius*: When getting wet from rain, these bugs change their color due to changing optical properties of the wetted cuticle. Clearly a phenomenon that involves the interaction of typically waxy insect cuticle with water. Chapter 3 of this work will show the research that has been done in order to reveal the physical and chemical principles that cause this observable behavior and show attempts how to transfer it to artificial systems.

Compared to the generic morphological features of Heteroptera in general (as shown in **Figure 1**), the family of Aradidae (bark or flat bugs like previously mentioned species of the genus *Dysodius*) shows slightly different morphological specialties. Towards this end the following **Figure 3** is presented in order to establish a uniform nomenclature for the reader to follow. One again finds the overall typical features of Heteroptera, like a sturdy and pronounced pronotum and a well-established scutellum, but the overall appearance is clearly more cryptic and delicate.

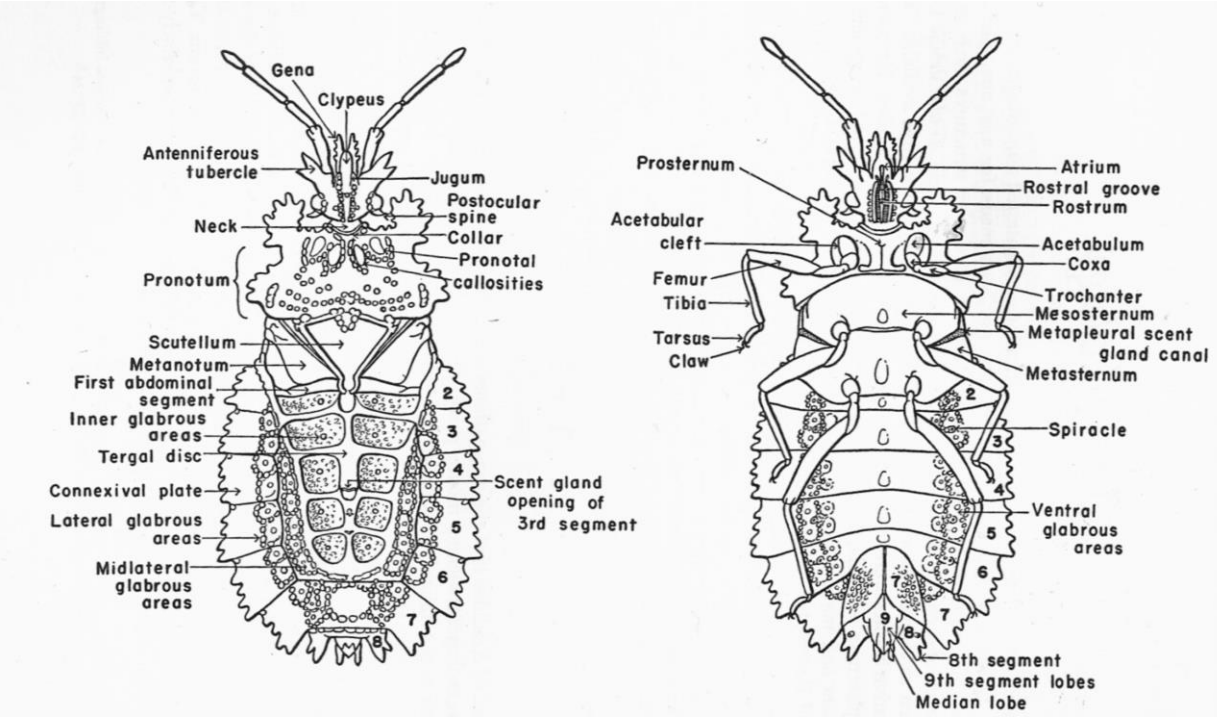

Figure 3: Body structures of Aradidae (from Usinger & Matsuda, 1959). *Schematically depicted are a dorsal (wings detached, left hand side of the image) and ventral overview (right hand side of the image).*

Reasoned by their mode of life – often on and underneath the bark of trees (e.g. Panizzi & Grazia, 2015) – Aradidae in most cases show a very dorso-ventrally flattened habitus. For camouflaging reasons, these animals often show mottled and environmentally fitting colors and are enhancing the camouflage effect by their frazzled and bumpy morphological features, which resemble the bark of their specific host trees. In the shown **Figure 3** , special attention should be paid towards the following body parts:

1. The scent gland opening. In contrast to the previously shown, generic morphology of Heteroptera (**Figure 1**), many Aradidae (but not all, as later discussed in Chapter 4), exhibit gland openings on their dorsal side underneath the wings.

2. The location of the defensive glands is dorsally placed along the central axis of the so called tergal disc, which is surrounded by the fields of lateral and midlateral glabrous area.

3. The individual abdominal segments are visible around the wings and are called connexival plates and can be numbered from I to VIII, whereas the first segment is usually melted with the metanotum and hard to identify, and the last plate is often hard to distinguish from the median lobe.

Since neither shown in **Figure 1**, nor **Figure 3**, but important for the results shown below in chapter 3, following figure 4 shows the specific parts and nomenclature for the wings of Hemiptera.

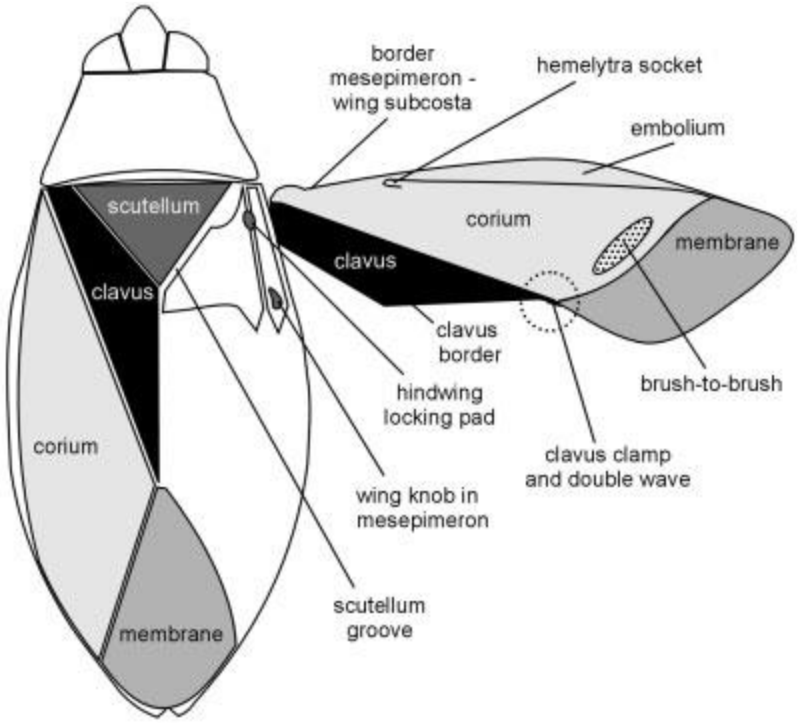

***Figure 4: Morphological features and nomenclature of the wing**. Example of a schematic, aquatic Heteroptera, dorsal aspect. Right hemelytra spread open, hindwing omitted. Image from Gorb & Goodwyn (2003)*

Figure 4 gives the generic overview for the wing morphology as typical for bugs. One can see the sclerotized part of the front wing (corium) with its inner edge (clavus), as well as the membranous outer part of the hemelytra. Also shown are different areas and features of the wing that enable wing locking (inter-wing and inter-body) when the wings are folded together in resting position.

After establishing the necessary background towards bugs in this chapter, the following part will try to cover the general physical bases of surface-liquid-interaction in order to deliver the full background knowledge for the present work.

2.2 Surface-Liquid-Interaction

Smooth surfaces

The general interaction between a perfectly smooth surface and a liquid in general takes place in form of one of the two cases depicted in **Figure 5**: either the interaction is ideal, meaning that a perfect film is formed immediately (perfect wetting), or the liquid sits on the surface, exhibiting a certain contact angle θ.

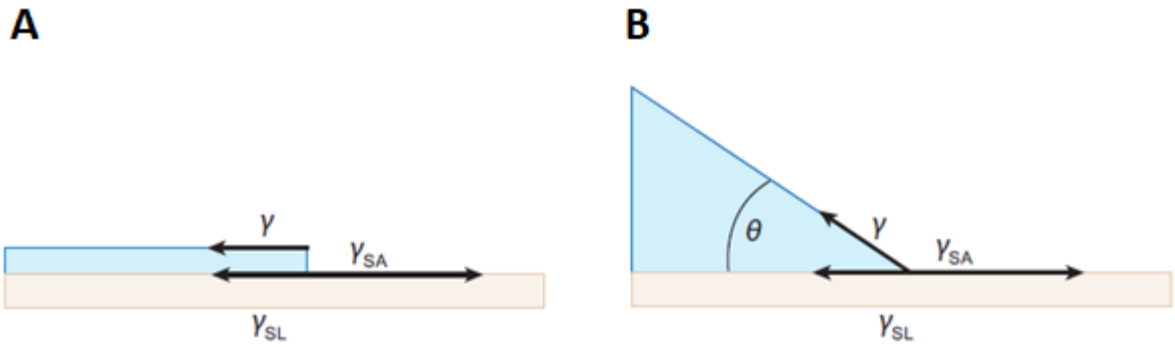

***Figure 5: Wetting cases that can occur on an ideal smooth surface**. A Perfect wetting. Fluid only partially wetting and exhibiting a certain contact angle θ, driven by the balance between the surface energies. (Image from Quéré, 2008).*

The contact angle θ hereby is a result of the balance conditions given by the Young-Laplace equation (Ball, 1960; Laplace, 1805), which puts the surface energies of all three involved systems (γ = surface energy between liquid/ air, γ_{SL} = surface energy between solid/liquid, and γ_{SA} = surface energy between solid/air) into context:

$$0 = \gamma_{SA} - \gamma_{SL} - \gamma \cdot cos\theta \qquad (1)$$

Equation 1 consequently can be formed into the so called Laplace-Equation, which gives back the static contact angle:

$$cos\theta = \frac{\gamma_{SA} - \gamma_{SL}}{\gamma} \qquad (2)$$

Obviously the contact angle as equated from Equation 2, therefore becomes majorly dependent from the surface energy γ_{SL}, which is determined by the chemistry of the surface and the respective fluid sitting on it. In case of water as a reference system on a certain surface, for contact angles below 90° the system is

considered to act hydrophilic, for angles above, hydrophobic. If contact angles reach below 10° the term superhydrophilic can be applied and such systems show the behavior of immediate fluid spread as depicted in **Figure 5 A**. For contact angles above 150° the term superhydrophobic has become popular, especially since the discovery of above mentioned Lotus-effect. The mathematical limit for the contact angle is 180°, resulting theoretically in a perfectly round fluid sphere sitting on a surface. In most cases, this described correlation is the opposite when considering systems with oil as fluid. A hydrophilic system is most often oleophobic and vice versa, though special cases have been reported where surfaces show both features at once (e.g. Zhu, Loo, & Bai, 2013)).

Rough surfaces

In reality most surfaces do not exhibit perfect smoothness but are rather rough to some degree. The roughness/wetting models of Wenzel (Wenzel, 1936) and Cassie-Baxter (de Gennes, Brochard-Wyart, & Quéré, 2004; Quéré, 2008) are the most commonly used models to describe the influence of surface roughness towards the contact angle.

The Wenzel model hereby assumes that a liquid drop sitting on a rough surface will penetrate the individual structures, resulting in a contact angle determined by the morphology of the roughness:

$$cos\theta^* = r \cdot cos\theta_0 \qquad (3)$$

In this case θ* is the resulting contact angle of the fluid sitting in/on the rough surface, θ_0 is the chemical contact angle that this fluid would exhibit on a perfectly smooth version of given surface, and *r* denotes the roughness factor, which gives the fraction of real to projected surface. A typical case of Wenzel-wetting is depicted in **Figure 6**.

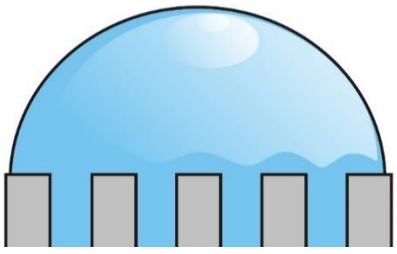

Figure 6: Example of typical Wenzel-wetting. *The liquid drop sits in between the surface features (roughness)*

In comparison to that, the Cassie-Baxter-Model assumes a case, in which the droplet is rather sitting on top of the surface features than within (**Figure 7**).

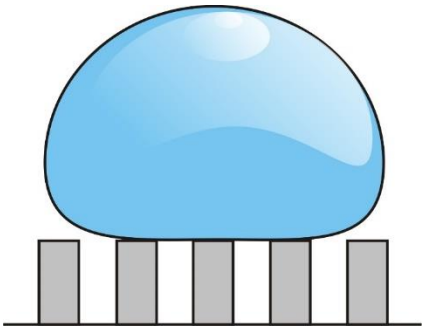

Figure 7: ***Example of typical Cassie-Baxter-wetting.*** *The liquid drop sits on the surface features (roughness).*

In this case, the resulting contact angle θ* can be calculated by the following equation:

$$cos\theta^* = \gamma_1 \cdot cos\theta_1 + \gamma_2 \cdot cos\theta_2 \quad (4)$$

Here the surface fraction *γ* and the corresponding contact angle θ are considered individually for the two materials (1 and 2) the liquid is in contact with (in shown case air trapped underneath the liquid drop and the surface of rough features of the base material). This incomplete wetting can also be described by using the roughness factor *r* (again as the fraction of real to projected surface) and the wetted fraction *f*, resulting in:

$$cos\theta^* = r \cdot f \cdot cos\theta_\gamma + f - 1 \quad (5)$$

When measuring static contact angles though, neither of both models always gives the correct prediction for resulting contact angles. This can have different reasons. For example, a transition is possible from Cassie-Baxter into Wenzel state and vice versa, especially when external energy (e.g. vibrations or irradiation) are introduced to the system. Secondly, it has been shown that sessile water droplets naturally oscillate with high frequencies (e.g. Chang, Bostwick, Steen, & Daniel, 2013) and enter over 30 different states while doing so. Thus, a lot of natural movement is already involved in sessile drops that might facilitate change of states.

If the transition case happens (usually from Cassie-Baxter to Wenzel, e.g. because trapped air underneath the liquid drop gets unstable/volatile), so called hemi-wicking is the consequence.

Figure 8: Example for the transition towards hemi-wicking. *A Droplet in Cassie-Baxter state.* ***B*** *Transition into Wenzel → the fluid penetrates the microstructure.* ***C*** *Hemi-wicking, the so called "mushroom state". Image modified from Vereecke et al., 2014)*

As shown in **Figure 8**, the transition from Cassie-Baxter into Wenzel state ends with the so called "mushroom state", or hemi-wicking. The droplet sits in between the surface structures, which act like a micro-capillary network → more and more fluid is imbibing the roughness. Further imbibing then is only possible when the criteria as given in Chandra & Yang (2011) are fulfilled:

$$\theta < \theta_C < 90° \tag{6}$$

and

$$\cos\theta_C = \frac{\varphi - 1}{r - \varphi} \tag{7}$$

Hereby θ_C is the critical contact angle that has to be smaller than 90° and bigger than the apparent contact angle θ, φ is the fraction of material surface in contact with the liquid and the projected contact area, and r is the roughness.

Capillary flow

Above mentioned phenomena and equations consider fluid phenomena on straight (possibly rough) surfaces. The second big field of fluid-surface-interaction concerned in this work is capillary flow though. In this case, same basic rules apply as mentioned above, but more complex surfaces are involved, since capillary interaction usually implies multi-dimensional contact of a liquid slug with surfaces. The most generic form of fluid interaction in capillaries is capillary flow in a straight, closed capillary with a radius r, the interfacial tension γ, and the contact angle θ between fluid and capillary material. In this case the capillary pressure p_c can be calculated with the Young-Laplace equation for closed capillaries, given by:

$$p_C = \frac{2 \cdot \gamma \cdot cos\theta}{r} \tag{8}$$

Hence, the smaller the capillary radius, the bigger the capillary pressure driving the fluid. For capillary systems that are open, a modified version of this Young-Laplace equation has to be used, since the surface of the water is in contact with air as a second interface. Consequently, such a system exhibits different contact angles between liquid/capillary walls, and liquid/air, resulting in different radii of curvature for the 3-dimensional meniscus of the total fluid front. The situation for an open and in addition conically capillary is depicted in following **Figure 9**.

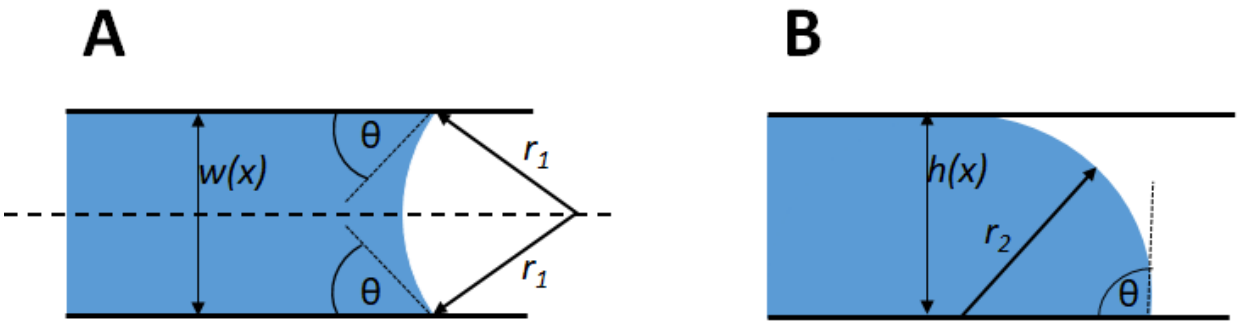

Figure 9: Situation of menisci in an open capillary. A *Top view. Marked are the width of the capillary (w), the contact angle* θ, *and the radius of the concave meniscus (*r_1*). **B** Cross-sectional view. Marked are the height of the capillary (h), the contact angle* θ, *and the radius of the concave meniscus (*r_2*).*

The capillary pressure in an open capillary therefore can be calculated by:

$$\Delta p = \left(\frac{1}{r_1} + \frac{1}{r_2}\right) \tag{9}$$

Hereby, $\Delta p > 0$ would result in forward movement of the liquid front, $\Delta p = 0$ in halting of the front, and $\Delta p < 0$ would cause the liquid front to move backwards. Hence, sign convention for the radii gives $r > 0$ → concave meniscus and $r < 0$ → convex meniscus.

3. Surface-Water-Interaction of *Dysodius magnus* and *D. lunatus*

As previously mentioned, *Dysodius magnus* as well as *D. lunatus* show the interesting behavior of darkening when getting wet, a behavior we dubbed “adaptive camouflage” (Hischen et al., 2017).When exposed to rain, the bark of trees these bugs live on darkens due to the change in reflection, caused by the coverage with water. In order to follow this change in appearance, the body surface of *D. magnus* and *D. lunatus* is able to interact with water in a positive way (hence adaptive camouflage), a rather untypical feature for insects, which usually show hydrophobic behavior due to the waxes covering their cuticle. This chapter deals with this phenomenon and tries to reveal the mechanisms behind.

3.1 Adaptive camouflage

In order to show the behavior, a photo series as mentioned in Silberglied & Aiello (1980) was done, to see the color change of *Dysodius* and capture it in full color (in contrast to the black & white only images presented in that work). Furthermore, reflective measurements were done to quantify the change in appearance of both, bark and bug. Parts of the work presented in this chapter were also shown in Hischen et. al (2017). Parts taken directly from that work are denoted individually as such.

3.1.1 Materials and Methods

Photo-series “adaptive camouflage”

After pretests, which determined that there is no apparent difference in camouflaging behavior between *D. magnus* and *D. lunatus*, one specimen of *D. magnus* was chosen for the photos, mainly because of the bigger body area, which simplified the process. As substrate, pieces of the bark of *Sequiadendron giganteum* were chosen (not a natural habitat of *Dysodius*, but similar in appearance and available). Images of dry and wetted bark and bug were obtained with a digital camera Nikon D5300 (Nikon Corp., Japan) with an attached 60 mm macro lens (AF-S Micro 88 Nikkor 1:2.8, Nikon Corp., Japan).

Reflectance measurements

One dried specimen of *D. magnus* was mounted in an integrating sphere (15 cm diameter, Gamma Scientific, USA), normal to the incident laser beam. A supercontinuum source, i.e. a white light laser (NKT SuperK, NKT Photonics, Denmark) equipped with a Varia filter box allowed color tuning. The diffuse reflection of the bug is recorded via a custom photodiode facing the backside of the sample mount. The

laser power was kept well below 1 mW to avoid optical and thermal damage. An overview of the setup used is given in the following **Figure 10**. All reflectance measurements were done with the help of Oskar Armbruster at the Institute for Applied Physiks, JKU Linz.

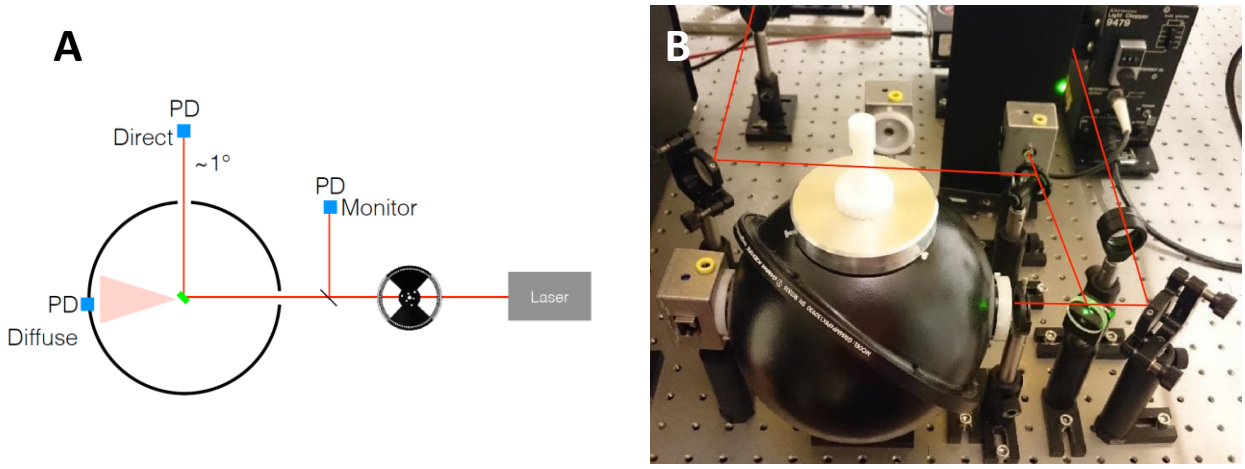

Figure 10: Measurement setup for the integrating sphere. A *Schematic overview for the measurement of diffuse reflected light. The green rectangle marks the position of the bug, PD stands for "Photo Detector".* ***B*** *Overview of the complete setup.*

3.1.2 Results

The image series shown in **Figure 11** depicts the camouflaging situations of *D. magnus* in different states of wetting (of itself and the bark it sits on).

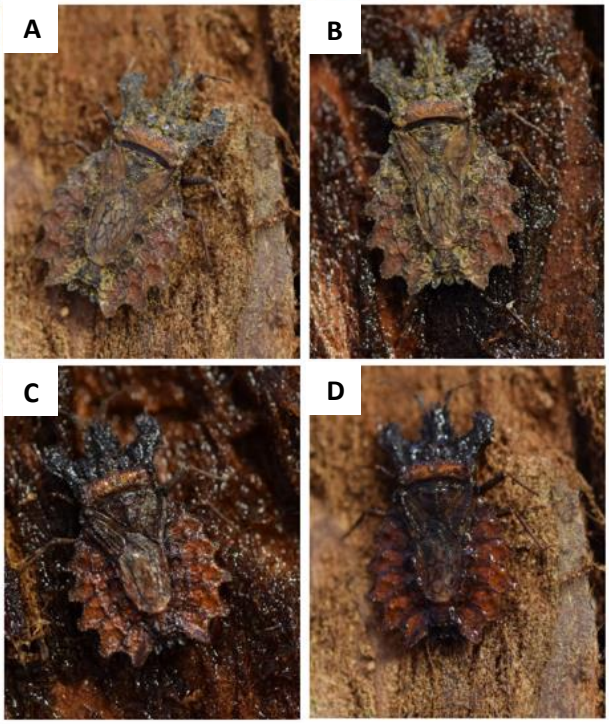

***Figure 11: Adaptive camouflage of Dysodius magnus. A** A dry specimen on dry bark. **B** A dry specimen on wet bark. **C** A wet specimen on wet bark. **D** A wet specimen on dry bark. Figure as shown in Hischen et al. (2017).*

The image sequence shown in **Figure 11** illustrates this behavior quite close to what would be observable in nature. A dry bug is due to its bark-mimicking body surface quite well camouflaged on a dry peace of bark, hence, it`s harder to spot for potential predators (**Figure 11 A**). The situation changes though, when either only the bug, or only the bark are covered with a film of water (as depicted in **Figure 11 B** and **C**): In both cases the bug becomes clearly visible in front of its background due to the difference in reflectance, or more precisely the diffuse reflectance, also called “albedo”. Only if both, bark and bug are wetted (as shown in **Figure 11 D**) camouflage is given again. The measurements also showed that a droplet of 5 µl water usually is enough to spread across the whole dorsal abdomen of *Dysodius*. It also became apparent that there is virtually no difference in the wetting behavior between the two tested species *D. magnus* and *D. lunatus*, for which reason only results for *D. magnus* are shown (since it was easier to acquire good images and results due to the bigger body surface). In later chapters of this work it will also be shown that both species share the same morphology and chemistry.

To measure the effect of "darkening" when wetted, we performed reflectance measurements in a so called integrated sphere (**Figure 10**). The following **Figure 12** shows the results for reflectance measurements in the integrated sphere. Results for measurements on bark and bug are shown, for wet and dry state respectively.

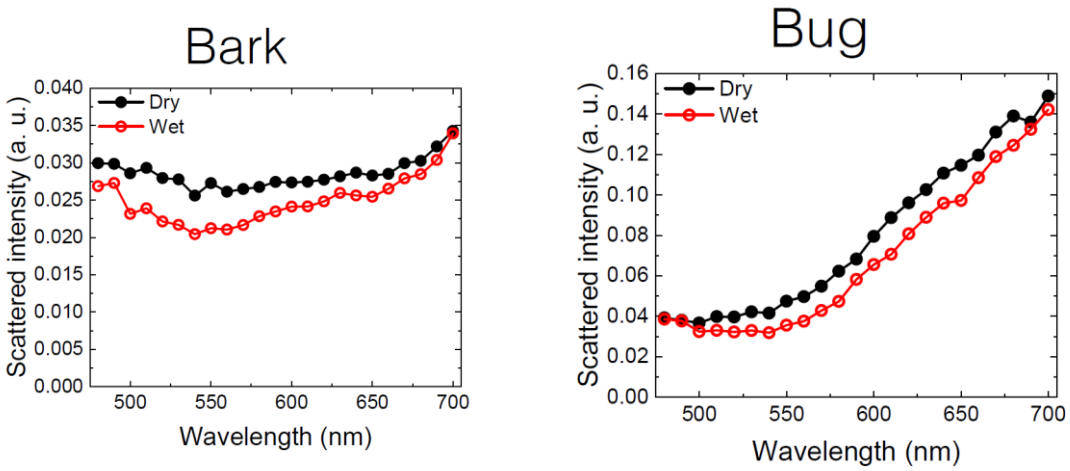

Figure 12: Exemplary results of reflectance measurements of bark and D. magnus in the integrated sphere. *Left hand side: Direct reflectance of dry and wet bark given in arbitrary units (a.u.) versus the wavelength in nanometers (n=1). Right hand side: Direct reflectance of dry and wet specimen of D. magnus given in arbitrary units (a.u.) versus the wavelength in nanometers (n=1). (Right hand side also shown in Hischen et. al (2017))*

A bug or a piece of bark were placed inside the sphere, which had an inside covered by highly reflective white varnish to trap all the light inside. A broadband white light laser then was used to irradiate a spot on the sample. A photo detector measured the reflectance by giving the scattered light intensity in arbitrary units. We only used the photo detector for direct scattered light since the second detector for diffuse light was constantly producing high noise peaks, most likely due to a defect sensor. Nevertheless, the setup showed nicely what was expected. As exemplarily shown in **Figure 12**, the difference in direct reflectance when comparing dry and wet bark and bug is measurable for wavelengths between 500 and 725 nm. In fact, one can see that in case of the bark for example, scattering intensity will be lowered up to ~30% for specific bandwidths. For the bug one can find scattering reduction of up to ~20%.

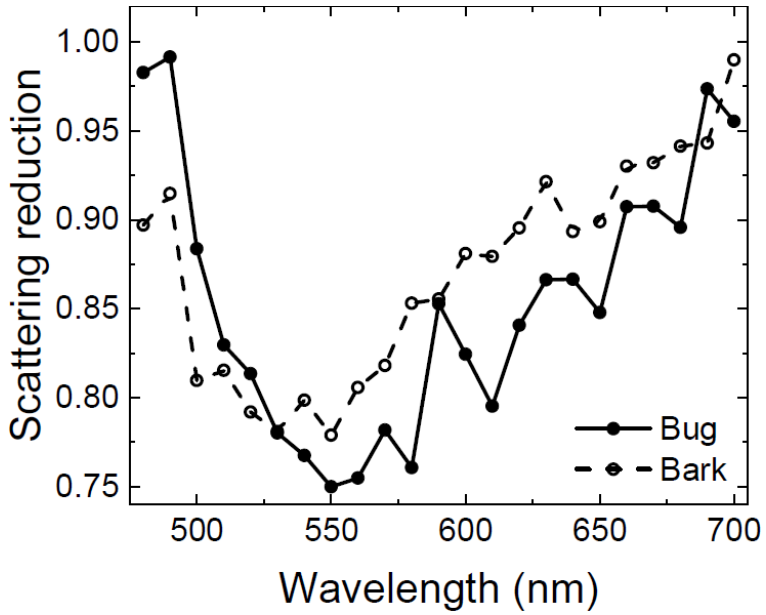

Figure 13: Comparison of the scattering reduction through wetting between bark and bug. *Presented is the relative scattering reduction (= reduction in direct reflectance) in percent versus the wavelength in nanometers. The graphs are generated by computing the relative scattering reduction between dry and wetted stage from the measurements shown in* ***Figure 12****. This graph has also been presented in Hischen et. al (2017).*

Figure 13 shows the relative scattering reduction (= relative reduction in direct reflectance) of bark and bug in comparison computed from the results shown in **Figure 12**. The graph shows very comprehensively, how close the trends for scattering reduction (and therefore the change in visual properties, in this case darkening) of wetted bark and bug really are. It is notable that both materials show little to none scattering reduction for wavelength bellow 500 nm and then again above 675 nm. In contrast to that we find that for wavelength around 550 nm, reduction of up to 25% can be reached.

3.1.3 Discussion

This chapter tries to spotlight the adaptive camouflage behavior of *Dysodius* as observable in nature: When wetted, the bark darkens in appearance and so does the bug. In the habitat of *Dysodius*, the rainforests of the neotropics, quick changes in humidity are a given and an animal that wouldn`t blend into its surroundings after a rainfall naturally gets exposed to its predators, which of course directly impacts its reproductive chances. It therefore can be assumed that it was crucial for *Dysodius* to evolve a camouflaging mechanism which adapts immediately towards the given circumstances of its surroundings. The image series shown in **Figure 11** visualizes this behavior once again, for the first time captured under controlled lab conditions and in color (in contrast to the findings of Silberglied & Aiello (1980), where pictures of animals in their natural surroundings were shown). Also for the first time, it was attempted to measure the "real" darkening of the wetted surface (e.g. bark and bug). Towards this end, reflectance measurements were done in order to find the scattering reduction of both, bark and bug. As can be seen from **Figure 12** this reduction, or the change in albedo, becomes indeed measurable and visualizes unmistakably that the surface of a specimen of *D. magnus*, as well as the surface of the tested bark, indeed become darker when covered with water. Of even bigger importance are the findings then shown in **Figure 13**. Here we see that the overall change in albedo follows the same trend on both surfaces with regard to the different tested wavelengths. A finding that makes a lot of sense, since it would be undesirable for an animal which camouflage tries to stay as close to the background as possible, to show different light scattering for specific wavelengths. At this point it has not been tested what the situation would be for wavelength over (infrared) or underneath (ultraviolet) the in this work tested bandwidth. This would be interesting to know, since different, potential predators of *Dysodius* (e.g. birds, lizards, and other insects) might use optical information from these spectra in order to hunt.

Explanation of the change in albedo (as noted in Hischen et. al (2017))

In order to understand the darkening effect found on the bark and *Dysodius*, one has to understand generally why most objects appear darker when wet. The amount of light seen from an illuminated and not self-lucent object is mainly dependent on its albedo, i.e. the reflectivity of the surface. This albedo depends on several but two main aspects (Twomey, Bohren, & Mergenthaler, 1986): 1.) the total reflection within a continuous water film and 2.) a modified reflection coefficient. The first aspect was proposed by Ångström (1925). The surface roughness leads to diffuse reflection and thus dependent on the angle, to total internal reflection. A rough surface can be treated as array of randomly oriented small facets reflecting specularly. Let's assume this rough surface is covered by a thin water layer. Light incident onto

this layer has a probability (1-R) of reaching the rough surface. Here R is the reflection coefficient of the liquid-air-interface. A fraction named *a* is then absorbed by the rough surface. Of the light reflected back by the rough surface, a fraction *p* is then reflected back by the liquid-air-interface so that it is once again incident on the rough surface. This process continues ad infinitum. Thus, the absorption probability of the water covered rough surface follows to be

$$A = (1-R)\cdot[a + a(1-a)p + a(1-a)^2p^2 + \ldots] = \frac{a(1-R)}{1-p(1-a)} \qquad (10)$$

According to Ångstrom *p* can be evaluated for a Lambertian surface as the fraction of diffusely reflected light that lies outside a cone with critical angle q_C, which follows to be

$$p \approx \frac{2\pi \cdot \int_{\theta_C}^{\pi/2} \cdot \sin\theta \cdot \cos\theta d\theta}{2\pi \cdot \int_{0}^{\pi/2} \cdot \sin\theta \cdot \cos\theta d\theta} = \cos^2\theta_C = 1 - \frac{1}{n_l^2} \qquad (11)$$

with n_l denoting the refractive index of the liquid. This is valid of course only for perpendicular illumination. If now the absorption *a* of the bug surface and of bark is identical and if both surfaces can be assumed to exhibit Lambertian (ideally matte) reflectance, the closed water film will reveal an identical change of the albedo.

If now the water film is not perfect and only a change due to a modified reflection coefficient can be observed, another theoretical consideration has to be made: At an interface of a medium 1 and a medium 2 (e.g. air – wax), the reflection coefficient *R* of an object illuminated under angle of incidence of a_1 (denotes is air) is

$$R = \left(\frac{n_1 \cdot \cos\alpha_1 - n_2 \cdot \cos\alpha_2}{n_1 \cdot \cos\alpha_1 + n_2 \cdot \cos\alpha_2}\right)^2 \qquad (12)$$

Here n_1 and n_2 denote the refractive indices of medium 1 and medium 2 respectively. The angle of incidence a_1 and the angle of the refracted light a_2 relate according to the refractive law as

$$n_1 \cdot \sin\alpha_1 = n_2 \cdot \sin\alpha_2 \tag{13}$$

If medium 1 is air, then n_1=1. When denoting the refractive index of medium 2 as n and the angle of incidence as a, we can simplify the equation for the reflection coefficient as

$$R = \frac{\left(n \cdot \sqrt{\frac{\cos(\alpha)^2 + n^2 - 1}{n^2}} - \cos(\alpha)\right)^2}{2 \cdot \cos(\alpha)^2 + n^2 - 1 + 2 \cdot \sqrt{\frac{\cos(\alpha)^2 + n^2 - 1}{n^2}} \cdot \cos(\alpha) \cdot n} \tag{14}$$

The refractive index of cellulose is approximately 1.5 (Fink, 1992), which is virtually the same as that of typical waxes like bees' wax. The refractive index of water is 1.3. The behavior of the reflection coefficient in dependence on the angle of incidence is depicted in **Figure 14** for n=1.5 (wax or cellulose) and for water.

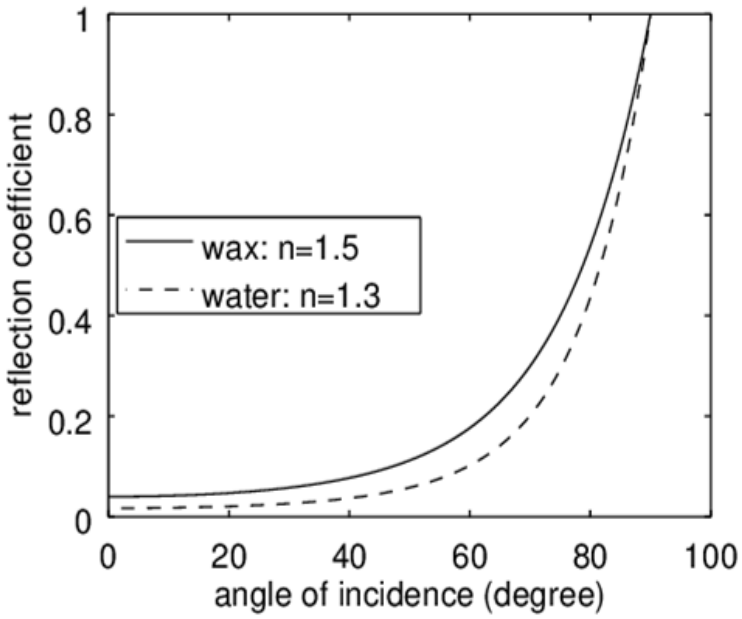

Figure 14: Reflection coefficient dependent on the angle of incidence. *The functions were calculated according to Eq. 3, using values for bees' wax and water covered bees' wax as a model. Clearly, the wetted surface has a lower reflection coefficient for all angles of incidence and thus would appear darker. (Image as shown in Hischen et. al (2017))*

Clearly the reflection coefficient of the dry material is much higher than for water. Thus the dry material appears brighter while the wetted material, keeping a water film on the surface is less reflective and thus

appears darker. As the reflection coefficients of wax and cellulose are virtually the same, the degree of darkening is similar for wood and for the wetted bugs covered with a wax layer.

Of course, this is only a rough estimation neglecting further reflections on deeper layers, light scattering and the influence of other materials than wax and cellulose, which of course also appear in our samples. Furthermore n=1.5 is the refractive index of bees' wax. Due to the very limited amounts of bug's cuticular waxes, we were not able to measure the refractive index of this material. Nevertheless, it appears plausible that a matched change of the reflection coefficient of cuticular waxes and bark material is the clue for the adaptive camouflage exhibited by the flat bugs under investigation.

This chapter so far, described and tried to explain the color change of Dysodius when exposed to water. As a matter of fact though, it is not that common for insects to show surfaces that interact with water in such a positive way, as we can find it on *Dysodius*. Hence it needs to be investigated, what morphological and chemical features render the bugs' surface wettable in the first place.

3.2 Wettability of *Dysodius*: Morphological and chemical investigation

As shown so far, the ability of *Dysodius* to change color when wetted depends on exactly this: The ability to get wetted, e.g. to spread water quickly across the whole dorsal body surface. As explained in chapter 2.2, liquid surface interaction always depends on two main features: 1) The chemistry of a surface, and 2) its morphological features (e.g. its roughness). In order to figure out why *Dysodius* is wettable as it is, it therefore it becomes necessary to know those two features. This chapter deals with the investigation of mainly named features in order to come up with an explanation on why adaptive camouflage becomes possible on *Dysodius* in the first place.

3.2.1 Materials and Methods

Chemical analysis

The first step to determine a materials behavior is to figure its chemical behavior. This will ultimately determine its basic contact angle and therefore its basic behavior towards a liquid: Hydrophilic or hydrophobic. Towards this end contact angle measurements have been performed and different chemical analysis were carried out in order to identify the substances responsible.

Contact angle measurements

The wax of two specimens of *Dysodius magnus* was dissolved from the bugs' abdominal, dorsal surface by carefully washing them with hot chloroform (Serva, Germany). The chloroform was heated in a beaker while stirring until the boiling point at 61° C was reached. While the bug was held with tweezers, it was rinsed multiple times with the hot chloroform from a pipette. The residue was collected in a fresh glass beaker and immediately covered to prevent evaporation loss. Three round glass coverslips (10 mm Ø) were washed in hot chloroform separately, additionally rinsed with ethanol (Serva, Germany) and left to dry. The dry coverslips were placed at the bottom of the beaker containing the wax-residue and the cover was removed. After all chloroform was evaporated, the coverslips were covered with a thin and even layer of cuticle wax. The waxed coverslips were then used to perform contact angle measurements on a custom build contact angle measurement setup. Each slip was measured on five different positions with 3 µl droplets of demineralized water (n = 15) and the contact angles were calculated.

Chemical analysis of cuticle waxes Part I: GC-MS (Gas chromatography with mass spectrometry, as presented in Hischen et al. (2017) and Reiswich (2013)

Chloroform (Serva, Germany) was used to dissolve the topmost layers of cuticle waxes on one specimen of *Dysodius lunatus* as well as *D. magnus*, where we expected to find surface active components that interact with water. TEM images in the following chapter show that this attempt was successful. The samples' abdomens were carefully rinsed three to four times with 5 ml of chloroform, in order to dissolve surface components. Samples were then dried in a heating module (Reacti-Therm Heating Modul, PIERCE, USA), down to a volume of 50 µl, before derivatization with 10 µl pyridine (Sigma-Aldrich, Germany) and 10 µl N,O-bis(trimethylsilyl)trifluoroacetamide (BSTFA, Sigma-Aldrich, Germany) was done. Samples then were again dried at 70° for 30 minutes before being re-dissolved in 50 µl chloroform and conveyed into auto-sampling veils. For *D. magnus* (first tested samples), this was the sole procedure. For gas chromatography, an Agilent 7890 A GC system (Agilent Technologies, USA) with mass spectrometer detector was used. A sample volume of 1 µl was injected via cool-on-column method into a DB1 column with a length of 30 m, 320 mm diameter and a stationary phase thickness of 100 nm. Carrier gas was helium, which was introduced for the first 5 minutes at 50 kP pressure before ascending to a final pressure of 150 kP in 3 kP/min steps. 150 kP were then held for 90 minutes. The heating protocol was 50 °C at injection for two minutes, raised by 40 °C min^{-1} till 110 °C, held for two minutes at 110 °C, raised by 3° min^{-1} till 320 °C and then held for 50 min at this final temperature.

Chemical analysis of cuticle waxes Part II: HPLC-MS (High-performance liquid chromatography with mass spectrometry, as shown in Hischen et. al (2017)

For HPLC-MS analysis the chloroform solution used to dissolve the topmost layers of cuticle waxes of two dried specimens of *Dysodius magnus* was brought to dryness with a gentle stream of nitrogen in a sampling vial and 0.5 mL acetonitrile was added to dissolve low molecular compounds. The resulting solution was used for injection. An Agilent 1100 series HPLC system (Waldbronn, Germany) equipped with a degasser, a quaternary pump and an autosampler was applied. Analytes were separated on a Kinetex C18 column (50 mm x 4.6 mm, particle size 2.6 µm; Phenomenex, Aschaffenburg, Germany) using a water/acetonitrile gradient. Starting conditions were set to 75% solvent A (water with 0.1% formic acid) and 25% solvent B (acetonitrile with 0.1% formic acid). Mobile phase B was linearly increased to 90% within 19 minutes, which was then kept constant from minute 19 to 23. The gradient was changed back to starting conditions

for re-equilibration; these conditions were held for 5 minutes. Flow rate was set to 1.0 mL min-1, temperature of the column heater was fixed at 30 °C and an injection volume of 20 µL was selected. MS detection was carried out using an Agilent 6520 QTOF equipped with electrospray ionization (ESI) and operated in the positive mode. MS parameters were as follows: drying gas flow 10.5 L min-1, drying gas temperature 350 °C, nebulizer pressure 50 psi, capillary voltage 3750 V, fragmentor voltage 175 V. The HPLC eluent flow was split (0.33 mL min-1) before entering the ESI source.

Morphological analysis

Scanning and transmission electron microscopy (SEM & TEM); Protocol as used in (Hischen et al., 2017; Reiswich, 2013)

SEM images were obtained with a Philips SEM 525 (Philips, Germany) at 15 kV. Air-dried bug samples were additionally dried on silica gel for 24 hours before sputter coating with gold using a Polaron E5200 auto-coating device (former Polaron Unlimited, Great Britain) at 1 kV for a duration of 180 s.

For TEM analysis, pieces of dried specimen were first fixated for 12 hours at 4°C in 2.5% glutaraldehyde solution (SERVA, Germany) in 0.2 M cacodylate buffer, followed by washing two times 15 minutes in pure cacodylate buffer. For further fixation and contrast enhancement, this was followed by 1 h incubation in 1% osmiumtetroxide (Fluka, USA) solution, again in cacodylate buffer, at 4°C. Two times washing for 15 minutes in pure cacodylate followed by two times 15 minutes in distilled water. Afterwards samples were dried in an ascending alcohol series (30%-70%). Negative staining was then applied by incubating in 1% uranylacetate (Serva, Germany, in 70% ethanol) for 2 hours, before washing twice in 70% ethanol and finishing the drying row up to 100% ethanol. Afterwards ethanol was replaced by 2 times 30 minutes in pure propyleneoxide (Serva, Germany) and followed by overnight incubation in a mix of two parts propylene oxide and one part epon (Epon quick mix, Serva, Germany). The samples were finally embedded in pure epon and polymerized for 72 hours at 70°.

Ultra-thin slices for TEM were cut with an ultra-microtome (OM 43, C.Reichert, Austria) and diamond knives. Post-staining of the slices was realized by 0.2% lead citrate (Fluka, USA) and 0.2% uranyl acetate. The former incubated for 7 minutes, the latter for 20, followed again by washing of the samples after each step. For image acquisition, a Zeiss EM 10 (Zeiss, Germany) was used at 60 kV.

3.2.2 Results

Chemical analysis

The contact angle measurements yielded a surprisingly low contact angle of 43.9° ± 4.7° (n=15), clearly showing that the surface waxes of *Dysodius* exhibit hydrophilic properties. A typical droplet situation of the measurement can be found exemplarily in **Figure 15**.

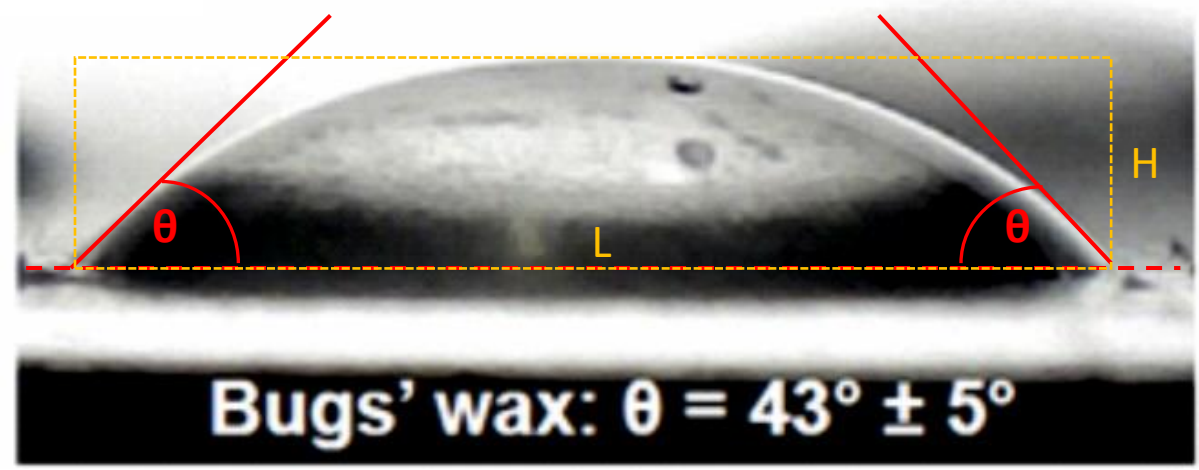

Figure 15: Example outcome of contact angle measurement on extracted surface wax of D. magnus. *Red, dashed horizontal line marks the horizon.* Θ indicates the resulting contact angle on both sides of the droplets triple point. The yellow dashed box marks the border used for calculating L (= length) and H (=height) of the droplet.

Figure 15 also shows exemplarily how the contact angle was calculated from the images acquired by the measurement setup. Following formulas were used in order to calculate θ from the length (L) and height (H) of the droplet, using the radian measure (b):

$$b = 2 \cdot arctan\left(2 \cdot \frac{H}{L}\right) \tag{15}$$

$$\theta = \frac{360}{2 \cdot \pi \cdot b} \tag{16}$$

At this point it is also interesting to note, that bugs (no matter if *D. magnus* or *D. lunatus*) that were washed with chloroform, showed no wetting behavior anymore. In contrary, the bugs turned even hydrophobic.

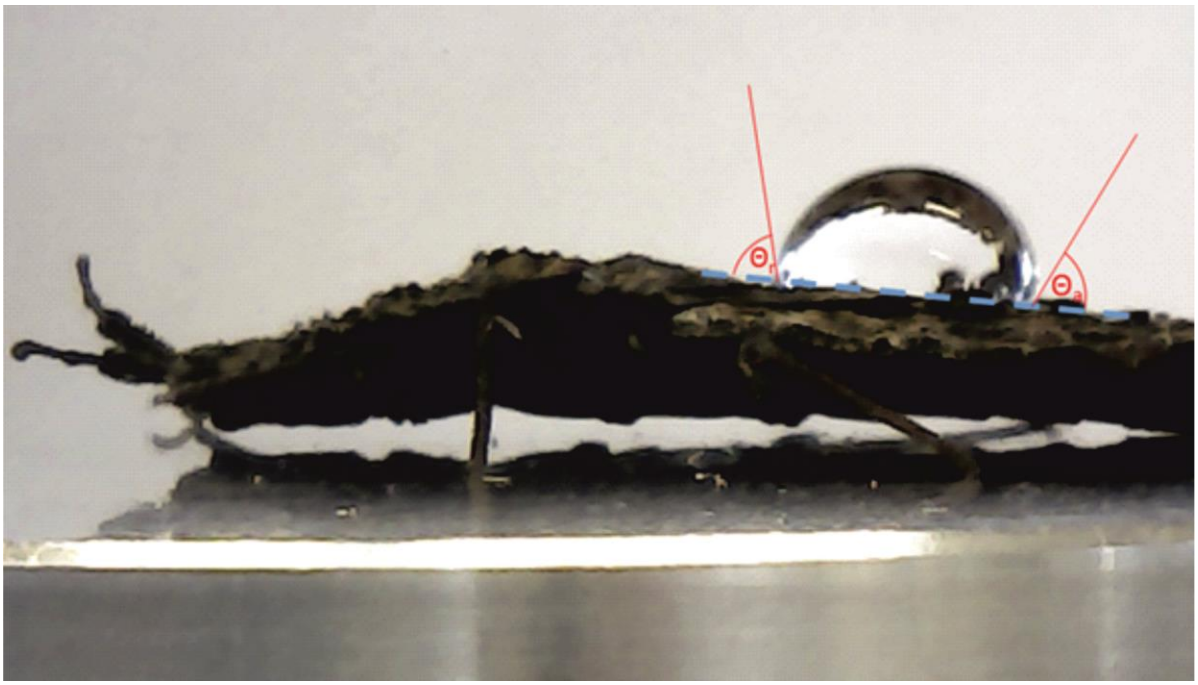

Figure 16: Contact angle situation on a de-waxed bug. *Due to the bumpy and rough body shape of Dysodius it is difficult to find the exact horizon for the sitting droplet (here 15 µl distilled water). For this example, we found an advancing contact angle (Θ_a) of approx. 115°, as well as a receeding contact angle (Θ_r) of approx. 104°. As both angles are clearly >90°, the bugs body surface shows a hydrophobic behavior after dissolving the surface waxes. Figure as shown in Hischen et. al (2017).*

As shown in **Figure 16**, a bug that was subjected to chloroform washing, does not show any hydrophilic behavior anymore. Contact angles above 100° indicate that the surface in fact turned hydrophobic.

Chemical analysis of cuticle waxes Part I: GC-MS (Gas chromatography with mass spectrometry, as presented in Hischen et al. (2017) and Reiswich (2013)

In order to be able to get a first idea of the physical and chemical properties of the cuticular wax, especially the outer layers which directly come into contact with water, the wax had to be removed gently from the cuticle without dissolving deeper layers or substances from within the bug's body. This was done by washing the animals with chloroform. Transmission electron micrographs of so treated animals show that in fact only the outer layers of the cuticle waxes was removed but basal wax was still present on the bug's body (see **Figure 32**).

To determine what molecules are present in the bugs` waxes, they were dissolved and subjected to gas chromatography with subsequent mass spectrometry (GC-MS). This first analysis yielded some main substance classes that could be identified. Besides mono- di- and triglycerides with chain-length ranged from C 12 to C 29, many free fatty acids (mono- and di-carboxylic acids) were detectable. It was not

possible to determine whether these are really fatty acids or soaps, i.e. salts of the fatty acid. An exact quantification of the amounts of the different substances was not possible due to the small amounts of samples available. An overview of the found glycerides can be found in following **Table 1**. A complete list of identified substances is attached in the appendix.

Table 1: Overview of most notable glycerides identified by GC-MS, as shown in Reiswich (2013).

Fatty acids	**Monoglycerids**
Chain length: C 12 to C 24 **Degree of Saturation** saturated mono-unsaturated poly-unsaturated **Most prominent** Hexadecanoid acid Octadecanoid acid	**Chain length:** C 16 and C 18 **Degree of Saturation** saturated mono-unsaturated **Most prominent** Hexadecanoid acid glycerinester Octadecanoid acid glycerinester
Diglycerides	**Triglycerides**
Chain length: C 16 to C 18 **Degree of Saturation** saturated mono-unsaturated **Most prominent** Bis-Hexadecanoid acid glycerinester Hexadecanoid acid glycerinester Octadecanoid acid glycerinester Bis-Octadecanoid acid glycerinester	**Chain length:** unknown **Degree of Saturation** unknown **Most prominent** Triacylglycerol

Chemical analysis of cuticle waxes Part II: HPLC-MS (High-performance liquid chromatography with mass spectrometry, as shown in Hischen et. al (2017)

Furthermore, high-performance liquid chromatography mass spectrometry (HPLC-MS) was performed in order to verify the GC-MS findings. Derivatization was not required in case of HPLC-MS. Detection was carried out in positive mode to be able to detect the glycerides. Glycerides were observed almost exclusively as sodiated $[M+Na]^+$ pseudomolecular ions. As expected fatty acids were detected as protonated $[M+H]^+$ as well as (in some cases more abundant) sodiated $[M+Na]^+$ species. Saturated and unsaturated fatty acids (mono- and di-carboxylic acids) were detected. For some compounds, a characteristic water loss due to in-source fragmentation was observed indicating that hydroxylated fatty acids are also present in the sample. Overall, the complementary HPLC-MS measurements confirmed the previous GC-MS findings, but in total, a smaller number of compounds was detected. Additionally to the fatty acids and glycerides, significant amounts of erucamide (cis-13-Docosenoamide) were identified in HPLC-MS. This substance is well known to be an often-found contamination in analytical chemistry. We are aware of this and therefore all treatment of the substances was done with glass equipment only avoiding any lab-plastics. All glassware was initially cleaned with chloroform (analytical grade) in order to avoid contaminations. Still, fatty acids, soaps and the dubious erucamide, had at least one commonality: All these substances have polar and non-polar sides (amphiphilic character) and make therefore good candidates to act as mediators between hydrophobic insect wax on the one side, and polar water molecules on the other.

Morphological analysis

As mentioned earlier, the resulting behavior of a surface towards a given liquid depends on two factors: The chemistry and the morphology. After investigating the apparent behavior of *Dysodius* – the wettability and resulting adaptive camouflage – as well as the chemistry, morphological analysis needed to follow up in order to complete the investigation. Towards this end electron microscopy was done to identify surface morphological features that might contribute to observed liquid interaction.

Under the SEM, both flat bug species revealed an interesting surface structure, mainly composed of small, pillar like microstructures (in the following called “naps”). The naps cover most of *Dysodius*’ body surface, the only exception being the wings.

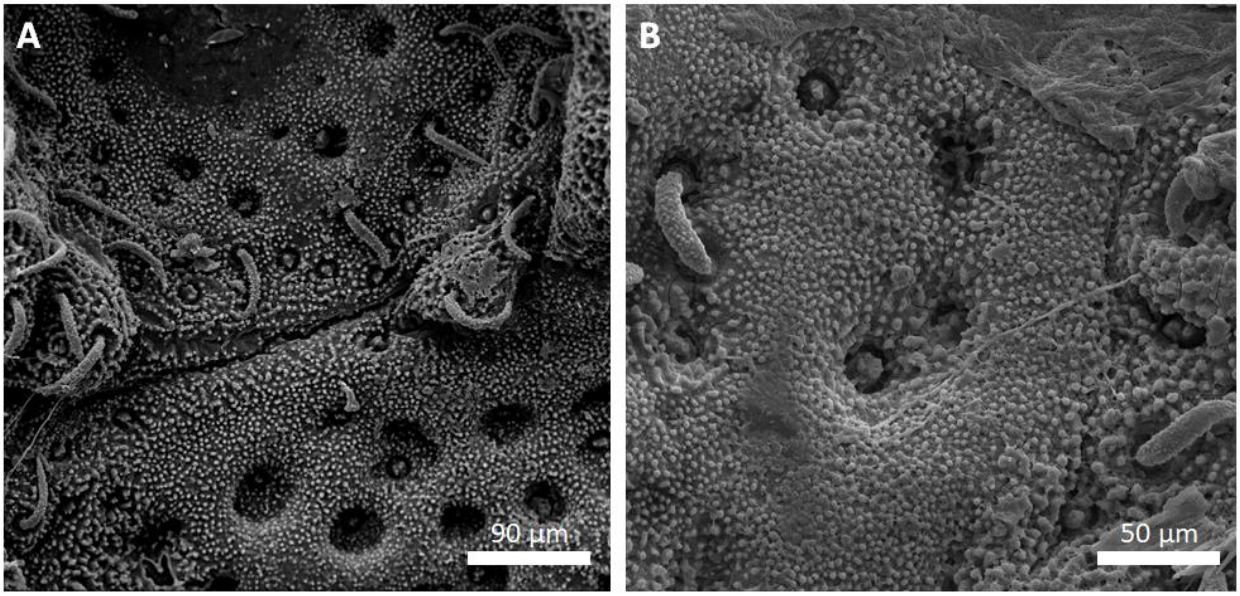

Figure 17: Surface of D. lunatus and D. magnus. A *Dorsal part of connexical plates of D. lunatus.* ***B*** *Dorsal part of connexival plates of D. magnus.*

As shown in **Figure 17**, the surfaces of both investigated species of *Dysodius* show virtually the same surface features. The naps can be found everywhere with exception of the wings' surface and the direct surfaces of the apodemes. Measuring the naps (*D. lunatus* n = 50, *D. magnus* n = 50) on different parts of the surface yielded mean values of 1.9 ± 0.4 µm for the diameter and 4.9 ± 1.4 µm for the distance between individual structures on both species. For the measurements the freeware Fiji (ImageJ, NIH, United States) was used. The found naps clearly play a role in the wetting behavior of *Dysodius* since they alter, or more precisely, shift the contact angle of an already hydrophilic surface according to the wetting model of Wenzel as explained in chapter 2.2. A detailed statement towards this will follow in the discussion.

When looking at the SEM images of *Dysodius*, one can identify even more interesting surface structures. Besides the above mentioned naps, the electron microscope images also reveal relatively even dristributed conglomerations of round, bowl-shaped indents in the surface and setae (**Figure 18**, **Figure 19**). In between the connexival plates and the glabrous areas, also the intersegmental sutures can be identified (**Figure 20**), which will play a role in the following Chapter 3.3.

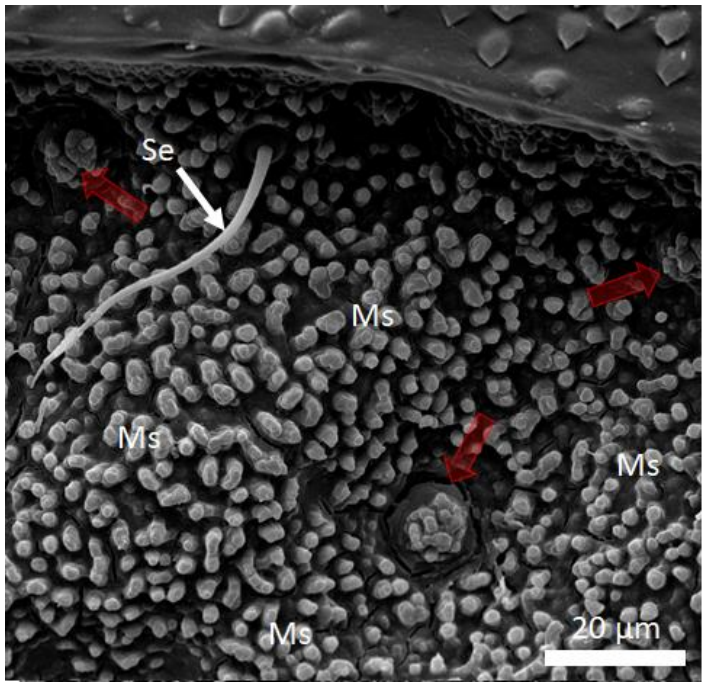

***Figure 18: Magnification of the surface features of Dysodius (in this case D. lunatus**). Most areas are covered by microstructures (Ms) in form of naps. Setae (Se) can be found (some covered in wax, other not) and also plenty of bowl shaped indents, which seem to have high densities of naps on them (red arrows).*

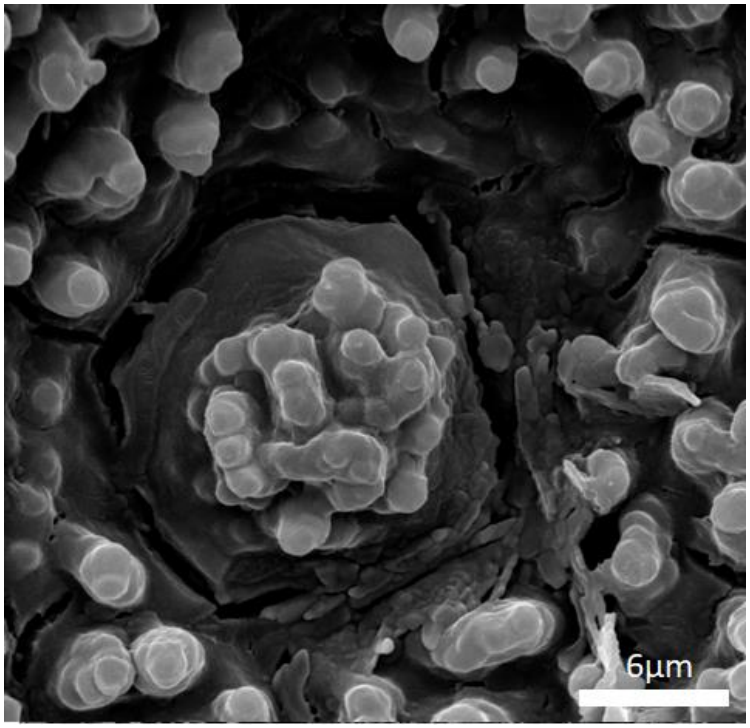

Figure 19: Magnification of the central, in Fig. 9 shown bowl-shaped indent with densely accumulated naps on its center top.

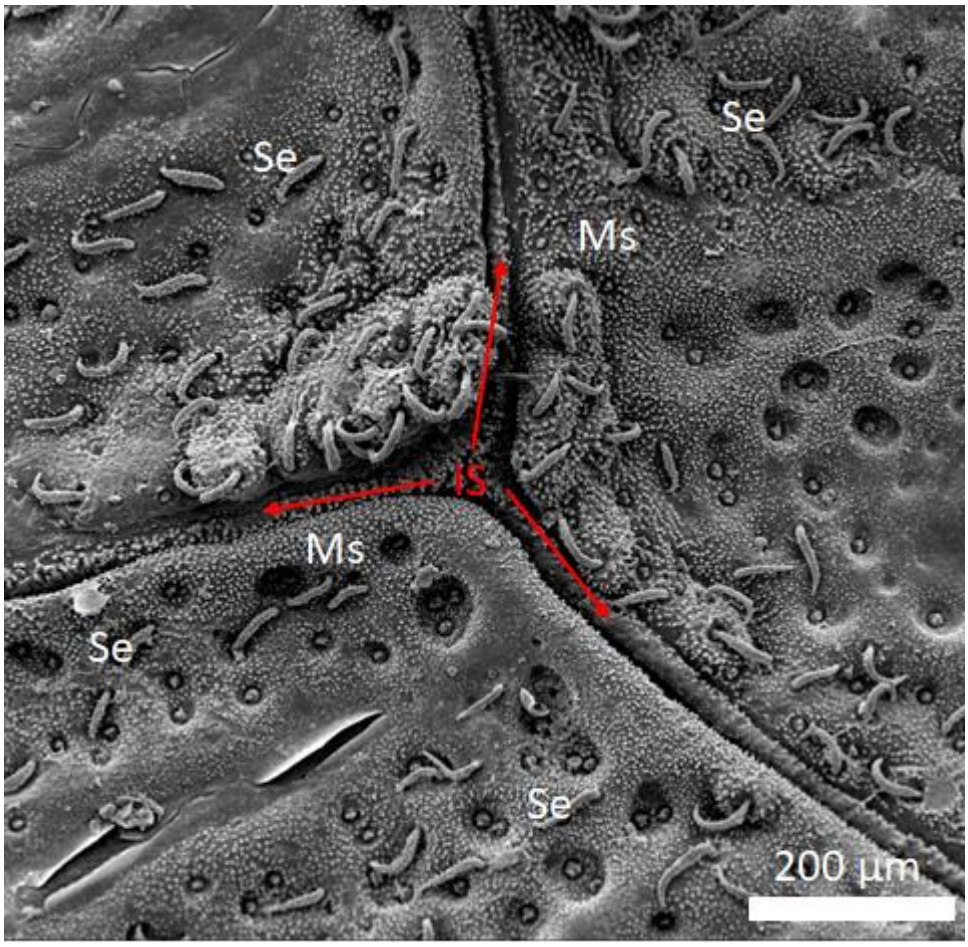

Figure 20: Overview of the crossing-point between connexival plates. *Again Setae (Se) and naps (Ms) can be found in abundance, covering most of the surface. In between the connexival plates clearly the intersegmental sutures (IS) can be identified. Depending on the stage of the dried and sputtered specimen the sutures were folded (like here) or more stretched. Interestingly enough, naps can also be found on the folds of the IS.*

While doing pretests for the observing the adaptive camouflage effect (see chapter 3.1) and for following wetting experiments (see chapter 3.3) it became apparent that the only non-wettable part of *Dysodius* is the membranous part of the wings. When a droplet of water is applied to the wings, it shows a rather hydrophobic behavior and tends to sit sessile. Slight movement however (e.g. shaking or vibrating the bug) usually is enough to bring the drop into contact with either the cuticle of the wing-surrounding glabrous area, or the corium. Since here the surface is covered with naps, the droplet gets spread across the abdominal surface. The following **Figure 21** and **Figure 22** capture the morphological situation of the wings' dorsal surface.

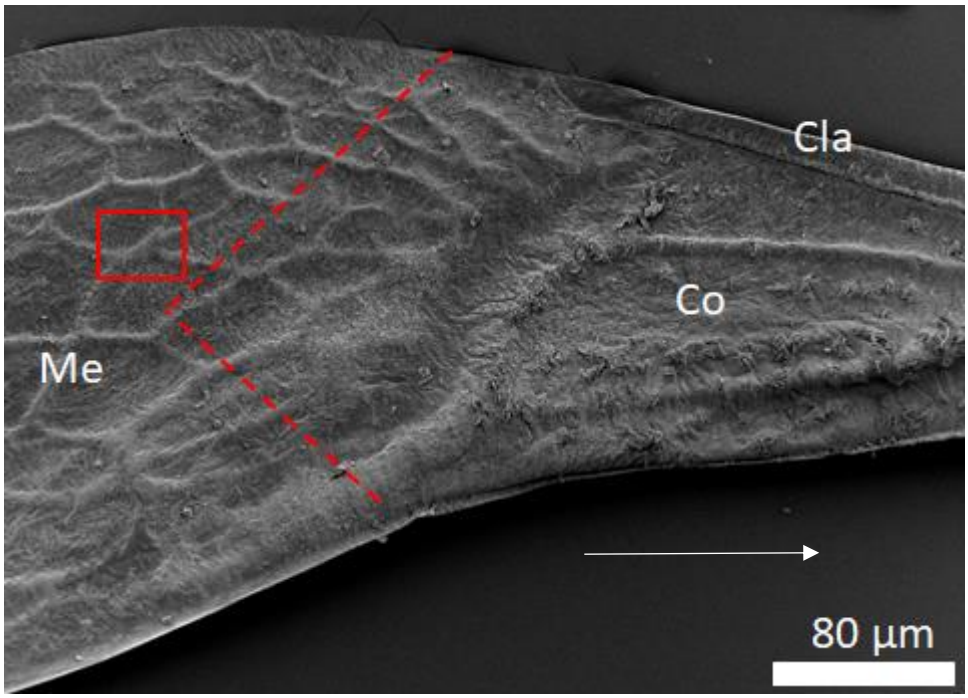

***Figure 21: Morphological hemelytra-overview (top) of Dysodius (in this case right front wing**). The top part of the wing (right hand side on this image) consists of the sclerotized corium (Co) and clavus (Cla), while the back part (left hand side) is the flight membrane. The red dashed line marks the transition zone from where on wetting in direction of corium is possible, while the membranous part acts hydrophobic. The red box marks the position for the magnified image in **Figure 22**. The white arrow shows the direction of the head.*

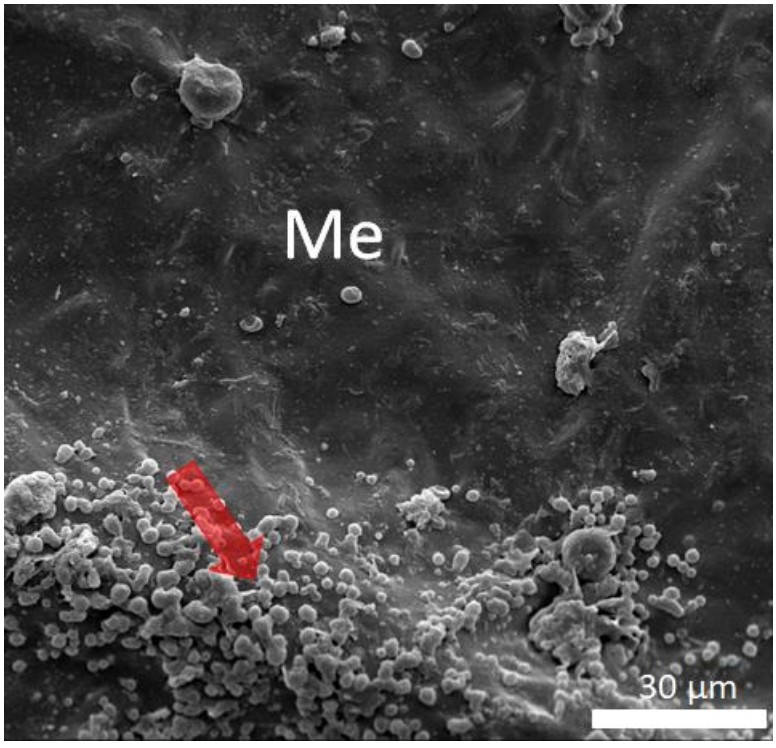

***Figure 22: Detail view of the red box in Figure 21.** The red arrow marks a vain coming from the corium that clearly shows naps, while the membranous part of the wing (Me) is virtually microstructure free.*

Since in natural resting position the hemelytra cover the hind wings, only the dorsal (top) surface comes in contact with water when it rains. Hence, it was expected that the bottom side, as well as the covered hind wings do not show any coverage with waxes and microstructures (naps). Exactly this was found, as the following **Figure 23** shows.

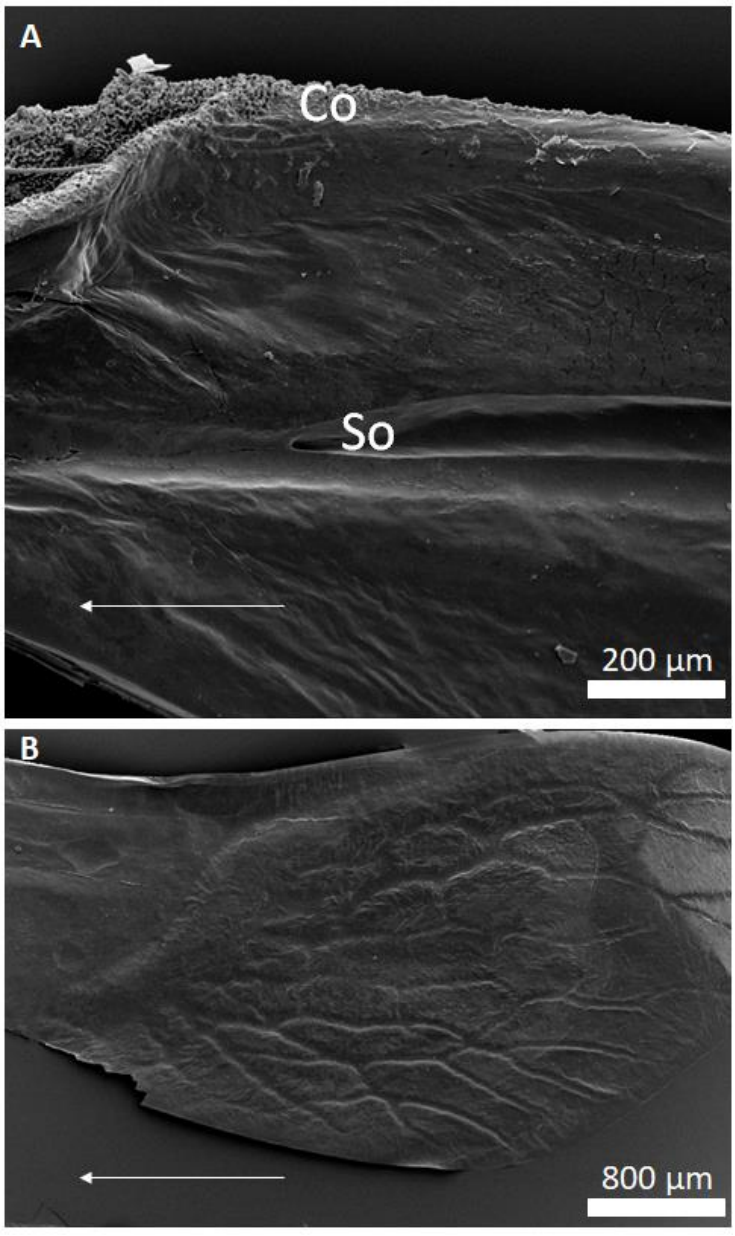

***Figure 23: Morphological features of bottom ventral side of hemelytra and hind wing**. **A** Ventral side of hemelytra, besides the edge of the corium (Co) no microstructure can be found. The central channel is the so called hemelytra socket (So). **B** Overview of left hind wing. Again, no microstructure could be identified.*

Figure 23 reveals that with exception of the sclerotized areas of the hemelytrae, no part of *Dysodius* wings exhibits wax coverage and/or microstructure. Or spoken differently: Only the dorsal side of the membrane shows no microstructure but supposedly comes into contact with water (rain) in a natural resting position of the wings. Furthermore, **Figure 23** shows the channel structure of the ventral side of the hemelytra, the so called socket (according to Gorb & Goodwyn, 2003). This morphological feature is part of the wing interlocking mechanism of bugs and enables hind wings and hemelytrae to be locked together in flight.

The fact that the membrane part of the hemelytra does not show hydrophilic behavior as the rest of *Dysodius* surface, and in addition also doesn`t exhibit any wax coverage and naps, fortified the suspicion that exactly these features play a key role in the wetting behavior of *Dysodius*. To verify this assumption, bugs that were earlier used for chemical analysis of the waxes (e.g. de-waxed), were investigated in the SEM as well, since they also showed hydrophobic behavior (refer to **Figure 16**). In order to make sure that the surface was as wax free as possible, the bugs were additionally washed for 2 min in boiling 10% KOH solution.

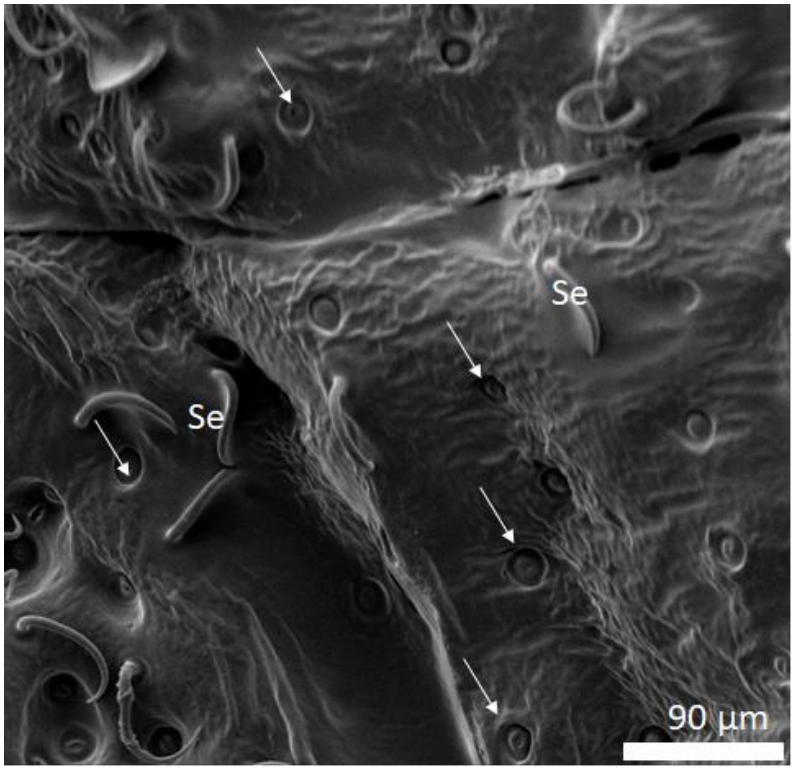

Figure 24: Image of completely de-waxed surface of D. magnus connexival plate. *Clearly, all waxes and all naps are removed. Setae are again visible and the bowl-shaped indents (as already shown in **Figure 18** and **Figure 19**) reveal their underlying structure (white arrows).*

The smooth chitinous surface that is revealed in **Figure 24** clearly shows two things: 1) All waxes are removed and with the waxes also the naps disappeared, and 2) without the surface waxes the bowl-shaped indents show that they have an underlying structure that strongly look like gland orifices. Magnification reveals even more details:

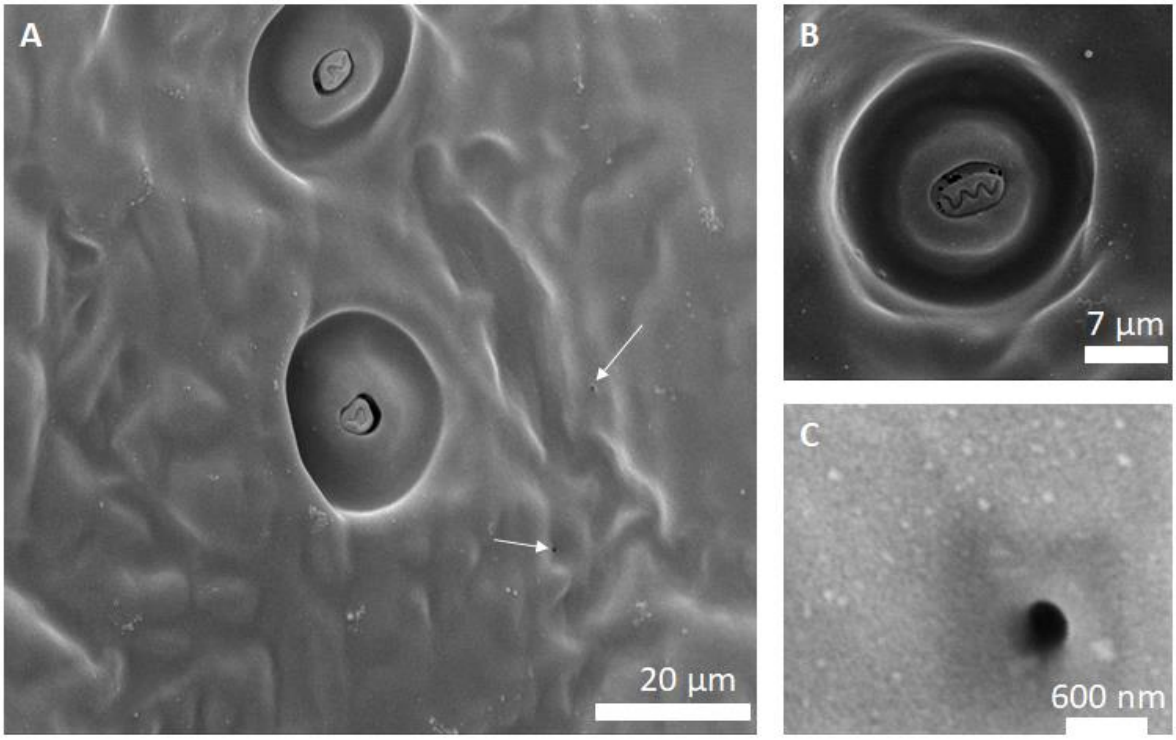

***Figure 25: Detail view of presumable glands**. **A** Magnified, the bowl-shape indents show similarities with glands and complex, often sinusoidal shaped openings. In addition, small openings in the cuticle become apparent at places were the surface waxes were completely cleaned away (white arrows). **B** Detail view of a sinusoidal shaped gland opening (as shown in Hischen et.al 2017). **C** Zoom of the lower opening marked by the arrow in A.*

Besides a more detailed look onto the microstructure of the presumable wax glands (bowl-shaped indents), which revealed complicated, often sinusoidal orifices (**Figure 25 B**), **Figure 25** also revealed the presence of even smaller openings in the chitin surface (**Figure 25 A,** white arrows; detail shown in **C)**. With diameters of ~ 200-300 nm, these might be secretion openings of smaller wax glands as well.

A common way to get cross-sectional views of tissue in SEM, for example to analyze the underlying morphology of the structures shown in **Figure 25**, are so called freeze-fractures. Towards this end, the biological sample needs to be frozen at very low temperatures and then cracked under strain. For this work, an abdomen of *D. magnus* was frozen for three minutes in liquid nitrogen (Linde, Germany) and then cracked into tiny fragments with the help of a scalpel. The fragments then were treated according to the protocol for SEM preparation (see chapter 3.2.1) and screened for glands and channels under the SEM.

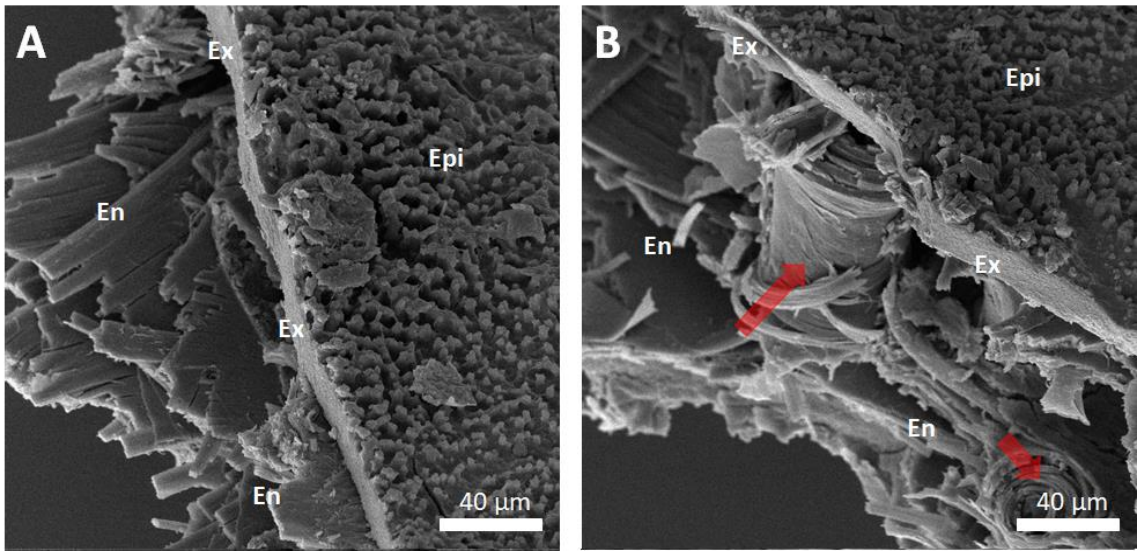

Figure 26: Overview of the cuticular layers of D. lunatus from freeze fractured sample. A *The layered composition of the bugs cuticle becomes apparent under the SEM. One can see the chaotic layered sheets of the endocuticula (En), the dense matter of the exocuticula (Ex) as well as the naps of the epicuticula (Epi).* ***B*** *On multiple places, cylindrical structures protrude through the whole cuticle (red arrows).*

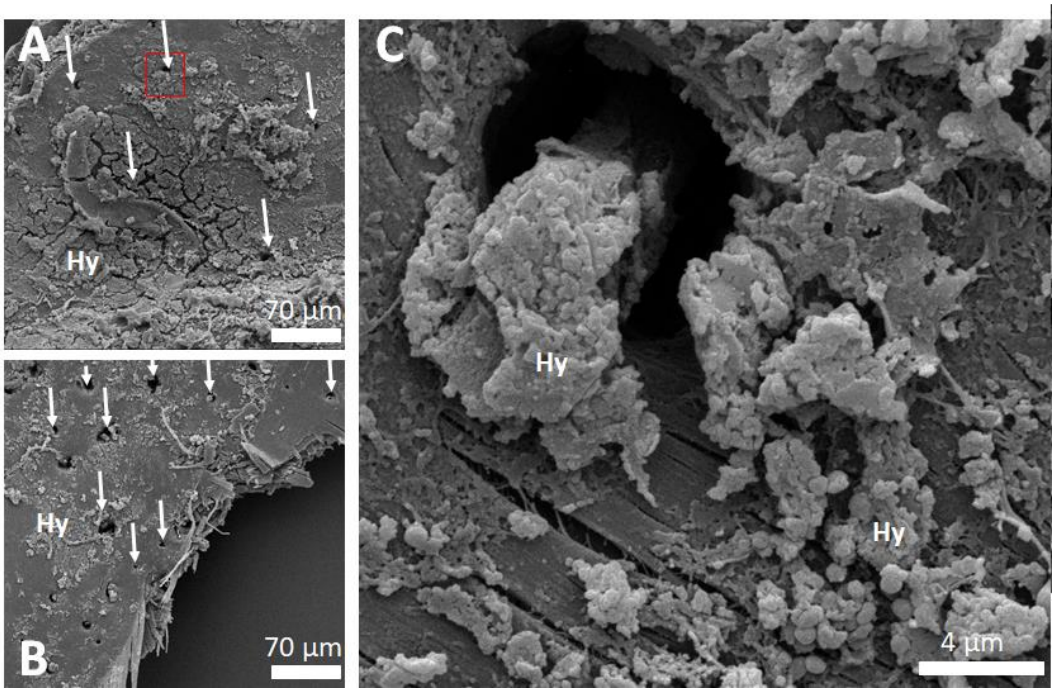

Figure 27: View from the inner lumen onto the endocuticula and hypodermis. A *and* ***B*** *Different positions of the inner endocuticula and hypodermis of D. lunatus. A "crusty" matter, covering most of the inner surface, is supposedly fragments of the hypodermis (Hy). The images also show a high density of holes through the cuticle (white arrows).* ***C*** *Magnification of the red box in A. The image shows a close-up of one of the cuticle holes, showing a diameter between 6 and 8 µm. Fragments of the hypodermis are covering the closest vicinity as well as are protruding into the whole itself.*

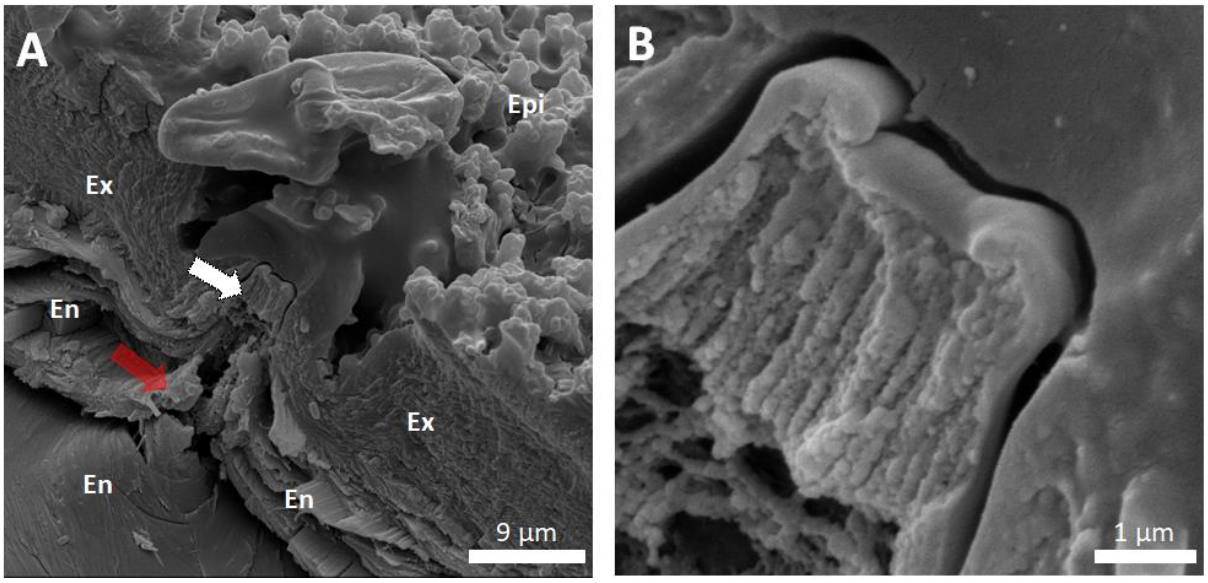

Figure 28: Cross-section through a gland (red arrow). A *Overview of what with high possibility is the cross-section through one of the gland-structures shown in* ***Figure 25****. Clearly a cuticular funnel protrudes from and through the endocuticula (En). It also protrudes through the exocuticula, forming and bowl-shaped indent. The tip of the structure (white arrow) ends on height with the surrounding endocuticula and is covered with wax of the epicuticula (Epi).* ***B*** *Magnification of the tip structure. The tissue within seems to be filamentous, while top and side walls are of denser, sturdy looking material. Probably due to the freezing treatment, the surrounding wax was cracked away from the structure itself.*

The results gathered by freeze-fracturing (**Figure 26** and **Figure 27**) give a closer insight to the composition of *Dysodius'* cuticle. One can see that the endo- and exocuticula are easy separable by eye: the former usually identifiably by its filamentous and chaotically stacked composition, the latter by its dense appearance (**Figure 26**). **Figure 26 B** also shows round, or cylindrical protrusions that run through the complete cuticle. At this point it is assumed, that theses cuticle structures are the continuations through the cuticle, of the holes shown in **Figure 27** and are usually surrounded by hypodermis tissue on lumen side (**Figure 27 C**). These findings are even deeper verified by the "lucky" cross-section that is shown in **Figure 28**: The funnel and complete pathway of a presumable wax gland through the whole cuticle is depicted. The gland protrudes through the complete cuticle and ends in a rather complicated tip, which seems to be filled with a delicate and filamentous tissue. Clearly the tip of this gland is covered with surface waxes and high densities of naps can be found in its surroundings.

To verify some of the morphological findings from SEM analysis and in order to get an even better idea what is happening underneath the surface of *Dysosius*, TEM images of both species were done. Once again it became apparent that there were no crucial differences in the general physiological features (besides the overall body size), because of which the results of *D. lunatus* were chosen to be presented

representatively. Main focus was placed onto a) measuring the height of the naps in the cross-sectional view to have complete knowledge of dimensions, b) analyzing the general composition of the cuticle and c) retrieving even more information about the bowl-shaped indents (as seen in TEM images) and to verify if they might be glands or not.

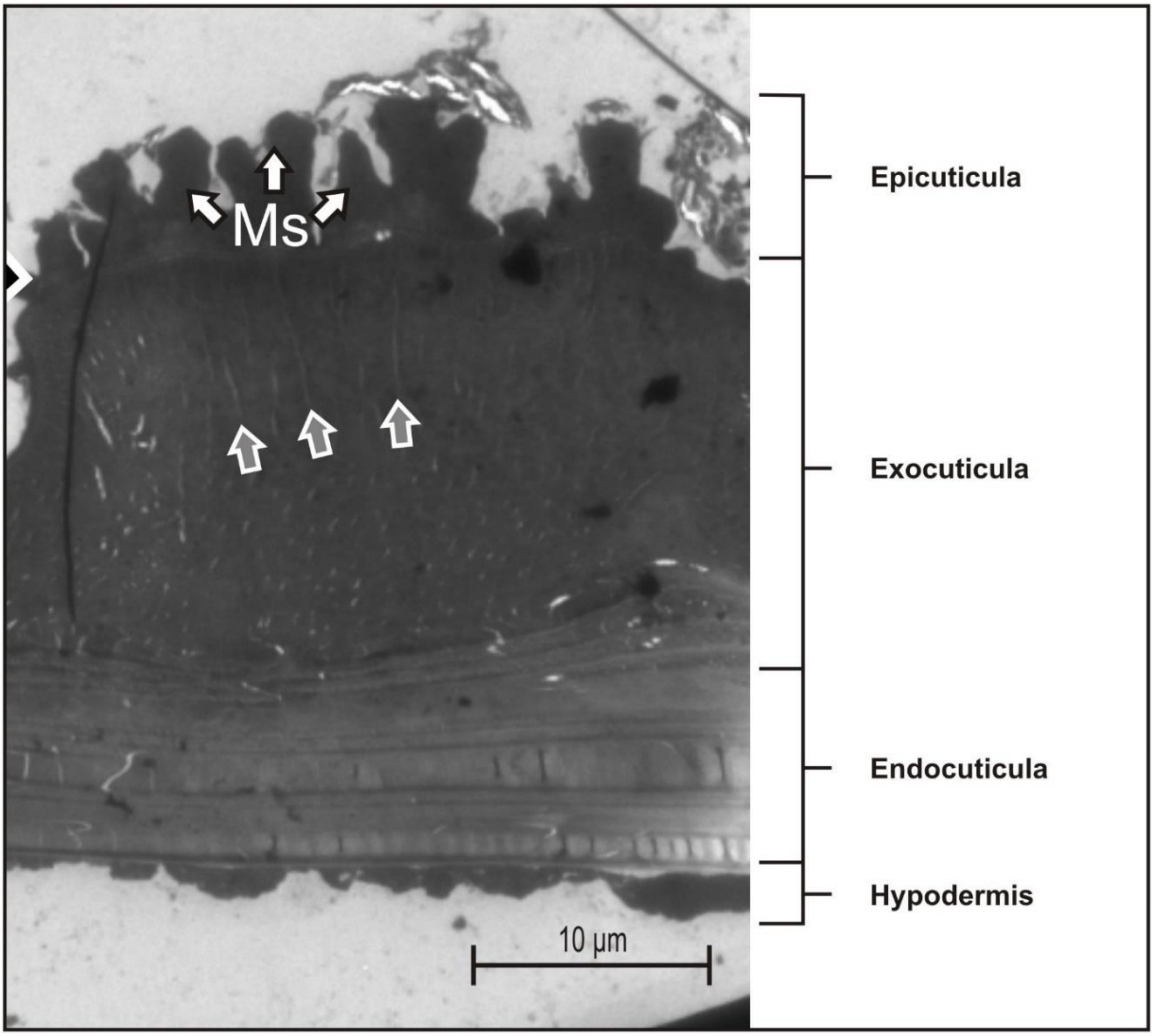

Figure 29: Overview of D. lunatus cuticle. *In the cross-section the naps (Ms, white arrows) of the epicuticula, as well as tiny channels everywhere in the exocuticula are visible (grey arrows). Image as shown in Hischen et. al (20017) and Reiswich (2013).*

Figure 29 reveals the layered composition of *Dysosius*' cuticle. The waxy epicuticula with the naps is followed by the chitinous exocuticula, which seemingly contains tiny channels. This is then followed by a comparably thin layer of chitinous endocuticula with a 90° degree flipped chitin orientation (when compared to exocuticula). The last layer then is formed by the hypodermis, which in this case only is visible as a fragmented leftover due to the dried state of the used specimen. 30 naps in cross-sections of *D.*

lunatus as well as *D. magnus* were measured with Fiji to determine the average height of the microstructures. As a result a mean height of 5.4 ± 1.5 µm was found.

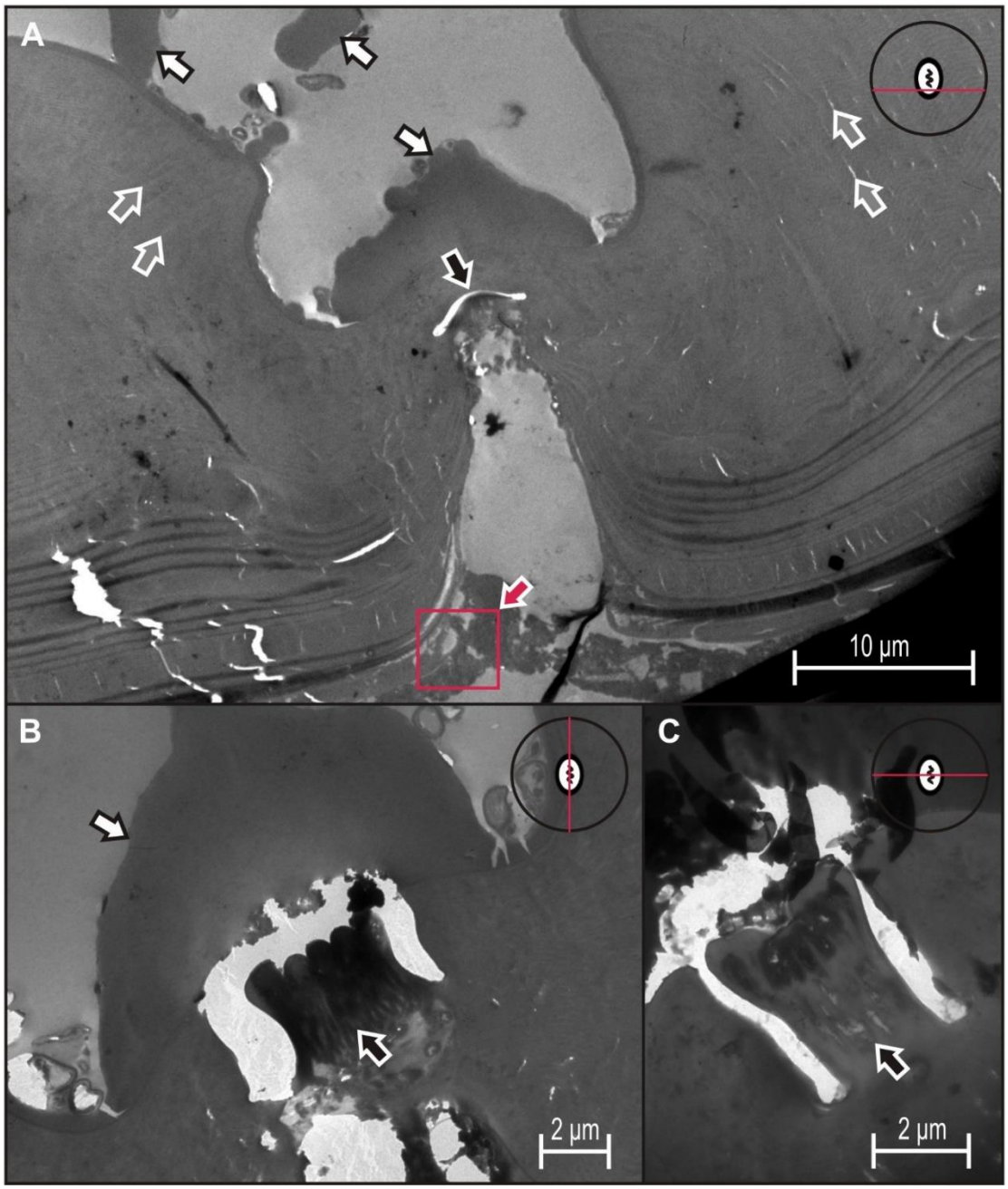

Figure 30: Different cross-sections of presumable glands as shown in Figure 28. A *Cross-section revealing the complete progression of the gland through all cuticle layers. Fragments of naps (white arrows), micro-channels (grey arrows) and the gland orifice (black arrow) could be identified. The red box and arrow mark a section of the image that is magnified in the following* ***Figure 31****.* ***B*** *Different cross-section of the gland. Surface wax (white arrows), as well as the microstructure of the orifice (black arrow) become apparent.* ***C*** *Vertical cross- section of a gland. Filamentous tissue can be recognized beneath the tip of the orifice (black arrow). The schematics in each top right hand corner of the images show the cut orientation. Figure as shown in Hischen et al. (2017) and Reiswich (2013).*

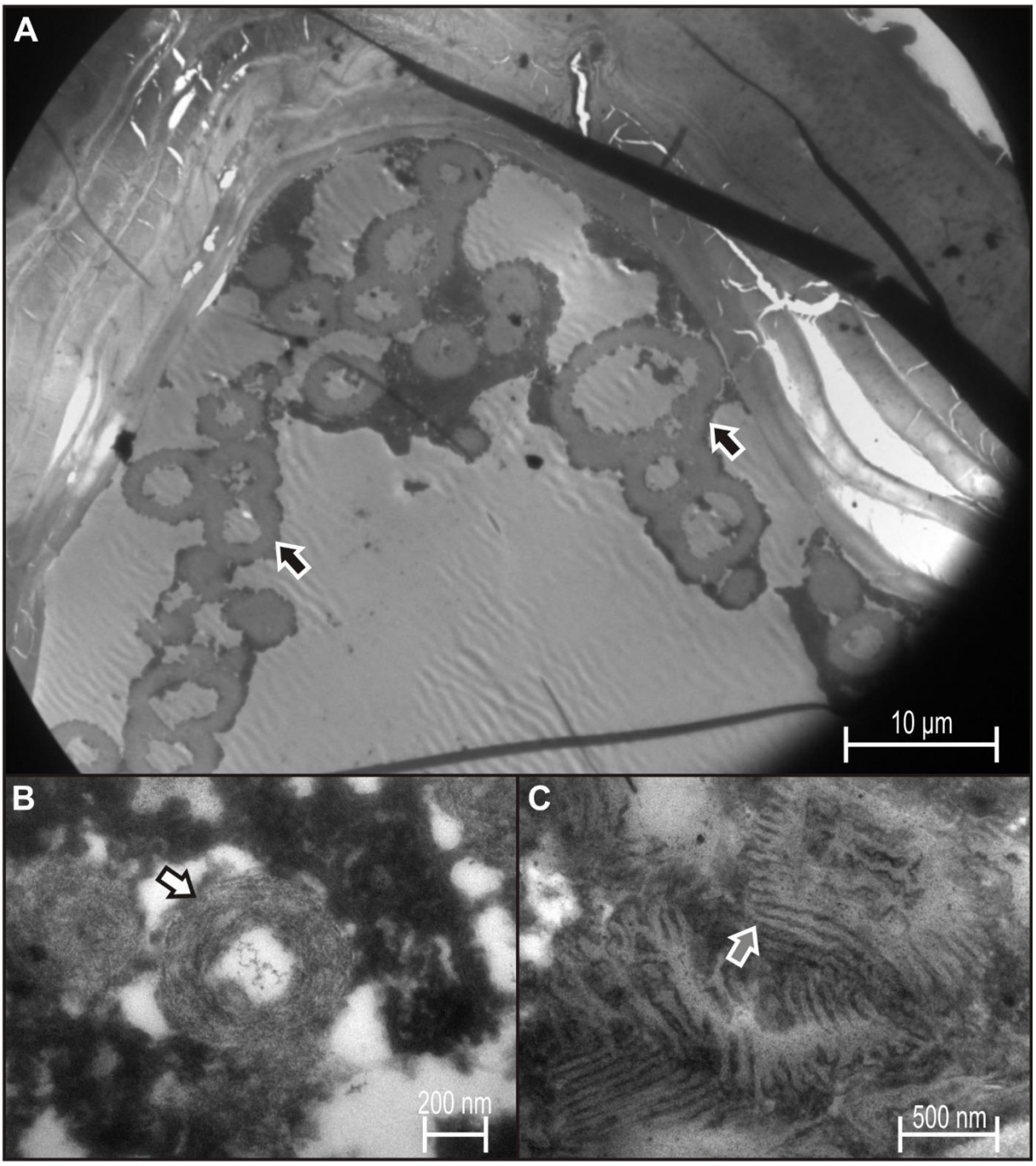

*Figure 31: Details of the red box shown in **Figure 30**. **A** Oenocytes (black arrows) could be identified in the hypodermis of direct proximity to the glands. **B** Also lamellar bodies were found (white arrow). **C** Smooth endoplasmatic reticulum was found in several spots of the hypodermis close to a gland channel through the cuticle. Figure as shown in Hischen et al. (2017) and Reiswich (2013).*

Figure 30 and **Figure 31** give a comprehensive overview of the morphology of the found glands with sinusoidal orifice, following their complete pathway through the cuticle and showing also attached cells and cell fragments in the hypodermis. The images indeed fortify the idea, that these structures indeed are

secreting glands that somehow are involved in the production of the waxy microstructures (naps), covering the surface of *Dysodius*.

As mentioned in the results for chemical analysis, additional TEM images were captured from specimen of *Dysodius* that were used in the wax analysis, and therefore were subjected to chloroform treatment (after which they were rendered hydrophobic).

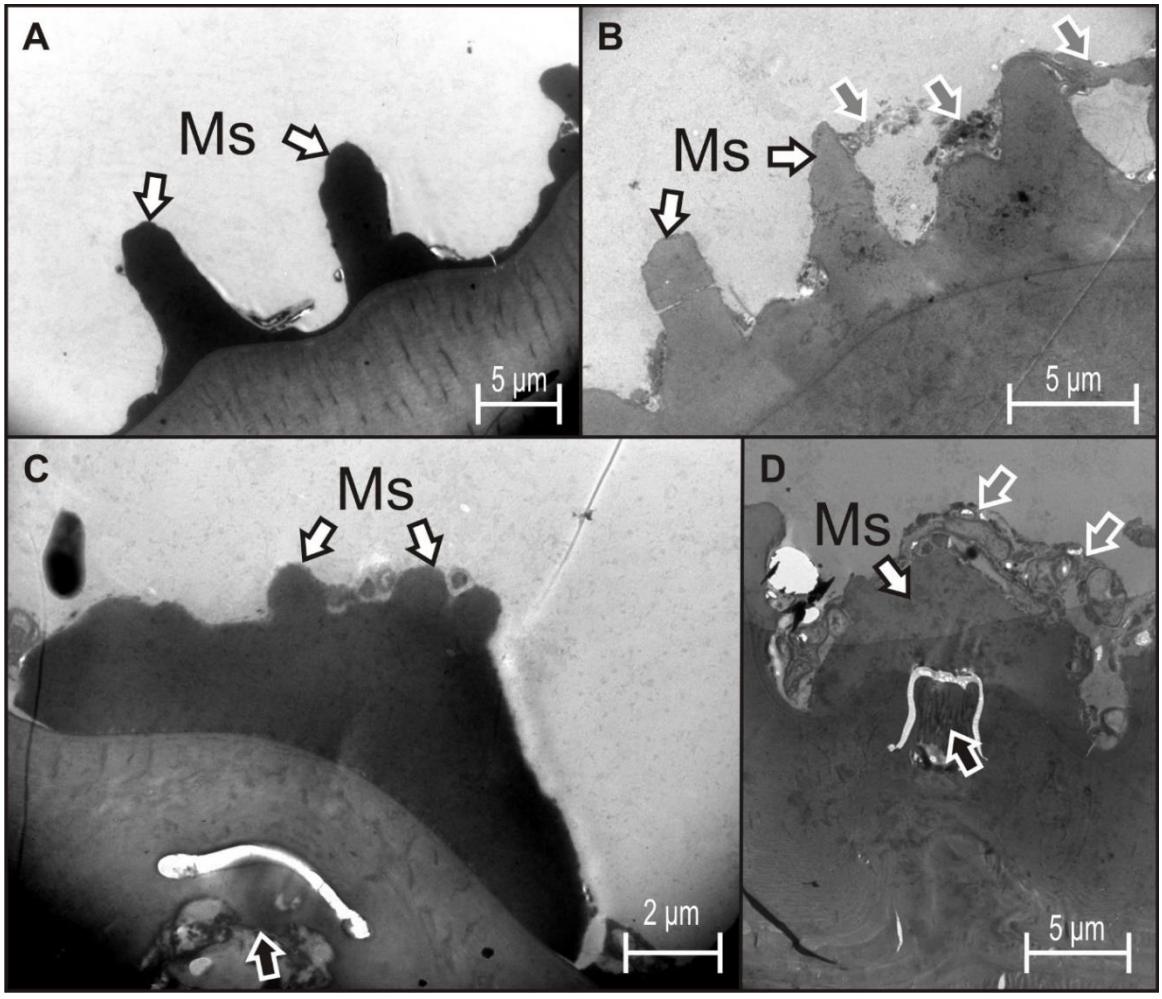

***Figure 32: Comparison of the naps before and after chloroform treatment for chemical analysis**. **A** and **C** are showing the intact wax layer before chemical treatment, white arrows mark the naps while black mark the gland. **B** and **D** show images of the same sample after washing with chloroform. As one can see, only the topmost layers of the wax had been dissolved without changing the overall dimensions of the microstructure. Grey arrows indicate semi-dissolved fragments of the wax. It should be noted that dissolving only this topmost part of the wax was enough to render the bugs hydrophobic. Image as shown in Hischen et al. (2017) and Reiswich (2013).*

From **Figure 32** it becomes apparent that only the topmost layers of surface waxes were dissolved by chloroform treatment. This leads to the assumption that substances (like glycerides or erucamide), responsible for rendering the bugs wettable in the first place, are located only in these topmost layers of the exocuticula.

3.2.3 Discussion

The purpose of the experiments done in this chapter was to figure out the individual players in the cuticle of *Dysodius*, which enable the bugs' surface to interact with water in a way that allows adaptive camouflage, i.e. quick wetting.

According to the concepts introduced in chapter 2.2, wetting of a surface by a given liquid is facilitated by a low contact angle. A low contact angle on the other hand is achieved by a) a chemistry that that brings the contact angle below 90° in the first place, and b) a morphology, i.e. a micro-roughness, which in accordance to the wetting model of Wenzel, lowers the contact angle of such a surface even more.

Contact angle measurements

The contact angle measurements done in this chapter verify indeed, that the pure chemistry of *Dysodius'* surface waxes enable low contact angles for water as low as 43.9° ± 4.7° on the smooth surface. This in itself is a rather interesting finding since the cuticles (and therefore waxy outer layers) of most insects show rather high contact angles in order to repel water (e.g. Sun et al., 2012); Hadley, 1994)). In this work, bees wax was used as a natural wax system to compare the contact angle of *Dysiodius* with. Applied to the same coverslips as *Dysodius* waxes, this wax shows drastically higher contact angles (**Figure 33**) and has even been reported to modify electrospun polycaprolactones in order to reach superhydrophobicity (Reshmi, Sundaran, A., & Athiyanathil, 2017).

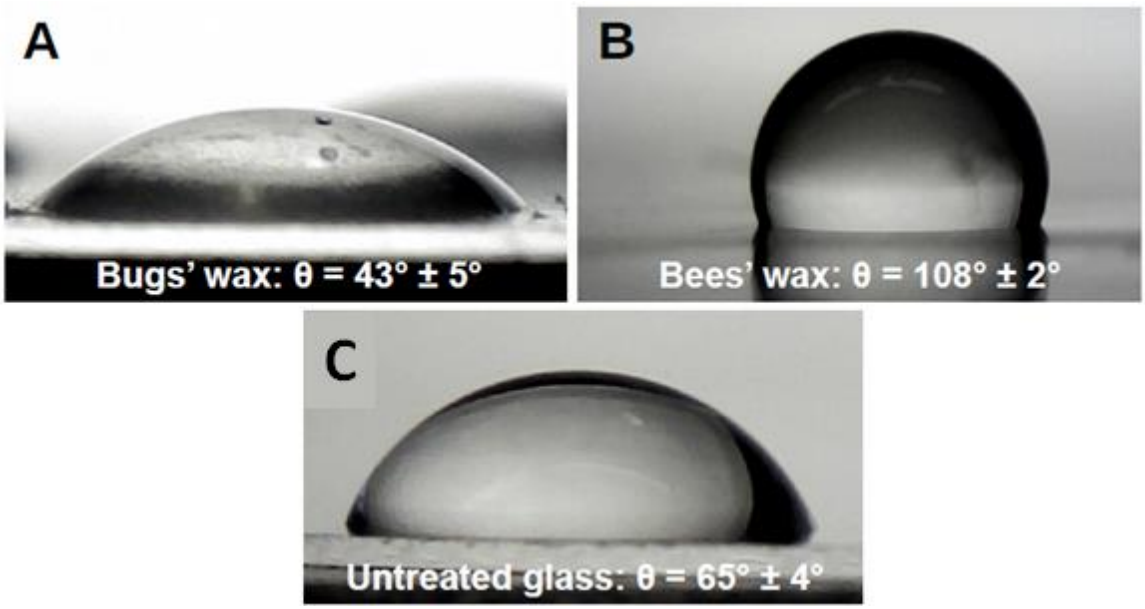

Figure 33: Comparison of distilled water contact angles between Dysodius' and bees' wax on glass cover slips. ***A*** *Dysodius' wax.* ***B*** *Bees' wax.* ***C*** *Untreated glass as reference. Images as shown in Hischen et al. (2017).*

Chemical analysis

The only way to understand why a wax is acting hydrophilic is to find out its chemical composition. As shown in **Figure 32**, only the superficial layers of the cuticular wax can be removed by chloroform-treatment while removal of the basal wax layers requires hot KOH. Thus the chemical composition is not uniform. Both used methods to analyze the chemical composition of the solved topmost layer brought valuable results though. A range of substance classes could be identified with GC-MS and further verified with HPLC-MS. Especially glycerides (mono-,di- and tri-) with varying chain length and different free fatty acids were found, which are common substances in the waxes of most insects according to different authors (Aldrich, 1988; Blomquist & Jackson, 1979; Lockey, 1988; Wigglesworth, 1957). HPLC-MS also revealed the presents of erucamide, an amphiphilic substance rather known for use in chemical processing of plastics.

Still, as also explained in Hischen et al. (2017) fatty acids, soaps and the dubious erucamide, had at least one commonality: All these substances have polar and non-polar sides (amphiphilic character) and make therefore good candidates to act as mediators between hydrophobic insect wax on the one side, and polar water molecules on the other. Different researchers already showed that aliphatic molecules can be arranged perpendicularly orientated (with regard to their longitudinal axis) on cuticular waxes of plants

(Domínguez, Heredia-Guerrero, & Heredia, 2011; Graça, 2002). This gives a high possibility for amphiphilic substances to do the same on insect cuticle waxes.

To test whether the erucamide and/or the free fatty acids or soaps are able to render insects wax hydrophobic, bees' wax was modified. As can be seen in **Figure 33**, bees' wax is hydrophobic, exhibiting a contact angle of about 108°. If simply melting the bees' wax and applying soaps, fatty acids or erucamide at small amounts to the liquefied material, the contact angle could only be changed marginally by a few degrees (not shown). Only when adding strong detergents like octoxinol-9, could the contact angle be lowered significantly. However, when an initial film of bees' wax was made and then soaps or erucamide was applied on top of the film as solution in chloroform or alcohol, a significant effect on the contact angle could be observed. **Figure 34** shows the effect of erucamide-application on a pre-established wax film. Here saturated erucamide-solution was applied and was allowed to dry on the wax. Then the surface was rinsed with water. Clearly the contact angle drops to very hydrophilic values of about 30°. However, in the SEM even the modified wax appears to be flat and no spontaneous nap-formation could be observed (not shown).

Figure 34: Snapshot of the contact angle of erucamide modified bees' wax on a glass coverslip. *Very low contact angles of around 29° can be achieved.*

Morphological analysis (modified from Hischen et. al (2017))

To understand how the wetting can be achieved, the surface morphology of the flat bugs was investigated by scanning electron microscopy (SEM). Typical scans of the dorsal surface of *Dysodius* are shown as overviews in **Figure 17**. Clearly, a micro structure covers the connexival plates as well as the glabrous areas. Furthermore, the sutures separating segmental borders can be identified (**Figure 20**). At higher

magnifications one can see a rough surface, i.e. that the microstructures are small naps (**Figure 18** and **Figure 19**). These naps have a diameter of 1.96 ± 0.37 µm and an average separation of 4.88 ± 1.38 µm (n=100). The height of the naps can be measured to be in the range of 2.5 to 4µm, as was found by TEM scans, such as shown in **Figure 29**. In between the naps occasionally bowl-shaped indents can be seen (**Figure 18** Figure **19**). Especially when the surface is de-waxed these structures become clear and the microstructures of their orifices become apparent (**Figure 24** and **Figure 25 B**). These structures have typical diameters of 21 ± 3 µm and are spaced by about 90 ± 40 µm (n=100). The naps were assumed to be made of cuticular waxes and it was tempting to speculate that these wax-structures are involved in the observed wetting behavior, since they represent the surface coming in contact with water. In order to test this, two bugs, which initially exhibited clear wetting (spreading of the water), were treated with hot 10% KOH-solution for 60 s, to remove wax by means of hydrolysis leaving only the underlying chitin surface intact. After this treatment, the bugs were not wettable anymore but became water repellent (showing contact angles >90°), as shown in **Figure 16**. Taken together we see that by KOH-treatment the waxy naps can be removed which concomitantly results in loss of the wetting capability of the cuticle. Thus, the waxy naps are vital for the wetting.

The surface morphology of these de-waxed animals is shown in **Figure 24**. Clearly the naps are removed. The bowl-shaped indent structures, which are under native conditions covered with wax-naps at high density (**Figure 19**) are again visible but the wax is removed. In the higher magnification (**Figure 25 A**, **B**) clearly the naps are gone. It seems, that here the orifice of a secretion channel can be seen which exhibits complicated, often sinusoidal shapes. It is assumed at this point, that these circular structures with the sinusoidal shaped openings in the center are the orifices of wax-glands, which produce the nap-shaped cuticular waxes. Supposedly the same structures are shown in the findings from the freeze-fractures, especially in **Figure 28**. The shown structure protrudes through the whole cuticle and ends in a very unique shaped tip. A comparison in dimensions also speaks for this theory: The averaged sizes for bowl-shaped indents (~21 µm) can compare to the structure shown in **Figure 28** and average distances of about 70 µm between neighboring indents correspond to the distances that can be seen between the holes in **Figure 27**.

This assumption is even further supported by the findings made by TEM analysis of these structures. Clearly, as seen **Figure 30**, a channel reaches from the tip of the structure through the complete cuticle and the tip of the structure reveals a filamentous tissue. The filamentous tissue might be an indicator for a porosity, i.e. tissue that enables viscous material to pass. In this case presumable waxes or precursor

waxes that are synthesized in the hypodermis. And indeed, in closer vicinity to the channel, fragments of hypodermal tissue also show cells and cell-fragments, revealing oenocytes, lamellar bodies and smooth endoplasmatic reticulum. These structures, according to Lockey (1988) and Schmitz & Müller (1991) , normally can be connected to the production and maintenance of lipids and carbohydrates of insects. Which in this case would fit to the report of Blomquist & Jackson (1979), in which the overall composition of insect cuticle for the most part is composed of free lipids and fatty acids, as well as alkanes and alkenes with varying chain length. In addition to that, **Figure 25 C** shows a magnification of small holes that have been found all across the dewaxed cuticle. These holes, or orifices, become even more apparent in TEM scans (e.g. **Figure 29**, arrows) and can be found in higher abundance around the formerly mentioned big glands. According to Lockey (1985), these channels are the "regular" wax channels, providing the surface of insects with a protective, consecutive wax layer.

Based on the findings of the morphological analysis, a model was developed that concludes the production and formation mechanism of *Dysodius*' naps.

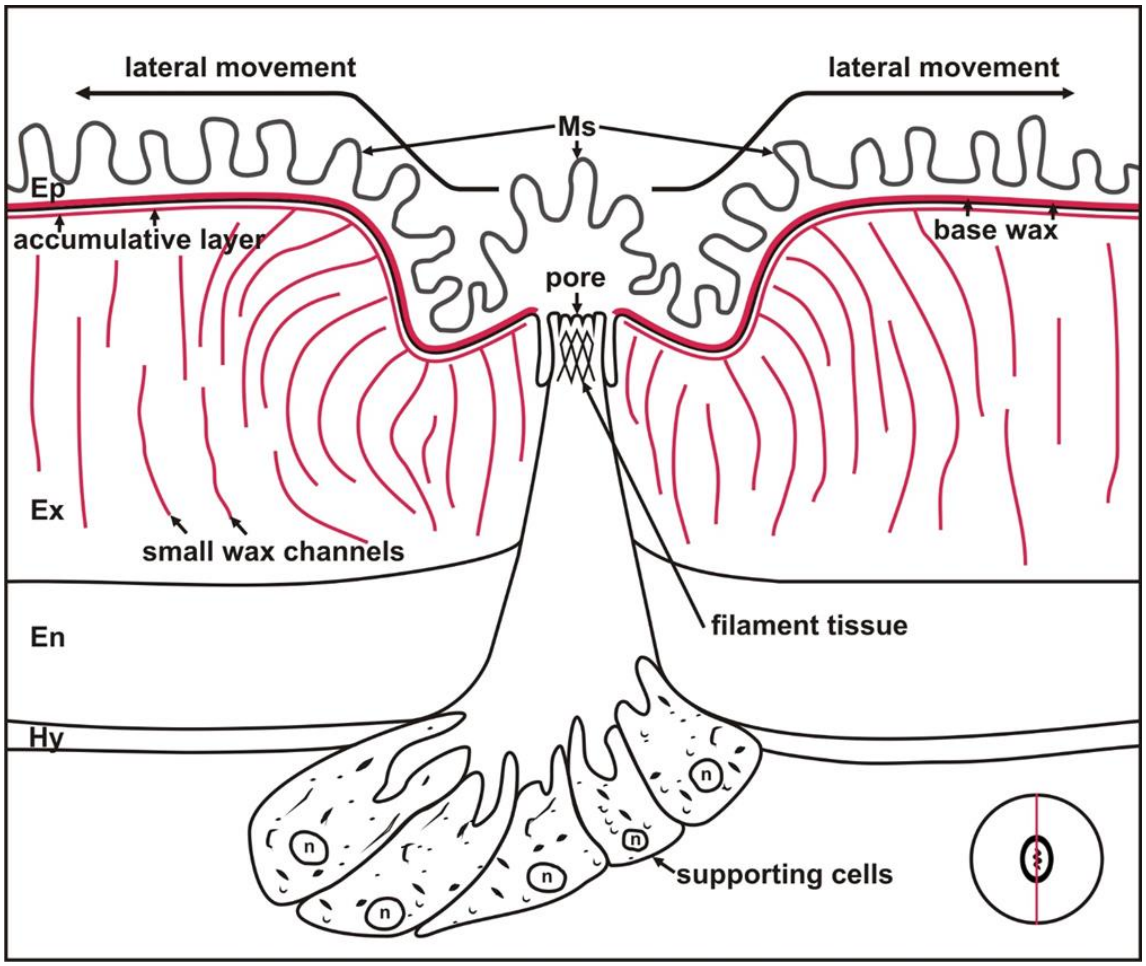

Figure 35: Schematic model for the nap secretion mechanism in Dysodius. *Centrally depicted is a wax gland stratificating though endo- and exocuticula (En, Ex). The tip of the gland consists of a filamentous tissue, ending with an often sinusoidal orifice (pore). Through this pore, waxy material produced by supporting cells in the hypodermis (Hy) is pressed, forming the nap microstructure (Ms). Small wax channels in the exocuticula secrete a basal wax layer (acting as a lubricate), enabling lateral movement of the naps produced by the big wax glands. Newly produced naps at the tip "shove" older once away laterally, covering the surface time by time. As a result the epicuticula (Ep) of Dysodius consists of a dense array of microstructures as seen in the SEM images. (Image modified from Reiswich (2013) and also shown in Hischen et. al (2017).*

The schematic draft shown in **Figure 35**, depicts a hypothesis, which might explain how the nap structure on *Dysodius* is formed. Small wax channels provide the surface with a consecutive, thin basal wax layer, on which then the nap structure is secreted by the bigger wax glands. Due to constantly fresh secreted naps on the glands tip, previous ones gets shoved across the basal layer, covering the surface of *Dysodius* over time. Such a wax secretion system is quite unique and hasn`t been reported yet. Complicated and specialized wax secretion mechanisms in general are not completely unheard of though. For example, (Foldi, 1981) showed that the wax gland system in subterranean scale insects can be quite complicated and delicate. Here too, adapted wax gland systems produce individually shaped wax secretions that have a single purpose.

3.3 Wettability of *Dysodius*: Liquid spread analysis

After introducing the behavior of adaptive camouflage in the previous chapters, and explaining the surface as well as the chemistry enabling *Dysodius* to show this behavior, this chapter deals with the wetting dynamics of the surface. How fast is the liquid spread? How is the water spread? Which ambient factors play a role? And how can it be explained? These are the core question to address in this chapter. Photo- and video-analysis will be the main methods to address.

3.3.1 Materials and Methods

Video-Setup

In order to measure the liquid spread on Dysodius in a controlled environment (e.g. constant ambient temperature and humidity), a custom measurement setup was constructed together with V. Reiswich ((Reiswich, 2013). The setup consisted of a reptile egg incubator (Incubator, Exo Terra, Germany) which allowed for constant temperature control (± 3°C). Additionally a supersonic fogger was installed in the chamber of the incubator to regulate the humidity (Super Fog Nano, Lucky Reptile, Germany). The fogger was controllable from in- and outside of the incubator but only enabled a rise and hold of higher humidity values as were ambient outside of the incubator. For lowering and holding values lower than that, silica gel in petri dishes was placed in the chamber. For constant monitoring of the ambient values, a thermo-/hygro-combimeter (GFTB 100, Greisinger, Germany) was fitted tight into the outer wall of the incubator. A see-through mount was fitted in the top of the incubator to allow the insertion of a highspeed-video-microscope (VW-9000, Keyence, Japan), equipped with an 50x magnification lens (VHZ00R, Keyence, Japan), that allowed video capturing of the wetting process on test specimen. The video-microscope was controlled by a remote control (Keyence, Japan) and linked to a PC with the control software (VW-900 MotionAnalyzer, Keyence, Japan). Since focusing of the camera itself was not possible in the custom mount, a scissor lift with an attached motor (Interactive Servo Motor, LEGO, Denmark) was used to move objects in the chamber up and down to be in focus. The motor was controlled wireless with the control software NXT Remote Control (LEGO, Denmark) that was installed on an android smartphone. The connection was realized via Bluetooth. Lighting of the sample was realized by and LED-ring that was part of the camera system, as well as a cold-light source (KL 1500 LED, Schott, Germany), which could be inserted into the camera mount next to the lens. For the external application of fluids onto the specimen, a needle on a moveable glass-tube was placed into the chamber, attached to a rubber hose which was connected to a syringe containing distilled water. An overview of the whole setup is given in **Figure 36**.

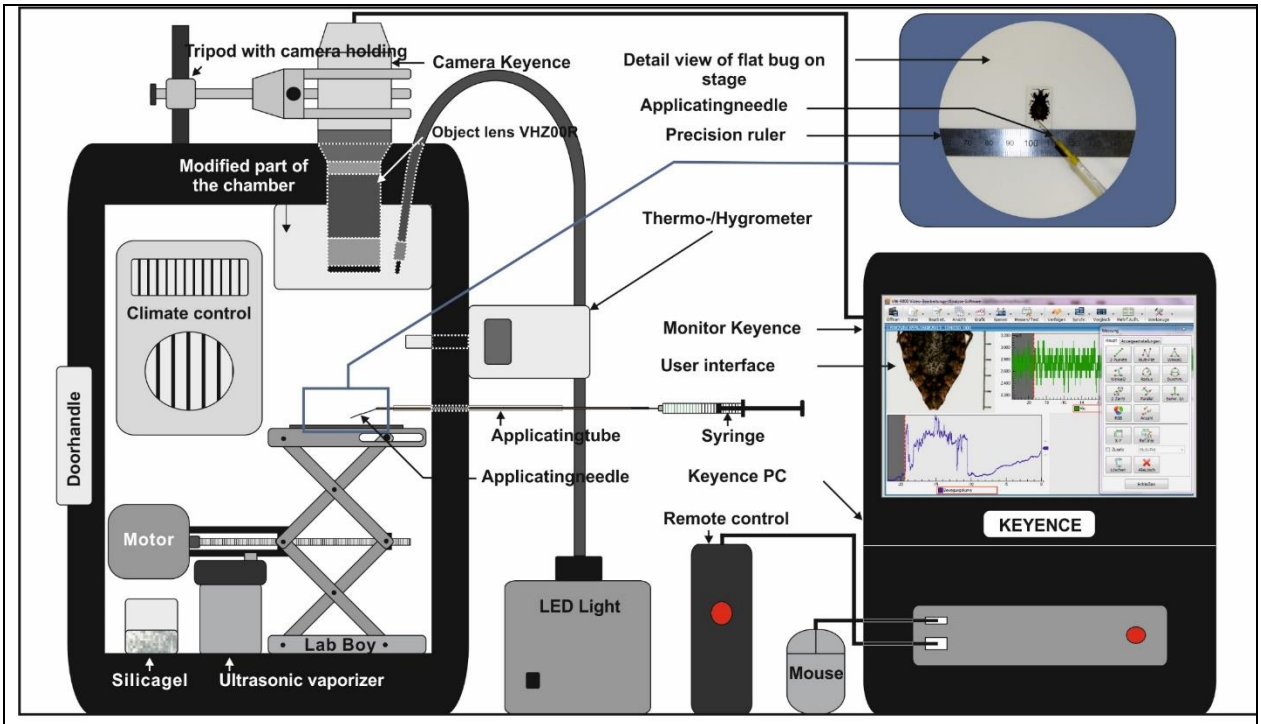

Figure 36: Schematic overview of the video measuring setup. *Image modified from Reiswich (2013).*

Capturing the liquid spread (modified from Reiswich (2013))

Two adult individuals of *D. magnus*, as well as two adult individuals of *D. lunatus* were used to analyze the liquid spread on the dorsal surface. The specimen were placed in the incubator individually and brought into focus. The water-application needle was placed carefully above the left connexivum #VI. This was chosen since it usually is one of the bigger segmental plates and was easy reachable with the used needle in this setup. The chamber was then set to desired values: Test regime A) 25° C and 30% rel. humidity; Test regime B) 30° C and 85% rel. humidity. The values were chosen in order to figure out an influence of temperature and humidity towards fluid spread. Lower values were chosen according to standard ambient values in the lab room, higher values were chosen according to the mean annual values stated for the rainforests of French Guyana (the natural habitat of *Dysodius;* values extracted from https://weatherspark.com/y/29664/Average-Weather-in-Cayenne-French-Guiana). The fluid volume for the test series was set to 5 µl per experiment and determined by pretests, showing that this fluid volume usually is enough to wet most of the dorsal abdominal surface of *D. magnus* and often the complete dorsal surface of *D. lunatus*. The 5 µl droplet was carefully placed on the specimen and the occurring water spread was captured by the video-microscope. Each individual was measured 10 times and in between of two

measurements dried outside of the chamber for 10 minutes. After each measurement, ambient chamber values were checked and adjusted if needed.

The videos were analyzed with the Keyence video analyzer software that came in bundle with the microscope (VW-900 Motion analyzer). Goal in this measurements was to a) measure the raw spreading speed of the water, and b) to figure the spreading dynamics. Towards this end, the videos were frame-by-frame analyzed and the progression of the liquid front was tracked. This way, it was possible to capture the liquid front progression in mm and compare it to the timescale of the video, which enabled calculation of the speed in mm/s. In addition, the liquid progression was measured in three different ways to learn more about the spread dynamics. The different measurement ways are depicted in the following **Figure 37**.

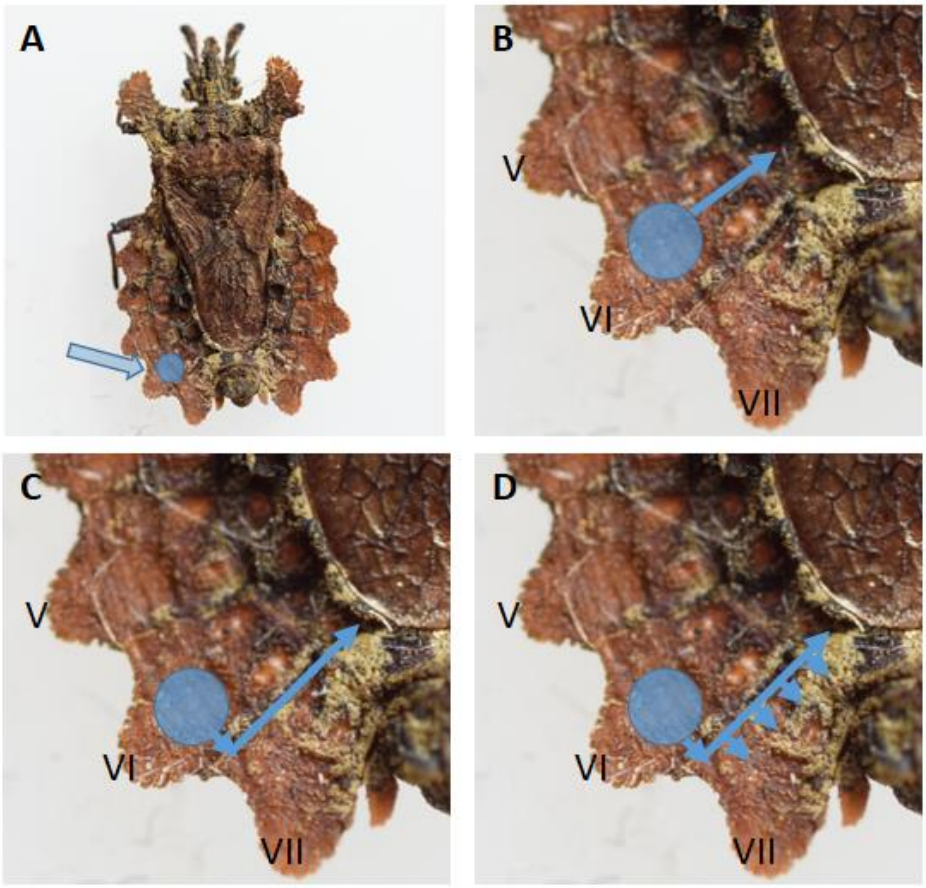

Figure 37: Overview of the measured liquid spread ways. A *Application direction (blue arrow) and droplet position (blue circle) on connexivum VI (Dysodius magnus in this case).* ***B*** *Surface spread on the connexivum (blue arrow).* ***C*** *Propagation of the liquid in the intersegmental surture between connexivum VI and VII, which acts like a capillary.* ***D*** *Spreading speed of the liquid that rises from the capillary onto connexivum VII.*

Mimicking the wetting behavior on polymer foils (from Hischen et. al (2017))

In order to see if the wetting (water spreading) behaviour which can be seen on native *Dysodius lunatus* and *D. magnus* can be fully explained by the findings so far, an attempt was made to mimic the effect. For this purpose, naps on PET-foils were produced by irradiation with nanosecond UV laser pulses. Fabrication was done by Johannes Heitz at the Institute of Applied Physics, JKU Linz. The spontaneous formation of the quasi-periodic naps occurs self-organized due to the release of the biaxial stress-fields and crazing in the irradiated but not ablated surface (Arenholz, Svorcik, Kefer, Heitz, & Bäuerle, 1991).

The native PET-foil is slightly hydrophobic. In order to mimic the wax material with an intrinsic contact angle (contact angle on the flat surface) of about 40°, we treated the foils with a sputter coater. Small amounts of gold were deposited in an argon-plasma until a contact angle of 40° was reached (same coating procedure as stated for SEM: 180 s at 1 kV, resulting in a layer thickness of approx. 20 nm). The wetting behaviour of such a foils is shown in **Figure 42**.

3.3.2 Results

The following image sequence depicts an example for the fluid propagation, as it was video captured on *Dysodius* (in this case *D. magnus*).

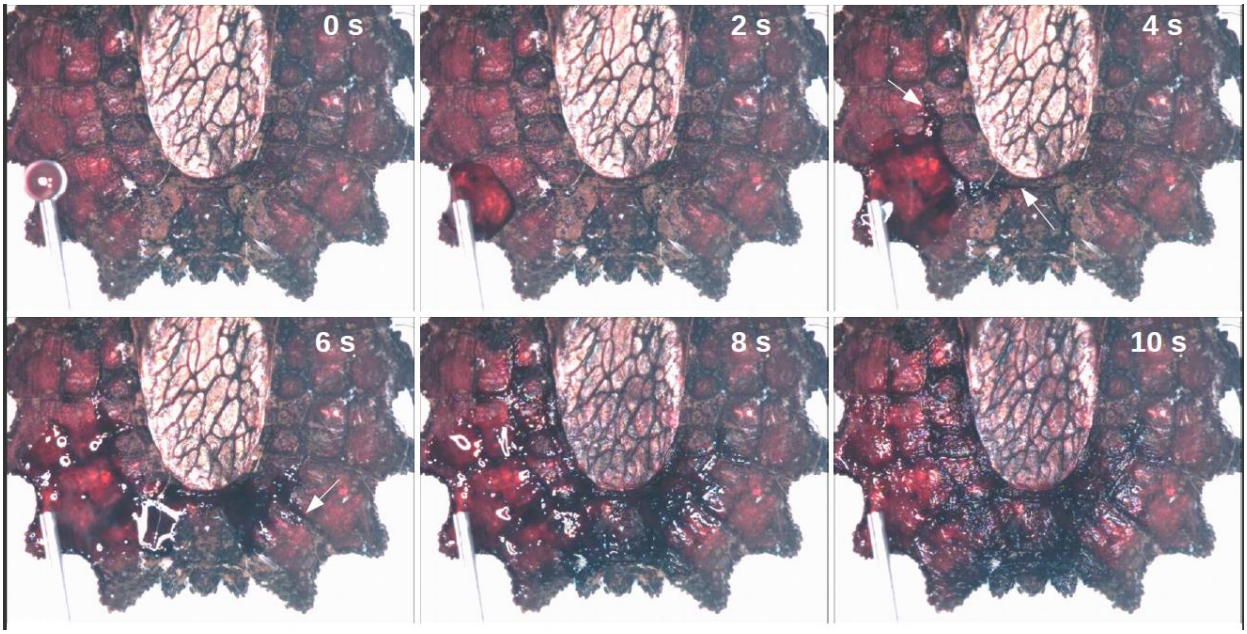

Figure 38: Example image sequence of the liquid spread as video captured on Dysodius (in this case D. magnus). *Fluid was applicated on connexivum VI (volume = 5 µl). The corresponding time stamp is given in the top right hand corner of each image. (Hischen et. al 2017).*

As can be seen from **Figure 38**, a droplet of distilled water that is applied to the surface of *Dysodius*, spreads immediately. After only 2 s, it already reaches the intersegmental suture between connexivum VI and VII from where it is quickly propagated through the connected intersegmental sutures, which act as capillaries (indicated by the arrows at 4 s). Also, at 4 s, the droplet already covered the complete surface of connexivum VI. After 6 s, the fluid front reached the opposite side of the abdominal surface of the bug (indicated by the white arrow) and the water rises from the capillaries and spreads over the surface of adjacent connexival plates. After only 10 s, most of the abdomen is covered with a thin layer of water.

Figure 38 illustrates quite well why the decision was made not only to measure the overall liquid spread speed, but rather individual speeds at different stations of the spread (**Figure 37**). Water that spreads over the surface, automatically reaches the intersegmental sutures between the connexival plates. These, acting as capillaries, forward the liquid way faster to farther distanced parts of the abdominal surface than spreading only over the surface would allow to. In different words: One can observe virtually three different individual ways in which water is propagated on *Dysodius*: 1) Water spread over the surface; 2) Water spread throughout the intersegmental sutures acting as capillaries. 3) Water spread from the

capillaries back onto adjacent connexival surfaces. The measured values for the individual spreading speeds are shown in the following **Figure 39**.

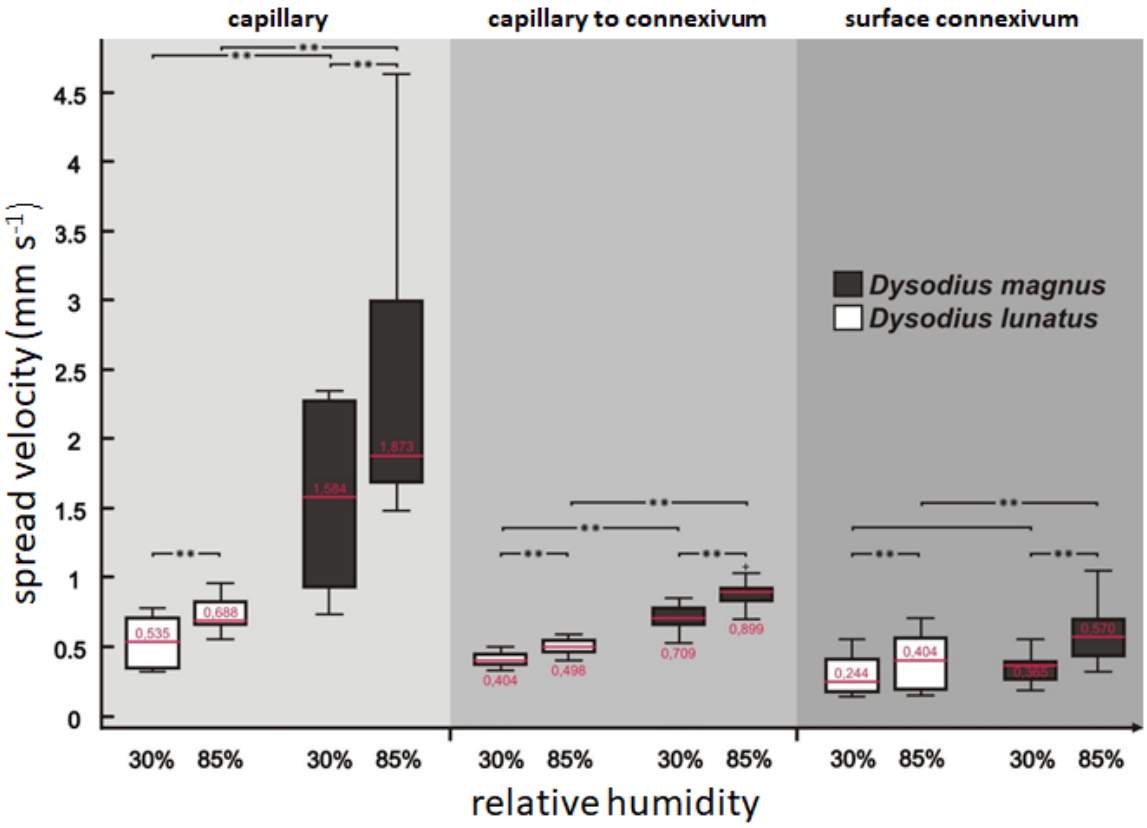

Figure 39: Summary of the fluid spread measurements on D. magnus and D. lunatus. *The figure shows the averaged velocities for the three different zones (capillary, capillary to connexivum, surface connexivum) on both species, versus the relative humidity. Number of measurements for each box was n=20. A Student`s T-test was used to check for significant differences. "*" marks significant (p < 0.05), "**" marks highly significant (p < 0.01), no "*" marks non-significant differences (p > 0.05). Figure modified from Reiswich (2013).*

The measurements shown in **Figure 39** document the observed liquid spread on both species with numbers. Unsurprisingly, the highest velocities of fluid propagation can be measured in the intersegmental sutures, which act here as capillaries. On *D. magnus* velocities of up to 1.8 mm s^{-1} were observable. The spread on the surface itself propagates way slower though, with velocities ranging between 0.2 and 0.8 mm s^{-1}. Another general trend, is the overall better wettability (or faster wettability) of *D. magnus* when compared to *D. lunatus*. For liquid spread on the surface these differences are relatively small (and sometimes even non-significant, e.g. when comparing the propagation on the connexivum`s surface only), but the spreading speed in the capillaries is about three times higher on *D. magnus*.

The last big trend that can be taken from the shown measurements is that in all cases it indeed makes a significant difference, if the measurement was done under ambient room conditions (30% rel. humidity),

or under simulated rainforest conditions (85% rel. humidity). This leads to the assumption that relative ambient conditions indeed play a big role in the wetting behavior.

In order to figure how the significant differences in capillary fluid propagation between the two species can be explained, images from the video analysis were used to measure the capillary width from on the surface. The software used for the measurements was once again the Keyence Motion Analyzer.

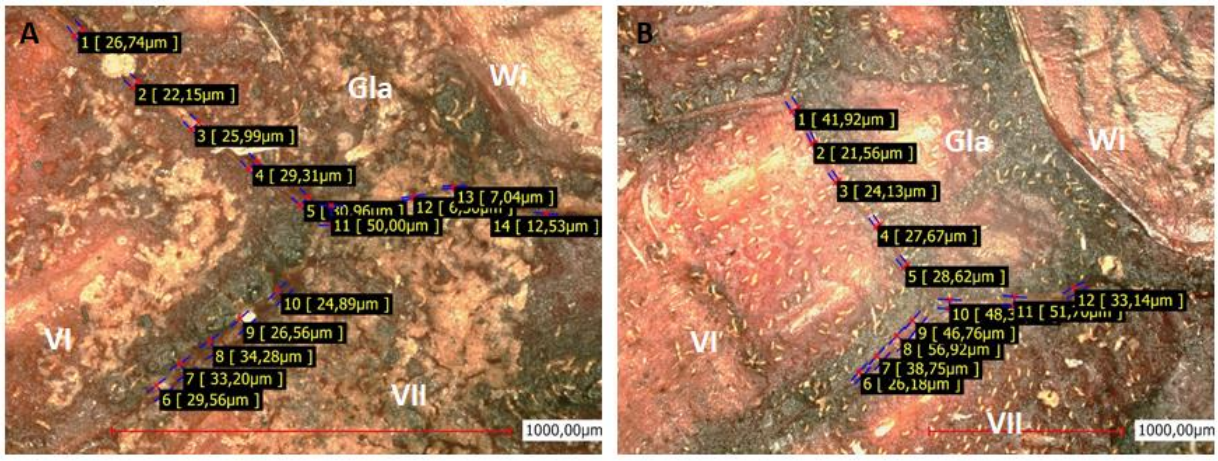

Figure 40: Measurement of capillary width. A *Dysodius lunatus.* ***B*** *Dysodius magnus. In both cases the width of intersegmental sutures between connexivum VI and VII, between connexivum XI and the glabrous area (Gla), and between connexivum VII and glabrous area were measure. In the top right hand corner of both images the bottom corner of the wings (Wi) can be seen.*

Figure 40 shows the comparative measurement of capillary width between *D. lunatus* and *D. magnus*. As one can see, capillary widths are quite uneven with widths ranging from ~6 to ~56 µm. Calculated, this leads to an average capillary width of 25.7 µm (±10) (n=13) for *D. lunatus* and 35.1 µm (± 13) (n=12) for *D. magnus*. A Student's t-test gives p = 0.062, confirming that the difference is not significant though. This leads to the assumption that there is no real difference in the average width of the capillaries of both species.

Mimicking the wetting behavior on polymer foils (from Hischen et al. (2017))

Figure 41 shows the surface morphology of PET-foil as seen in the SEM. While the untreated PET is virtually flat, areas which were irradiated with the laser are covered by naps. These naps have a diameter of about 2 µm. The PET-naps are slightly denser (average distance 3.5 µm) than the naps observed on *Dysodius* but on the other hand they are not that high (about 1µm) resulting in similar surface enlargement when compared to the natural archetype (see discussion section).

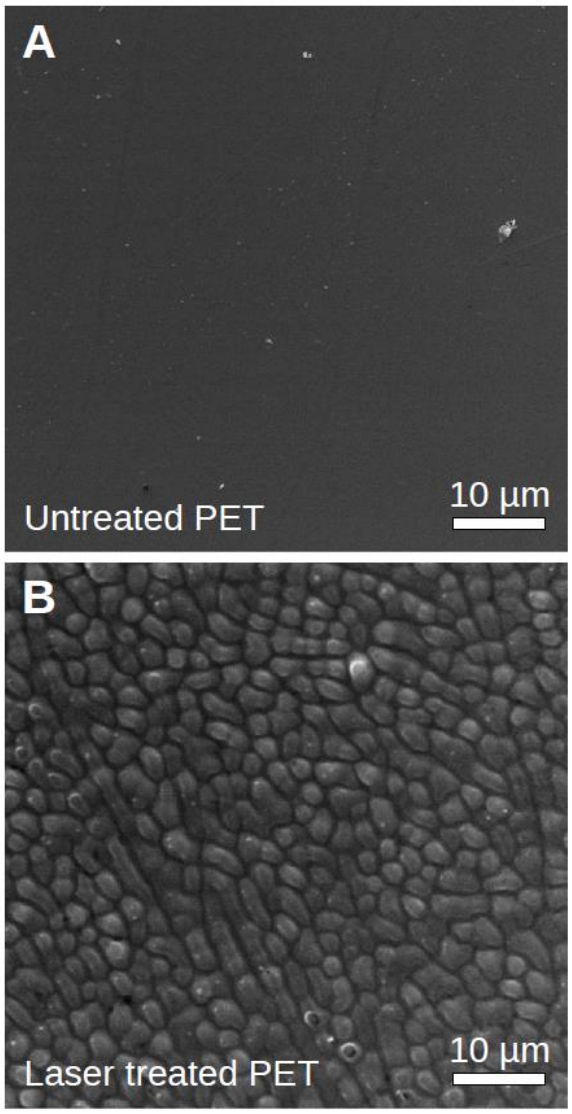

Figure 41: Comparison of untreated and laser treated PET foil under the SEM. *The untreated foil (**A**) was found to be virtually flat. If the PET was treated by a pulsed UV laser (**B**), individual naps can be induced. These naps are with respect to the surface-area amplification very similar to the microstructures observed on Dysodius magnus and D. lunatus, resulting in similar values for the Wenzel roughness (r is approx. 1.4 for the bugs and 1.2 for the PET foil and thus determining the needed contact angles for Cassie-Baxter impregnating with 50.5° and 48.2° respectively).From Hischen et al. (2017).*

The native PET-foil is slightly hydrophobic. In order to mimic the wax material with an intrinsic contact angle (contact angle on the flat surface) of about 40° (± 3.5, n = 10). We treated the foils with a sputter coater. Small amounts of gold were deposited in an argon-plasma until a contact angle of 40° was reached (same coating procedure as stated for SEM: 180 s at 1 kV, resulting in a layer thickness of approx. 20 nm). The wetting behaviour of such a foils is shown in **Figure 42**. The glossy part (upper, left and right margins) of the foil shown there is not irradiated, corresponding to the flat foil shown in **Figure 41 A**. However, the opaque part in the lower centre of **Figure 42** is structured by laser processing as shown in **Figure 41 B**. Initially a drop of dyed water was placed on the unstructured PET. A stable droplet is formed which stays at a contact angle of about 40°. On the contrary, if water is applied onto the laser-structured part, the water

immediately begins to spread and to form a film of water. The apparent contact angle is below 10°; thus, the surface is superhydrophilic. At the water front, a margin with slightly different colour can be observed.

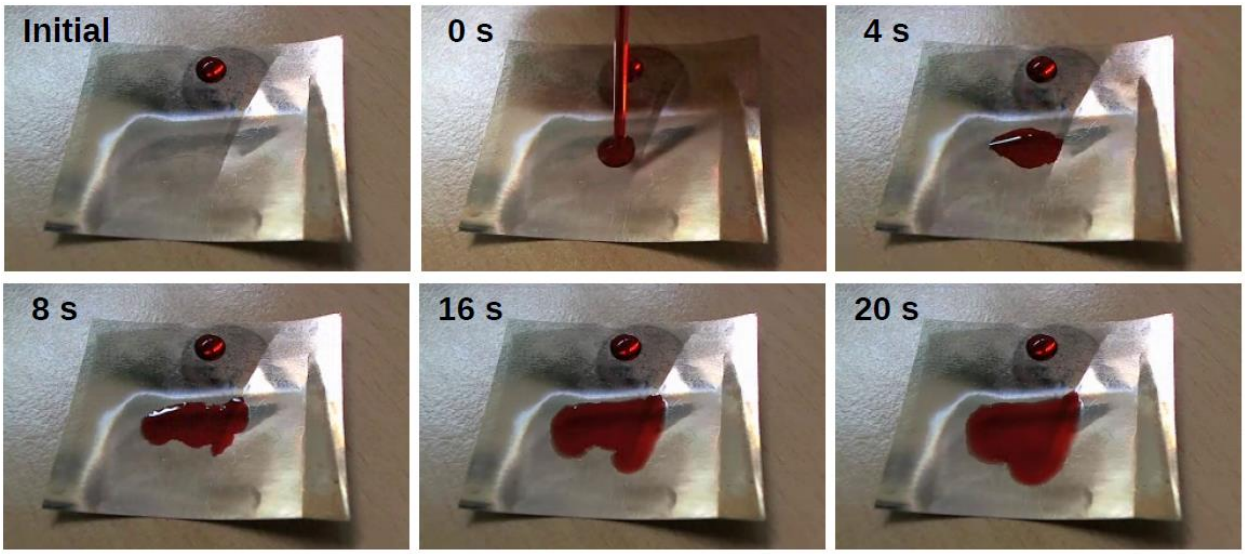

Figure 42: Time series of the behavior of dyed demineralized water on a PET-foil mimicking the surface topography of Dysodius lunatus and D. magnus. *The PET was partially laser-structured. The glossy part (upper, left and right margins) is untreated, while the opaque part in the lower center is structured by laser processing as shown in* ***Figure 41****. The PET-foil piece has a width and length of 40 mm. From Hischen et al. (2017).*

In addition, contact angle measurements on the foil were performed according to the protocol mentioned in Chapter 3.2.1, yielding contact angles of approximately 40° for the unstructured part. A definitive measurement of the exact contact angle was impossible due to the slight surface bends of the foil and a very disturbed horizon in the pictures as a result. For the structured area a contact angle of < 10° has to be assumed, since immediate water spread (=superhydrophilicity) is reached. Unfortunately this could not be verified by a distinct measurement with the used contact angle measurement, since the droplet spreading takes place faster than the time resolution of the capturing process allows to follow. Confirmed measurements showed that the limit for the system is at ~ 16°, therefore allowing to say that the apparent contact angle definitely was below this value.

3.3.3 Discussion

The overall goal of chapter 3.3 was to figure out the dynamics of fluid spread on both species of flat bugs, *D. lunatus* and *D. magnus*. Towards this end, video analysis of the fluid propagation on the abdominal surface was done. By applying a droplet of distilled water on connexivum VI, it was possible to observe how the water usually first spreads over the surface and then enter the intersegmental sutures, which act as capillaries and forwards the water quickly to farther distanced parts of the abdominal surface. Astonishingly, the water then again rises from the capillaries and starts to wet the surface of adjacent body parts (e.g. neighboring connexival plates and the glabrous area). This overall dynamics are exemplarily documented in **Figure 38**.

Furthermore, the direct velocities of the three different fluid propagation ways were measured (**Figure 39**). Here we see, that there are indeed big differences when comparing a) the spread velocity between the two species of interest, b) the ambient conditions, and c) the fluid velocities of the three pathways. Overall *D. magnus* shows slightly higher velocities than *D. lunatus*. This accounts also for the two different tested ambient conditions. Concerning these, the measurements reveal that there indeed seems to be a dependence between higher values for relative humidity and apparent wetting performance: All measurements at 85% relative humidity yielded higher velocities of liquid spread when compared to 30%. The fact that also higher temperatures were chosen to perform these measurements (25°C at 30% vs. 30° C at 85%) can be ignored in the context of wettability performance. Pretests with constant humidity at both temperatures showed no significant difference (not shown). The main reason for using higher temperatures for higher relative humidifies is justified by the capacity of air to hold a certain amount of water vapor at a given temperature (Eastop & McConkey, 2006; Mollier, 1904; Rajput, 2010), and it was necessary to heat the chamber up to 30° in order to reach 85% of relative humidity (as would be the average yearly humidity in the natural habitat of *Dysodius*). At this point it is assumed, that higher humidity might influence the wetting performance in terms of pre-wetting. Vapor condensation on the surface of *Dysodius* (using the naps as condensation nuclei) could be the reason that a) capillaries fill or partwise fill up and b) the surface in general spreads additional water drops faster. This behavior has previously been shown on the skin of moisture harvesting lizards, which also benefit from pre-wetting in their wetting performance (Comanns, Effertz, Hischen, Staudt, Böhme, et al., 2011). Detailed condensation experiments would be beneficial in order to reveal the true dynamics of what is happening on *Dysodius'* surface. Towards this end, Chapter 6 of this work concerns with the development of artificial replicas of surfaces

that allow controlled temperature adjustment – a feature that is absolutely needed in order to monitor and measure condensation phenomena.

Concerning the different fluid pathways that were investigated in **Figure 39**, one can see that the biggest differences in fluid spread can be found when comparing the spreading velocities in the capillaries versus the spreading velocities on the surface. While surface velocities range between 0.2 and 0.9 mm s^{-1}, capillary velocities can reach up to almost 2 mm s^{-1}. Interestingly the differences between the two species when concerning the liquid propagation on the surface only is little (and partwise even non-significant), while the difference in capillary velocity can be a factor of 3.

These observations make sense nevertheless: Since *D. magnus* has a bigger body surface to cover (measuring the surface without legs, head and antennas shows that *D. magnus* has between 30 and 42% more surface area then *D. lunatus, n= 3*), overall liquid spread should be higher in order to achieve camouflage as quickly as possible. On the other hand, as findings from electron microscopy and chemical analysis show, both species have virtually the same surface chemistry and morphology (naps plus hydrophylicity). Hence, the only way to alter the overall liquid spread velocity (and therefore adapt it to the bigger body size of *D. magnus*) would be a faster propagation of water in the capillaries. According to Equation 9 (chapter 2.2), the capillary driving pressure p is dependent from the surface tension γ, and the two main radii of curvature r_1 and r_2 of the liquid slug in contact with the capillary walls and bottom. Since the surfaces of *D. magnus* and *D. lunatus* exhibit the same chemical and morphological properties and water is the used liquid in both cases, surface tension as well as contact angle can be assumed to be the same. Hence, a change in the size and geometry (e.g. depth, width) of the capillary could explain the different velocities, since the geometry also influences the radii of curvature. This hypothesis has its limits though, since it for example doesn`t include the viscous forces which would influence the velocity as well (e.g. a very narrow and deep capillary would result in high capillary driving pressure, but the impact of viscous forces and friction would get bigger).

Unfortunately though, the measurements shown in **Figure 40** do not fully support either hypothesis so far. The measurements of the capillary surface width show no significant difference for the two species and therefore allow explanation with regards to the capillary radius at this point. Hence, the answer probably lies “underneath”, i.e. in the three dimensional morphology or maybe even the surface of the capillaries inner walls that are covered by the edges of the connexival plates and the glabrous area. Attempts to retrieve this depth and/or morphological information have not been successful so far though: Semi-thin slices of embedded samples failed to hit the capillaries, or cracked exactly at the critical areas. The same

applies for the executed freeze fractures. Optical analysis by SEM only shows the surface part and is overall unsuited to gain true depth information and the attempt to analyze the capillaries by means of optical coherence tomography (OCT) failed due to insufficient penetration depth of the laser. Uncovering the full, 3-dimensional and morphological information of the capillary network therefore remains as a task for future work at this point.

Explanation of the observed surface-water-explanation (modified from Hischen et al. 2017)

It still remains to be addressed, how shown liquid propagation on the surface occurs and how the microstructured wax surface yields a superhydrophilic effect (e.g. fluid propagation on the connexivum or from the capillary back to the connexivum, as shown in **Figure 39**). Observing the initial droplet state after application on the surface of connexivum VI, one can see that in fact a drop of water sits on the substrate while the liquid appears to penetrate the interconnected grooves in between the naps. Thus the droplet faces a patchwork of solid and liquid. This is exactly the scenario of the so-called Cassie-Baxter impregnating wetting or also called hemi-wicking. This wetting has to be distinguished from the pure Wenzel wetting (Wenzel, 1936). In the latter case, the solid outside of the triple line is dry, whereas in the Cassie-Baxter impregnating situation the grooves, acting as micro-capillaries, are wetted. The apparent contact angle θ^C of the drop sitting atop of the structure results to be

$$\cos(\theta^C) = 1 - f_s + f_s \cdot \cos(\theta) \tag{17}$$

where θ is the contact angle of the unstructured solid material and f_s is the relative fraction of the solid underneath the droplet. As explained in detail in Bormashenko (2013), Cassie-Baxter impregnating wetting is possible if and only if the contact angle of the unstructured material θ fulfils

$$\cos(\theta) > \frac{1 - f_s}{r - f_s} \tag{18}$$

with r denoting the Wenzel-roughness. This is the ratio of the total surface area and the projected area, i.e. the factor of surface enlargement due to the structuring. If a regular array of cylindrical naps of radius R spaced by a distance d occurs, the ratio f_s follows to be

$$f_s = \frac{R^2 \cdot \pi}{d^2} \tag{19}$$

Thus, in case of *Dysodius* $f_s \approx 0.3$ and in the case of the naps on the PET-foil $f_s \approx 0.6$. The Wenzel roughness can be estimated to be $r \approx 1.4$ in the case of the natural archetype while for the PET-foil one can estimate $r \approx 1.2$. This leads to the condition that for the *Dysodius* surface structure to allow Cassie-Baxter impregnating wetting the contact angle of the wax needs to be below 50.5°. For the artificial naps on the PET, the contact angle has to be below 48.2°. Not surprisingly this is found in the corresponding cases.

Finally, it remains to be determined why and how the water is transported through the capillary channels between the connexival plates and/or the glabrous areas and how it escapes from the channels to wet the surface. From the observation of the image sequence (**Figure 38**), it appears clear that slow imbibition wetting could occur all over the surface. However, the capillary transport is much faster yielding a complete wetting of the dorsal surface in short time even if only one droplet of water hits the animal at any position. To understand the dynamics of imbibition wetting, one has to follow the approach of Washburn (Washburn, 1921). At time t the imbibition length l of a liquid of surface tension γ and viscosity η from a reservoir into an array of randomly distributed micro-pillars of height δ and the roughness parameters ρ and ϕ as defined above follows to be

$$l = \sqrt{\frac{2 \cdot t \cdot \delta \cdot \gamma \cdot [\cos\theta \cdot (\rho - \phi) - 1 + \phi]}{\kappa \cdot \eta \cdot l^2}} \tag{20}$$

Here κ is a parameter defined as $\kappa = 1 + \delta^2 \cdot p^{-2} \cdot \ln(p/\sigma)$ with p being the average centre-to-centre distance (pitch) of the pillars. This equation can be obtained by equating the viscous dissipation rate to the rate of change of the capillary energy (Chandra & Yang, 2011).

Since Washburn included the randomized distribution of micro-pillars as a criteria, the average distribution of *Dysodius* naps was confirmed via fast-Fourier-transformation (FFT; e.g. in Smith, 2003)). Towards this end, a random SEM scan of surface was picked and the central position of in this case 2467 naps were marked, as shown in **Figure 43**. Afterwards, the resulting dot-map was converted into a frequency image, using the FFT function of ImageJ and compared to the frequency image of an artificial dot-map of absolutely periodical distributed pillars (see **Figure 44 B**). The resulting frequency images show a typical result for aperiodic distributions for *Dysodius* (**Figure 44 A**).

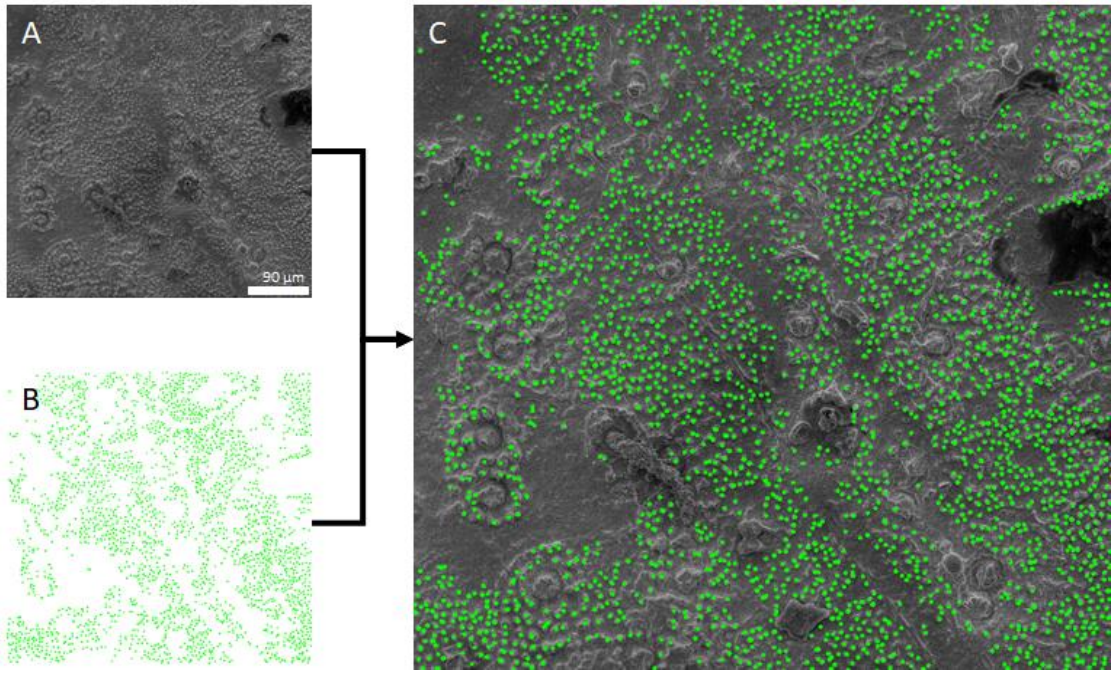

Figure 43: Evolution of the dot-map for Dysodius. A *Randomly selected scan of Dysodius surface.* ***B*** *dot-map of the naps in A.* ***C*** *Overlay of A and B, verifying the positioning.*

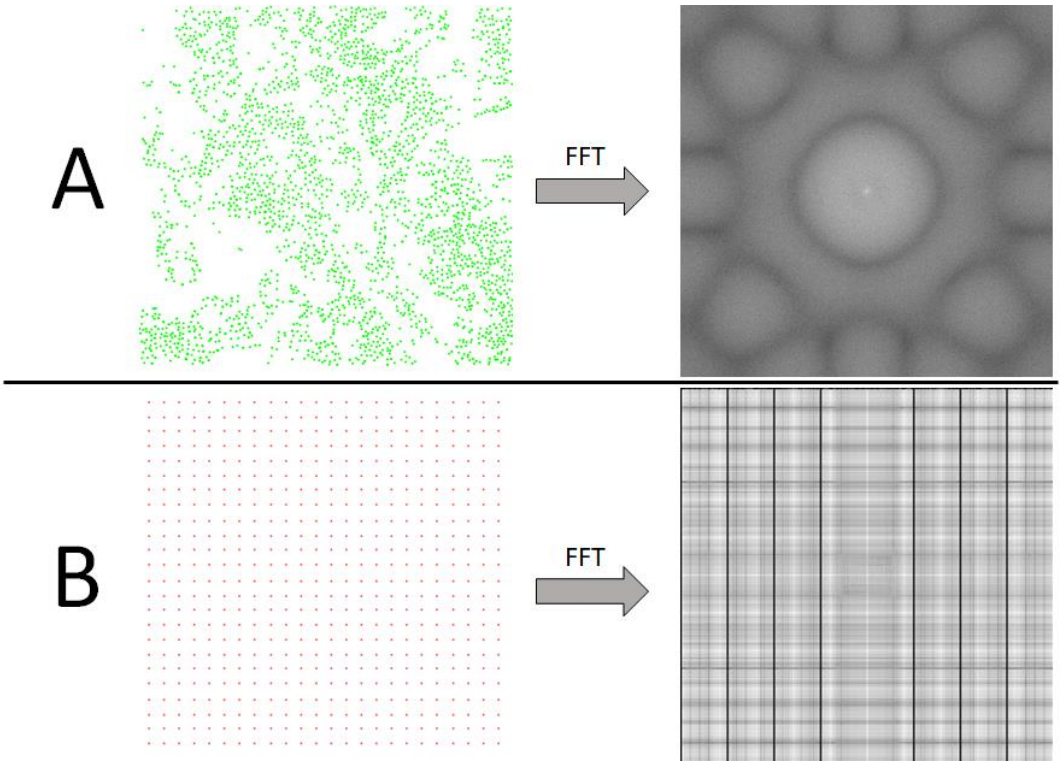

Figure 44: Fast-Fourier-Transformation of Dysodius dot-map (A) and periodic distributed animated pillars (B).

Following Formula 20, a dense array, i.e. an array with small pitch p leads to high capillary forces (wetting is energetically favourable). However, the viscous frictional losses due to the denominator in Formula 20 ($\kappa\eta l^2$) slow the spreading. The smaller p the slower the spreading.

On the other hand, in a relatively broad capillary channel although the driving capillary pressure is smaller than in between the pillars, the viscous friction is much lower. Thus, the water rapidly fills the network of capillary channels and from there the wetting of the surface occurs due to imbibition wetting. This can be shown easily as exemplified in the following image sequence in **Figure 45**. Here a piece of glass was subjected to grinding so that the surface is rough and exhibits imbibition wetting. An open capillary channel of 500 µm width was then grounded into the glass using a diamond milling head. When applying a drop of water, one can clearly see that the channel is filled throughout its length (approx. 10mm) rapidly and then from the filled channel the water starts the imbibition of the surface slowly but steadily. Thus the additional channels speed up the wetting process of the rather large *Dysodius* species and show once again, why it is of importance for the bigger species *D. magnus*, to exhibit faster capillary transport.

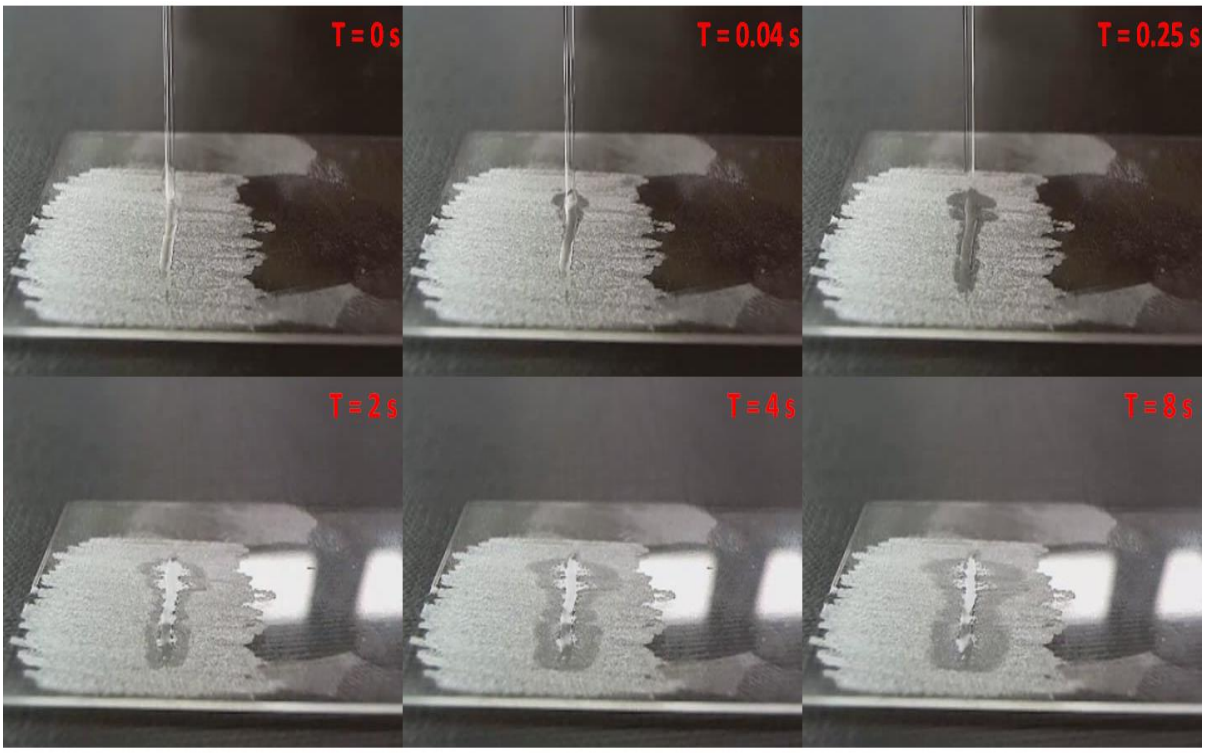

Figure 45: Image sequence of water dropped into a capillary on glass and imbibing the adjacent, rough surface. *The water is quickly transported through the whole capillary (within 0.25 s). The capillary then acts as a reservoir, allowing for slow imbibition of the adjacent rough surface. Image series from a video shown in Hischen et al. (2017).*

4. Surface-Oil-Interaction: The scent efferent system of bugs

As introduced in Chapter 2.1, true bugs exhibit a fascinating way of self-defense. Oily, often stinky and sometimes even poisonous fluids are produced in specialized gland systems and transported through channels to the surface. From the channel opening (orifice), the defense fluid is forwarded to body parts with enhanced surface area where the evaporation process of the fluid is maximized. In some species this so called evaporium is located directly next to the orifice, in others it is forwarded through specialized channels, the so called peritreme. Together, orifice, pereitreme and evaporium make the total of the scent efferent system in Heteroptera.

Interestingly enough, not only there are big differences within certain families, concerning the position and distance of orifice and evaporium to each other (hence the need for individual lengths and solutions for the peritreme), but rather the fact that the position of the orifice on the body is not conserved throughout the suborder of Heteroptera itself. As also already described in Chapter 2.1, Pentatomids for example usually exhibit scent gland openings between the coxa of leg pairs two and three, while on Aradids (confirmed so far for *Dysodius* only), the gland orifice can be found underneath the wings on their dorsal abdomen. Hence, it is only logical, that different species have found various solutions for their scent efferent system in order to fulfill the job of transporting the defense fluid from orifice to evaporium.

Previous works (Kupsch, 2015; Plamadeala et al., 2017; Reiswich, 2013) have shown that an especially extraordinary form of scent efferent system can be found on *Dysodius*: Here, the scent efferent system is located underneath the wings. Since the glands orifices are located centrally on the dorsal abdomen, but the evaporium at the wing joint, the fluid needs to be transported all the way through a very long peritreme. It was found, that this transport is facilitated by a microstructure covering the peritreme, that allowed for passive, directional transport of the oily defense fluid and that this can be abstracted and applied to technical surfaces in order to invoke similar transport dynamics on these.

The question this chapter deals with therefore is as follows: Are there similar microstructures to be found in a) different species within the family of aradids, and b) can one find such structured peritremes in completely different species and families. If this were the case, an attempt would be made to abstract the general features and apply them to technical surfaces in order to copy the effect of passive, unidirectional fluid propagation.

Towards this end, morphological investigations of several different species from various families of bugs are presented in this chapter.

4.1 Materials and methods

For this investigation, bugs from different locations all over the world were collected and analyzed by means of SEM. Analogous to the protocol described in Chapter 3.2.1, the bugs were air-dried, silica-gel dried and sputter coated before images were taken under the SEM. Research focus was put on the investigation of the scent efferent system, i. e. the gland orifice, the peritreme and the evaporium. Investigated species are listed below.

Family of Aradidae (Bark bugs)

Aradus betulae (LINNAEUS, 1758), collected in Kazakhstan and Austria; Provided by Ernst Heiss

Figure 46: Example picture of A.betulae.

Aradus depressus (FABRICIUS, 1794), collected in Czech Republic; Provided by Ernst Heiss

Figure 47: Example picture of A. depressus.

Aneurus macrotylus (JAKOVLEV, 1880), collected in Eastern Siberia (Russia); Provided by Ernst Heiss

Figure 48: Example picture of A. macrotylus.

Brachyrynchus membranacaeus (FABRICIUS, 1798), collected in Malaysia; Provided by Ernst Heiss

Figure 49: Example picture of B. membrnacaeus.

Dysodius magnus (HEISS, 1990) and *D. lunatus* (FABRICIUS, 1775), collected in French Guyana; Provided by Ernst Heiss

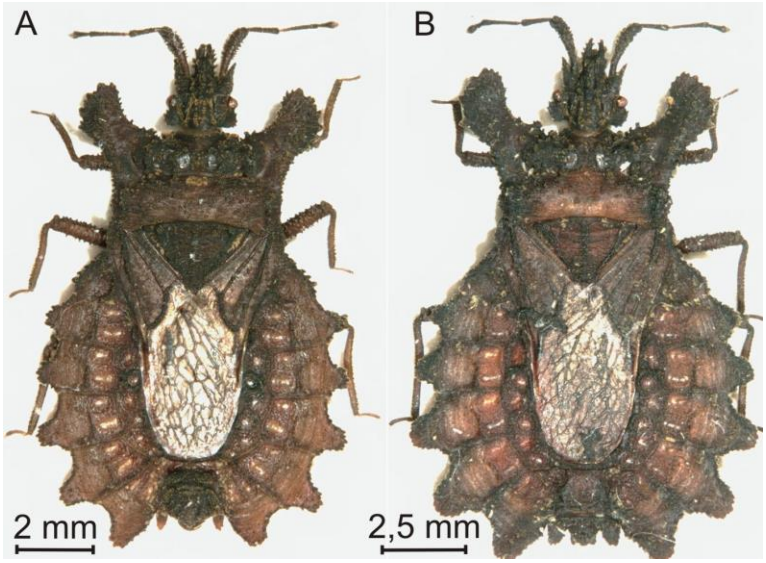

Figure 50: Example pictures of D. lunatus (A) and D. magnus (B). Images from Reiswich (2013).

Hesus subarmatus (STÅL, 1873), collected in Ecuador; Provided by Ernst Heiss

Figure 51: Example picture of H. subarmatus.

Neuroctenus hyalinipennis (KORMILEV, 1971), collected in Cambodia; Provided by Ernst Heiss

Figure 52: Example picture of N. hyalinipennis.

Family of Coreidae (Leather bugs)

Coreus marginatus (LINNAEUS, 1758), collected in Austria by Florian Hischen

Figure 53: Example image of C. marginatus. *Image source: https://de.wikipedia.org/wiki/Lederwanze, 26.07.2017.*

Family of Cydnidae (Earth bugs)

Tritomegas bicolor (LINNAEUS, 1758), collected in Austria by Florian Hischen

Figure 54: Example picture of T. bicolor*. Image source: https://de.wikipedia.org/wiki/Schwarzwei%C3%9Fe_Erdwanze, 26.07.2017.*

Family of Pentatomidae (Tree bugs)

Palomena prasina (LINNAEUS, 1761), collected in Austria by Florian Hischen

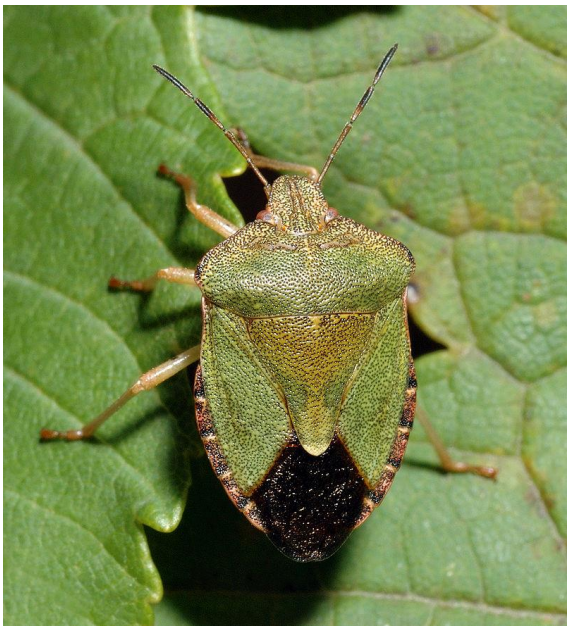

Figure 55: Example picture of P. prasina. *Image source: https://de.wikipedia.org/wiki/Gr%C3%BCne_Stinkwanze, 26.07.2017.*

Raphigaster nebulosa (PODA, 1761), Collected in Austria by Florian Hischen

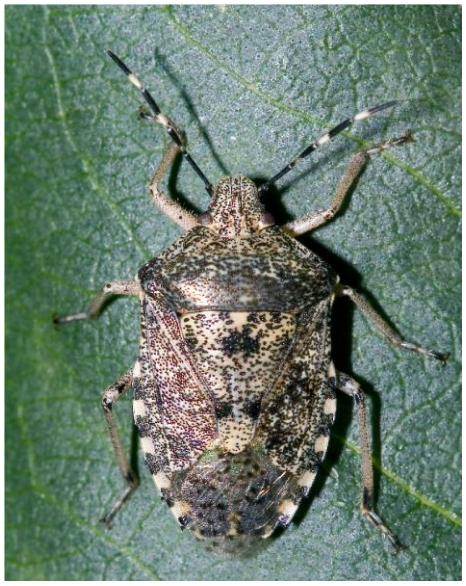

Figure 56: Example picture of R. nebulosa. *Image source: https://de.wikipedia.org/wiki/Graue_Gartenwanze, 26.07.2017.*

Family of Phyrrhocoridae (Fire bugs)

Phyrrhocoris apterus (LINNAEUS, 1758), collected in Austria by Florian Hischen

Figure 57: Example picture of P. apterus. *Image source: https://de.wikipedia.org/wiki/Gemeine_Feuerwanze, 26.07.2017.*

4.2 Results

In the following, the SEM scans of the scent efferent system (SES) of all species introduced in 4.1 are presented. Order of presentation is analogous to order of introduction in the materials and methods part.

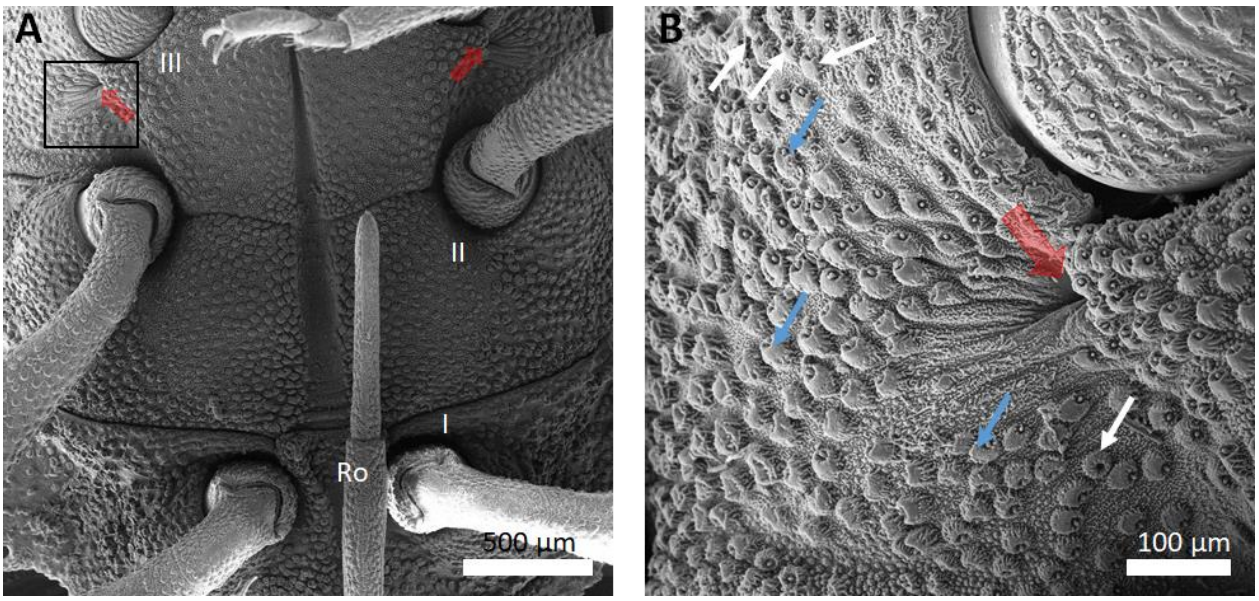

Figure 58: Ventral top view of the scent efferent system of A. betulae. A *Overview of the ventral side. Position of the gland orifice is marked by red arrows. Numbers I-III mark the leg pairs from rostral to caudal. The tip of the rostrum is visible (Ro).* ***B*** *Magnified image of the black box from A. Again, a red arrow is marking the orifice of the scent gland. Blue arrows mark surface microstructures that cover the whole surface. White arrows mark surface structure that are missing the central "hair" compared to the ones indicated by the blue arrows.*

Figure 58 gives an overview of *A. betulae's* SES. Clearly, the orifices of the glands are located between leg pair II and III on the ventral side of the metathorax, but slightly closer to the coxa of leg pair III. In the magnification (**Figure 58 B**) one can see that no apparent form of evaporium and/or specialized peritreme structures are connected to the scent gland opening. It is notable though, that the whole surface of *A. betulae* is covered with microstructures (blue and white arrows in **Figure 58 B**). Some of them exhibiting a central opening with a very delicate tip or hair (blue arrows), while others appear to have a hole at their tip (white arrows). According to Schmitz et al. (2010), these microstructures are mechanosensors (blue arrows) and possible infrared sensors (white arrows). It is assumed at this point, that these microstructures serve as a form of evaporium for *A. betulae*, since they are in immediate vicinity of the gland opening and by default enlarge the surface area for any fluid that is secreted by the glands. It also interesting to note that according to Davidová-Vilímová (2006), the scent gland openings of the juvenile bugs are located dorsal on the abdomen, while the adult individuals show the gland openings as pictured. Unfortunately,

no nymphs of this species were available during this work, but a comparison would be suggested for future work.

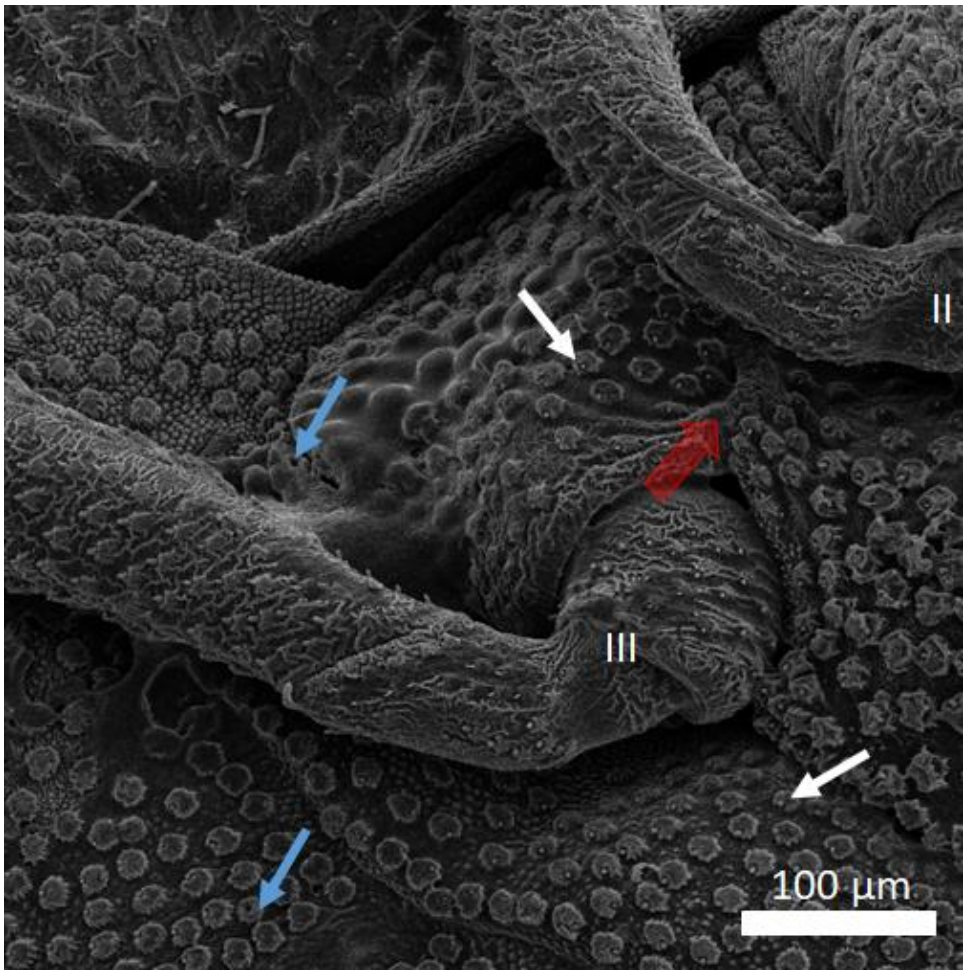

Figure 59: SES of A. depressus. *Ventral overview of the scent gland orifice (red arrow) located between leg pair II and III. White arrows mark microstructures with a central hair, blue arrows microstructures with a central hole.*

Shown in **Figure 59** is the SES as found in *A. depressus*, which is overall quite comparable to the situation found on *A. betulae* (**Figure 58**). Again, the orifice of the scent gland is located between leg pair II and III with the orifice being slightly closer to the coxa of leg pair III. Also again, one finds the whole surface of the bug covered with the same kind of microstructures (blue and white arrows) as already seen on *A. betulae*. It is assumed that function of these structures is analog to *A. betulae*, meaning that structures marked by white arrows are mechanosensors while blue arrows indicate infrared sensors, since both species are closely related. Not surprising, again no apparent SES in the sense of functional parts is visible. This leads to the assumption that the microstructures on *A. depressus* also take over the role of a directly to the orifice connected evaporium. Obviously, an extra peritreme obsolete in this case.

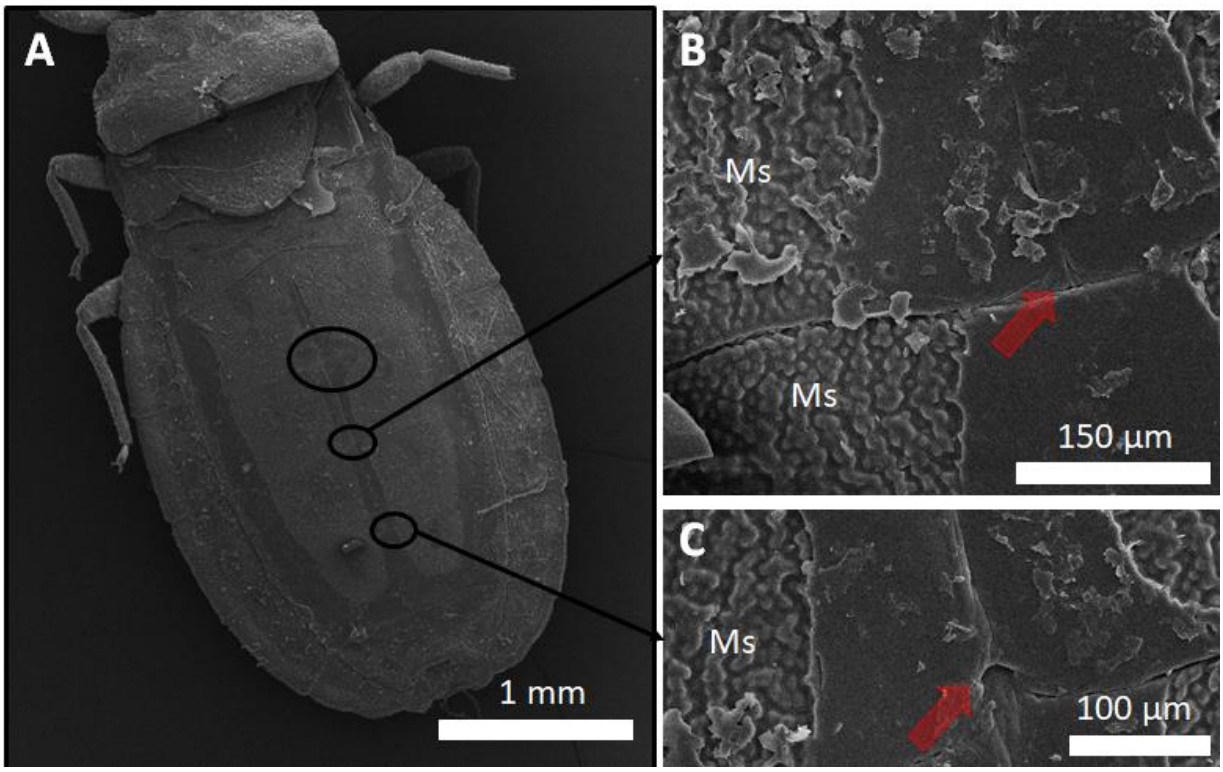

Figure 60: SES of A. macrotylus. A *Overview of the dorsal side with detached wings. Marked with black circles are the three scent gland orifices.* ***B*** *Detail view of the second orifice (red arrow) and the microstructured fields surrounding it (Ms).* ***C*** *Detail of the third orifice (red arrow) and surrounding microstructure (Ms). Orifice of gland one looks virtually the same as B.*

Figure 60 shows the SES of *A. macrotylus*. In a direct comparison to the two former mentioned species of *Aradus*, it becomes immediately obvious that the position of the scent glands is completely different. In this case, three gland orifices can be found on the dorsal abdomen, usually covered by the wings of the animal (detached for the pictures). The glands are located along the middle axis of the abdomen and show no functional parts of a typical SES. The details shown in **Figure 60 B** and **C** reveal the orifices to be surrounded by very smooth surface of the tergal disc. At the edges, some kind of rougher microstructure can be detected but there is no apparent connection between these and the scent gland openings. It can only be assumed that the evaporation of defense fluid takes place in immediate vicinity to the gland orifices itself, without the enhancement of surface enlarging structures as shown before.

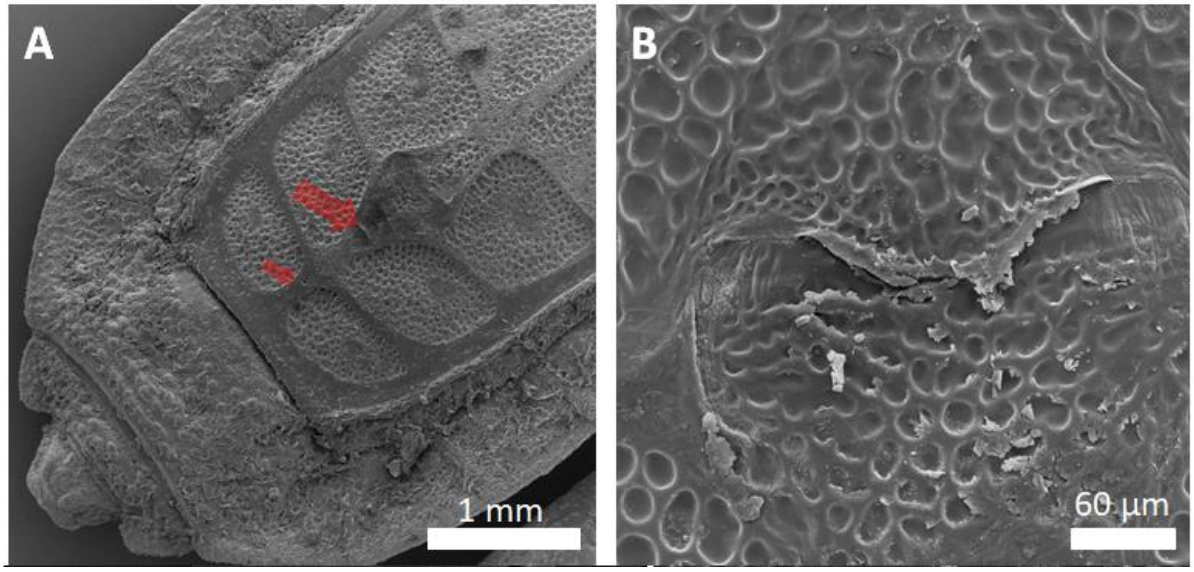

Figure 61: SES of B. membranacetus. A *Dorsal Overview of the abdomen (wings removed). Red arrows mark the position of two scent gland orifices.* ***B*** *Detail of the bigger orifice (marked by the top arrow in A). It appears as if a part of the cuticle is covering the central part of the orifice, allowing fluid to be secreted to the sides only.*

In **Figure 61** the SES situation of *B. membranacetus* is depicted. Again, one finds the SES orifices on the dorsal side as shown for *A. macrotylus* before. In this case though, it was only possible to identify two orifices on the central axis of the tergal disc (red arrows). The topmost one shows an interesting, waved shape (**Figure 61 B**) that appears as if fluid only can be secreted to the sides of the opening, while the bottom one is just a simple, circular hole in the cuticle. It has to be assumed though, that there should be a third gland opening somewhere closer to the scutellum (along the axis of the tergal disc), which was not to be found in this SEM session. It is possible that the orifice was covered with surface waxes and therefore was missed.

The images shown in **Figure 61** also reveal that *B. membranacetus* does not exhibit any kind of microstructure protruding from the surface, in order to enlarge the surface area for evaporation of the defense fluid. In contrast, *B. membranacetus* exhibits small, densely packed indents on the body surface surrounding the scent glands, giving the surface the overall appearance of a “golf ball”. It can only be speculated if or if not these indents serve the function of evaporation enhancement, since one would assume that a fluid would rather be pooled in the little indents, than being evaporated with higher velocity – this might speak for a specialization of this species to rather extend the duration of defensive smell than maximizing the intensity.

The following **Figure 62**, **Figure 63** and **Figure 64** summarize the findings for *Dysodius lunatus* and *D. magnus.*

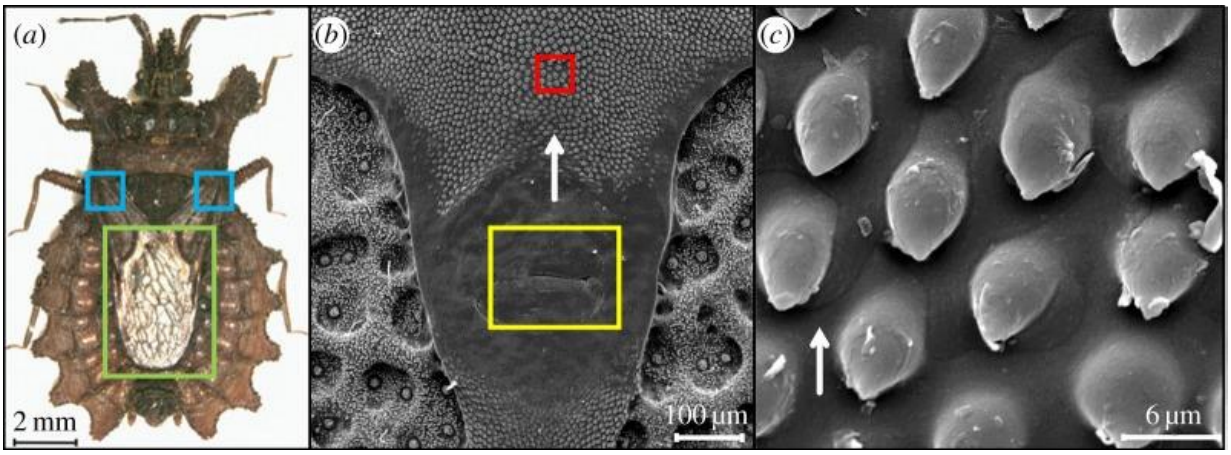

Figure 62: Overview of the SES as found on Dysodius (shown is D. magnus as representative, since D. lunatus virtually shows the same features). (a) *Overview of the whole bug. Green box marks the position of the SES underneath the wings, blue boxes mark the position of the presumptive evaporia at the connection joints of the wings.* ***(b)*** *Central scent gland in the middle of the tergal disc (yellow box) and adjacent areas of orientated microstructures. The white arrow marks the direction of defense fluid propagation.* ***(c)*** *Detail of the microstructure (red box in b). The tips of all microstrcutures are orientated against the fluid transport direction. Image as shown in Plamadeala et. al (2017).*

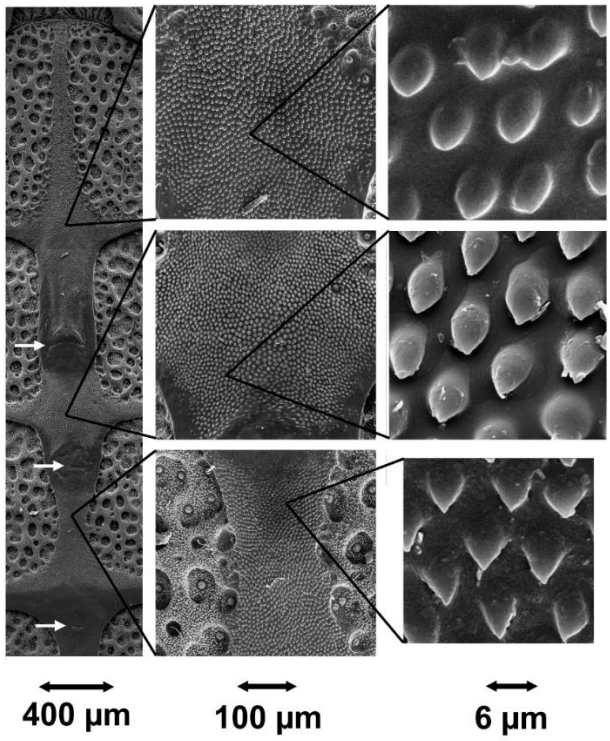

Figure 63: Position of the scent orifices along the central axis of the tergal disc (white arrows*). The second column of images shows microstructured areas adjacent to the orifices. The third column of images shows in detail the orientation of the microstructures in there corresponding areas. As one can see is the orientation highly conserved across the whole structured area and represents the peritreme on Dysodius. Image as shown in Plamadeala et al. (2017).*

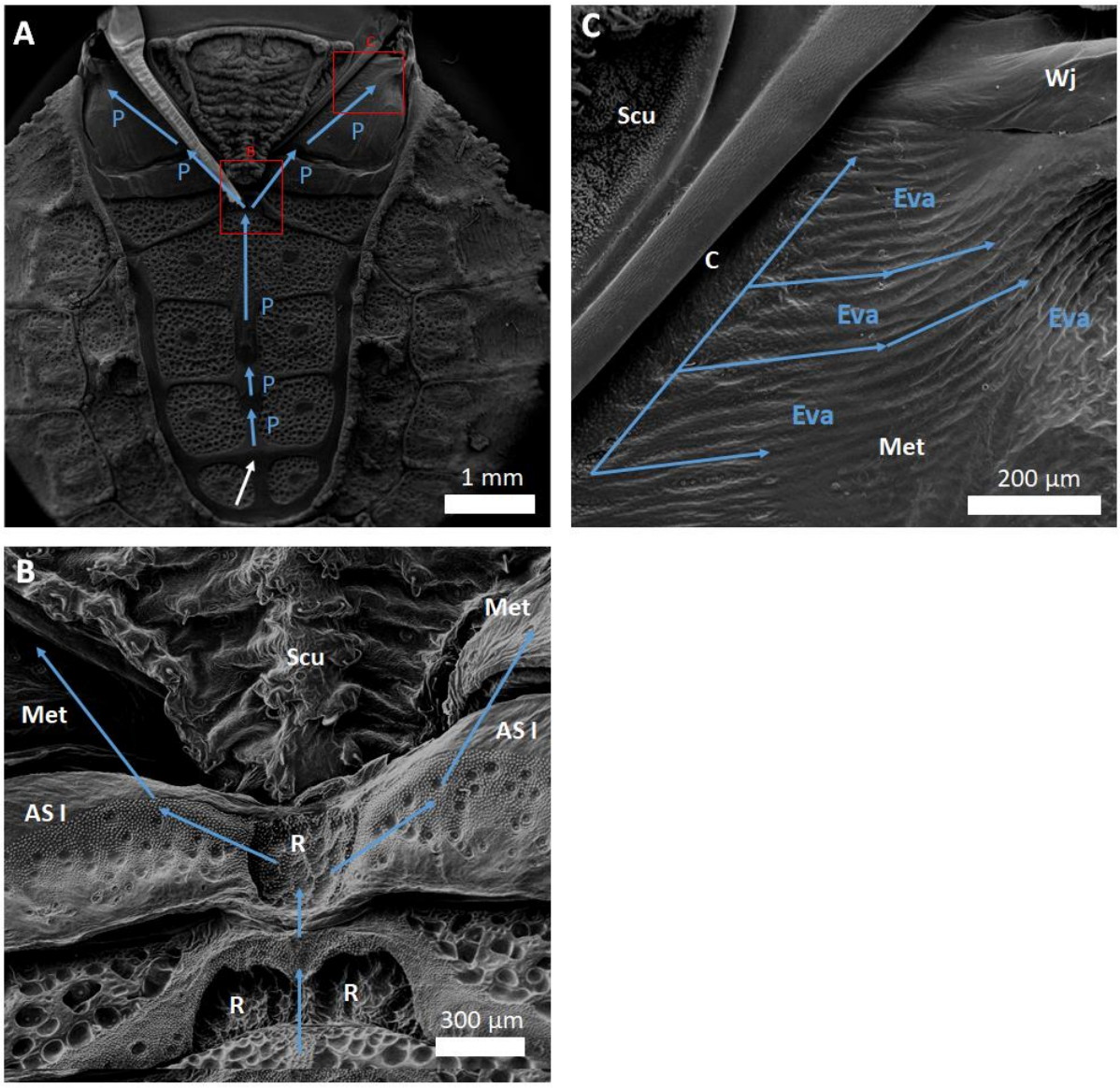

***Figure 64: Propagation of microstructure across the whole SES of Dysodius (again only D. magnus is shown represntatively)**. **A** Overview of the complete SES. Beginning from the most caudal scent orifice(white arrow), orientated microstructure can be found along the complete axis of the tergal disc, splitting into two pathways, left and right (tip of scutellum, red box "B"), onto the dorsal surface of the metanotum, finally reaching the supposed evaporia at the attachment joints of the wings(red box "C"). This whole way (path of blue arrows) can be considered the peritreme (P) of Dysodius. **B** Magnified detail of red box "B" in A. The transition of the peritreme from the tergal disc, onto the surface of abdominal segment I (AS I) is realized by the three pockets marked with "R" (supposedly reservoir function). From here the peritreme progresses at the edge of the scutellum across the surface of the metanotum (Met). **C** Magnified detail of the evaporium (Eva, red box "C" in A). The edge between metanotum and scutellum acts as a capillary (C), aided with orientated microstructure, and propagates fluid to the ridged fields underneath the wing joint (Wj).*

Figure 62 and **Figure 63** give a comprehensive overview of the position, composition and microstructures that together make the SES of *Dyosidus*. Three scent gland orifices are located across the middle axis of the tergal disc, dorsally on the abdomen. The orifices are connected by fields of microstructures that all have tips pointing in the same orientation (always pointing caudally). These microstructure fields are

supposedly the functional component of *Dysodius*' peritreme, in total helping to passively transport defense fluid underneath the wings to evaporative areas located at the wing joints. The complete fluid propagation way is depicted in **Figure 64**, showing that fluid transport is further aided by cuticle pockets that possibly have reservoir function, helping the defense oil to overcome the ridges between abdominal segment I and the metanotum. Here, the ridge between scutellum and metanotum seems to act as a form of additional capillary, forwarding the fluid to the evaporia underneath the wing joints. It has not been proven yet, how *Dysodius* unleashes the active substances from its defense fluid from here (in case the wings are folded and therefore covering the evaporia) but it is assumed that vibration of the wings may facilitate the active substances to evaporate from here. Additinonally, we already succeeded in copying the fluid transport in Kupsch (2015) and Plamadeala et al. (2017), proving that the theory is feasible. An investigation of living specimen would be the best way to proof it.

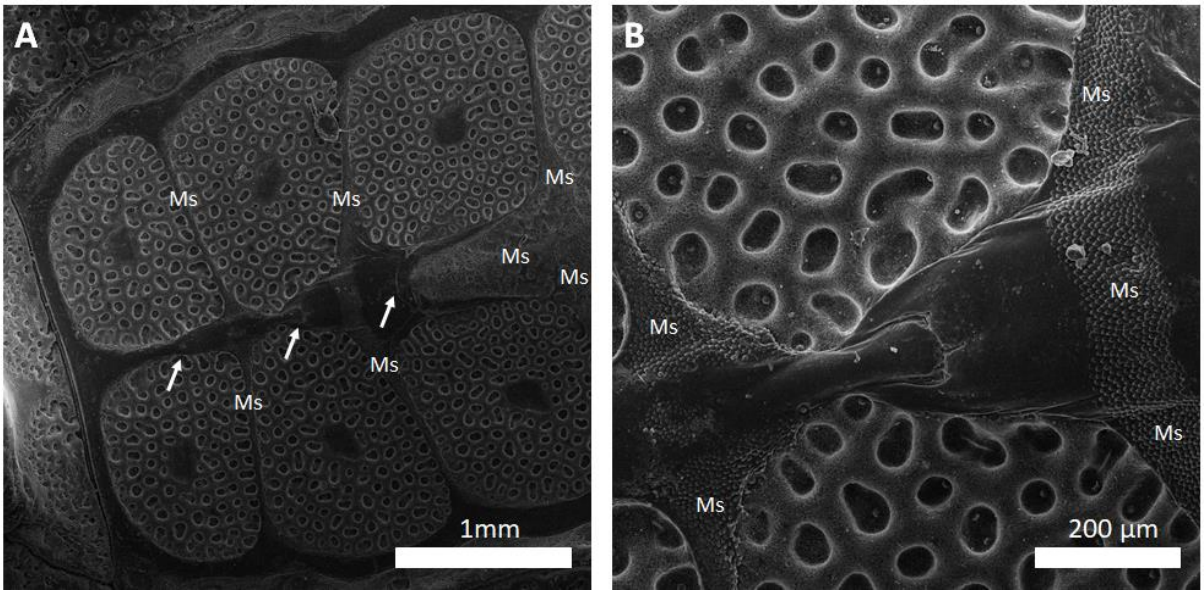

***Figure 65: Overview of the SES in H. subarmatus (wings detached). A** Dorsal top view of the tergal disc and the position of the three scent gland orifices (white arrows). Microstructures (Ms) very similar to Dysodius can be observed at different parts of the tergal disc. **B** Magnified detail of the centrals scent gland orifice and attached microstructured areas of the tergal disc.*

In **Figure 65** the situation of the supposed SES is summarized for *H. subarmatus*. Again, as one can locate three scent gland orifices along the middle axis of the tergal disc. In contrast to *Dysodius*, the scent glands are not consecutively connected with microstructured areas but instead very similar microstructure can be found in laterally radiating rows ("Ms" in **Figure 65 A**). **Figure 65 B** shows such microstructures around the central scent gland orifice in higher magnification. Interestingly though, no such microstructure can be found outside of the tergal disc on *H. subarmatus*, the last fields can be found close to the edge of

abdominal segment I (not shown). Additionally, no trace of evaporative fields around the wings or elsewhere could be found on the investigated samples. This leads to the assumption that in case of *H. subarmatus* probably the microstrcutured fields act as both, peritreme (for transportation and spread of the defense fluid), as well as evaporium.

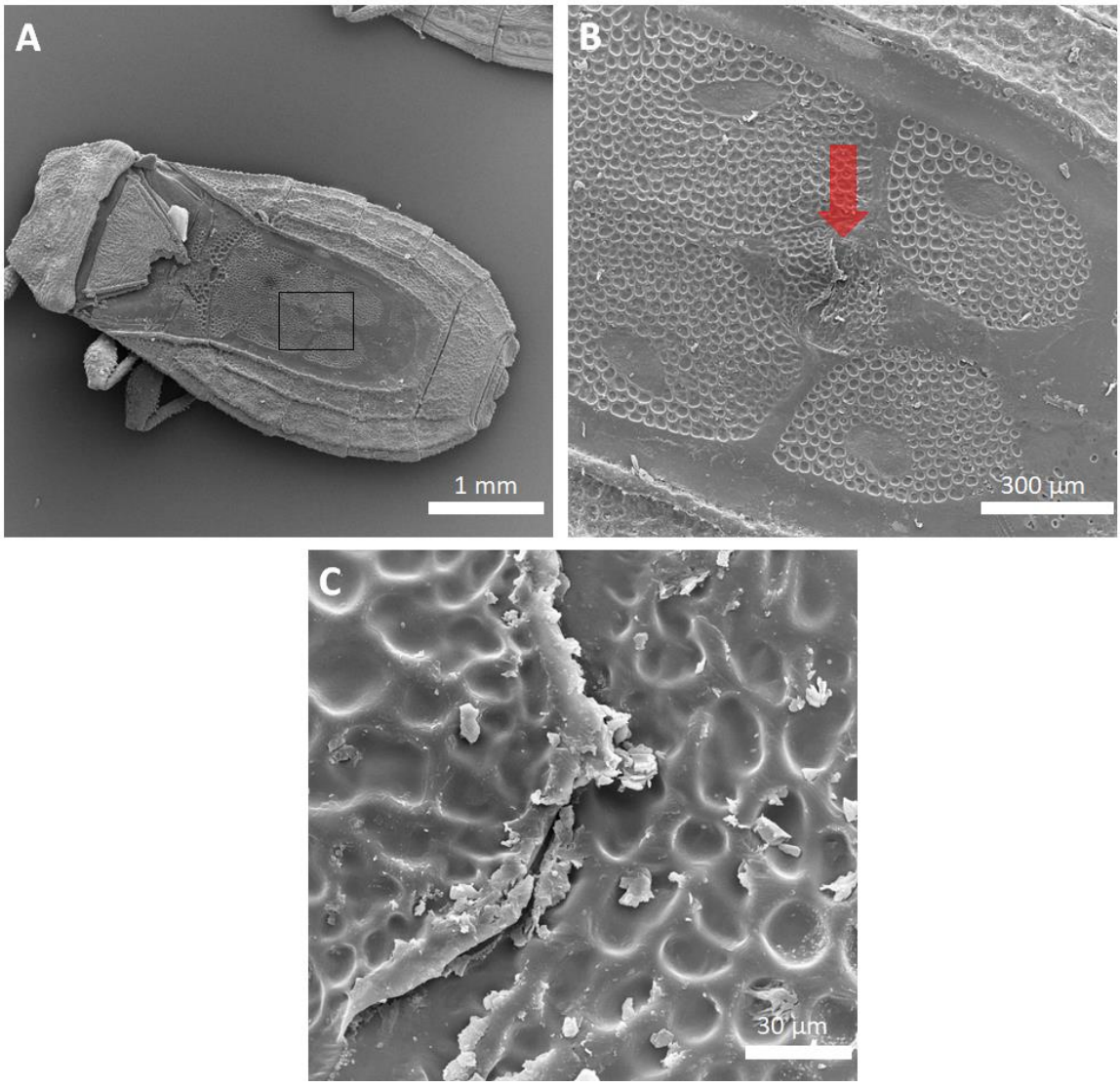

Figure 66: SES situation on N. hyalinipennis (wings detached). ***A*** *Overview of the dorsal side.* ***B*** *Magnified detail of the black box in A. The red arrow marks the only scent orifice that was found.* ***C*** *Detail of the scent gland (red arrow from B).*

Figure 66 shows the SES as it was found on *N. hyalinipennis*. In contrast to previously shown results, *on N. hyalinipennis*, only one scent gland orifice could be discovered. Placed centrally on the tergal disc, the opening resembles a lot of similarity compared to the one found on *B. membranacaetus*. And like previously discovered for *B. membranacaetus*, again no surrounding microstructure or specialized surface area could be detected that either resembles a preitreme or evaporium.

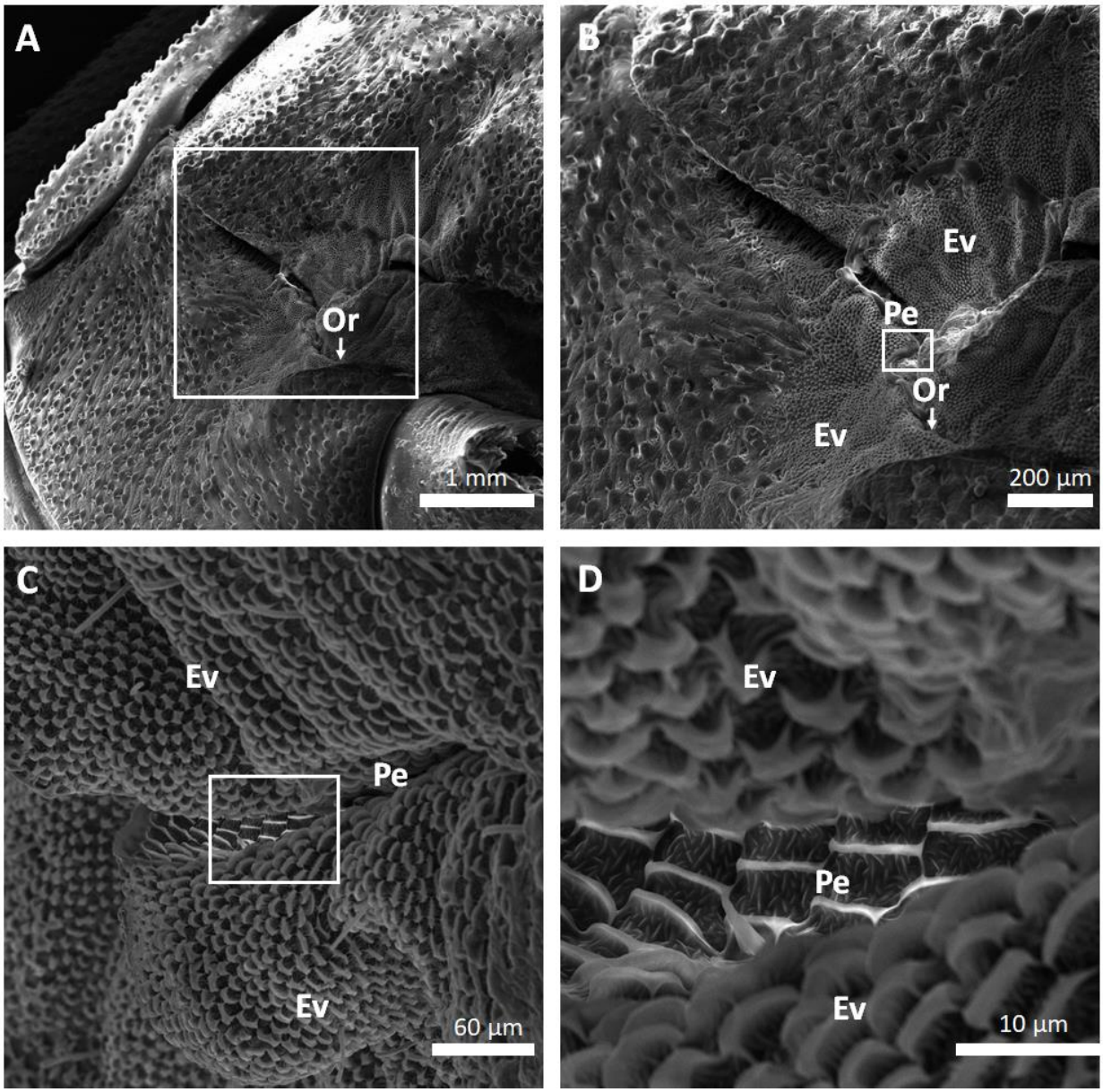

Figure 67: Overview of the SES of C. marginatus. A *Ventral view of the location of the SES (here right system of the bug). The orifice of the scent gland lies covered by folds and ridges beneath the coxa of leg pair II.* ***B*** *Detail of the white box from A. Adjacent to the orifice runs a deep suture in lateral direction (possibly the peritreme, "Pe"), which is surrounded on both sides by vast fields of microstructured evaporium (Ev).* ***C*** *Detail of the evaporium surrounding the peritreme suture (magnified from the white box in B).* ***D*** *Close-up of the microstructures of evaporium and peritreme (white box from C). Clearly the surface of the evaporium is heavily enlarged by lamellar like microstructures, which in less denser arrays also seem to cover the insides of the peritreme suture.*

The SES of *C. marginatus* is shown in **Figure 67**. Like already shown for both investigated species of *Aradus*, the scent efferent system is also located between the coxa of leg pair II and III in this species. The orifice is well covered by the ridges and sutures of the adjacent cuticle, which simultaneously form a channel for the peritreme (**Figure 67 B**). Left and right, the preitreme is surrounded by vast evaporative areas, showing a very complex form of microstructure for surface enlargement. Shaped like little plates or lamellae, these

microstructures also can be found at the bottom of the peritreme. Despite the complete and complex implementation of the SES on this species, no evidence for orientated structures have been found that might serve the purpose of forwarding fluid in special directions.

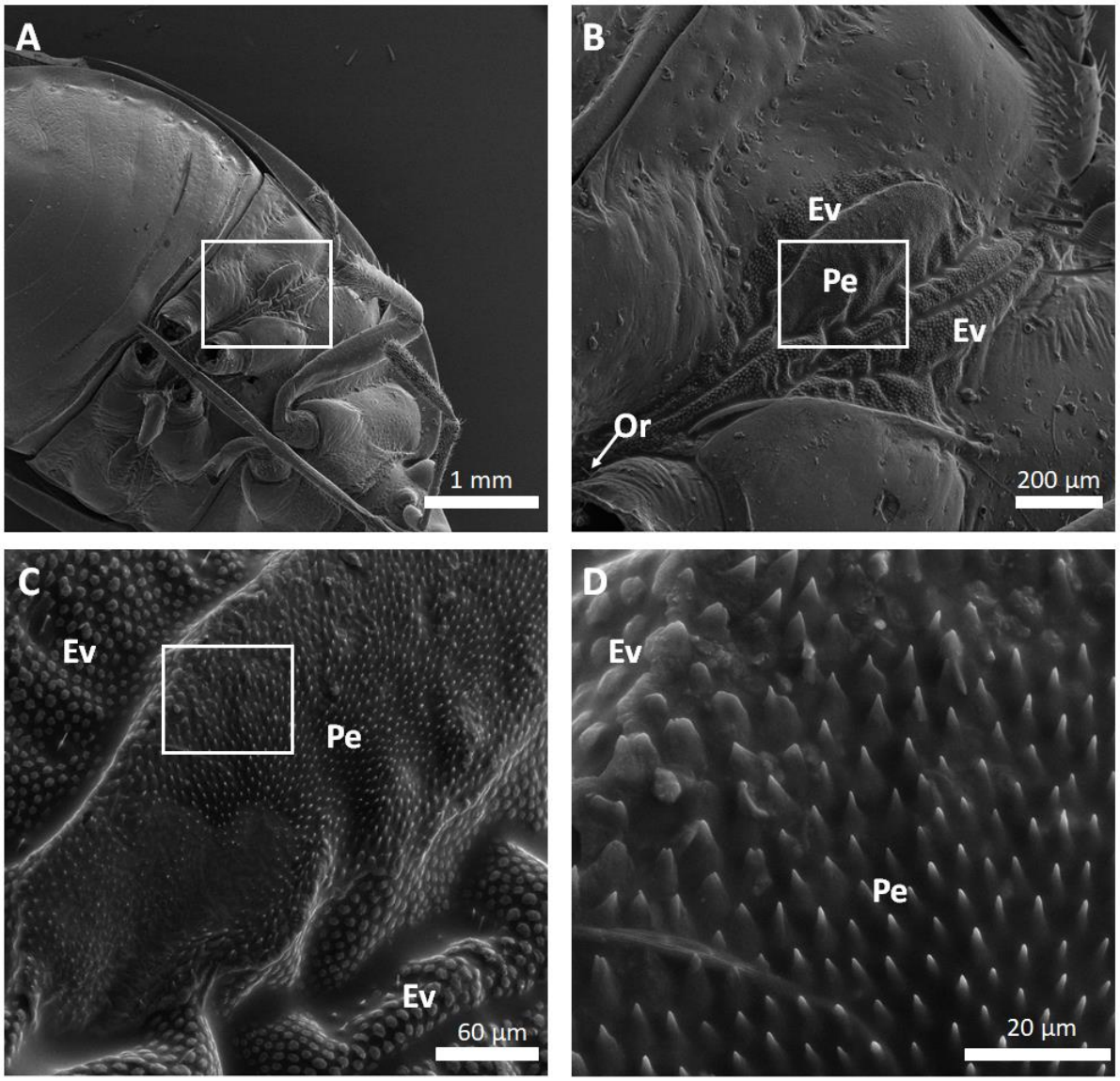

Figure 68: Overview of the SES of T. bicolor. A *Ventral view of T. bicolor. Marked with the white box is the right part of the SES, which can be found analog on the left side of the bug too.* ***B*** *Detail of the white box in A. Visible is a complete SES with all functional parts: The orifice of the gland (Or) is located underneath the coxa of leg pair II. A folded channel connects the orifice with the peritreme (Pe) which slightly protrudes from the body surface. The evaporium is framing the peritreme from both sides.* ***C*** *Detail from the white box in B. The microstructures of peritreme and evaporium can clearly be distinguished from each other: While the peritreme exhibits small, pointed and orientated microstructures, structures of the evaporium are bigger and round or hexagonally shaped.* ***D*** *Magnified detail of the microstructures of peritreme and adjacent evaporium (magnified image of the white box in C).*

Figure 68 shows that *T. bicolor* exhibits a SES with all functional components: Orifice, preitreme and evaporium could be located between leg pair II and III on both sides of the bug. The orifice is connected with a folded, shallow channel to a raised peritreme (**Figure 68 B**), which itself is surrounded by the microstructures of the evaporium. (**Figure 68 B** and **C**). We find that peritreme and evaporium exhibit two different kinds of microstructure (**Figure 68 D**): While the peritreme exhibits small, pointed and orientated microstructures, structures in the evaporium are slightly bigger, roundish of hexagonally shaped and without any recognizable orientation. Concerning the function, it has to be assumed that the orientated microstructures of the peritreme aid passively the transport of the defense fluid across the raised slope of the evaporium, in order to reach the fields of evaporial microstructures, which serve the purpose of surface enlargement for better/faster evaporation. The microstructures of *T. bicolors'* peritreme resemble enough similarities with the ones found on *Dysodius* (in that is: form, dimension and orientation), for which they were chosen as candidates for the abstraction and replication process introduced in following Chapter 5.

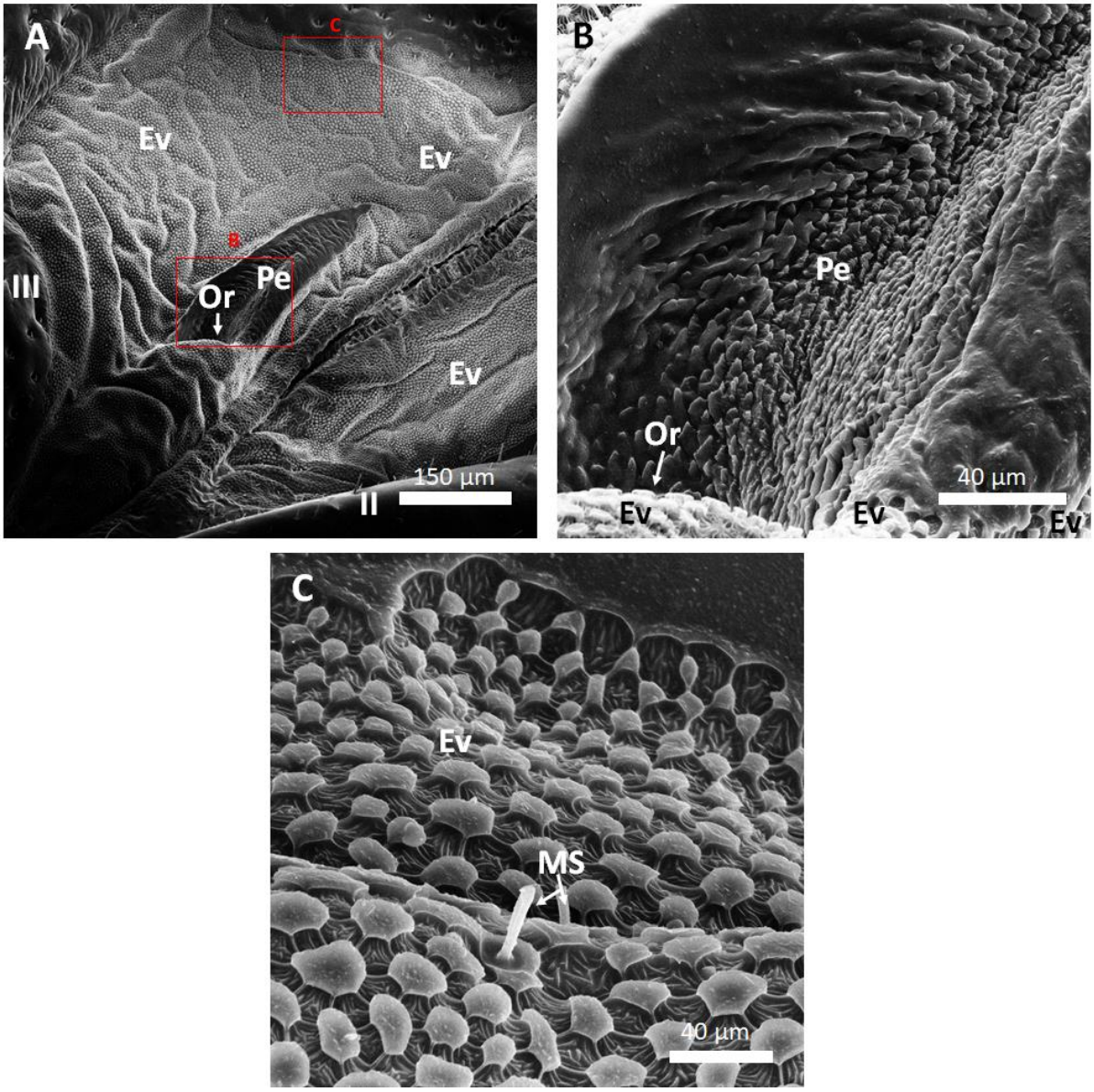

Figure 69: SES of P. prasina. A *Overview and location of the SES (shown is a ventral image of the bugs left side system). Close to the coxa of leg pair III, the orifices (Or) of the scent gland are positioned. The orifice is adjacent to a tongue-shaped peritreme (Pe) area and both, orifice as well as preitreme are surrounded by vast fields of evaporium (Ev).* ***B*** *Detail of the peritreme (red box "B" in A). One can clearly see a pointed, small microstructure at the bottom of the peritreme. All tips are pointing in lateral direction.* ***C*** *Magnification of the microstructure of the evaporium (red box "C" in A). Mushroom like, or hexagonally shaped protrusions of the cuticle are enlarging the surface area.*

Figure 69 summarizes the situation of the SES as found on *P. prasina*. Again, one can find a completely composited system of orifice, peritreme and evaporium, ventrally located between leg pair II and III on both sides of the animal. Despite only exhibiting a comparably short peritreme, the bottom of it is covered with an interesting microstructure, which once again is exhibiting features of interest: small, pointed and orientated in one direction, are the microstructures forming an dense array, possibly aiding the defense fluid to raise from the orifice onto the evaporium (**Figure 69 B**). The surface enlarging microstrcutures of

the evaporium can be seen in **Figure 69 C**. Here we find structures that are protruding from the cuticle and forming mushroom-like heads, while being interconnected by very small folds. An overall classical composition of SES as introduced in Chapter 2. Nevertheless, due to its intriguing features (pointed, small and strictly orientated), the peritreme microstructures of *P. prasina* were chosen for biomimetical abstraction (see Chapter 5) too.

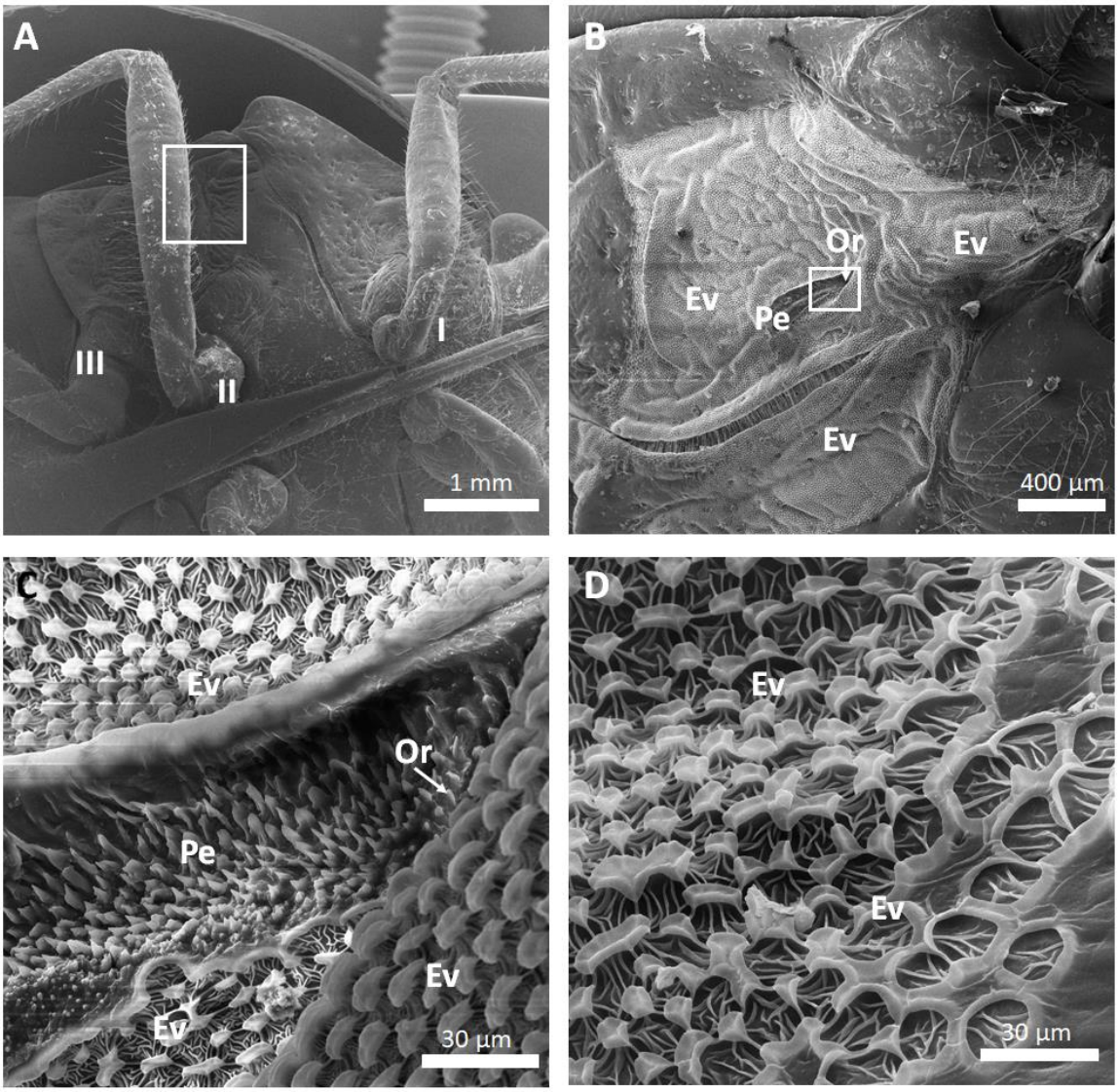

Figure 70: SES of R. nebulosa. A *Ventral overview and location of the SES. Laterally located next to the coxa of leg pair II, the SES can be found on both sides of the bug (here right hand system is marked by white box and magnified in B).* ***B*** *The orifice (Or) is adjacent to a tongue-shaped peritreme (Pe) area and both, orifice as well as peritreme are surrounded by vast fields of evaporium (Ev).* ***C*** *Detail of the peritreme (white box in B). One can clearly see a pointed, small microstructure at the bottom of the peritreme. All tips are pointing in lateral direction.* ***D*** *Magnification of the microstructure of the evaporium. Mushroom or flower like structures are covering the vast evaporative fields.*

Figure 70 summarizes the findings for the SES of *R. nebulosa*, a species closely related to *P. prasina*. Not surprisingly, both species show relatively similar results. With the exception that the orifice of *R. nebulosa* is located more laterally and closer to the coxa of leg pair II, form and shape of the peritreme, as well as the microstructure of peritreme and evaporium, are quite close to what has been found previously on *P. prasin*a. Mainly due to also exhibiting a similarly dimensioned and orientated microstructure in the peritreme, *R. nebulas* was also selected for the biomimetic abstraction process in the following Chapter 5.

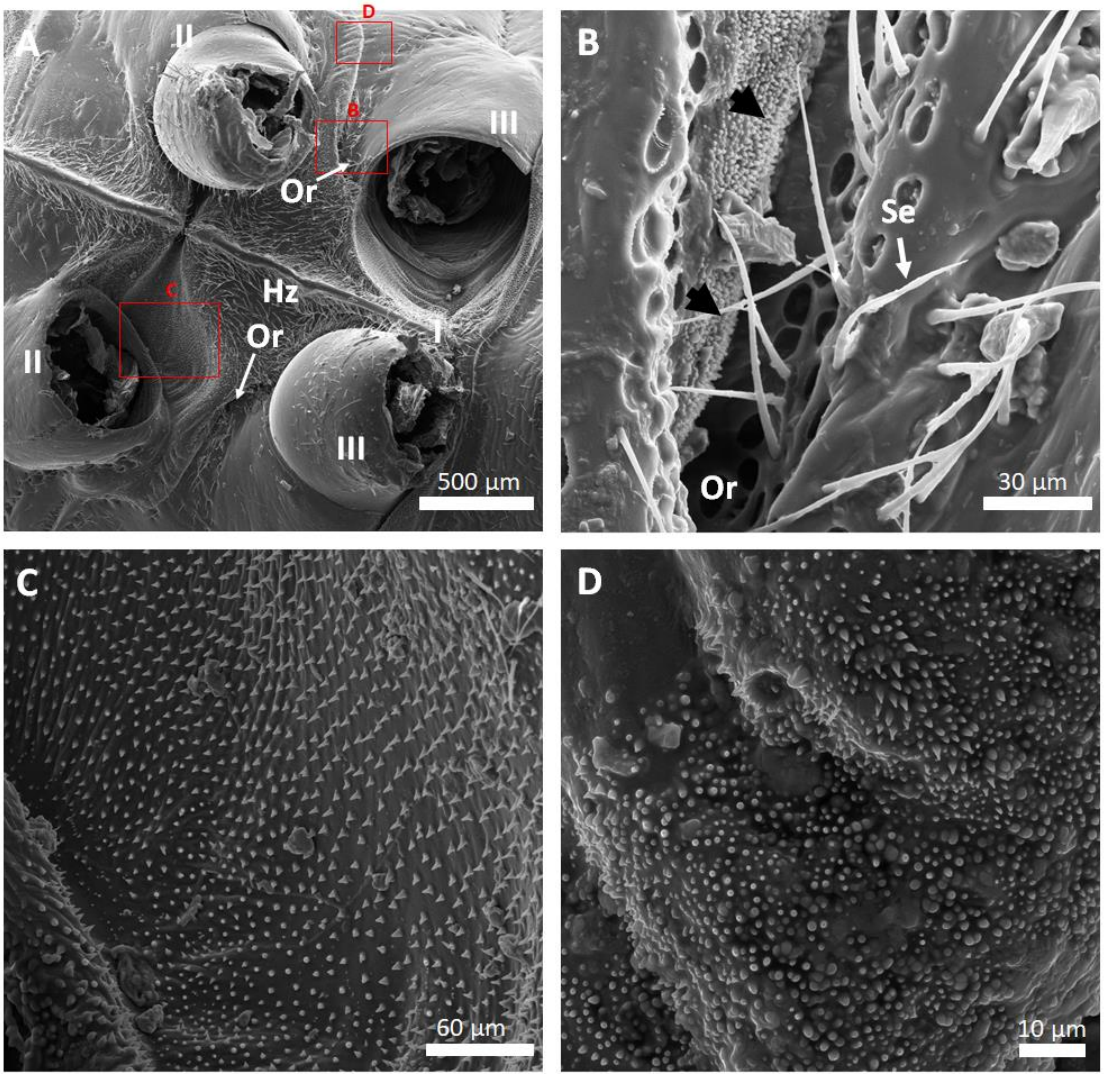

Figure 71: SES of P. apterus. A *Ventral overview. Visible are the coxa of leg pair II and III (legs detached), the orifices of the scent glands (Or), as well as a zone with dense setae (Hz = "hairy zone").* ***B*** *Detail from red box "B" in A. In the magnification the orifice of the gland and an adjacent suture become visible. The suture itself exhibits very small and dense microstructures (black arrows) on one side wall and dense setae on the other side.* ***C*** *Detail from the red box "C" in A. Between leg pair II, two relatively big indents can be found in the cuticle, densely covered with saw-tooth-like microstructure.* ***D*** *Detail from the red box "D" in A. In continuation of the sutures edge (also shown in B) more microstructure can be found. Individual structures exhibit sizes of ~1 µm and show no apparent orientation*

Findings for the SES of *P. apterus* are summarized in **Figure 71**. Once again, a species, which exhibits scent glands in between leg pairs II and III on its ventral side. In contrast to other shown representatives of other European true bugs (e.g. *P. prasina*, *R. nebulosa, C. marginatus* and *T. bicolor*), *P. apterus* does not show the typical composition of a complete SES though. As shown in **Figure 71 B** and **D**, neither a true peritreme, nor a true evaporium can be identified with absolute clarity. Instead, P. apterus exhibits gland orifices that seem to secrete the defense fluid into a suture, which is covered with a very fine microstructure on side and densely standing setae on the other. The microstructure in this case also does not show any trend of orientation. Interestingly though, one can find big indents in between the coxa of leg pair III (**Figure 71 C**), which are covered with a microstructure similar looking (also dimension wise) to those previously found on true bugs with a complete SES. It is not known as of now if these structures are in any form involved in the secretion/evaporation process of defense fluid in *P. apterus*, a reason for which they were not chosen for biomimetic abstraction.

4.3 Discussion

The goal of this chapter was to figure out more about the scent efferent systems of different species and families of bugs. Inspired by the work of Kment & Davidová-Vilímová (2010), in which light was shone on the thoracic scent efferent system of Pentatomidae and the findings of Kupsch (2015), Plamadeala et al. (2017) and Reiswich (2013), 11 species (including *Dysodius lunatus* and *D. magnus*) were selected in order to further deepen the knowledge about the morphological treats of the SES. The selected species cover a total of six different families and seven different subfamilies from various areas of the world.

Despite the fact that the investigated species were introduced in alphabetical order in chapter 4.1 and 4.2, discussion of the results should start with the findings shown for *Dysodius* – the so to say "golden standard" for this work. **Figure 62**, **Figure 63** and **Figure 64** depict the situation of the SES as found and previously investigated on *Dysodius*. In total, one finds a complex scent efferent system, consisting of the three functional elements orifice, peritreme and evaporium. In contrast to the idea of SES as introduced by (Kment & Davidová-Vilímová, 2010; also introduced in Chapter 2.1) for Pentatomidae, the SES of *Dysodius* is positioned at the back of the animal, underneath the wings (**Figure 62 A**). Three gland orifices are located along the middle axis of the tergal disc, interconnected by small, pointed microstructures that orientate in caudal direction. (**Figure 62 B** and **C**, **Figure 63**). This microstructured peritreme – which function mainly is supposed to be facilitation of passive fluid transport – continues across the ridge of abdominal segment I, and along the edge of the scutellum, laterally across both sides of the metanotum, bevor reaching the evaporia which are located underneath the attachment joints of the wings (**Figure 64 A**, **B** and **C**). Big indents at the transition between abdominal segment I, metanotum and scutellum (**Figure 64 B**), supposedly act as reservoirs for the fluid that is climbing rostral underneath the wings, to facilitate and overcome the ridges.

The works of Kupsch, as well as Plamadeala et al., successfully showed that it is indeed possible to transfer these found principles of the scent efferent system from *Dysodius* onto technical surfaces and copy the effect of passive, directional fluid transport – in other words, to copy the peritreme and the found microstructures in it. A focus of this chapter therefore was, to find morphological similarities in different species that would allow for the same. Towards this end, species that would show small, pointed and most importantly orientated microstructures within their peritreme would be selected for the attempt to abstract and transfer the structures and underlying mechanisms onto technical surfaces (see chapter 5).

As already mentioned, the order of investigation was coupled to the introduced, alphabetical order, as counted down in chapter 4.1. Hence, first shown are representatives of the family Aradidae. This makes

sense not only from the alphabetical order, but also since previously stated findings of *Dysodius* suggested, that close (or relatively close) relatives might show similar SES.

The first two species investigated were *Aradus betulae* and *A. depressus*, both members of the Aradidae family, subfamily of Aradinae and European-situated. Morphological results, as shown in **Figure 58** and **Figure 59** interestingly show major differences when compared with *Dysodius*: The scent gland system is located on the ventral metathorax, between leg pair two and three, as opposed to the abdominal scent gland system of *Dysodius*, which is located centrally on the tergal disc. Well, this is not totally precise though. Yes, the found metathoracal scent glands of *Aradus* seem to be the more prominent and seemingly main-used ones for defense purpose, but Davidová-Vilímová (2006) reported that it is or was false believe of many authors, that dorsal abdominal glands (DAGs, e.g. as found for *Dysodius*) are reduced or missing in adult *Aradinae.* In general, several authors have confirmed the existence of DAGs in Heteroptera that previously were thought to exhibit only ventral, metathoric scent glands as adults (e.g. Gough et al., 1985; James, Heffer, & Amaike, 1996; Usinger & Matsuda, 1959). It is not always stated how or if those DAGs are functional, therefore in this work, only scent glands with confirmed functionality are under investigation – in case of *Aradus*, this is the metapleural scent gland system (MTG). As seen from the images presented for *Aradus* (**Figure 58** and **Figure 59**), the considered MTG does not exhibit all components of a SES as given by Kment & Davidová-Vilímová (2010): Around the orifice no peritreme or specialized evaporia can be found. Given the abundance of different microstructure around the scent gland opening though (mechanosensors, infrared sensors and setae), it is assumed that these provide enough surface area enlargement for the shown species, to effectively spread and evaporate the defense fluid. Unfortunately, no living specimens were available during this work, to confirm the secretion and evaporation mechanism live – a fact that needs to be considered for future work.

Following, the situation of SES for the subfamilies of investigated Aneurinae and Mezerinae (both family of Aradidae) is discussed, in comparison to *Dysodius* as “golden standard” (due to the already successfully abstracted SES in this species, as previously stated). Since *Dysodius* itself being a member of Mezerinae, and the Aneurinae being closer comparable in morphology to these than Aradinae, it was expected to find more similar SES in the investigated species than previously stated for *Aradus.* Unsurprisingly, the results as a start confirm the scent system of all investigated species being located dorsally on the abdomen – hence, confirmation of DAGs and confirmation of the findings presented in Panizzi & Grazia (2015), and Usinger & Matsuda (1959).

For *A. macrotylus* (Aneurinae, **Figure 60**) and *H. subarmatus* (Mezerinae, **Figure 65**) three DAGs could be identified along the axis of the tergal disc, while for *B. membranacetus* (**Figure 61**) two DAGs and for *N. hyalinipennis* (**Figure 66**) one DAG have been found respectively. It is unclear at this point, if the incomplete number of DAGs on *B. membranacetus* and *N. hyalinipennis* is originating from the fact that missing gland orifices were covered by surface waxes and overlooked, undetectable due to alteration of the surface morphology because of the used preparation protocol for SEM, or are plainly not developed in these species. Further work should be invested towards this in the future in order to verify the findings.

Interestingly, only one of the four previously mentioned species exhibited microstructures comparable to *Dysodius*. While *A. macrotylus*, *B. membranacetus* and *N. hyalinnipenis* exhibit either no microstructure at all (e.g. A. macrotylus, **Figure 60**), or round indents, reminding of golf ball surfaces (e.g. *B. membranacetus*, **Figure 61**; *N. hyalinipennis*, **Figure 66**), only *H. subarmatus* showed microstructures (**Figure 65**) that are comparable to the ones found in the peritreme of *Dysodius.* Even though being comparable in shape and dimensions (also being orientated caudally, i.e. the same direction as in *Dysodius*), the microstructure found on H. subarmatus does not seem to be part of a sophisticated SES. The images show that there is no connection either between the orfices of DAGs, or between the stripes of laterally across the tergal disc running microstructures themselves. Further, no evidence of similar microstructure has been confirmed for positions on either the dorsal edge of abdominal segment I, or the metanotum. Same applies for investigated areas in the vicinity to the attachment joints of the wings: No microstructure and no seemingly specialized areas that might be connected to evaporation have been found.

The findings so far are suggesting that the genus *Dysodius* developed the reported, complex SES independent from other shown closely related species. Within the family of Aradidae, investigated species of Aneurinae and Mezerinae show comparable positioning and morphology of the DAGs, but intrinsic similarities of peritreme and evaporium are missing. At this point it can only be speculated that habitat and mode of life are the reason behind the different characteristics of shown scent gland systems and that most probably the need for and frequency of flight, hence the frequency of wing usage, might be a driving force for obvious adaptations. Field studies are suggested and comparison of more closely related species from the same habitat might give a final answer.

Another question that comes up, after seeing the results for the investigated species, is: What is the benefit of DAGs and MPGs respectively? For species able to use their wings (reportedly the case for all shown Aradidae), what is the use of exhibiting DAGs that are covered by the wing membranes most of the time and therefore rendering the evaporation of defense fluids less effective as if uncovered (with the

exception of *Dysodius*, where obvious adaptation has been performed to overcome this). Or is it vice versa, and the positioning underneath the wings has the advantage of facilitating scent distribution (e.g. to "wag the scent away")? For long time it was believed, that the natural development of scent glands in Heteroptera follows the trend of DAGs during larval development and complete shift (or substitution) into MPGs in the adult animal. First reports of DAGs in adult bugs can seemingly be found in contributions of Dupius (1949) and Henrici (1939), and the modern knowledge towards this topic is mainly formed by the work of Staddon (1979). As mentioned earlier, Davidová-Vilímová (2006) also irrevocably proofed the existence of DAGs in *Aradus* and therefore, for a member of Aradiadae. What we know so far therefore is, that Aradinae seemingly develop both, DAGs and MPGs, while Mezerinae and Aneurinae (at least the investigated species in this work), skip the transformation when becoming adults and keep the DAG system. It is definitely a must to investigate the ventral side of shown members of Aradidae in future work too, in order to confirm this. Nevertheless, up to this point the question of why DAG or MPG, or even both, remains unanswered and to the knowledge of the author hasn`t been answered by any other work either.

In further results of this chapter, MPGs and SESs of different European true bugs have additionally been investigated with regard mainly to intrinsic structures/microstructures of the peritreme. Most authors agree, that especially Pentatomidae (and therefore related Pentatomorpha families like Coreidae, Cydnidae and Pyrrhocoridae) are considered to be closely related to the family of Aradidae (e.g (Schaefer, 1993) and therefore suitable for comparison.

Following the order in alphabetical fashion (family wise), findings for the SES of *C. marginatus* (Coreidae) are depicted in **Figure 67 A** and **B**. Even though the orifice is quite hidden in this species, one can find a complete SES consisting of orifice, a very narrow peritreme channel and adjacent evaporia, ventrally between the coxa of leg pair II and III. Here again, as seemingly normal for Pentatomorpha that are not Aradidae, the bug exhibits MPGs, rather than a DAGs. The evaporative fields are vast and composed of a lamellar or micro-plate like microstructure, which also covers the inside of the peritreme (**Figure 67 C** and **D**). Clearly, this microstructures' function is the enlargement of surface for enhanced evaporation of defense fluids, though no obvious directionality or orientation of structures within the peritreme or adjacent evaporative fields could be detected. Since the found microstructure furthermore doesn't show any morphologic resemblance compared to *Dysodius*, it was discarded for further biomimetic abstraction processes.

A representative for the family of Cydnidae is shown in **Figure 68**, namely *T. bicolor*. Unsurprisingly, since also a pentatomorph bug, we again find a SES in form of MPGs located ventrally between leg pair II and III.

Morphologically, immediately many differences become obvious though, when comparing this bug to *C. marginatus*: The peritreme channel is quite long, very shallow and lanced by folds of the cuticle. Additionally it seems to rise on its way ventrally in height **Figure 68 B** and **C**. Surrounded by evaporative fields on both side with small, roundish microstructures, this risen part of the peritreme exhibits a microstructure which is very similar to what has been found on *Dysodius*: Pointed microstructures cover the risen part of the peritreme, perfectly orientated with their tips in lateral direction (the part of evaporium that is adjacent behind this part of the peritreme) (**Figure 68 C** and **D**). Since such structures usually are serving a purpose on an animal and no wings that needs to be locked in resting position, are close (as it is the case on *Dysodius*), one should assume, that these microstructures play a role in the defense-liquid distribution on *T. bicolor*. In this context, a clear difference shall be noted though: The found microstructure of *T. bicolor* is pointing in the reverse direction when compared to *Dysodius*, meaning that on *Dysodius*, the microstructures' tips are pointing away from the evaporium, while in case of *T. bicolor*, they are pointing towards. The relevance of this directionality will be further discussed in chapter 5.3. Nevertheless, reasoned by morphologic and dimensional similarities, peritreme structures of *T. bicolor* were chosen for biomimetic abstraction and transfer process as described in following Chapter 5.

Following the findings of *T. bicolor*, two very close related representatives of the pentatomid family are shown in **Figure 69** and **Figure 70**. Namely *P. prasina*, the classical European green stink bug, and *R. nebulosa*, also a very common visitor in European gardens. Reasoned by their close relation and attended similarities in mode of life as well as habitus, both species shall be discussed in conjunction. The SEM images of both species show that once again the typical, ventrally located MPG can be found. A complete and perfectly "classical" SES as described by Kment & Davidová-Vilímová (2010) is determinable, nicely showing orifice (ostiole), peritreme and evaporium (**Figure 69 A** *P. prasina*; **Figure 70 B** *R. nebulosa*). Even more interestingly: Both species show very similar microstructure covering the inside of the concave peritreme. In both cases, small, pointed microstructures can be found, pointing laterally, towards the evaporium and away from the orifice (**Figure 69 B** *P. prasina*; **Figure 70 C** *R. nebulosa*). This microstructure is very well comparable to that found on *T. bicolor* (therefore again: reverse direction of the tips when compared to *Dysodius*) and was chosen for further investigation and abstraction in Chapter 5, for obvious reasons. Interesting to note is, that the evaporia (**Figure 69 C** *P. prasina*; **Figure 70 D** *R. nebulosa*) of both investigated species also show more or less the exact same microstructure for surface enlargement. It seems to be assumable, that in the family Pentatomidae, this surface enlargement structure is highly conserved and has been also reported for *Graphosoma lineatum* (Durak & Kalender, 2007).

Finally, in **Figure 71** the findings for the last investigated species of this chapter are described. The SES of *P. apterus*, a member of the family of firebugs (Pyrrhocoridae) is shown, again, pentatomorpha typical located ventrally in form of a MPG. One can see in **Figure 71 B** in contrast to previous scent systems presented in this chapter, the orifice of *P. apterus'* scent glands are quite covered and connected to a very narrow and deep channel. This channel does not exhibit any close resemblance to previously shown SES, i.e. it does not show a continuous microstructure, nor does it project towards a clearly identifiable evaporium. One side of the channel is covered by microstructure, smaller than anything described before (> 1 µm and with no obvious orientation), while the opposite channel wall is densely covered with setae (**Figure 71 B** and **D**). At this point, function and meaning of this secretion channels' morphology are unknown and it can only be speculated that both structures, microstructure and setae, are to some degree involved in the secretion process of the defense fluid. The former possibly for enhanced wetting of the surface, the latter maybe as a kind of sensory feedback about fluid flow. Also completely unknown at this point is the function of the microstructure that can be found in between leg pair II (**Figure 71 C**). This structure remarkably reminds of the orientated, pointed microstructures previously found on *T. bicolor*, *P. prasina* and *R. nebulosa*, but position and function are cryptic. For this reason, the found microstructure was not included in the abstraction process in Chapter 5, since no substantiated conclusion about the functionality of *P. apterus* scent system could be made.

In summary, this chapter showed, that aside from *Dysodius*, other species undoubtedly do exhibit microstructures function of which seems to be forwarding, or facilitation of fluids towards a certain direction. Surprisingly, we do not find such structures on very close related species (which also exhibit DAGs), but rather on bugs from farther related families in form of specialized MPGs. Overall much more work should be invested in the morphological comparison and even more species should be screened, but for this work, three species have been found that seem worthy of attempting the abstraction process of their SES, in order to transfer it to technical surfaces. The species of interest are *T. bicolor, P. prasina* and *R. raphigaster* and the abstraction process for their SESs is documented in the following Chapter 5.

5. Abstracting the scent efferent system and technical application

Using the findings from Chapter 4, an attempt was made to transfer the morphology of scent efferent channels microstructures into technical surfaces. The goal was to structure different surfaces with a micro-pattern that allowed directional and passive fluid transport throughout the artificial channel. Towards this end, steel and polymer replicas were designed and fabricated and tested with different oil- and water-based fluids. The fluid behavior was then analyzed by video analysis and automated evaluation algorithms.

5.1 Materials and Methods

Abstraction process

SEM images from the scent glands of *Palomena prasina*, *Raphigaster nebulosi* and *Tritomegas bicolor* were obtained with a Philipps 525 SEM (Philipps, Germany). Two dead and air-dried specimens of each species were dried in an ascending ethanol row (50%-100%) and afterwards sputter coated with gold (Polaron E5200 auto-coating device, former Polaron Unlimited, Great Britain). Coating took place at 10 mA and 1 kV for 180 s in order to achieve a coat thickness of approximately 20 nm (value according to the coater's manual). Images of the respective scent gland of each species as well as of the adjusted channel, evaporative structures and the spikey structures were taken, the structures were measured by means of length, width and slope inclination, using the freeware ImageJ. Between 10 and 25 individual structures were measured in different sections of each specimens scent efferent system. As mentioned before in Chapter 4, the measurements concluded average aspect ratios of 2.3 (± 0.26) : 1 (length : width) and approximately 4.3 (± 0.15) : 1 (length : height). These ratios then were used to abstract the microstructure into a 3D model via the freeware Blender (see **Figure 74 A**), while at the same time scaling them up to dimensions that were suitable for laser ablation. For the actual model used in the laser process, individual structures were composed into a symmetric array and placed at the bottom of a capillary channel with the dimensions of 5 x 1 cm and a depth of 100 µm (see **Figure 74 C**). The abstracted model was laser-engraved into a hardened piece of working steel. A second steel plate was engraved with the same model but inverted z-dimensions, in order to achieve a negative version of the structure that could be used as a mold for producing polymer replicas.

Steel replicas of the scent gland channel (positive, as well as negative as mold)

First demonstrator plates with the bug inspired structures were manufactured at the Fraunhofer Institute for Production Technology IPT (Aachen, Germany) by Kai Wienands and Holger Mescheder, using the process of laser ablation. Therefore an ultra-short pulsed laser (SuperRapid, previously LUMERA LASER GmbH, now Coherent Inc.), integrated in a 5-axis precision machine (KERN Microtechnik GmbH), was used. The laser source emitted a pulsed laser radiation with a wavelength of 532 nm and constant pulse duration of 9 picoseconds. A laser scanner intelliScan10 and a dynamic beam expander VarioScan20i realized the beam guidance (both SCANLAB AG). The laser beam was focused on the surface of the demonstrator plates using a telecentric f-theta lens (Linos Ronar) with a focal length of 100 mm. The base material of the plates was quenched and tempered steel X37CrMoV5-1 with a hardness of 50 HRC. The laser structuring of the steel material was finally performed with a pulse energy of 12.5 µJ achieved by selecting an average laser power of 5 W and a pulse repetition rate of 400 kHz. The active feed rate of the laser beam was 500 mm per seconds. The programming and calculation of the laser paths was done with special CAM software "FlexOStruk", developed at the Fraunhofer IPT. All the programs for laser surface structuring included a contour following strategy with a defined path overlap of 10 µm. The effective ablation depth per single laser reached was 0.75 microns at the positive bug structure and 1.25 microns at the negative bug structure.

PMMA replica of the scent gland channel

The negative patterned steel plate was used as a mold to create a polymer replica of the channel structure from poly(methyl-metacrylate) (PMMA) by means of hot-embossing. PMMA pellets (Lucite Diakon, Lucite International, Netherlands) were placed into a steel bowl, distributed evenly and the mold plate (laser ablated steel negative) was placed on top. The structured side hereby faced the PMMA-pellets. Both, steel bowl and steel negative mold had been thoroughly cleaned with ethanol and dust-free cloths. Onto the mold, a steel weight (13 kg) was placed to supply pressure for the hot embossing process. This hot-embossing composition was incubated in a vacuum drying chamber (Binder VD115, Binder, Germany). The chamber was heated to a final temperature of 210° C and evacuated to a pressure of 30 Pa, using an Edwards Stage 5 E2M5 dual stage mechanical vacuum pump (Edwards Limited, Atlas Copco Group, Sweden). The vacuum served the purpose of evacuating gas from the PMMA and achieve a bubble-free final result. After two hours of incubation, heating was switched off and the chamber was opened for cooling. The PMMA sample was left to slowly cool down for 45 minutes in the chamber. Before the

embossing mold was removed, the embossed PMMA cake was set to cool for additional 10 minutes outside of the chamber at room temperature. After this the PMMA replica of the scent gland channel was removed from the steel bowl and ready to test. Production of the replica was performed at the Institute of Polymer Science and with the help of Gerda Buchberger.

PDMS replica of the scent gland channel

The same steel mold as previously, was also used to create a polymer replica from poly(dimethylsiloxzane) (Sylgard 184 Silicone Elastomer Kit, Dow Corning, USA). The mold was placed into a glass petridish, structured side facing upwards. The setup was carefully leveled in order to avoid thickness inhomogeneity and afterwards poured with the PDMS mix. A needle was used to get rid of bubbles. The poured PDMS was then set to cure for 3 hours at 50° C and then left for 24 hours at room temperature, before the replica was cut out and retracted from the mold. Production of the replica was performed with the help of Gerda Buchberger.

Quality survey of the replicas

All replicas, especially their surface topography, were analyzed with a 3D-microscope Alicona Infinite Focus G4 (Alicona, Austria). This microscope enables detailed surface measurements with resolutions up to 30 µm in x-y-direction and 10 nm in z-direction, using white light interferometry and the patented Alicona Focus Variation Technology.

Testing and analyzing the fluid behavior

All three replicas of the bug-inspired channel (steel, PMMA, PDMS) were tested with different fluids in order to see fluid movement or fluid/surface interaction in general. Steel and PDMS were tested with oils and lubricants in preliminary test series in order to find fluids in a suitable contact angle range. Pre-tests showed, that oils and oily emulsions with contact angles smaller than 35° would lead to relatively slow, omnidirectional fluid movement. Therefore, the final measurements presented in this work where conducted with Sonax P 809 cutting oil (Sonax, Germany) on the steel prototype. PDMS was tested with the multi-purpose oil WD-40 (WD-40 Company, USA). PMMA on the other hand was pre-tested primarily with water-based solutions, like soapy water or alcohol. Pre-tests again showed similar fluid behavior for fluids with contact angles bigger than 35°, but with increased spreading velocities when compared to oils

and emulsions on steel and PDMS. The ideal fluid for the PMMA was found in 1% of soapy solution (DAWN liquid dish soap, Procter & Gamble, USA). All fluids were colored with dyes in order to improve contrast for video analysis. Water based solutions were colored with 0.5% of Ponceau red (Sigma Aldrich, Germany), while oil based fluids were colored with 0.5% of Sudan black (Sigma Aldrich, Germany).

Static contact angles were measured on a custom-made contact angle measurement setup. The contact angles of above mentioned test fluids were measured on an unstructured and cleaned piece of their corresponding material, resulting in the contact angles shown in **Table 3**. The fluid volume was 3 µl for each droplet; six droplets of each fluid were measured on each corresponding material.

For the video analysis of fluid movement on the bug inspired channels, 7 µl droplets of the respective fluid were used for the corresponding channel. Droplets were applied onto the channel structure using a pipette. The fluid movement through the structure then was filmed in a custom video booth, using a Nikon D5300 (Nikon Corp., Japan) with macro lens (AF-S Nikkor 1:2.8, Nikon Corp., Japan). Each structure was tested three times with the corresponding fluid and the capturing frame rate was set to 50 fps. The video was started as soon as the fluid drop hit the structured surface and was terminated if either the fluid stopped to move on its own, or reached the end of the artificial channel. The recorded movies then were transformed into series of frame stacks, using the freeware Avidemux. Typical examples for the resulting frame series are shown in **Figure 72**, whereas the increment between two pictures was set according to the movement speed of the different fluids on the different channel prototypes.

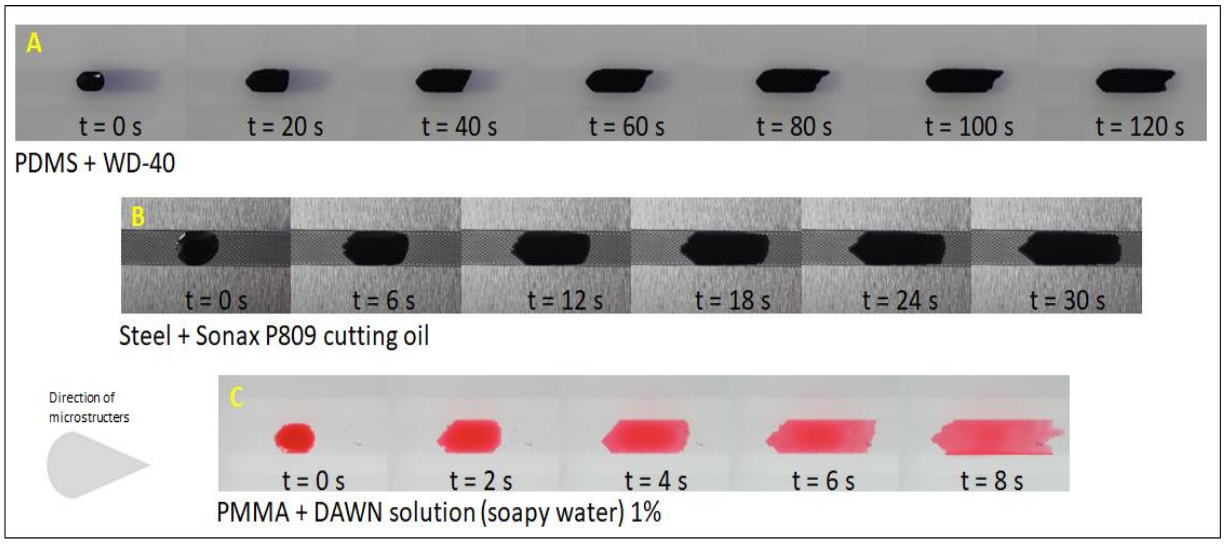

Figure 72: Example image rows, showing the fluid movement of the different test fluids on their corresponding, artificial bug channel. A *WD-40 on PDMS structure, increment between two images is 20 s.* ***B*** *Sonax P809 cutting oil on steel, increment between two images is 6 s. C Cutting oil on Steel, increment is 6 s again.* ***C*** *1% soapy water solution, increment between images is 2 s. The direction for the microstructures within all channels is depicted in the bottom left hand corner.*

Frame stacks of each video were analyzed with a custom-written Matlab script (The MathWorks Inc, USA; Idea for the script: Florian Hischen; Scripting and testing: Gerda Buchberger, Thomas Fritz, Florian Hischen), whereas following steps were undergone: 1) an average background image of the structure without fluid on it is generated from the first 100 frames of each video. 2) The first image with a droplet sitting on the channel structure is set as starting frame for the analyzing process. 3) Each frame from here on is then subtracted from the averaged background image, resulting in a high contrast image in which (almost) only the wetted area of the channel structure is distinguishable from the rest of the image. 4) A Gaussian filter is applied in order to smooth out the edge areas of the liquid front to a degree that fits the maximal structure size of the individual structure features within the channel. 5) A detection algorithm is run over the image to detect the actual wetted area of the channel via a threshold value. The result of this algorithm is a data set, which gives back the wetted area for each individual frame that was analyzed, as well as the minimum and maximum values for fluid movement in x- and y-axis over time. An example outcome of the algorithm is shown in **Figure 73**.

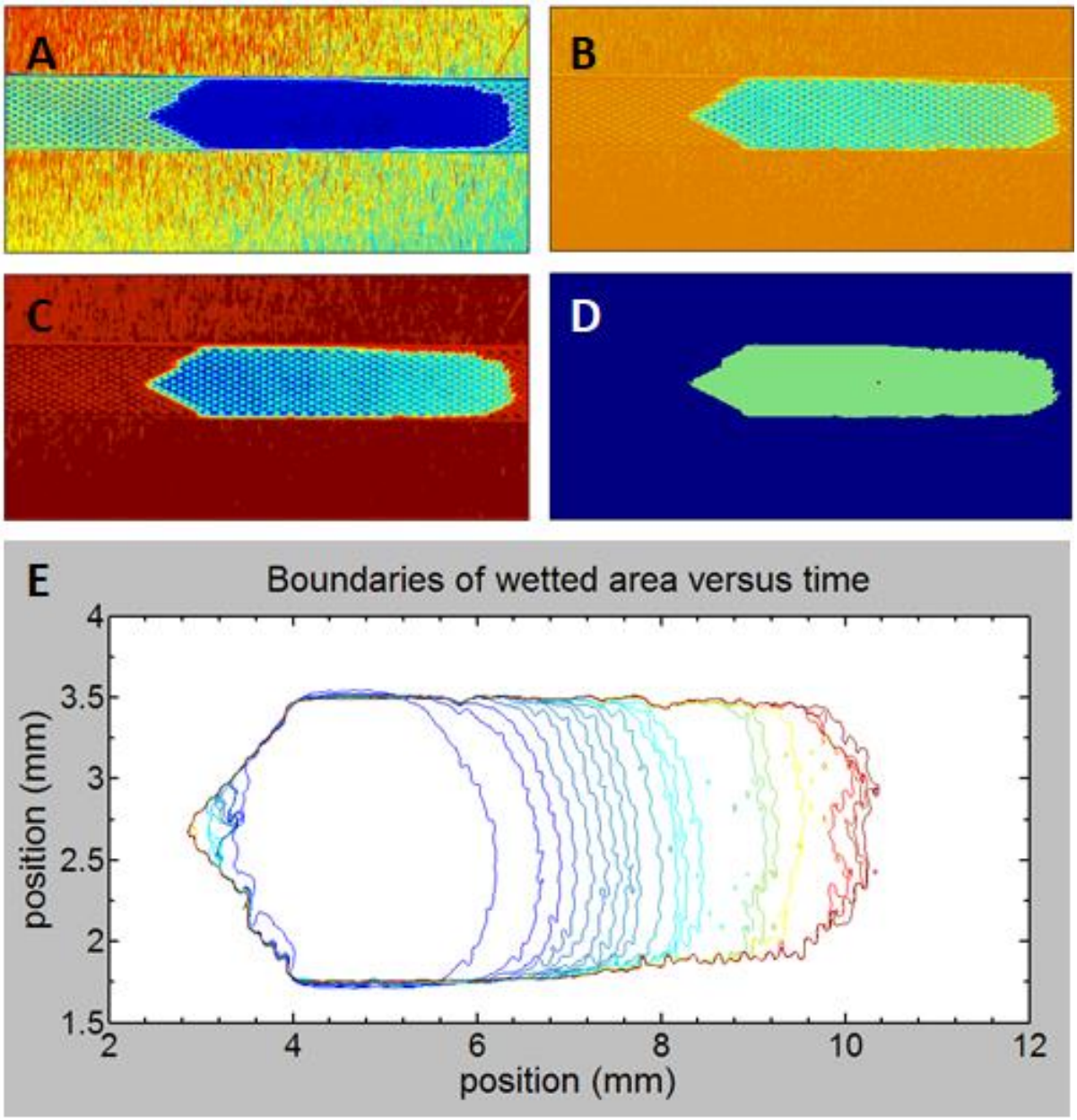

Figure 73: Example overview of the automated video analysis functions used to evaluate fluid movement. Depicted is the last evaluated frame from a video of Sonax cutting oil on steel. ***A*** *Shows the original image in false color scale (= raw image)* ***B*** *Image from A after Background subtraction.* ***C*** *Image from B after the Gaussian filter function has been applied.* ***D*** *Wetted area as recognized by the algorithm.* ***E*** *Boundaries for the wetted area over time for a complete video. Increments between the boundaries are 1 s in this case.*

5.2 Results

As a result from the abstraction process, computer models of individual microstructures were developed, that fulfilled both desired dimensional aspects: 1) Aspect ratios according to the findings in the natural archetype, and 2) size and spacing that is suitable for laser engraving with the chosen setup. The result is schematically shown in **Figure 74 A.** Periodic arrays of these structures were then placed into a 3D channel model (**Figure 74 B**) and the channel was laser engraved into working steel as described in materials and methods. An example image for the outcome is shown in **Figure 74 C.**

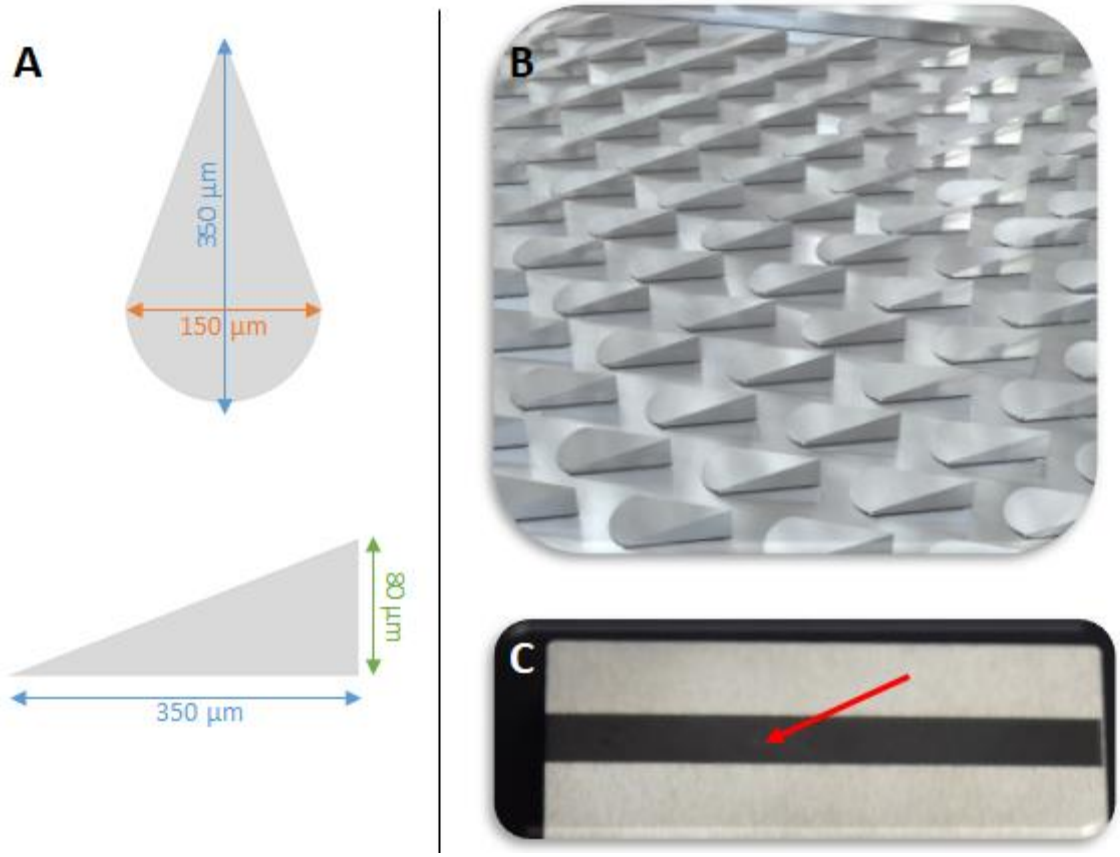

Figure 74: Model and outcome of the laser ablation. ***A*** *Dimensions for an individual microstructure. There dimensions were chosen according to the evaluated aspect ratios (2.3 : 1 for length : width; 4.3 : 1 for length : height).* ***B*** *Complete Model for the array within an artificial channel.* ***C*** *Laser engraved positive of the biomimetic abstracted scent gland channel. The arrow marks the tested channel.*

Additionally, a negative version (converted z-coordinates) of the same channel was laser engraved into a second steel plate, which was then used for the replication process of the polymer duplicates. In the following **Figure 75**, the three final, artificial replicas of the bug channel that were used for measurements are shown.

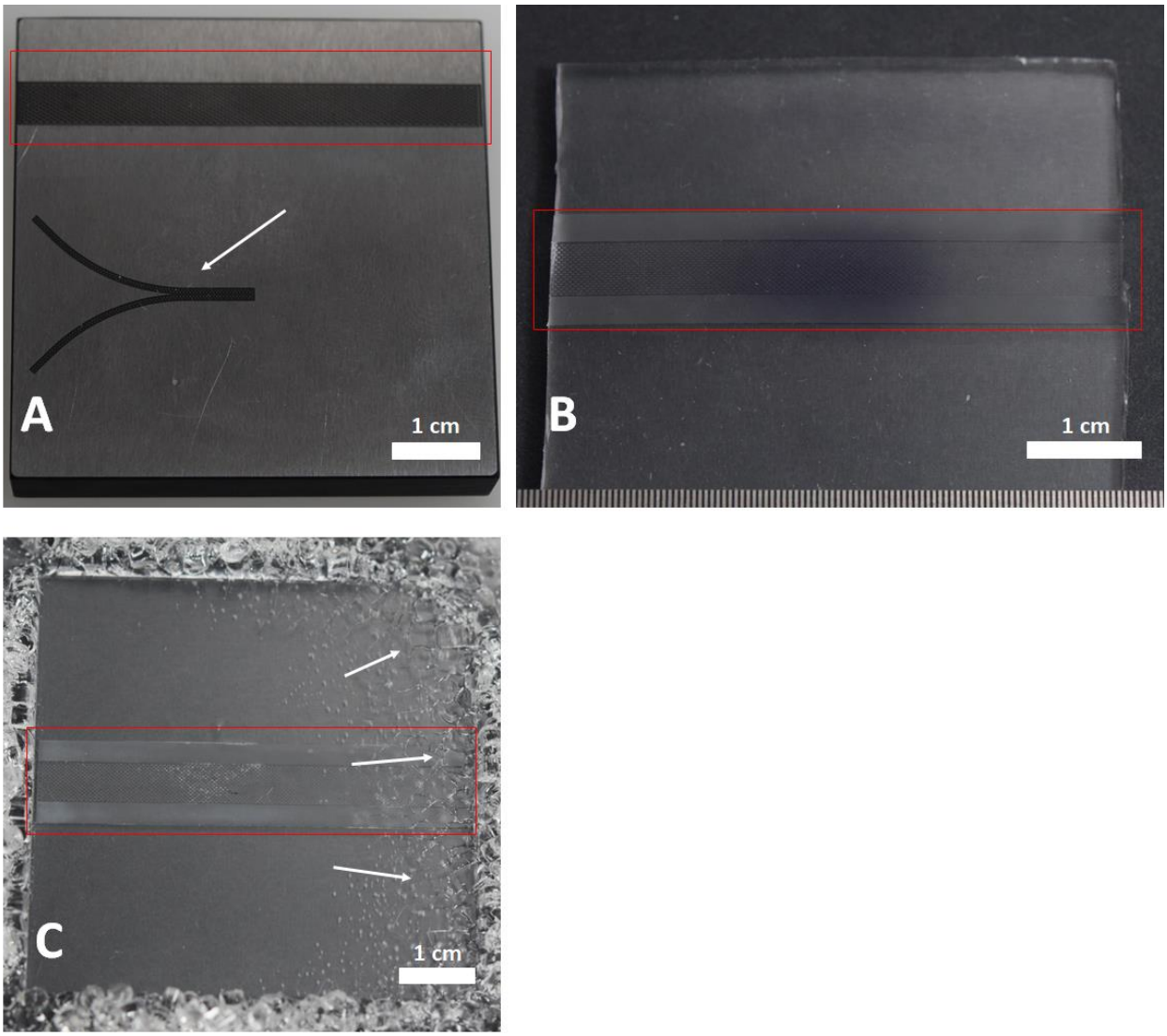

Figure 75: Overview of the three technical replica variants that were used for fluid experiments. A *Steel positive. A 5 cm long and 1 cm wide artificial channel is laser engraved in hardened working steel (red box). The white arrow marks unrelated laser structures that were used for laser calibration in different experiments.* ***B*** *PDMS silicone replica, produced with a steel negative mold, exhibiting the channel shown in A. The tested channel is again marked by a red box. The image also shows a dark stained area in the middle of the channel. Since the picture was taken after several measurements, the replica got slightly stained from the dye used to give the test fluid more contrast.* ***C*** *PMMA replica, produced with the same steel mold as used in B. The red box again marks the tested channel. White arrows indicate inhomogeneities in the PMMA that occurred due to the hot-embossing process. It has to be noted that these are only on the bottom side surface and did not affect the tested channel itself.*

To ensure quality and outcome of the replicas, 3D surface maps were generated via Alicona surface-captures.

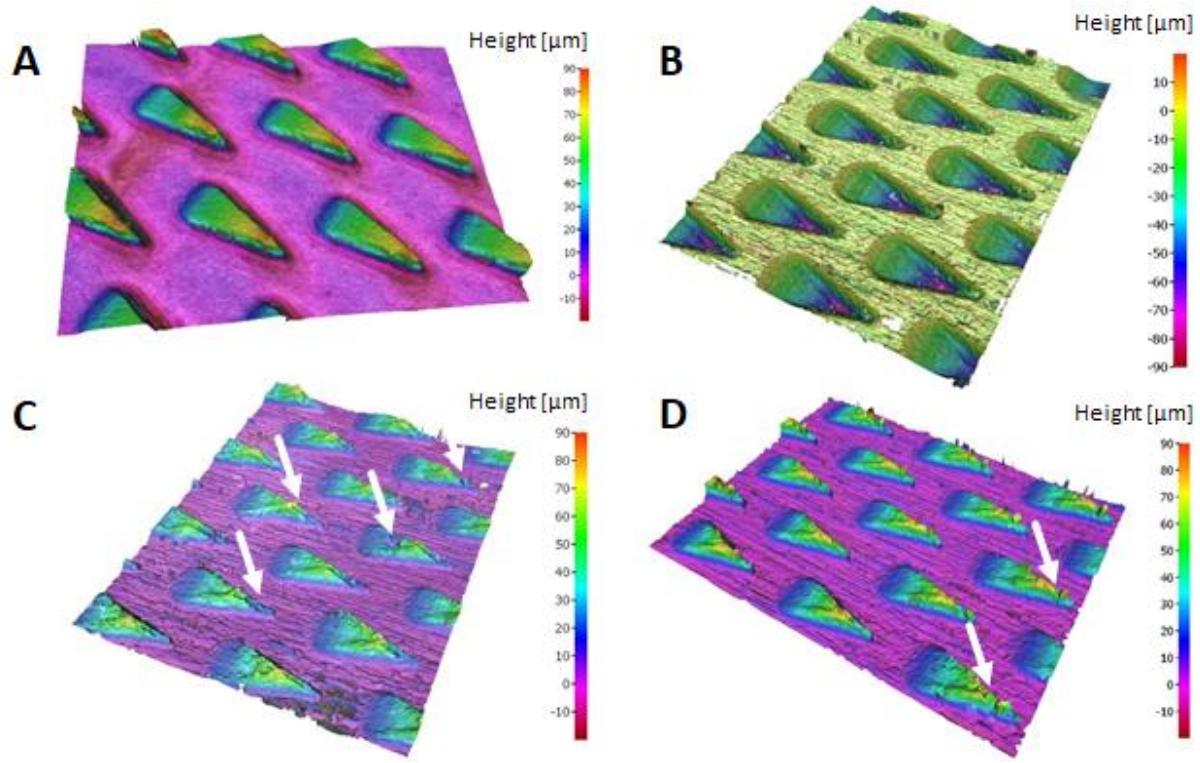

Figure 76: Quality survey of the artificial channel structures, measured with an Alicona Infinite Focus system at the Fraunhofer IPT. A *Steel positive as achieved by laser ablation.* ***B*** *Steel negative (used as mold for C and D) as achieved by laser ablation.* ***C*** *PMMA positive achieved by hot-embossing. The white arrows mark the most prominent defects: Missing tips (when compared to the original design) and overall rougher surface than desired.* ***D*** *PDMS replica as achieved by silicone casting. Again, white arrows mark casting defects. As one cone see the surface is slightly smoother than in C, but some of the tips still aren`t replicated perfectly.*

As one can see in **Figure 76**, the surfaces of all four crafted replicas (counting steel positive and negative individually), yielded quite different results when comparing their respective surface morphologies. The steel positive (**Figure 76 A**) shows very nice and smooth surfaces on both, the channel bottom, as well as the microstructures. Additionally, the overall morphology of the original design is kept and all details have been replicated to a certain degree. Comparing this with the steel negative (**Figure 76 B**), one immediately sees the differences: The steel surface (which after casting obviously would become the bottom surface of the channel) is way more rough than on the positive. It also stands out, that seemingly not the complete shape of the initial design was perfectly transferred. The deepest points of the negative (the points which will translate into the highest tip of individual structures after casting) are not in the tip of individual structure pockets, but rather slightly in front. The result of these small imperfections is visible in the polymer replicas shown in **Figure 76 C** and **D**. In both cases the tips of the microstructures are missing and the overall roughness of the channel bottom surface is way higher than in the steel positive. In addition, probably as a result from separating mold and replica, both, PDMS and PMMA, exhibit rough surfaces on the microstructures' top side. In total, the replicas were sufficient though. Overall, they showed the main

aspects the design was aiming for: Periodic spacing, the right shape and ramped height transition. To figure out whether the most important feature, the aspect ratio, was replicated correctly or not, ten individual structures per replica were measured.

Table 2: Dimensions of microstructures, measured from the Alicona images shown in Figure 76. *For each replica ten individual structures were measured (n=10), mean and standard deviation (STD) were calculated.*

	length	width	height
Steel positive			
Mean	342.2	150.6	77.2
STD	9.5	5.2	3.5
Steel negative			
Mean	382.6	189.1	81.4
STD	5.1	3.5	4.2
PMMA			
Mean	339.4	168.7	68.0
STD	8.1	3.3	3.7
PDMS			
Mean	352.0	151.0	83.4
STD	7.5	3.5	3.2

The values given by **Table 2** show that overall the dimensions of the artificial microstructures were replicated quite nicely, when compared to the values given in **Figure 74**. The steel negative shows slightly exceeding values for length and width, but this is rather an effect of the energy distribution of the laser, forming a Gaussian distribution pattern, which results in rounded edges, rather than sharp ones. Hence, it was difficult to determine the exactly widest points on the falling slopes, since the PDMS copy (which shows a positive of the steel negative) does not show different values when compared to the original design. The slight shrinkage in length, while at the same time exceeding values for width, measured for the structures in PMMA are most likely explainable by the hot-embossing process and the fact that the steel negative didn`t expand and relax in equal amounts during heating and cooling. Overall though, the plates exhibit an aspect ratio of 2.15 (± 0.14) : 1 (length : width) and 4.56 (± 0.29) : 1 (length : height), which is sufficiently close to the design. For this reason, the three replicas shown in **Figure 75** were accepted for fluid measurements.

To verify that chosen test liquids showed contact angles in the desired range on the respective test material (after confirmation by pretests that liquids in general are suitable), static contact angle measurements were done immediately before testing the channel structures.

Table 3: Static contact angles for the different fluids on their corresponding test material. *Static contact angle measurements were performed and theta/half method was used to calculate the contact angle. Droplet volume was 3 µl.*

Material/Liquid	n	Contact angle (STD)
PDMS/WD40	6	23° (± 2)
Steel/Sonax P809	6	24° (± 1)
PMMA/ DAWN 1%	6	31° (± 2)

The values shown in **Table 3** confirm indeed that the three chosen fluids (WD 40, Sonax P809 and DAWN soapy water) show contact angles in a suitable range between 23 and 31°.

Liquid spread tests were then performed and analyzed as described in materials and methods. Only successful measurements were chosen to be evaluated for final analysis, whereas the decision if a test run was successful or not was mainly determined at the point of droplet application. For an ideal, successful trial, the droplet needed to be placed as centered into the middle position of the artificial channel as possible, mainly to suppress so called edge-effects: At the edge of all fabricated artificial channels, a geometry was evident, namely a sharp edge, transitioning into a 90° angle of the channel wall. Due to the laser process here a micro-capillary was formed, surrounding the complete array of microstructures. As a result, this micro-capillary would transport fluid all around the test structure as soon as it got contact with the fluid. Experiments that showed this effect (as exemplarily shown in **Figure 77**), were discarded.

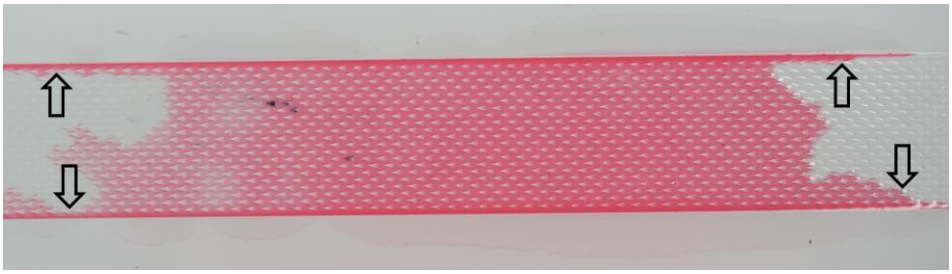

Figure 77: Example case of unwanted fluid movement caused by edge-effects. *Shown is an unsuccessful trial of soapy water on the PMMA prototype. Indicated by the black arrows, one can see the fluid getting dragged through the micro-capillaries at the edges of the channel. As a result fluid gets quickly transported everywhere in the channel (filling the array of microstructures consequently).*

In contrast to above shown unsuccessful trial, successful measurements (i.e. droplet was applied in a way that circumvented edge-effects) showed a typical, desired behavior as already shown in **Figure 72**. For a better comparability to **Figure 77**, the image sequence shown in **Figure 72 C** is given individually and

magnified in the following **Figure 78**. As one can see, results a suitable droplet placement in full functionality of the artificial bug channel prototype. A typical experiment will spread fluid predominantly in the forward direction – which means in the same direction as the microstructure tips are pointing – while halting it at some point in the backwards direction. In this direction, we usually find a stopping front forming a v-shaped formation that was typical on all tested prototype-material-combinations.

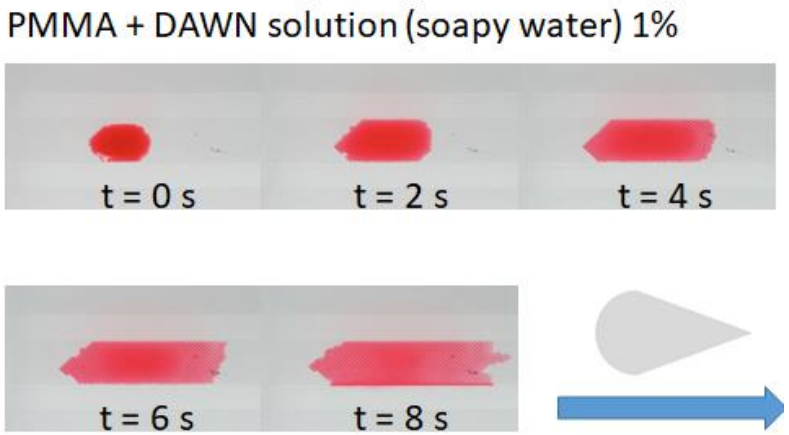

Figure 78: Example for a successful trial, in this case soapy water on PMMA. *In the backward direction (here left hand side) the fluid is halted, forming a typical v-shaped front, while being transported in the forward direction (here right hand side). The corresponding direction of bug inspired microstructure is given in the right hand bottom corner. The blue arrow marks the direction of fluid movement.*

A

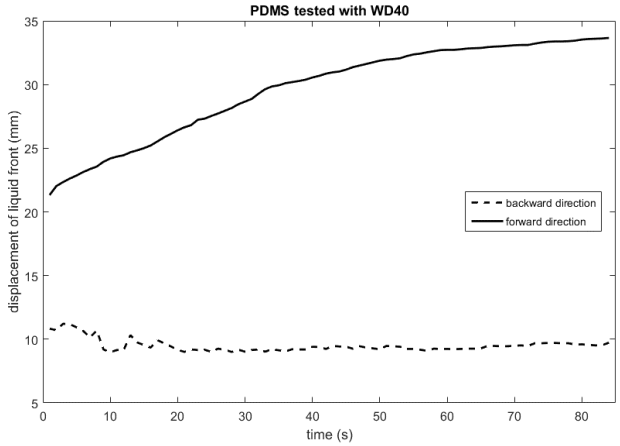

B

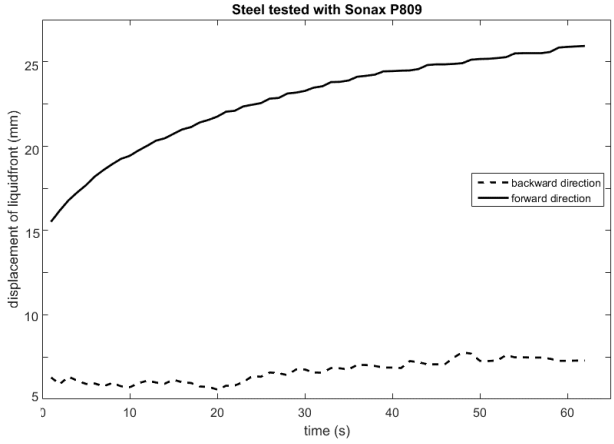

C

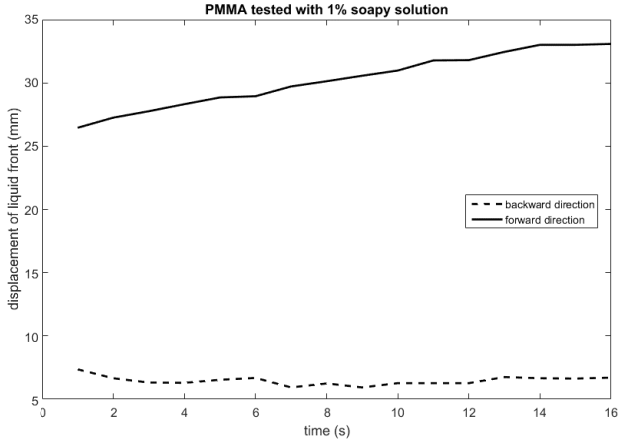

Figure 79: Comparison of typical results of fluid movement in forward and backward direction. *Shown is the displacement of the liquid front (with regard to the initial droplet center = center of wetted area) versus the time. Solid lines indicate the fluid front in forward direction, dashed lines indicate backwards.* ***A*** *Example result for the liquid transport of WD-40 on micro-structured PDMS.* ***B*** *Example result for the liquid transport of Sonax cutting oil on micro-structured steel.* ***C*** *Example result for the liquid transport of soapy water solution (1%) on micro-structured PMMA.*

Figure 79 shows example plots of measurements that were accepted for analysis with the Matlab algorithms. Shown is the displacement of the liquid front versus the time, for forward and backward direction respectively. The fluids in these cases behaved like anticipated (similar to the sequences shown in **Figure 72**), meaning that a droplet was placed carefully enough into the center of the channels' structured part, no edge-effect occurred, and a pronounced unidirectional fluid movement was observable (subjective perception). It becomes clear from the plots, that this perception was not subjective only: Whereas the forward direction in all cases showed a pronounced slope (in most cases stronger in the beginning of the experiment and less pronounced towards the end), the curves representing the backward direction show little to now displacement of the fluid.

Besides the obvious similarities of the fluid spread between the three shown examples, individual differences are evident, the biggest one being the timescale: Whereas the oil-based fluids (WD-40 and Sonax P809) show fluid movement occurring in the range of minutes, the soapy water (DAWN-solution) is transported within seconds.

Something that also becomes apparent from shown examples is the differences that occur in the stopping direction. **Figure 79 A** (WD-40 tested on steel) for example exhibits stronger fluctuations for the liquid spread in the backwards direction in the beginning of the experiment. Fluctuations in this case mean actual movement of the liquid front away from and towards the center of the initially applied droplet. The longer the experiment goes on, the more steady the graph becomes though, meaning that fluid movement came to a complete halt. Different behavior is the case in **Figure 79 B**. Here one sees a relatively steady initial phase of the experiment (again, meaning no fluid displacement), when concerning the backwards direction. After ~ 20 s though, fluid displacement in the backwards starts to incline, meaning that the fluid was not stopped at point anymore. In contrast to that, **Figure 79 C** shows relatively steady fluid flow across the whole experiment.

Despite the shown differences, it has to be noted that the shown example cases are exactly that: exemplarily. Over several different trials, all of the replica channels showed slightly different behavior for the backwards direction, sometimes resulting in steady stopping, sometimes in fluctuations in the beginning, sometimes towards the end. Overall, the behavior nevertheless was constantly the desired one: Fluid displacement in the forwards direction and halting in the backward. To compare the displacement velocities in both directions, as well as the different tested systems against each other, pooled results are shown in the following **Figure 80**.

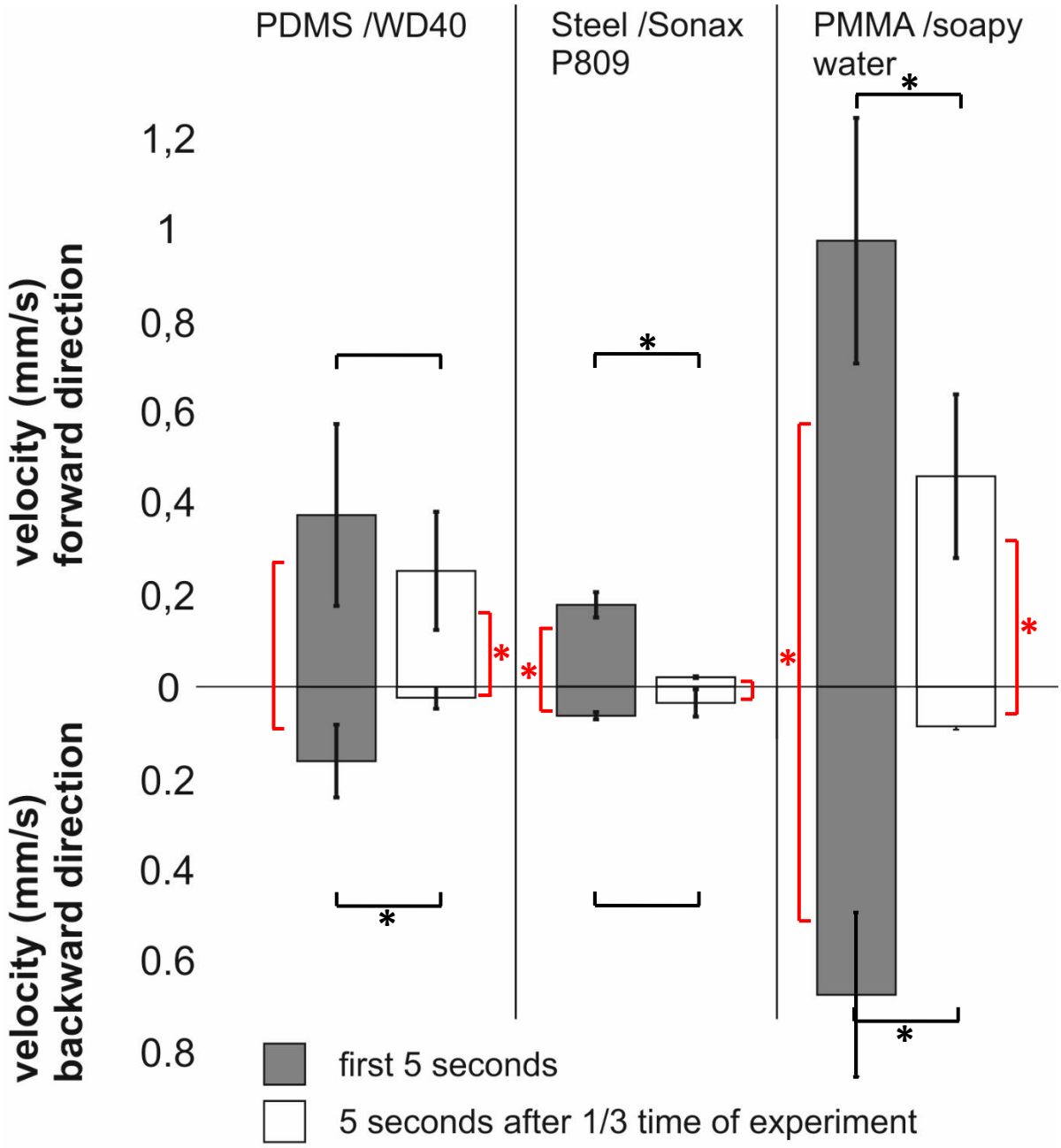

***Figure 80: Pooled results for the liquid movement measurements on all three tested prototypes (PDMS, steel, PMMA**). Depicted is the averaged velocity of the liquid front in forward (desired) and backward (undesired) direction. Dark grey bars show the averaged velocity for the first 5 seconds of the experiment, while white bars show the averaged velocity for 5 s after one third of the overall experiment has passed. Students T-test was used to test for significant differences (p = 0.05), stars mark significant differences, no stars means p > 0.05. Number of evaluated experiments for all shown test regimes was three (n = 3).*

Above shown **Figure 80** gives a comparative overview of the fluid behavior that was observable over the course of three evaluable experiments (meaning experiments without edge-effects). The top half of the figure gives the resulting mean liquid velocities for the forward, the lower half the mean velocities for the

backwards direction with regards to the center of the initially applied droplet. Since the experiments showed a trend for different fluid behavior at the beginning phases of the experiments (as shown in **Figure 77**), it was decided to also compare the mean velocities between the first five seconds of a measurement and the mean velocities (of again five seconds) after one third of the experiment had passed. The individual pairs were tested against each other for significant differences via t-test.

Figure 80 validates the previously assumed trends:

1.) Liquid velocities in forward direction are always higher than in the backwards. This behavior is not significant for the test of the PDMS prototype with WD-40 though.

2.) In general the liquid spread is faster in the beginning of an experiment when compared to the velocities after 1/3 of the experiment has passed. This behavior is significant for forward and backward direction for the PMMA prototype tested with soapy water, forward direction on the steel prototype, and backward direction on the PDMS prototype. Interestingly (even though not significant), the steel prototype tested with Sonax P809, showed higher velocities for the backwards direction after 1/3 of the experiment time, than for the forward. This confirms what has been exemplarily shown in **Figure 79 B** and indicates that this trend was conserved throughout the different measurements of this prototype.

Additionally, **Figure 80** shows two more trends that have not been addressed before:

- Water based test liquids seem to be transported faster through the tested channel geometry than oil based fluids, despite exhibiting comparable contact angles on the respective channel material. This is an indicator for the influence of viscous forces playing a role for the reachable velocities.

- Water and oil based fluids differ in the ability to halt the fluid in the backwards direction, i.e. they differ in their ability for unidirectional transport. Comparing the fluid velocities it becomes apparent that with velocities of ~0.7 mm s^{-1} (soapy water) versus 0.1 - 0.17 mm s^{-1} (WD-40, Sonax P809) in the backward direction, the water based solution is transported faster in the backwards direction than both oils in the forward (despite still having a significantly faster transport in the forward direction). This holds especially true for the beginning phase of the experiments.

5.3 Discussion

The found results show that the external scent efferent system of different European true bug species indeed serves as a successful inspiration for unidirectional fluid transport on technical surfaces. Considerable fluid spreading velocities were achieved on all prototypes with different fluids in one direction, whilst halting the fluid in the opposite. A deciding factor for whether a prototype will work with a given fluid or not, was found in the contact angle. Pretests showed that the geometry will only show pronounced, unidirectional fluid movement, if the contact angle is in between 20 to 35°, a requirement that was fulfilled with all tested material-liquid combinations in this chapter. As shown in **Figure 72** and **Figure 78**, fluid will always flow preferably in the direction of the pointed microstructure tips and will form a stopped, v-like shaped front in direction of the microstructures' bases.

Furthermore, this chapter proves that the used method for recording and analyzing the fluid behavior worked. In a reproducible fashion the algorithms of the used Matlab-script traced the fluid movement captured in the videos. This enabled an easy way to track the moving liquid front in both directions (forward and backward with regard to the center of the initial droplet center) and compare measurements in terms of fluid front displacement versus time – a perfect way to follow the dynamics of the spread (as shown in **Figure 79**). These findings furthermore justified to not only compare the total mean velocities of liquid spread, but rather divide the experiments into two stages: 1) The first 5 seconds (usually showing the highest spreading velocities) and 2) the first 5 seconds after 1/3 of the complete experiment.

The comprehensive compilation of results given in **Figure 80**, showing mostly what was expected: Liquid is faster transported in the forward direction when compared to the backward and velocities are higher in the beginning of the experiment. Furthermore, a clear connection between the reachable top-velocities of transport and the used fluid can be derived. Oily liquids (like WD-40 and Sonax P809) are transported slower than water based liquids (DAWN solution). On the other hand, it seems, as if the halting ability of the structure is better for oily liquids. The first trend most likely is explainable with the difference in viscosity, since the contact angle range as well as the geometry and dimensions of the microstructures did not differ between the three

tested channel prototypes. The fact that some of the shown plots do not exhibit desired, significant differences, needs to be blamed to the small number of measurements used for the graph. N = 3 was indeed not the desired number to work with, but from the 9 -13 measurements that were done for each individual liquid-surface combination (plus additional ones for different fluids, data not shown), the majority had to be discarded due to edge-effects. This is a point that needs to be addressed in future work and future replicas: The width of the array should have always been chosen in a way that a undisturbed droplet spread can be assured, without the fear of having edge interference.

To imagine the trend of viscosity being responsible for the resulting peak velocities in the shown channels, the simplest approach is to imagine the channel as a closed capillary with the radius *r* and the length *l*, and assume that the pressure difference *Δp* between start and end of the capillary (or bug channel) in all measured cases was identically. In this case, the law of Hagen-Poiseuille (Sutera & Skalak, 1993) becomes applicable:

$$V = \frac{\pi \cdot r^4 \cdot \Delta p}{8 \cdot \eta \cdot l} \tag{21}$$

With everything else constant but the viscosity *η,* the volume flow *V* is solely dependent from the viscosity. Obviously, the higher the viscosity, the smaller becomes *V*. This would explain, why a water based soapy water solution (DAWN solution), kinematic viscosity below 0.89 $mm^2\ s^{-1}$ (at 25° C, source: www.viscopedia.com, 23.07.2017), would reach about three times higher velocities than for example WD-40 with a kinematic viscosity of 2.79-2.96 $mm^2\ s^{-1}$ (source: WD-40 datasheet). Of course, this doesn't explain the observed directionality and obviously, in reality the liquid spread in a micro-structured channel is dependent from more variables.

How do the fabricated channels differ from previous work and why do they exhibit unidirectional, passive flow?

As mentioned before in Chapter 4, previously to this work attempts were made to copy the scent efferent channel of *Dysodius*. Kupsch (2015), as well as Plamadeala et al. (2017) succeeded in

creating a copy of the channel in different ways: Kupsch's work succeeded in creating a laser engraved metal replica comparable to the one presented in this work (also magnified dimensions due to the laser process limitations), while in Plamadeala et al., a real-scale replica was achieved by means of two-photon-polymerization (2PPL). Both showed passive, unidirectional fluid transport with oil but in contrast to the present work, three main differences are notable:

1.) Kupsch and Plamadeala both created covered (or closed) capillary systems as a result of copying the scent efferent system in *Dysodius* being covered by the wings, in contrast to the open system introduced here (and abstracted from the uncovered MPGs of Pentatomorpha).

2.) As a result of 1.), the fluid transport takes place in the opposite direction when compared to the present work: Fluid is transported against the direction of tips of the microstructure.

3.) Both authors only succeeded in making the transport happen with one fluid on one material.

The most important points here being 1.) and 2.), since it is imaginable that both authors would also have succeeded in the shown transport of different fluids if the contact angle between fluid and respective channel regime was fit. Therefore, it needs to be addressed, what makes the difference in fluid transport when using a closed capillary system and why the observed transportation direction is opposed.

In Plamadeala et al. we found that the explanation for fluid movement in one direction only, can be explained as follows (from Plamadeala et al., 2017):

In the case of a free surface (uncovered), the liquid droplet's height is larger than that of the microstructures. Thus, the structure acts as surface roughness, leading to enhanced wetting, i.e. to a uniform spreading of the liquid in all directions. This can be explained by the Wenzel-model for wetting of structured surfaces (see also Chapter 2.3). In the case of capillary transport (covered), the droplet-like microstructures can be interpreted as distributed defects on a smooth surface. Joanny & de Gennes (1984) derived a theory for the pinning of a liquid front, i.e. the hysteresis of the advancing and receding contact angle on a surface containing an ensemble of identical defects distributed over it. They obtained a relationship between the advancing and receding contact angles, θ_A and θ_R, respectively, to be

$$cos\theta_R - cos\theta_A = nW = \frac{nf_m^2}{2\pi\gamma^2} ln\frac{L}{r} \quad (22)$$

where n is the number of defects per unit area; *W* is the total energy dissipated by one defect; f_m is the maximum force a defect can exert on the triple line before a jump occurs (maximal pinning force), which is dependent on the materials involved; *γ* is the surface tension; *L* is the average distance between adjacent defects; and *r* is the typical dimension (radius) of a defect. In our case, *n*, f_m, *γ* as well as *L* are identical in both directions. However, the defect radii are different.

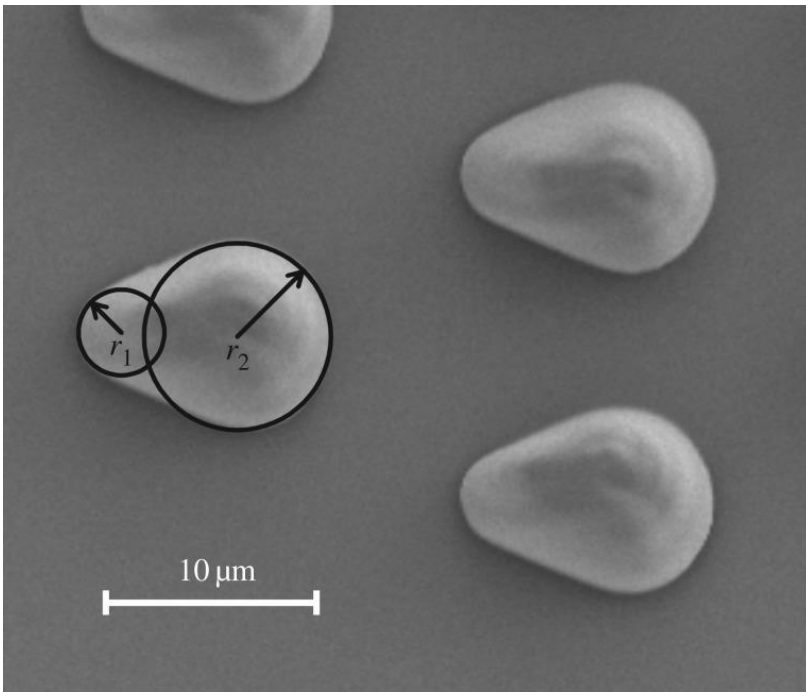

Figure 81: Different radii of the drop-like microstructures as defects on the glass slide surface. *The smaller radius r_1 is about 2 µm and the larger radius r_2 is about 4.5 µm. Image and legend from Plamadeala et al. (2017).*

As can be seen from **Figure 81**, the smaller radius r_1 of our microstructures is about 2 µm, while the larger radius r_2 is about 4.5 µm. The average distance *L* between the defects is approximately 13 µm. The fraction in the above formula is constant for the given material combination, but the logarithm of *L/r* is different for the two transport directions by a factor of approximately 2. Thus, the liquid flows and increases the contact angle at the fronts until the advancing contact angle is reached and then the liquid jumps. While at the larger radius r_2 the advancing contact angle is

overcome and the liquid front jumps, the small radius r_1 pins the front better and due to the jump in the direction of r_2, increasing the apparent wetted area, the contact angles are decreased again. This can be observed repetitively until the one side of the structure is completely filled with liquid. Then the flowing liquid can increase the contact angle at the sides of r_1 and also overcome the pinning. When the oil front moves transversally to the microstructures (i.e. down in the figures), it encounters defects with even much larger radii (almost infinite) than both r_1 and r_2. According to the formula, this should result in less pinning making the liquid front move faster, as is observed experimentally. Hence, as a conclusion one can find for closed, capillary transport derived from *Dysodius*: Due to the pinning effect of different sized radii within the defects (microstructures), fluid is transported always against the direction of the microstructures' tips.

However, in case of the abstracted structures of Pentatomorpha, and the resulting artificial surfaces exhibiting the observed transport, the explanation based on Joanny & de Gennes as seen above is not applicable. This is due to the one big difference: Dealing with an open capillary system, instead of a covered closed capillary system as derived from *Dysodius*. Hence, the abstracted surface structures shown in Chapter 5.2 unfortunately cannot be seen as surface defects and pinning as shown above is seemingly not the explanation. This is good on the one hand, bad on the other: It would have been nice to reason both fluid transports (closed capillary of *Dysodius*, open capillary of Pentatomorpha) by the same means, on the other hand this would have led to problems explaining why the direction of fluid transport is opposite for the two systems. As the fabricated open capillary transport systems show clearly transport in direction of the pointed tips (despite showing comparable dimensions to the ones shown in Kupsch (2015)), the explanation has to be found somewhere else.

As a matter of fact, all three tested prototypes (steel, PMMA, PDMS) show exactly the same transportation dynamic for their respective test fluid (with the exception of different transportation velocities due to viscosity differences, as shown above). In all tests performed, the fluid progression was always observed as depicted in following **Figure 82**.

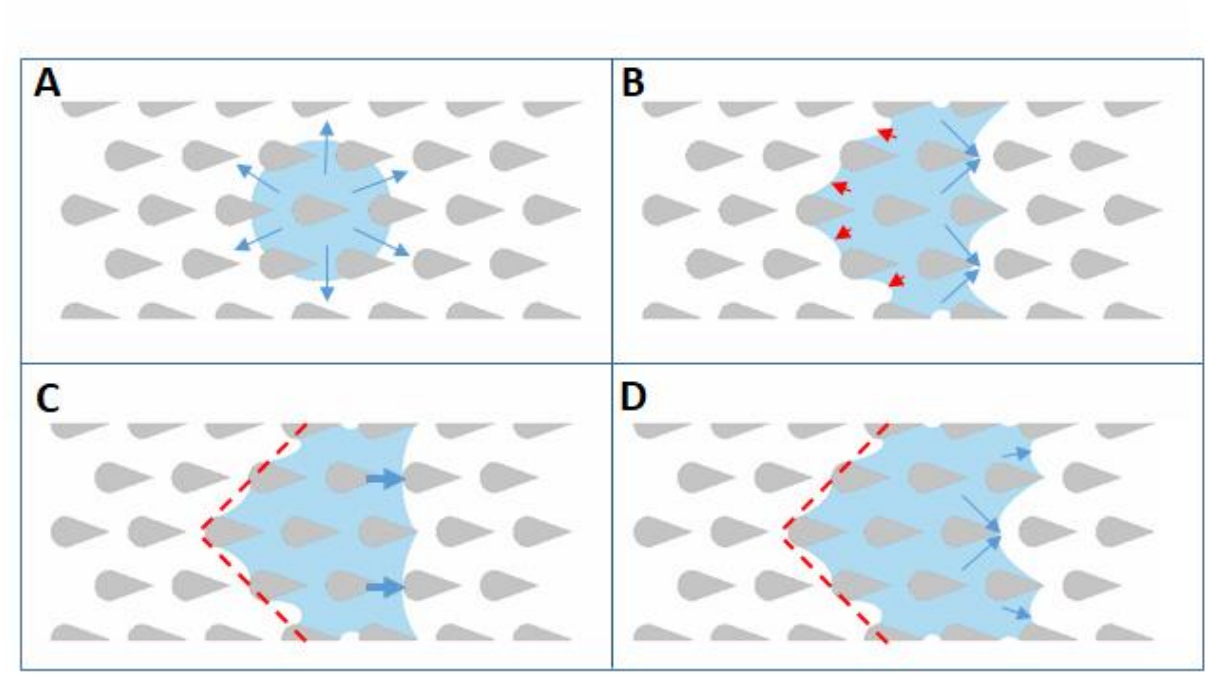

Figure 82: Step-by-step explanation of the observed liquid spread in micro-structured channels, inspired by the external scent efferent system of European Pentatomorpha. A *Situation after a liquid droplet has been applied into the structure. Due to capillary forces, the liquid spreads in all directions and penetrates the structure.* ***B*** *Between the structures, the liquid front exhibits menisci according to the given contact angle, thus forming the v-shaped stopping front in direction of the structures' round sides (red arrows). Due to the shift in lines, in the forward direction (direction of pointed structure tips), the menisci of three vertically neighboring structures will converge always at the tip of the middle one (blue arrows).* ***C*** *The newly formed meniscus is able to span across the distance between one vertical iteration and therefore gets contact to the next neighboring microstructure column.* ***D*** *Always alternating between three structure rows, steps B and C are repeated in forward direction until the liquid reservoir (initial drop) is distributed completely, or the viscous forces exceed the capillary driving pressure.*

Figure 82 briefly summarizes what can be observed. Whenever a drop is introduced into the structure, capillary forces spread it in between the microstructures. In between microstructures a meniscus is formed, shape and form determined by the contact angle (in observed cases therefore between 20 and 30°, depending on material liquid combination). For the backwards direction (red markings in **Figure 82**), this means that liquid front will form a v-shaped stopping front, since the meniscus between microstructures of horizontally neighboring rows is unable to overcome the distance towards the respective next microstructure in reach. This is in detail shown in following **Figure 83**.

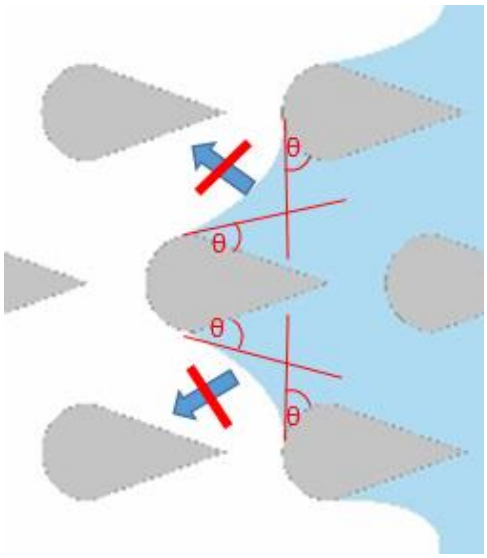

Figure 83: Detail of the fluid menisci in backwards (=stopping) direction. *Determined by the contact angle θ between fluid and channel-/microstructure-material, a meniscus between the base of neighboring microstructures is formed. The curvature of this meniscus is not fitting to overcome the gap towards the nearest neighboring microstructures further in backwards direction (crossed blue arrows). Hence, the fluid movement is stopped.*

Basically, the same principle applies for the fluid flow in forward direction too: Determined by the contact angle, menisci between the microstructures are formed, but in this case between the tips of neighboring structures, as shown in detail in following **Figure 84**.

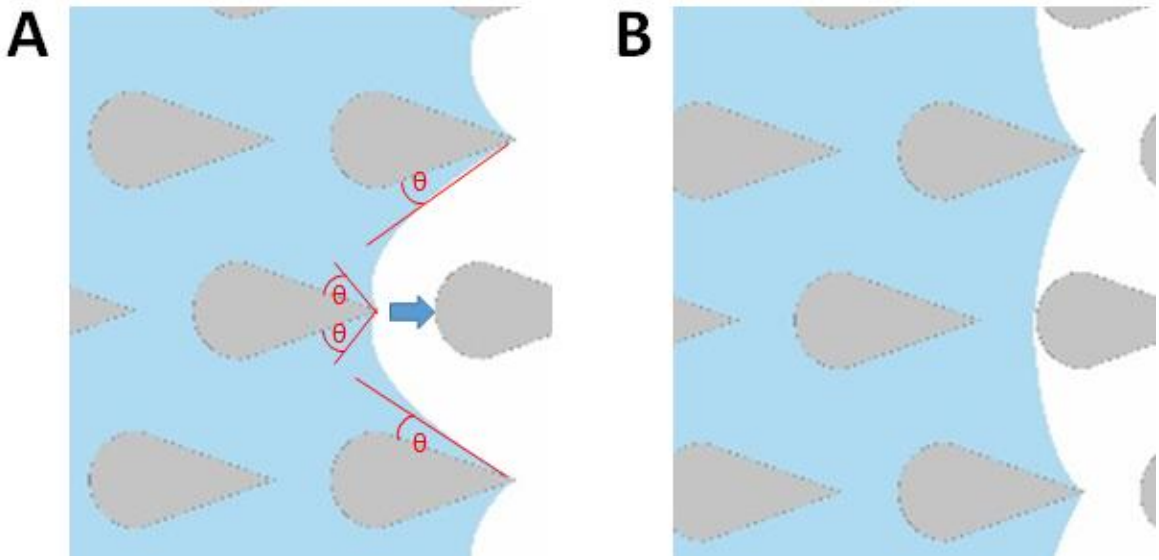

Figure 84: Detail of the fluid menisci in forward direction. A *Determined by the contact angle θ between fluid and channel-/microstructure-material, a meniscus between the tips of neighboring microstructures is formed. If the menisci of three neighboring microstructures converge at the tip of the central one, a new meniscus is formed that is able to overcome the gap towards the next in line (blue arrow), resulting in the situation shown in **B**.*

Since the situation shown in **Figure 84** occurs periodically again and again (**Figure 82**), fluid is transported in the forward direction. Unfortunately, this contact angle and menisci based theory does not cover for the laterally occurring distribution of fluid (until a channel wall is reached), and also not for the case when not three microstructures can offer a converging meniscus in the center (e.g. only two). How does the liquid front reach the next iteration of microstructures in that case, and why is a v-shaped stopping front not also formed in the forward direction in that case?

Unfortunately, up to this point, no plausible answer has been found to cover for these last raised questions. It is well possible, that the slope of the produced structures (which so far has not been accounted for, with regard to the explanation of the transport process) plays a bigger role than anticipated. It is therefore suggested to reproduce the prototype channels with structures of same shape and dimension, but without the slope, in order to verify the influence of this variable. First steps towards this have already started by fabricating 3D-printed ABS prototypes as well as milled PMMA prototypes (magnified structures sizes) that exhibit no slope. The prototypes show general functionality but have not been sufficiently analyzed up to this point. Additionally an attempt should be made to capture videos that follow the progressing liquid front at higher magnification. Videos used for the results shown in this work, were taken at a relatively low framerate and with a magnification (and distance) that allowed for total observation of the whole channel. Detailed capturing of the exact process of what happens with the fluid in between individual structures most definitely will give more hints towards an exact physical explanation.

6. A novel approach for the replication of biological surfaces

The previous Chapter 3.3 showed that there is a substantiate need for biological surfaces (and therefore biological samples) to be tested under varying ambient conditions, for example: Lizard skin samples to verify the theory of fog harvesting due to condensation, or flat bug samples to better understand the influence of pre-wetting effects (also due to condensation). Overall, such testing requires three basic conditions that needs to be met:

1) An adjustable ambient temperature,

2) adjustable ambient humidity, and

3) adjustable sample temperature.

Condition 1 and 2 can be met by conventional environmental climate chambers (or a custom build one like introduced in Chapter 3.2.1), where chamber temperature and humidity can be set as needed. The third condition though, can only be met when the actual biological sample can be adjusted temperature wise itself. This requires the sample to have a rather good thermal conductivity to be quickly adjusted from an external driven heat-/cold-source. Most biological samples show rather low thermal conductivity values though (e.g. human skin with a conductivity value of around 1-3 W m^{-1} K^{-1} (Cohen, 1977), compared to copper with around 400 W m^{-1} K^{-1} (Quick, Child, & Lanphear, 1895). Additionally, there is often also the problem of disposability of given samples (and a possibility that such samples will get destroyed in such measurements). Therefore, exact artificial replicas of biological surfaces with a high thermal conductivity are desirable. This chapter deals with the question if and how such replicas can be realized.

From the big number of possible ways to replicate a certain surface to get a replica of a surface, one way to achieve this, is to obtain a negative cast of the actual surface that is as detailed as possible and then fill it with a material of choice. A common way to obtain such a cast, is the use of soft polymers such as dental silicone, which can reproduce surface features in the low micrometer range. Such a negative mold then can be filled with the desired material (e.g. epoxy resins, plastics or even metals/metal-alloys) which after the extraction from the mold represent the actual replica. Such a replication process is rather simple and fast to achieve but also leads to replicas with a high replication accuracy. Unfortunately, most of the mentioned materials either show also a very low temperature conductivity (most resins and polymers), or are unsuitable for reproducing very small surface features (e.g. most metal alloys when simply liquefied

by means of heat). Due to this, the idea was formed to create biological surface replicas via electrochemical deposition of metals onto the surfaces of the negative casts. Metals like copper, silver, chrome and their derived alloys (e.g. brass and bronze) can be easily deposited by the means of electroplating and also show very high thermal conductivity values as exemplarily mentioned for copper previously. Another benefit of this technique is that in the electroplating process, the metals are deposited atom by atom and therefore even can reproduce the finest surface features possible.

6.1 Materials and Methods

Imprinting and Casting

All casts of technical and biological samples, used for this chapter were created by imprinting a surface into a dental silicone (President JET Plus – Light body, Coltene Whaledent, Switzerland). The samples were covered with an approximately five millimeter thick coat of silicon, which then again was covered with the bottom side of a plastic petri-dish. The petri-dish served two functions: On the one hand the dish served as a helper for distributing the pressure when pressing the silicon onto the sample, on the other hand it makes sure that the bottom side of the cast will be smooth and even. All casts were given time to thoroughly polymerize (approximately 15 minutes of curing time) before the petri-dish was removed. After that, sample and silicone were separated from each other by carefully pulling the sample out of the cast.

For this work, and especially for test reasons, diffraction grid foils (varying grid sizes from 1-2 µm distance between rows, Product DG-500 and DG-1000 diffraction foils, Amazon) were used to make silicon molds for quality survey of the reproducibility of copper replicas. After successful pretests (as shown later in the results section of this chapter), various biological surfaces were imprinted into dental silicone, in order to reproduce the surface in copper replicas. Towards this end, dorsal skin of *Phrynosoma cornotum*, as well as the dorsal side of one specimen of *Dysodius lunatus* were imprinted according to above mentioned protocol.

Electroplating (Galvanizing)

One of the easiest and most common ways to cover a certain surface with a stable metal layer (with a freely adjustable thickness) is the so-called electroplating, or galvanizing. Named after the Italian physician

Luigi Galvani, who first used and described this method, electroplating describes a procedure where a layer of metal particles is applied onto a surface via electrochemical deposition. The material that needs to be plated is dipped into an electrolyte solution, which contains metal ions. In addition, a pure and solid version of this metal is also dipped into the electrolyte, acting as a stock for metal ions. By connecting the stock-metal to the positive pole of an electric circuit (anode), and the soon to be coated material to the minus pole (cathode) a closed circuit is formed across the electrolyte. If a current is now applied, the dissolved metal ions within the electrolyte (positive charge) will be attracted to the negative charged cathode where they will pick up electrons. The de-oxidized metal ions will stick in their now atomic form onto the material of the cathode and form a dense coat. The disequilibrium of ions within the electrolyte is simultaneously filled with metal ions dissolved from the anode where they are oxidized. In this way, a smooth and even layer of metal coat can be formed on the cathode. The thickness of this layer is defined by a) the duration of the electric current, and b) by the amperage. **Figure 85** shows the principle for a simple electroplating setup (here for the case of depositing copper onto an arbitrary metal).

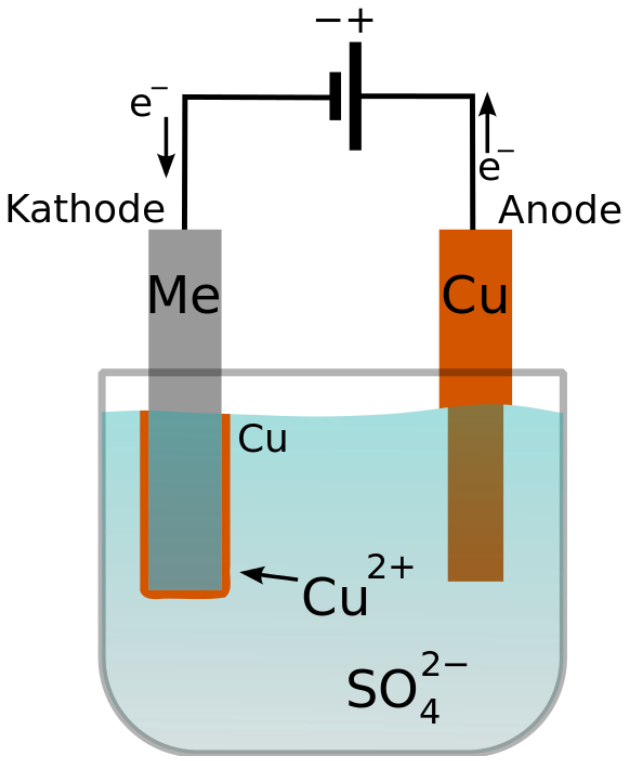

Figure 85: Schematic overview of electroplating process. *A copper anode is submerged into a solution of copper sulfate. The salt in solution naturally dissociates into copper anions (Cu^{2+}) and sulfate cations (SO_4^{2-}). The copper anions get attracted by the negative Metal (Me) cathode and deposit on its wall in form of elemental copper (after picking electrons from the cathode). On anode side, missing copper anions are replenished by dissolving from the anode material. (Image source: https://de.wikipedia.org/wiki/Galvanotechnik, 30.07.2017)*

The basic redox reaction that takes place can generally be described as following:

$$\text{Anode: Metal} \rightarrow \text{Metal}^{+} + e^{-}$$

$$\text{Cathode: Metal}^{+} + e^{-} \rightarrow \text{Metal}$$

Suitable metals or metal alloys than can be used in an electroplating process are for example: copper, chrome, cadmium, manganese, nickel, brass, silver, iron, gold and lead (Bachmann & Bachmann, 1989).

In summary, successful electroplating involves the following demands:

- The material to be coated has to act as the cathode.
- The chosen metal for the coating needs to be dissolved within an electrolyte solution and the same metal needs to act in its pure form as the anode and reduction has to take place before reduction of H^{+} (e.g. the reason why electroplating of titan is almost impossible).
- An electric current has to be applied across the whole circuit.

As one can see from the basic description of the electroplating process, the first of the four basic demands calls for the “to-be-coated material” to act as the cathode. This of course also means, that this material has to show at least a minimum of electric conductivity, which is in fact uncommon for most biological samples and several synthetics too. Hence, in order to achieve the needed conductivity samples have to be pre-treated. Different ways of treatment that were used to render a sample conductive are introduced in the following passages “Gold coating”, “Carbon coating” and “Metal coating via chemical deposition).

Samples rendered successfully conductive were placed in a custom made electroplating setup, depicted in following **Figure 86**.

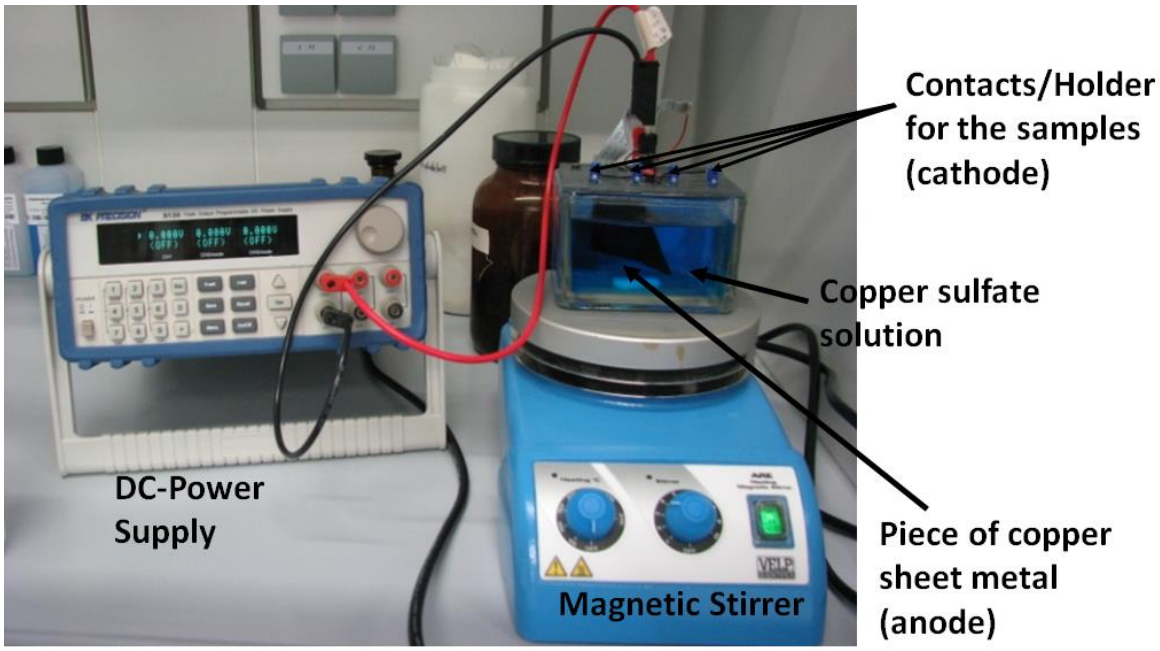

***Figure 86: Custom electroplating setup**. A glass vessel is filled with copper sulfate solution and covered with a top lid (air-tight). The lid contains plugs for the power supply and respectively connected holders for the anode (copper sheet metal) and the cathode (samples to be electroplated). A DC-power supply allows for adjusting voltage and amperage.*

The actual electroplating in this work was planned and executed individually for each sample, whereas some general rules needed to be fulfilled:

- Copper sulfate solution (phosphoric acid, shine enhancers, Conrad Elektronik, Germany) has to be replaced or filtered after every 8 hours of plating time due to the amount of too many suspended particles (mainly copper oxides) that will influence surface attributes of plated samples.
- Voltage and amperage need to be adjusted individually for each new plating experiment. As a rule, 3.0 – 3.2 V and 40 – 45 mA per square centimeter of plating area worked best for consistent results (determined by pretest series). For three-dimensional samples the total conductive area therefore needs to be calculated carefully and individually.
- Sample were coated at above values for 8hs in total but sacrificial copper anode had to be cleaned/replaced every 2hs due to the forming of heavy oxide layers. Usage of an air-tight lid and constant stirring reduced the formation of these layers though.
- Ideally the copper anode is facing the face of the samples that have to be coated for best results.

In the following, some general ways to achieve electro conductive surfaces that were tested within this work are explained. They are necessary to render samples “usable” for above mentioned setup and electroplating process.

Sputter Coating

Sputter coating describes a simple and commonly used way to coat a sample with a thin layer of material particles. Hence, in case of using a conductive material for sputter coating, the sample surface becomes also conductive. There are different ways of sputtering, as well as several metals and materials that can be used. Two major coating ways will be described in the following sections, both tested in this work.

Gold Coating (direct current sputter coating)

Sputter coating with different precious metals is a quite common technique of physical vapor deposition (PVD), often used for the preparation of samples for electron microscopy or the finishing for high-purity surfaces . Metals like copper, silver, gold, palladium or platinum possess high electric conductivity, as well as rather high atomic numbers – both of which are properties highly desirable in electron microscopy. Since commercially available in varying applications and residing in the mid-levels price wise, gold is one of the metals most frequently used. There are several different ways and techniques for the actual metal-sputter process, mainly distinguished by the reactive gas used, the level of vacuum maintained and/or the current value and direction. The following description will only describe the detailed process for so-called direct current sputter coating (DC-sputter coating) with argon as the reactive gas.

For this technique, a target (gold) is connected to the negative pole of a direct current power supply (therefor acting as the cathode), while the sample (or substrate) is connected to the positive pole (anode). Enclosed within a vacuum chamber the setup resembles a basic plate-capacitor. The evacuated chamber now can be flooded with a defined stream of inert gas (in this case argon) and a voltage of several hundred volts can be applied. Induced by the current the argon atoms are impact ionized and a plasma is formed. The different polar portions of this plasma (electrons and Ar^+ ions) are accelerated into different directions due to their charge and the direction of the applied current. A constant stream of electrons will penetrate the target (anode) while a constant stream of argon ions (Ar^+) will impact on the gold target (cathode). Here, due to momentum transfer, the argon ions will spurt out atoms from the targets surface, which then again will decent down onto the target (particle deposition). The layer thickness of the deposited material is determined by a) the current flowing across the plasma bridge (which is determined by the flow-rate of argon and therefore the absolute number of argon atoms within the vacuum chamber) and b) the absolute

time the voltage is maintained (freely adapted from Andersen, Bay, Robinson, Roosendaal, & Sigmund, 1981; Sigmund, 1969).

In this chapter, gold sputter coating was performed using a Hummer V coating device (HUMMER Technics Inc., USA) at 1 kV for a duration of 360 s. According to the machine`s manual, this results in a layer thickness of approximately 20 nm.

Carbon coating (arc evaporation coating)

Analog to the previously described gold coating, carbon coating via arc evaporation is also a technique from the group of PVDs. In contradiction to DC-sputter coating, arc evaporation strikes the target (in this case a solid piece of carbon) with a high current but low voltage electrical arc that evaporates a small fraction of the target. The process is highly exothermic (peak temperatures of >15.000°C in vicinity of the striking spot) and the vaporized carbon material is jetted with tremendously high velocities through the coating chamber. Samples are typically placed in close vicinity to the target and both, sample and target are connected to a power supply. The target (carbon) is connected as the cathode, the sample that needs to be coated is connected as the anode and by regulating the voltage across the circuit it can be determined how strong the carbon vapor is attracted towards the sample anode. Hence, the applied voltage, together with the coating time determines coat thickness. Naturally, the whole process takes place in an evacuated chamber in order to minimize collisions, ionization and unwanted chemical reaction with air molecules in general (freely adapted from Boxman, Sanders, & Martin, 1995).

For this work, carbon coating was performed using an Agar SEM Carbon Coater (Agar Scientific, Germany). The samples were placed in approximately 3 cm distance to the target and coating took place in pulsed mode for a total of 5 s. Each pulse was 1 s at 50 A, resulting in a layer deposition rate of 1.5 – 2 nm per second. Continuous mode was tested for 5 s at same current but caused the coater to overheat each time.

Metal coating via chemical precipitation

A completely different approach to cover a surface with a thin layer of atomic metals, is the deposition of metals through chemical precipitation. In this process, a pure metal is precipitated through reaction from a solution containing chemical compounds of this given metal. In many cases the precipitation itself is not the original goal of such a chemical reaction, but rather the byproduct of a reaction designed for e.g. detection-reactions of certain chemicals. In the present work, the TOLLEN`s reaction (as described for example in Benet, Lewis, Yang, & Hughes, 2011; Dondi, Su, Griffith, Clark, & Burley, 2012), a reaction

originally designed for the detection of aldehydes, was used in order to precipitate thin layers of silver nano-particles onto molds.

The reaction takes place thanks to the mutarotation potential of sugar: in solution, a-D-Glucopyranose and b-D-Glucopyranose are in equilibrium. A small portion of the glucose exists in its open-chained aldehyde form though (thanks to mutarotation), as shown in **Figure 87**.

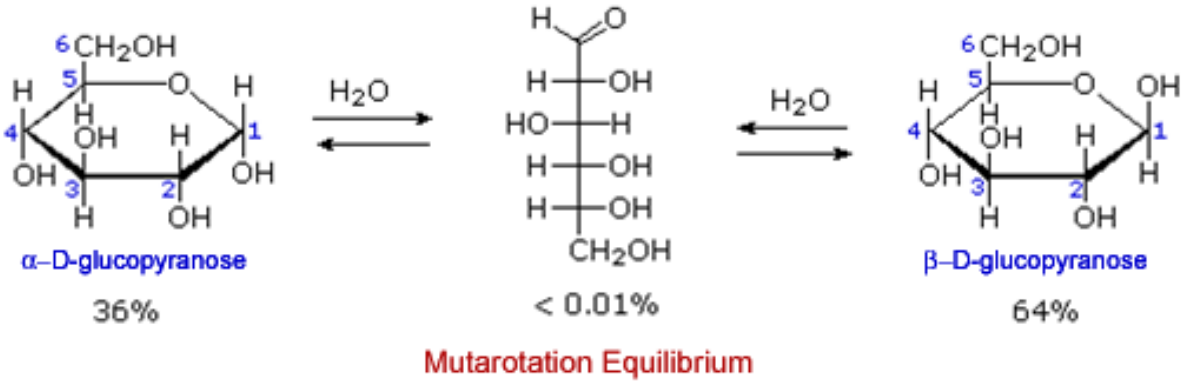

Figure 87: Mutarotation equilibrium of Glucose. *In the middle the open chained aldehyde from is depicted. Image source: http://www.namrata.co/chemistry-of-carbohydrates-lecture-3-ring-structures-and-mutarotation/, 31.07.2017.*

Mixing glucose and TOLLEN`s reagent oxidizes the aldehyde form of sugar to its carboxylate salt. The TOLLENs reagent itself consists of a solution of ammoniacal silver nitrate, usually created by mixing sufficient amounts of ammonia to a slightly basic solution of silver nitrate. As a result, pure silver is precipitated. The complete reaction is depicted in the following **Figure 88**.

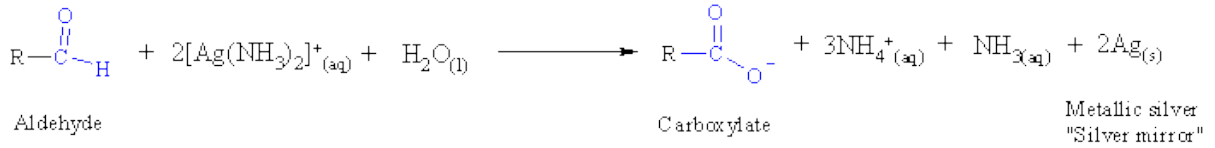

Figure 88: Reaction mechanism of the TOLLEN`s reaction with glucose (aldehyde form depicted). *Image source: http://staff.um.edu.mt/ratk1/AldeKetProps.htm, 31.07.2017.*

For the experiments of this work, a fixed protocol of the TOLLEN`s reaction was established in order to achieve reproducible silver films on samples. Towards this end, 1g of silver nitrate (Sigma-Aldrich, Germany), was dissolved in 10 ml of distilled water and then ammonia (32 % solution, Carl-Roth, Germany) was carefully added until the solution cleared. 0.15 g of ammonium sulfate (Sigma-Aldrich, Germany) were added to this solution and filled up with distilled water to a total of 50 ml. Additionally, 25 ml of a KOH-

solution (18 g/L) (KOH pellets, Carl-Roth, Germany) and 25 ml of a 2.5% glucose (D+-Glucose, Carl-Roth, Germany) solution were prepared. The solutions were then mixed in a beaker in the order of: 1.) KOH-solution, 2.) Glucose solution, 3.) ammoniacal silver nitrate solution, in total filling 100 mL. Dental silicon molds, wrapped with copper wire, were attached to the side of the beaker via tape, in such a fashion that the mold itself was well covered with the reagent. Preciptation took place under stirring on a magnetic stirrer for 2.5 minutes, or, depending on ambient temperatures (the higher the temperature, the faster the reaction takes place) a little less. Success of the reaction was observable by a silver mirror precipitate that covered the glass of the beaker. Per sample, the whole reaction was repeated four times in total, in order to achieve an even, thin layer of precipitated silver on the samples. Samples were then carefully rinsed with distilled water to get rid of random chunks of carboxylated aldehyde salts. Samples dried for at least 24h at ambient conditions before further treatment took place (e.g. electroplating).

6.2 Results

First replication attempts were made using approximately 1 cm^2 pieces of diffraction grid foil. The reasoning behind the usage of these foils was that they exhibit regular, periodic microstructures. If replication would be successful it would be proved that the process is suitable to replicate fine microstructures even on biological samples without the risk of damaging valuable and possibly scarce (e.g. in case of *Dysodius*) sample material. The foil pieces were imprinted into dental silicone with a thickness of approx. 5 mm, as described previously in the materials and methods section (chapter 7.1) and cut out carefully. Each individual sample then was wrapped with silver wire in order to provide a conductive frame that could be plugged into the cathode holders of the electroplating setup. **Figure 89** exemplarily shows this process.

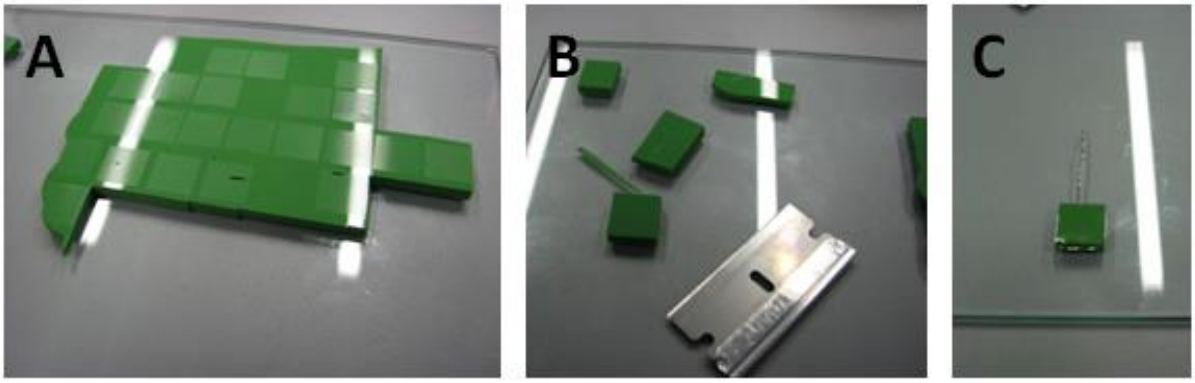

Figure 89: Overview of the replication process with dental silicone. *A Square pieces (~1 cm^2) of diffraction grid foil were imprinted in the silicone. B the individual samples were cut out carefully. C A thin silver wire was wrapped around to act as a frame and an attachment option for placement in the electroplating setup.*

Samples were then subjected to the three different ways of coating (gold sputter coating, carbon coating, and chemical silver deposition) as described. At least four diffraction foil samples were tested for each coating procedure. After this, the now conductive samples underwent electroplating, performed with individually fitted values for amperage (depending on the total area, as described in Chapter 7.1). After a successful plating process, samples needed to be separated from the silicone mold and a copper replica of the original surface was the result. Obviously, these surfaces still contained the individual metals, used to render them conductive in the first place, enclosed in the copper matrix. An example outcome of this process is shown **Figure 90**, for samples that were deposited with silver.

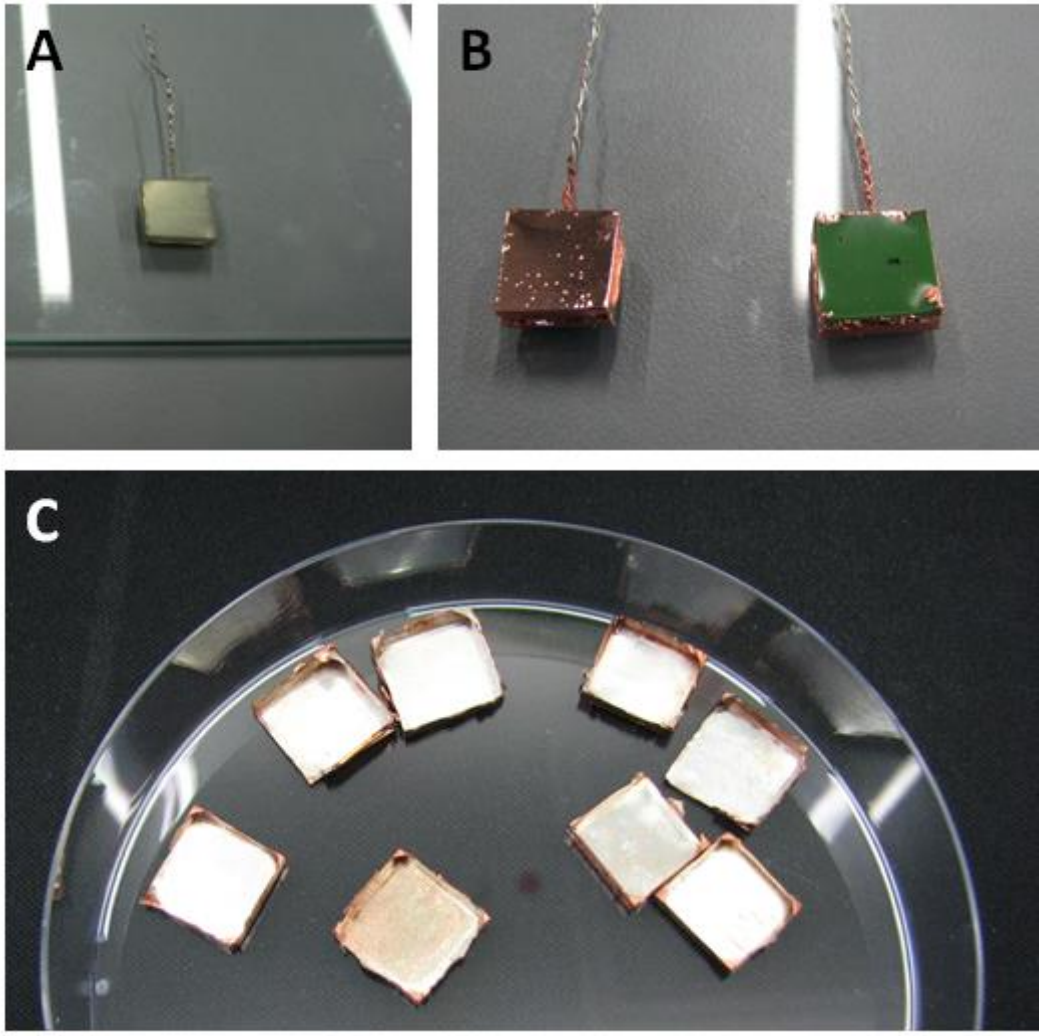

Figure 90: Example outcome for a successful all-metal-replica made from silicon imprints of diffraction foil. A *Silicone mold after chemical deposition of a thin silver film.* ***B*** *Example silicone molds from the silver deposition row, after successful electroplating.* ***C*** *Finished all-metal-replicas, after the silicone mold had been removed. One can see that the surfaces exhibit a mixture of copper matrix and enclosed silver particles.*

It has to be noted that vast differences were found for the individual applicability of the used ways to render samples conductive. Silicone samples that were gold coated (sputtered) showed the strong tendency to not be stuck to the outer layers of copper that were applied during electroplating. Only with massive force (e.g. cutters, knives and tweezers) it was possible to separate silicon mold and copper positive from each other. This usually led to the destruction of either the fine microstructure that was tried to replicate, or the copper positive in total. Due to this gold coating as a way of rendering the mold surface conductive was discarded.

The results made for carbon coating were also rather unsuccessful. Indeed it was possible to carbon coat and afterwards electroplate the samples and even the separation of mold and positive was positively easy, but carbon coating always lead to a different kind of sample defect: Due to arc evaporation being such an thermally excessive process, temperatures of approximately 300 – 400° C were reached in vicinity of the samples. The silicone molds were able to handle these temperatures surprisingly without showing any signs of breakdown, but due to the heat, they expanded during coating. Consequently, the samples shrank down in size while cooling afterwards. As a result, the thin coating of carbon was subjected to quite excessive warpage, faulting and ripping. These samples were unusable for further treatment, since all surface features of the original surface got altered in an undesirable way. In equal measure towards the previous gold samples, all carbon coated samples were discarded therefore for further experiments.

From all tested metal deposition ways, only chemical precipitation of silver lead to promising and successful results. The copper positives of firstly tested diffraction grids turned out to be well replicated and the process was easily reproducible. Images of successfully replicated diffraction foil surfaces (silver deposit with copper matrix) are shown in following **Figure 91**, in comparison to the original surface of the foil. The images were taken using the same SEM previously mentioned in Chapters 3.2, 4.2 and 5.2 respectively and the diffraction foil was sputter coated using the generic protocol for gold coating mentioned in Chapter 7.1

Figure 91 nicely shows that the individual grid lines of the foil were successfully replicated into the copper-silver surface matrix of the copper replicas. Individual lines are copied cleanly (**Figure 91 B** and **C**) and no apparent damages, which might have been introduced in the de-molding process, were found. Due to this promising results it was decided to use chemical silver deposition, followed by copper electroplating as the way of choice for attempting replicas of biological replicas.

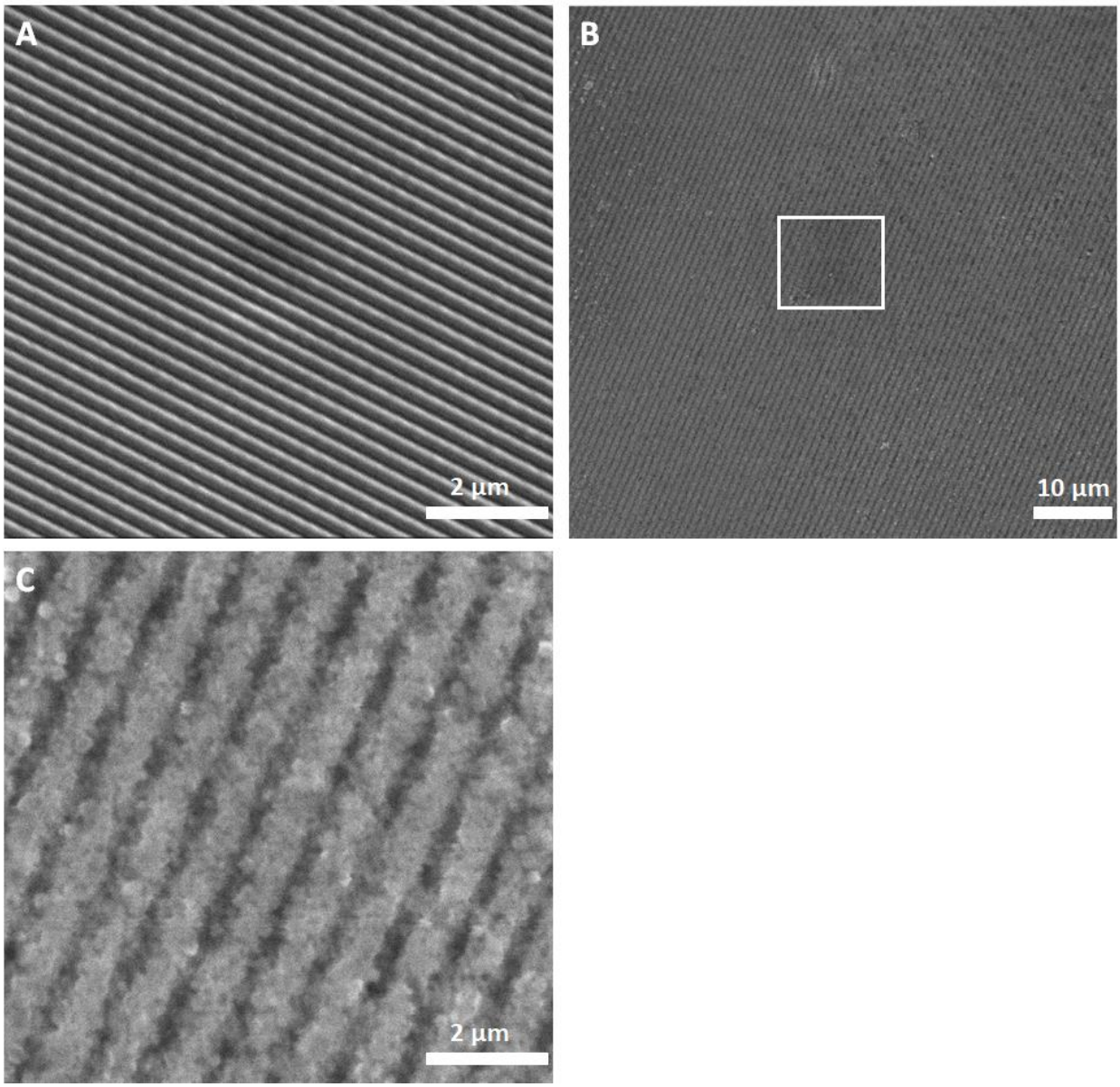

Figure 91: Example outcome of copper replica from silicon molds of diffraction foils (grid size of 1 µm). A *SEM overview of a diffraction foil with 1 µm grid size.* ***B*** *SEM overview of a 75 x 75 µm area of the copper replica.* ***B****. Detail of the individual replicated grid lines from the center of A (white box).*

Additionally, in order to verify quality and reproducibility, a small test series was done in order to find out the relative deposition thickness per time and the overall nature of the copper layers after electroplating. Towards this end, four standard SEM mounts (smooth surface) were electroplated with copper twice, according to the protocol mentioned above (40 mA/cm^2, 3 V, 2h deposition per layer). Covered samples were then cut in half with a saw to allow for measurement of layer thickness and evaluation of connection

quality in between the two coating layers. Following **Figure 92** shows exemplarily images of the samples that were measured and evaluated.

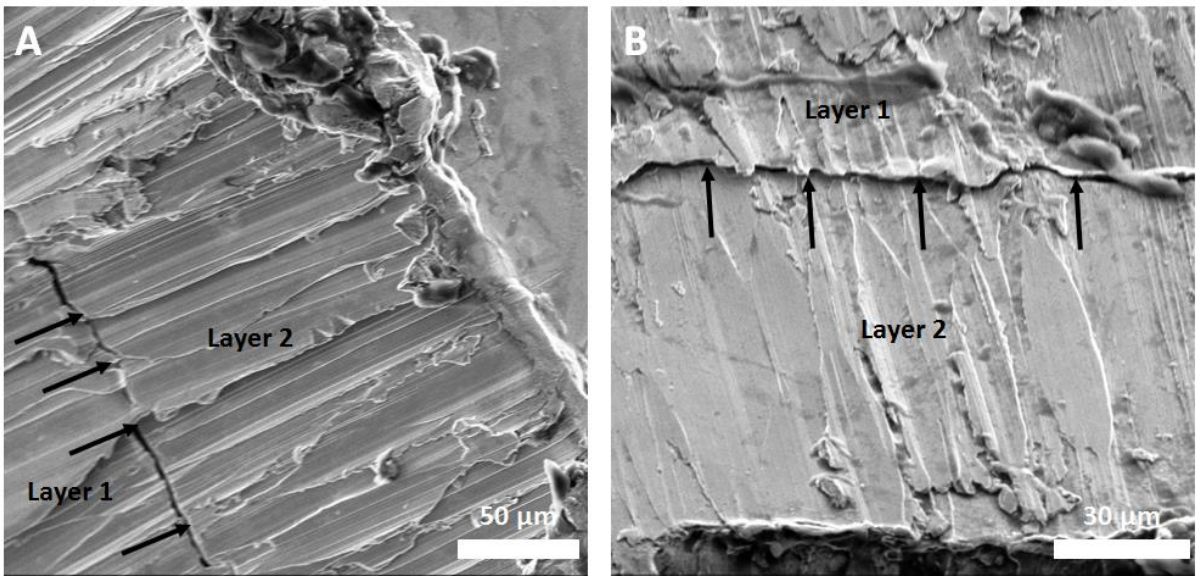

***Figure 92: Exemplary images of two layers of copper, deposited on top of each other via electroplating. A** and **B** show the cross-section of two different samples after cutting it with the saw. Clearly, a seam between first (Layer 1) and secondly deposited layer (Layer 2) can be seen (black arrows). Layer 2 was used in all four fabricated samples for measuring the deposition thickness.*

Figure 92 shows that the seam in between them clearly can distinguish two layers of copper that were deposited on top of each other. However, this seam does not directly affect the bonding of the two layers – at no time it was observed that layers were separated after electroplating – but rather seems to be an artifact from the heat that was generated during sawing → In close vicinity to the cut, the material expanded due to heat and the bond between layers was possibly cracked while cooling. On the other hand, this seam allowed for clear identification of the respective layers, and therefore allowed for measuring the thickness. The thickness of layer 2 was measured 10 times for each of the four manufactured samples, resulting in an average thickness of 129.4 µm (± 22.1). This means, that the deposition rate of copper with used values (e.g. amperage and voltage) can be estimated to approximately 130 µm per hour. Four cycles of electroplating (as mentioned before) therefore will result in samples exhibiting a wall strength of ~0.5 mm – a wall strength that is durable enough to endure further experiments.

Since quality and production reproducibility were indeed confirmed after the experiments shown so far, first experiments with biological surfaces were started. For starters, the relatively robust skin of a dead and in alcohol conserved specimen of *Phrynosoma cornotum* was used to make dental silicon imprints of

different parts of the body. Body parts chosen are: left side of the back, left side of the ventral scales (belly), dorsal side of the left front foot, and dorsal side of the tail (center). The silicon negatives (molds) then were covered with a thin layer of precipitated silver (according to the protocol given in Chapter 7.1). After washing and drying for 24hs, the silver covered molds were electroplated (see Chapter 7.1). Evaluation of the replica quality took place under the SEM. For better contrast and in order to stop any oxidation processes that might occur between copper and silver in the surface matrix of the replicas, they were also sputter coated with gold (according to the protocol mentioned in Chapter 3.2). Example images of the outcome are shown in the following **Figure 93** and **Figure 94**.

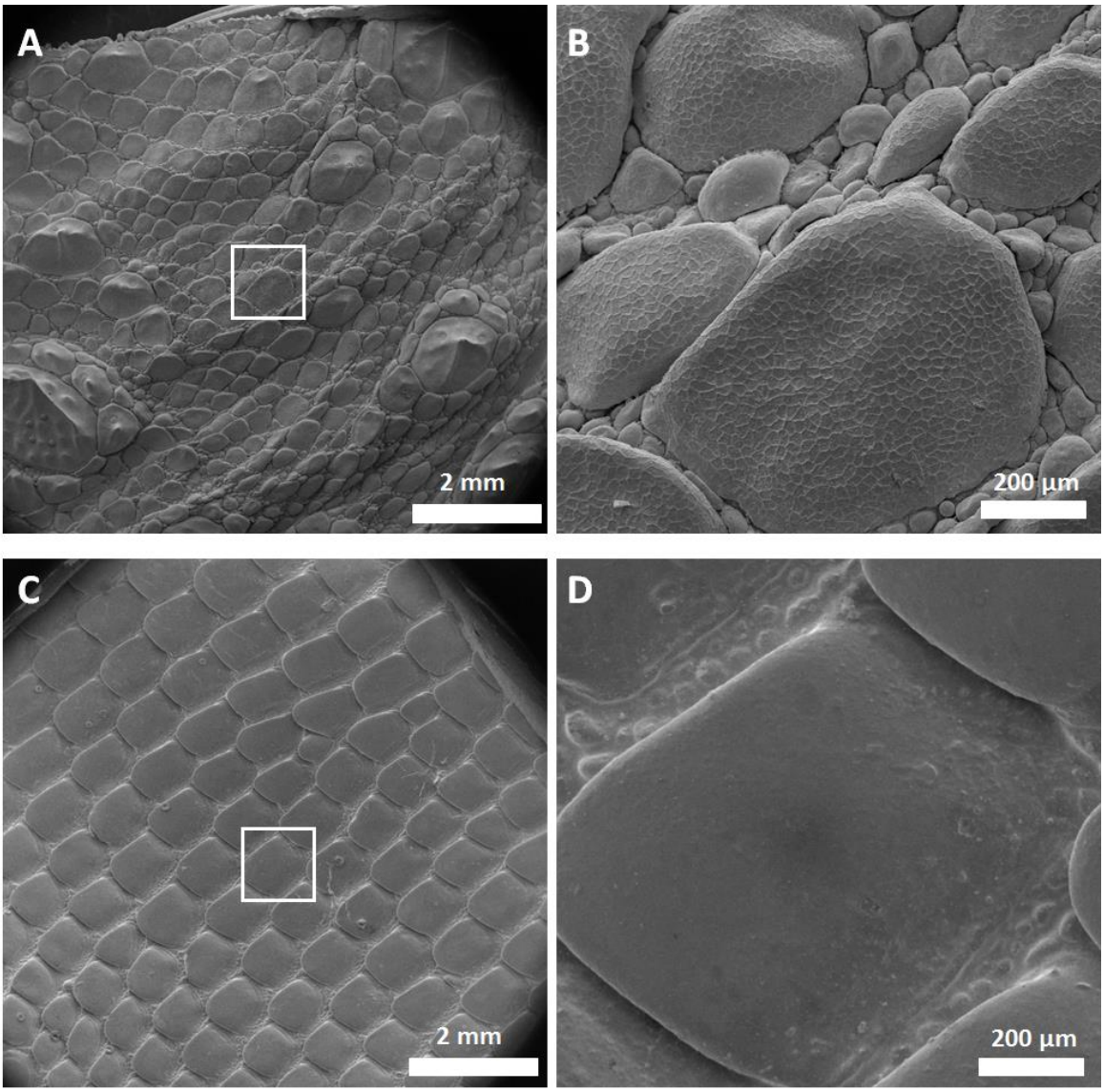

Figure 93: Copper replicas from the skin of P. cornotum, part I. A *Overview of scales from the left side of the animals back.* ***B*** *Detail from the white box in A. Clearly one can see the successful replication of the lizards scales' micro-ornamentation as described in Comanns, Effertz, Hischen, Staudt, Böhme, et al. (2011)* ***C*** *Overview of ventral scales (left side of the animal).* ***D*** *Detail from the white box in C.*

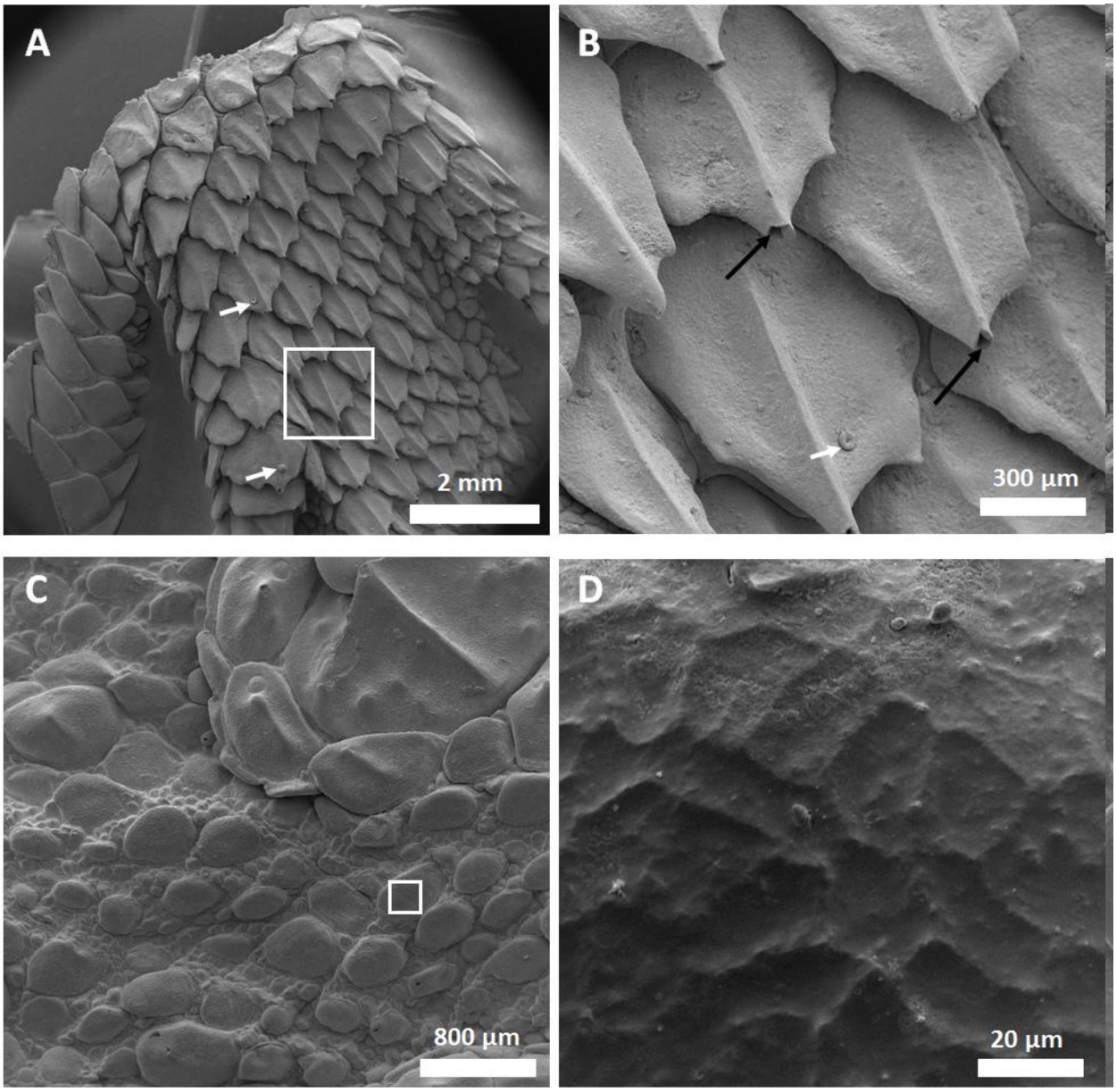

Figure 94: Copper replicas from the skin of P. cornotum, part II. A *Overview of scales from the animals left front foot (dorsal). White arrows mark casting defects (small bubbles).* ***B*** *Detail from the white box in A. The overall morphology of the scales was replicated quite successful, only some of the scales' tips show minor defects (black arrows). The white arrow marks one of the bubbles mentioned in A.* ***C*** *Overview of the replicated dorsal skin from the lizards' tail.* ***D*** *Detail from the white box in C. Again, the micro-ornamentation, as already shown in* ***Figure 93 B****, was successfully replicated, though not as detailed and pronounced as previously.*

Figure 93 and **Figure 94** both show the great success of the replication process into all-metal replicas. All replicated parts of the lizards' skin showed the typical morphological features as they were described in Comanns, Effertz, Hischen, Staudt, Böhme, et al. (2011) and as they were observable on SEM images of the real skin. Scales from the dorsal parts of the animal (back and tail, as shown in **Figure 93 A/B** and **Figure 94 C/D**), clearly showed that the specialized hexagonal micro-ornamentation of these animals, with

dimensions of about 20 µm in diameter, was successfully copied in the copper replicas. In contrast to that, the relatively smooth scales on the lizards' belly were exactly that in the replica: smooth and well copied (**Figure 93 C** and **D**). The biggest defects can be found in the copper replicas of the lizards' foot. Probably already during the imprinting of the dental silicone, small air bubbles were trapped between lizard skin and silicone (**Figure 94 A** and **B**, white arrows). As a result, these pockets were either filled with copper in the electroplating process (defects/bubbles on the scales, white arrows), or were not sufficiently reached in the process of silver coating. This probably happened at the scales' tips (black arrows), hence, in the electroplating process, no copper was deposited here.

Finally, the attempt was made to replicate a specimen of *Dysodius lunatus* in all metal. Towards this end, a dried specimen was imprinted into the dental silicone as described before. Unfortunately, the specimen didn't handle the separation process well. It had to be removed forcefully from the silicon mold and broke into pieces, which didn`t affect the quality of the already cured silicone mold though. Afterwards, the silicone negative got covered with four layers of chemically deposited silver (as described before) and was electroplated according to the protocol. The finished copper replica was washed and dried and sputter coated with goldto stop oxidation processes of the surface and to improve contrast in the SEM (coating and SEM process analogous to previously described experiments for the lizard replicas). Example images of *D. lunatus'* copper replica, as well as a comparison between the original surface and the replica are shown in the following **Figure 95** and **Figure 96**.

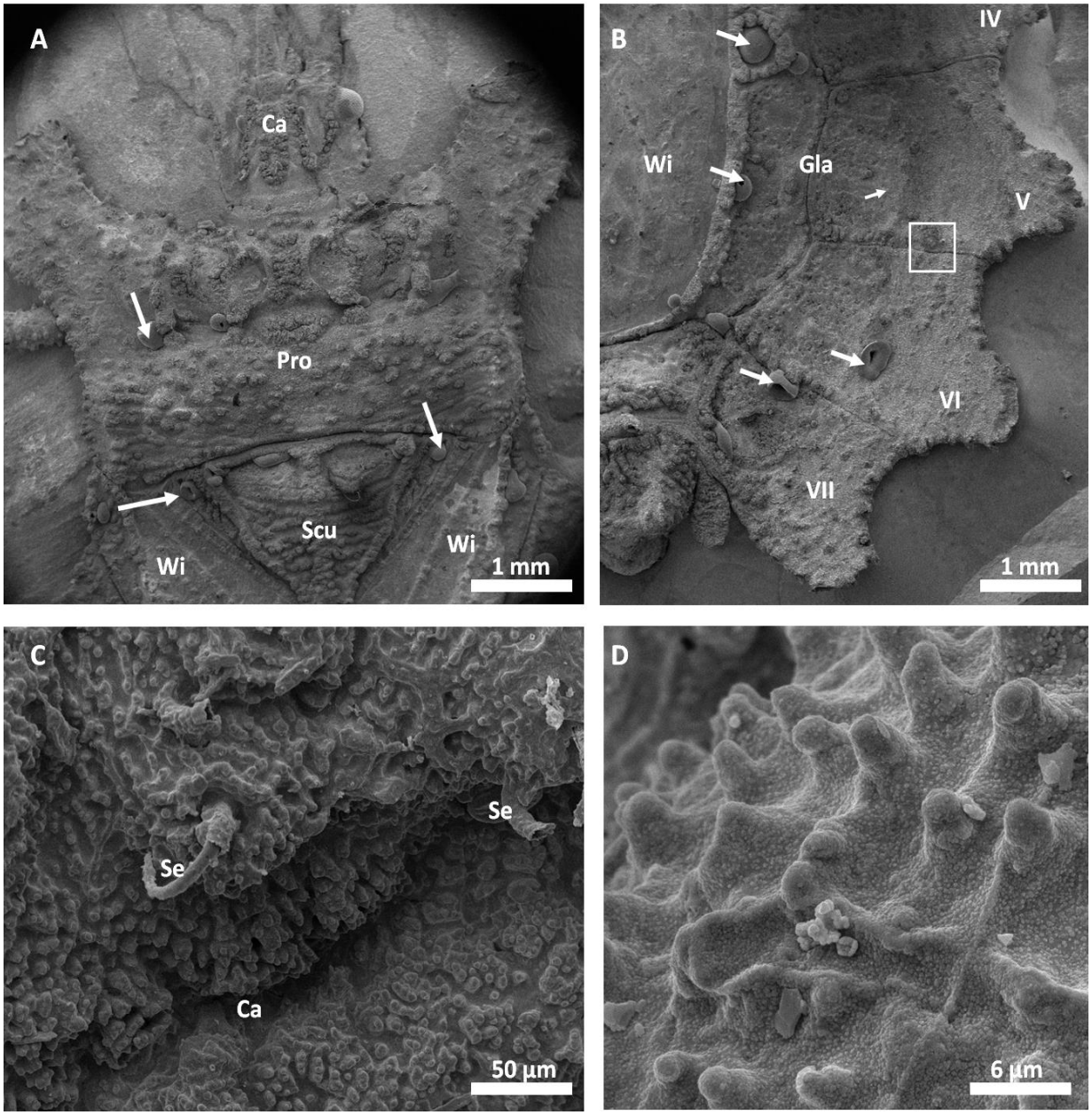

Figure 95: Copper replica of D. lunatus. ***A*** *Dorsal overview of front part of the replica. One can see that all relevant dorsal body parts have been replicated successfully. Head (= caput, Ca), pronotum (Pro), scutellum (Scu) and the sclerotized parts of the front wings (Wi) are visible. White arrows mark bubble-like defects.* ***B*** *Dorsal overview of right bottom part of the replica. Visible are connexival plates VI-VII with all their respective intersegmental sutures, the glabrous area (Gla) and the wing membrane (Wi). Once again bubble-like defects can be observed (white arrows).* ***C*** *Detail from white box in B. Shown is the intersegmental suture between connexivum V and VI (=capillary, Ca), the surrounding, typical surface microstructure of Dysodius, and setae (Se).* ***D*** *A magnified section of the surface microstructure is shown. Clearly, the morphological and dimensional features have been successfully copied.*

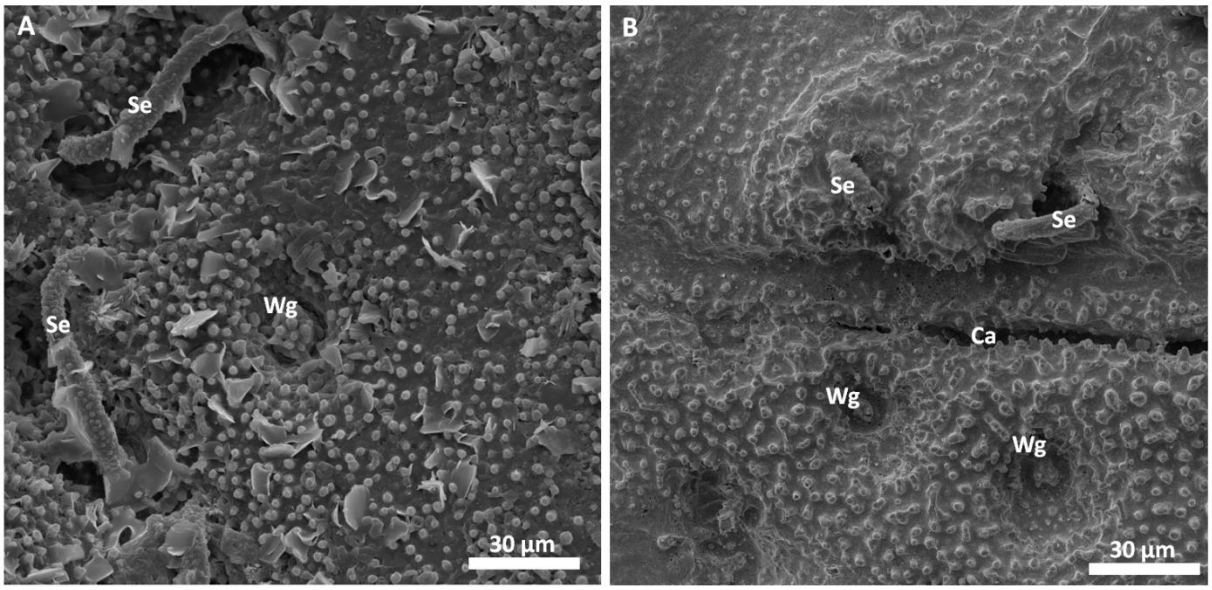

Figure 96: Comparison between the original surface of a sputter coated specimen of D. lunatus (A) and the copper replica (B). *The images depict nicely, how well the copper surface replicates the natural counterpart. All relevant features are copied in detail: Wax glands (Wg), setae (Se) and, as shown before, even the typical surface microstructure. Image B furthermore shows that even deep crevasses of intersegmental capillaries can get replicated to a certain degree.*

Figure 95 and **Figure 96** show the successful replication of the dorsal surface from *Dysodius lunatus* into an all-metal copper replica. **Figure 95 A** and **B** depict that indeed all surface features of a complete specimen were replicated and that the amount of surface defects in this replica is relatively low (bubbles, marked by white arrows). The reason for visible defects possibly is the same as previously stated for the replicas of *P. cornotum*. Higher magnifications under the SEM also reveal that the intrinsic, morphological acuteness of *Dysodius* surface has been conserved in the copper replica (**Figure 95 C** and **D**). The typical microstructure was successfully replicated and even features with higher aspect ratios (or even undercuts) like intersegmental capillaries and setae got copied to a certain degree.

In the direct comparison between natural counterpart (**Figure 96 A**) and replica (**Figure 96 B**) this becomes even more apparent. Except for the fact that the overall surface “resolution” is slightly grainier on the copper replica, virtually no difference can be found between real surface and (defect free) parts of the copy.

6.3 Discussion

The experiments presented in this chapter had one ultimate goal: The establishment of a setup that allows to reproduce biological surfaces into a material that is durable and, even more importantly, thermally conductive. This goal has been achieved by the production of copper-electroplated replicas of different biological surfaces. The way towards reaching this goal has been difficult though.

Different approaches were undergone and presented, in order to find the most suitable and reproducible way of replicating biological surfaces in a thermally conductive material. Relatively early it was clear, that replicas in copper would have certain benefits: 1) They would show excellent thermal conductivity, 2) durability and sturdiness would be better than in most biological samples, and 3) ideally a once made mold would serve for several replication processes, therefore the amount of biological samples needed for certain experiments could be drastically reduced. In the same line of thought it was equally clear that the best way to achieve such copper replicas would be by means of electroplating, an easy and well established method to deposit sturdy and bonded layers of a metal (see Chapter 6.1). Since the deposition in this glavano-chemical process takes places atom by atom, it was to be expected that even finest surface features could be reproduced and conserved with this procedure. Since electroplating directly onto a biological surface would consequently lead to a negative copy of given surface (and not a 1:1 copy), an intermediate step towards electroplating had to be molding the desired surfaces first. Molding with dental silicon is and has been a well-established way at the Institute and therefore this method was chosen as the mean to achieve first molds of surfaces. Pretest done by P. Comanns showed that molds of the skin of different lizards could be used to replicate the structure in different resins and he could prove that even the finest microstructures could be reproduced this way (not published). Unfortunately, the pure resin replicas, as well as the silicon molds themselves, exhibit poor electric conductivity – as previously mentioned an absolute need for electroplating. Hence, experiments needed to be done in order to find out a solution.

As it turned out, the biggest problem was to find a way that serves both, electric surface conductivity and the ability to still de-mold a sample. As described in Chapter 6.1, three different ways of surface preparation were tried in order to render silicon molds electrically conductive: sputter coating with gold, carbon arc evaporation coating, and chemical silver precipitation. All three ways thought to be suitable to produce a thin, conductive layer that still would not cover micro surface features of the mold. As described in Chapter 6.2, only one method lead to desired effect though: chemical silver deposition. Gold sputter

coating as well as carbon coating turned out to be unsuitable due to different reasons: gold coated samples that were tested with electroplating indeed allowed for electro-chemical deposition of copper, but the resulting copper layers were bonded too well with the gold and the silicone underneath. De-molding was impossible. Carbon coating on the other hand didn`t even lead to tests in the electroplating setup. Due to the intense heat during coating, and the resulting shrinkage during cooling afterwards, all tested samples exhibited carbon coats with warped, cracked and overall unsuitable surface features and were therefore discarded. Therefore, and nicely proven by the images depicted in **Figure 90** and **Figure 91**, chemical silver deposition became the successfully established method to render non-conductive molds suitable for electro-chemical deposition.

Following this approach, copper replicas of different surface parts of lizard skin (*P. cornotum*) and the flat bug *D. lunatus* could be fabricated (**Figure 93** - **Figure 96**). The SEM scans of these replicas reveal the great success of the established replication method: individual morphological features of the given natural counterparts were virtually copied 1:1. Features like the typical honeycombs on the scales of *P. cornotum* (**Figure 93 B** and **Figure 94 D**) are pronounced almost as sharply as on the natural skin, and even the fine and delicate wax microstructures of *Dysodius* exhibit the typical appearance (**Figure 95 C** and **D**). In a direct comparison with the natural counterpart (**Figure 96**) one can clearly see how exact the surface got replicated into copper. Astonishingly, even shapes that exhibit fine and hollow features like setae (**Figure 95 C** and **Figure 96 B**) can be reproduced with this novel technique. This clearly speaks for two things: 1) The molding process with silicone is an appropriate way to mold even the finest of surface structures without destroying them, and 2) the following surface coatings with silver and copper produce a matrix that is fine enough to follow and fill these most delicate imprints in the mold.

Obviously, the replicated copper surfaces are not completely void of smaller defects. As depicted in **Figure 94 A** and **B**, as well as in **Figure 95 A** and **B,** small, bubble-like artefacts may occur in the replicas. These are most likely the result of either small enclosures of air during molding with silicone (and therefore result in the empty pockets that are getting filled with copper in the electroplating process). A possible way to avoid these in the future would be to execute molding and curing in an evacuated environment. Secondly, small empty spots may occur on the replicas, as exemplarily shown for the lizard-scale tips in **Figure 94** B. Here we most likely have the case that deposition of conductive material (silver) did not reach the very deepest spots (hence the tips of the scales) in the silicon mold. Consequently, no copper is being deposited in these places, since the electroplating process fills the mold in a consecutive manner. To avoid this kind

of defect in the future, it is suggested to carefully choose the orientation of how molds are placed in the silver precipitation bath → precipitation "shadows" need to be avoided.

In summary, it can be concluded that this introduced novel approach of surface replication will fulfill the goals it was designed for. Samples made with via this technique do and will exhibit:

- Excellent thermal conductivity
- Excellent replication of desired morphological features
- High durability and endurance
- Fixed and uniform surface chemistry (achieved by uniform gold coating)

The first two statements will allow the originally desired experiments to be carried out in the future. Thanks to the excellent thermal conductivity (while still exhibiting original surface morphology), experiments concerning wetting and especially evaporation and condensation, will become possible. In addition to that, the sturdy qualities of the all-metal replicas will allow for multiple usage of the same sample, a feature that not necessarily apply to biological samples. Furthermore, thanks to the achievable, uniform surface chemistry, all metal replicas can be used with explicitly designed chemical surfaces for individual experiments. In case of *Dysodius* for example it is thinkable to coat the metal replicas with thin layers of artificially designed waxes. This could be achieved by vacuum deposition as already successfully shown for technical replications for waxes that show self-organization, biomimetically inspired by plant surfaces (e.g. Koch, Schulte, Fischer, Gorb, & Barthlott, 2008). Then, ideally, the liquid-surface interaction of flat bugs as presented in Chapter 3 of this work, would become totally reproducible and adjustable. Additionally, gold used as a surface finish (in the presented work mainly to prevent oxidation) is an excellent candidate for altering the surface chemistry in general: the mercapto-headgroup of thiols is known to excellently bind and complex with gold, whereas the rest of the molecule can be designed and modified to certain needs. Known from various applications in the field of self-assembling nanotechnology (e.g. Rong et al., 2001; Vericat, Vela, Benitez, Carro, & Salvarezza, 2010), specifically designed thiols can be used to achieve desired surface chemistry. Combining this feature with gold-sputtered copper replicas could allow for diverse experiments that include a stable surface morphology and adjustable surface chemistry, while still exhibiting excellent thermal and electrical conductivity.

7. Summary

The research presented in this work was aimed towards the identification and (better) understanding of two different liquid-surface-interaction phenomena that were discovered on bugs. Firstly, we have the surface-water interaction on neotropical flat bugs (Aradidae), which enables a phenomenon called adaptive camouflage. Secondly, we find that some Aradidae, as well as some European true bugs exhibit means to passively transport oily fluids directional, in the so called scent efferent system. Using various research methods, it was possible to identify the underlying mechanisms of both interactions and even abstract and transfer them onto technical surfaces. Hence, artificial, biomimetically bug inspired applications for wetting enhancement and directional, passive fluid transport could be achieved.

Concerning the water based interaction, two investigated species of flat bugs from the genus *Dysodius* (namely *D. lunatus* and *D. magnus*) were investigated. Both species show the amazing behavior of color change when getting in contact with water – the so called “adaptive camouflage”, a camouflage that allows the bugs to change their colors according to their surroundings. This is in most cases the bark of rainforest trees they live on. A color change occurs on the bark when it gets wet, a need for the bugs therefore, to copy this effect. Reflection measurements of both, bugs and bark showed that indeed the darkening, or better the change in albedo, is both, measurable and calculable. The measured graphs for bark and bug followed the same trends for the different tested wavelengths – a clear indicator that adaptive camouflage in *Dysodius* is more likely to be an adaption that was evolutionary beneficial for this genus, than it was coincidence.

To figure the reasons and mechanisms behind this way of camouflage, it was necessary to investigate multiple things: Surface morphology and chemistry, in order to understand why water is being spread on the waxy surface of these animals in the first place, and secondly, the physics behind the observable change in coloration. In the curse of chemical analysis mainly two things were discovered:

1. *D. lunatus* and *D. magnus* show virtually no (detected) difference in composition of their surface waxes.

2. Dissolved and recovered flat on glass coverslips, surface waxes of *Dysodius* exhibit contact angles of approximately 44° - a contact angle range that clearly shows the chemical hydrophilicity of the surface.

3. Most promising candidates enabling the waxes to exhibit such behavior, are possibly different glycerides (mono- and di-) as well as erucamide. Both substances can be placed in the class of amphiphilic molecules, and are therefore excellently suited to mediate the interaction between wax-matrix and water.

Morphological analyses then showed that the surface of both *Dysodius* species also exhibits the same morphological features: Small wax naps (about 2 µm diameter, 5.5 µm height and 5 µm distance in between neighboring structures) could be identified. This helps to explain the excellent wetting properties: A chemically hydrophilic surface (see above) gets even more hydrophilic, if a microstructure (roughness) is introduced. Furthermore, sophisticated gland structures, that are most probably accountable for the production of naps on *Dysodius* cuticle, were found and investigated and a theoretical model was formulated, putting all identified parts into context.

Using the findings of chemical analysis it was possible to artificially render bees wax hydrophilic and copying the influence of surface naps was achieved by reproducing the surface naps via laser ablation on PET-foils – both ways delivering a proof of concept on artificial materials, showing that the findings are indeed abstract- and transferable. Future experiments hopefully will allow for combining both: hydrophilized waxes with artificial nap structures.

Video-analysis of the water spreading mechanism on *Dysodius* also showed that spreading is not only occurring on the surface: intersegmental sutures act as capillaries that forward water very fast (with up to 1.2 mm s^{-1}) across the whole dorsal surface. From the filled capillaries the water then again is spreading across the surface of adjacent structures. A very fascinating observation, because it enables the water to cover far more area than it would be possible by means of surface wetting only. We succeeded in modeling this behavior theoretically and were able to produce a working prototype with engraved glass.

The second fascinating liquid-surface interaction, as stated before, is the passive and directional transport of oily defense fluids that some species obviously exhibit. Described first on *Dysodius* studies were made in order to investigate the existence of such transport systems (as parts of the external scent efferent system) in closer and distant relatives. The investigated species brought forth some very interesting observations. Not only is the basic principle as found in *Dysodius* by no means conserved throughout the investigated species (not even in close relatives), but it was found that even the position of scent glands on the body can vary significantly. An observation to which up to this point, no satisfying explanation has been found (neither in this work, nor in the literature). Nevertheless did the investigation show that some

species indeed came up with similar solutions, hence, structures in their SES that promote unidirectional, passive fluid transport.

In the following, structural features of the SES from *Palomena prasina*, *Raphigaster nebulosa* and *Tritomegas bicolor* were extracted and abstracted, before being transferred onto different technical surfaces (steel and polymers). Extensive video-analysis and the help of custom written algorithms indeed showed that this attempt succeeded. If a fluid exhibited a contact angle between 25 and 31°, the fabricated, bug inspired channels showed unidirectional, passive fluid transport with velocities of up to 1 mm s^{-1}, while being able to inhibit fluid flow in the opposite direction. Depending on the material, oily or watery fluids were tested and it showed that major differences in performance (velocity) can be explained by differences in viscosity of those fluids. Unfortunately it was not fully possible to find a satisfying explanation for the physical mechanism that exactly describes the observed fluid transport. Future work will have to address this.

In the last chapter of this work, an interesting, new approach towards the reproduction of biological surfaces is presented. Using dental silicone as a molding medium, it was possible to replicate complete biological surfaces and samples in metal. The need for this procedure grew from previous wetting experiments with bugs, that showed that ambient temperature and humidity indeed can make significant differences in sample performance and thermally conductive sample material would enable experiments where these phenomena could be better investigated. Testing several routes in order to achieve such, it was found that silicone molding, followed by chemical silver precipitation and additional copper deposition via electroplating, seems to be the most suitable way. The produced samples showed almost perfect replication of the original surfaces and open up several new, interesting ways for doing experiments.

8. References

Aldrich, J. R. (1988). Chemical ecology of the Heteroptera. *Annual Review of Entomology*, *33*(1), 211–238.

Andersen, H. H., Bay, H. L., Robinson, M. T., Roosendaal, H. E., & Sigmund, P. (1981). *Sputtering by Particle Bombardment I Physical Sputtering of Single-Element Solids*. Springer-Verlag Berlin Heidelberg New York.

Ångström, A., & Angstrom, A. (1925). The Albedo of Various Surfaces of Ground. *Geografiska Annaler*, *7*, 323. https://doi.org/10.2307/519495

Arenholz, E., Svorcik, V., Kefer, T., Heitz, J., & Bäuerle, D. (1991). Structure formation in UV-laser ablated poly-ethylene-terephthalate (PET). *Applied Physics A Solids and Surfaces*, *53*(4), 330–331. https://doi.org/10.1007/BF00357196

Bachmann, H.-G., & Bachmann, G. (1989). Oberflächenvergoldung: Alte und neue Techniken. *Chemie in Unserer Zeit*, *23*(2), 46–49. https://doi.org/10.1002/ciuz.19890230203

Ball, W. W. R. (1960). *A short account of the history of mathematics*. New York, NY: Dover.

Barthlott, W., & Neinhuis, C. (1997). Purity of the sacred lotus, or escape from contamination in biological surfaces. *Planta*, *202*(1), 1–8. https://doi.org/10.1007/s004250050096

Benet, W. E., Lewis, G. S., Yang, L. Z., & Hughes, P. D. E. (2011). The mechanism of the reaction of the Tollens reagent. *Journal of Chemical Research*, *35*(12), 675–677. https://doi.org/10.3184/174751911X13206824040536

Blomquist, G., & Jackson, L. (1979). Chemistry and biochemistry of insect waxes. *Progress in Lipid Research*, *17*(4), 319–345. https://doi.org/10.1016/0079-6832(79)90011-9

Bormashenko, E. Y. (2013). *Wetting of real surfaces*. Berlin ; New York: De Gruyter.

Boxman, R. L., Sanders, D. M., & Martin, P. J. (1995). *Handbook of Vacuum Arc Science and Technology*. Noyes Publications, Park Ridge, N.J.

Chandra, D., & Yang, S. (2011). Dynamics of a Droplet Imbibing on a Rough Surface. *Langmuir*, *27*(22), 13401–13405. https://doi.org/10.1021/la202208x

Chang, C.-T., Bostwick, J. B., Steen, P. H., & Daniel, S. (2013). Substrate constraint modifies the Rayleigh spectrum of vibrating sessile drops. *Physical Review E*, *88*(2). https://doi.org/10.1103/PhysRevE.88.023015

Cohen, M. L. (1977). MEASUREMENT OF THE THERMAL PROPERTIES OF HUMAN SKIN. A REVIEW. *Journal of Investigative Dermatology*, *69*(3), 333–338. https://doi.org/10.1111/1523-1747.ep12507965

Comanns, P., Effertz, C., Hischen, F., Staudt, K., B?hme, W., & Baumgartner, W. (2011). Moisture harvesting and water transport through specialized micro-structures on the integument of lizards. *Beilstein Journal of Nanotechnology*, *2*, 204–214. https://doi.org/10.3762/bjnano.2.24

Davidová-Vilímová, J. (2006). *Dorsal abdominal glands in Aradus betulae (Heteroptera, Aradidae)*. na. Retrieved from http://www.zobodat.at/stable/pdf/DENISIA_0019_0137-0148.pdf

de Gennes, P.-G., Brochard-Wyart, F., & Quéré, D. (2004). *Capillarity and Wetting Phenomena*. New York, NY: Springer New York. https://doi.org/10.1007/978-0-387-21656-0

Dickerson, A. K., Shankles, P. G., Madhavan, N. M., & Hu, D. L. (2012). Mosquitoes survive raindrop collisions by virtue of their low mass. *Proceedings of the National Academy of Sciences*, *109*(25), 9822–9827. https://doi.org/10.1073/pnas.1205446109

Domínguez, E., Heredia-Guerrero, J. A., & Heredia, A. (2011). The biophysical design of plant cuticles: an overview: Research review. *New Phytologist*, *189*(4), 938–949. https://doi.org/10.1111/j.1469-8137.2010.03553.x

Dondi, R., Su, W., Griffith, G. A., Clark, G., & Burley, G. A. (2012). Highly Size- and Shape-Controlled Synthesis of Silver Nanoparticles via a Templated Tollens Reaction. *Small*, *8*(5), 770–776. https://doi.org/10.1002/smll.201101474

Dupius, C. (1949). Données sur la morphologie des glandes dorso-abdominales des Hémiptères – Hétéroptères. Historique et discussion. *Feuille Natur*, (49), 13–21.

Durak, D., & Kalender, Y. (2007). Fine structure and chemical analysis of the metathoracic scent gland of Eurygaster maura (Linnaeus, 1758)(Heteroptera: Scutelleridae). *Folia Biologica*, *55*(3–1), 133–141.

Durak, D., & Kalender, Y. (2009). Fine structure and chemical analysis of the metathoracic scent gland secretion in Graphosoma lineatum (Linnaeus, 1758) (Heteroptera, Pentatomidae). *Comptes Rendus Biologies*, *332*(1), 34–42. https://doi.org/10.1016/j.crvi.2008.10.004

Eastop, T. D., & McConkey, A. (2006). *Applied thermodynamics for engineering technologists* (5th ed., repr). Harlow: Pearson/Prentice Hall.

Farner, D. S., King, J. R., & Parkes, K. C. (1982). *Avian biology. Volume VI Volume VI*. Retrieved from http://public.eblib.com/choice/publicfullrecord.aspx?p=1817836

Fink, S. (1992). Transparent Wood – A New Approach in the Functional Study of Wood Structure. *Holzforschung*, *46*(5), 403–408. https://doi.org/10.1515/hfsg.1992.46.5.403

Florkin, M., Scheer, B. T., & Brush, A. H. (1978). *Chemical zoology Vol. 10., Vol. 10.,*. New York; London: Academic Press. Retrieved from http://public.eblib.com/choice/publicfullrecord.aspx?p=1178436

Foldi, I. (1981). Ultrastructure of the wax-gland system in subterranean scale insects (homoptera, coccoidea, margarodidae). *Journal of Morphology*, *168*(2), 159–170.

Gohlke, D. J., & Tanner, J. C. (1976). Gore-Tex® Waterproof Breathable Laminates. *Journal of Coated Fabrics*, *6*(1), 28–38. https://doi.org/10.1177/152808377600600104

Gorb, S. N., & Goodwyn, P. J. P. (2003). Wing-locking mechanisms in aquatic Heteroptera. *Journal of Morphology*, *257*(2), 127–146. https://doi.org/10.1002/jmor.10070

Gough, A. J. E., Hamilton, J. G. C., Games, D. E., & Staddon, B. W. (1985). Multichemical defense of plant bugHotea gambiae (westwood) (Heteroptera: Scutelleridae): Sesquiterpenoids from abdominal gland in larvae. *Journal of Chemical Ecology*, *11*(3), 343–352. https://doi.org/10.1007/BF01411421

Graça, J. (2002). Glycerol and glyceryl esters of ω-hydroxyacids in cutins. *Phytochemistry*, *61*(2), 205–215. https://doi.org/10.1016/S0031-9422(02)00212-1

Hadley, N. F. (1994). *Water relations of terrestrial arthropods*. San Diego: Academic Press.

Haeberle, S., & Zengerle, R. (2007). Microfluidic platforms for lab-on-a-chip applications. *Lab on a Chip*, *7*(9), 1094. https://doi.org/10.1039/b706364b

Heiss, E. (1990). A review of the genus Dysodius Lepeletier & Serville 1828, with descriptions of two new species (Heteroptera,: Aradidae). *Anales Del Instituto de Biología de La Universidad Nacional Autonoma de México, Ser. Zoologia*, *61*(2), 279–296.

Henrici, H. (1939). Die Hautdrüsen der Landwanzen (Geocorisae), ihre mikroskopische Anatomie, ihre Histologie und Entwicklung. Teil 1: Die abdominalen Stinkdrüsen, die Drüsenpakete und die zerstreuten Hautdrüsen. *Zool. Jb. Anatomie*, *65*, 141–228.

Hischen, F., Reiswich, V., Kupsch, D., De Mecquenem, N., Riedel, M., Himmelsbach, M., … Baumgartner, W. (2017). Adaptive camouflage: What can be learned from the wetting behaviour of the tropical flatbugs Dysodius lunatus and D. magnus. *Biology Open*.

James, D. G., Heffer, R., & Amaike, M. (1996). Field attraction of Biprorulus bibax Breddin (Hemiptera: Pentatomidae) to synthetic aggregation pheromone and (E)-2-hexenal, a pentatomid defense chemical. *Journal of Chemical Ecology*, *22*(9), 1697–1708. https://doi.org/10.1007/BF02272408

Joanny, J. F., & de Gennes, P. G. (1984). A model for contact angle hysteresis. *The Journal of Chemical Physics*, *81*(1), 552–562. https://doi.org/10.1063/1.447337

Kadiyala, A. K., & Bijwe, J. (2013). Surface lubrication of graphite fabric reinforced epoxy composites with nano- and micro-sized hexagonal boron nitride. *Wear*, *301*(1–2), 802–809. https://doi.org/10.1016/j.wear.2012.11.069

Keis, K., Huemmer, C., & Kamath, Y. (2007). Effect of oil films on moisture vapor absorption on human hair. *Journal of Cosmetic Science*, *58*(2), 135–145.

Kment, P., & Davidová-Vilímová, J. (2010). Thoracic scent efferent system of Pentatomoidea (Hemiptera: Heteroptera): a review of terminology. *Magnolia Press*, *2706*, 1–77.

Kment, P., Stys, P., & Vilímová, J. (2012). Thoracic scent efferent system and exponium of Aphylidae (Hemiptera: Heteroptera: Pentatomoidea), its architecture and function. *European Journal of Entomology*, *109*(2), 267.

Koch, K., Schulte, A. J., Fischer, A., Gorb, S. N., & Barthlott, W. (2008). A fast, precise and low-cost replication technique for nano- and high-aspect-ratio structures of biological and artificial surfaces. *Bioinspiration & Biomimetics*, *3*(4), 046002. https://doi.org/10.1088/1748-3182/3/4/046002

Kovalchenko, A., Ajayi, O., Erdemir, A., Fenske, G., & Etsion, I. (2005). The effect of laser surface texturing on transitions in lubrication regimes during unidirectional sliding contact. *Tribology International*, *38*(3), 219–225. https://doi.org/10.1016/j.triboint.2004.08.004

Krall, B. S., Bartelt, R. J., Lewis, C. J., & Whitman, D. W. (1999). Chemical defense in the stink bug Cosmopepla bimaculata. *Journal of Chemical Ecology*, *25*(11), 2477–2494.

Kupsch, D. (2015). Benetzungsphänomene auf Rindenwanzen: Flüssigkeits-Oberflächeninteraktion und möglicher Transfer auf Technische Oberflächen. Masterthesis, RWTH Aachen.

Laplace, P. S. (1805). An essay on the cohesion of fluids. *Philosophical Transactions of the Royal Society of London*, *95*, 65–87.

Lockey, K. H. (1985). Insect cuticular lipids. *Comparative Biochemistry and Physiology Part B: Comparative Biochemistry*, *81*(2), 263–273. https://doi.org/10.1016/0305-0491(85)90311-6

Lockey, K. H. (1988). Lipids of the insect cuticle: origin, composition and function. *Comparative Biochemistry and Physiology Part B: Comparative Biochemistry*, *89*(4), 595–645. https://doi.org/10.1016/0305-0491(88)90305-7

Malik, F. T., Clement, R. M., Gethin, D. T., Beysens, D., Cohen, R. E., Krawszik, W., & Parker, A. R. (2015). Dew harvesting efficiency of four species of cacti. *Bioinspiration & Biomimetics*, *10*(3), 036005. https://doi.org/10.1088/1748-3190/10/3/036005

Malik, F. T., Clement, R. M., Gethin, D. T., Krawszik, W., & Parker, A. R. (2014). Nature's moisture harvesters: a comparative review. *Bioinspiration & Biomimetics*, *9*(3), 031002. https://doi.org/10.1088/1748-3182/9/3/031002

Mark, D., Haeberle, S., Roth, G., Von Stetten, F., & Zengerle, R. (2010). Microfluidic Lab-on-a-Chip Platforms: Requirements, Characteristics and Applications. In S. Kakaç, B. Kosoy, D. Li, & A. Pramuanjaroenkij (Eds.), *Microfluidics Based Microsystems: Fundamentals and Applications* (pp. 305–376). Dordrecht: Springer Netherlands. https://doi.org/10.1007/978-90-481-9029-4_17

Marmur, A. (2004). The Lotus Effect: Superhydrophobicity and Metastability. *Langmuir*, *20*(9), 3517–3519. https://doi.org/10.1021/la036369u

Mollier, R. (1904). Neue Diagramme zur Technischen Wärmelehre (New Graphs for Technical Thermodynamics).

Nadel, E. R., Bullard, R. W., & Stolwijk, J. A. J. (1971). Importance of skin temperature in the regulation of sweating. *Journal of Applied Physiology*, *31*(3).

Paiero, S. M., Marshall, S. A., McPherson, J. E., & Ma, M.-S. (2013). Stink bugs (Pentatomidae) and parent bugs (Acanthosomatidae) of Ontario and adjacent areas: A key to species and a review of the fauna. *Canadian Journal of Arthropod Identification*.

Panizzi, A. R., & Grazia, J. (2015). *True Bugs (Heteroptera) of the Neotropics*. Dordrecht: Springer Netherlands. Retrieved from http://ezproxy.unav.es:2048/login?url=http://link.springer.com/book/10.1007/978-94-017-9861-7

Plamadeala, C., Hischen, F., Friesenecker, R., Wollhofen, R., Jacak, J., Buchberger, G., … Heitz, J. (2017). Bioinspired polymer microstructures for directional transport of oily liquids. *Royal Society Open Science*, *4*(3), 160849. https://doi.org/10.1098/rsos.160849

Quéré, D. (2008). Wetting and Roughness. *Annual Review of Materials Research*, *38*(1), 71–99. https://doi.org/10.1146/annurev.matsci.38.060407.132434

Quick, R. W., Child, C. D., & Lanphear, B. S. (1895). Thermal Conductivity of Copper. *Physical Review (Series I)*, *2*(6), 412–423. https://doi.org/10.1103/PhysRevSeriesI.2.412

Rajput, R. K. (2010). *Engineering thermodynamics* (3rd ed). Sudbury, Mass: Jones and Bartlett Publishers.

Reiswich, V. (2013). Untersuchung südamerikanischer Rindenwanzen (Dysodius) im Hinblick auf ihr bionisches Potenzial. Masterthesis, RWTH Aachen.

Reshmi, C. R., Sundaran, S. P., A., J., & Athiyanathil, S. (2017). Fabrication of superhydrophobic polycaprolactone/beeswax electrospun membranes for high-efficiency oil/water separation. *RSC Adv.*, *7*(4), 2092–2102. https://doi.org/10.1039/C6RA26123J

Robbins, C. R. (1988). *Chemical and Physical Behavior of Human Hair*. New York, NY: Springer New York. Retrieved from http://public.eblib.com/choice/publicfullrecord.aspx?p=3083666

Rong, H.-T., Frey, S., Yang, Y.-J., Zharnikov, M., Buck, M., Wühn, M., … Helmchen, G. (2001). On the Importance of the Headgroup Substrate Bond in Thiol Monolayers: A Study of Biphenyl-Based Thiols on Gold and Silver. *Langmuir*, *17*(5), 1582–1593. https://doi.org/10.1021/la0014050

Schaefer, C. W. (1993). The Pentatomomorpha (Hemiptera: Heteroptera): an annotated outline of its systematic history. *European Journal of Entomology*, *90*, 105–122.

Schleger, A., & Turner, H. (1965). Sweating rates of cattle in the field and their reaction to diurnal and seasonal changes. *Australian Journal of Agricultural Research*, *16*(1), 92. https://doi.org/10.1071/AR9650092

Schmitz, A., Schätzel, H., & Schmitz, H. (2010). Distribution and functional morphology of photomechanic infrared sensilla in flat bugs of the genus Aradus (Heteroptera, Aradidae). *Arthropod Structure & Development*, *39*(1), 17–25. https://doi.org/10.1016/j.asd.2009.10.007

Schmitz, G., & Müller, G. (1991). Structure and function of lamellar bodies, lipid-protein complexes involved in storage and secretion of cellular lipids. *Journal of Lipid Research*, *32*(10), 1539–1570.

Schuh, R. T., & Slater, J. A. (1995). *True bugs of the world (Hemiptera:Heteroptera): classification and natural history*. Ithaca: Comstock Pub. Associates.

Sigmund, P. (1969). Theory of Sputtering. I. Sputtering Yield of Amorphous and Polycrystalline Targets. *Physical Review*, *184*(2), 383–416. https://doi.org/10.1103/PhysRev.184.383

Silberglied, R., & Aiello, A. (1980). Camouflage by Integumentary Wetting in Bark Bugs. *Science*, *207*(4432), 773–775. https://doi.org/10.1126/science.207.4432.773

Smith, S. W. (2003). *Digital signal processing: a practical guide for engineers and scientists*. Amsterdam ; Boston: Newnes.

Staddon, B. W. (1979). The scent glands of Heteroptera. *Adv. Insect Physiol.*, *14*, 351–418.

Sun, M., Liang, A., Watson, G. S., Watson, J. A., Zheng, Y., & Jiang, L. (2012). Compound Microstructures and Wax Layer of Beetle Elytral Surfaces and Their Influence on Wetting Properties. *PLoS ONE*, *7*(10), e46710. https://doi.org/10.1371/journal.pone.0046710

Sutera, S. P., & Skalak, R. (1993). The History of Poiseuille's Law. *Annual Review of Fluid Mechanics*, *25*(1), 1–20. https://doi.org/10.1146/annurev.fl.25.010193.000245

Twomey, S. A., Bohren, C. F., & Mergenthaler, J. L. (1986). Reflectance and albedo differences between wet and dry surfaces. *Applied Optics*, *25*(3), 431. https://doi.org/10.1364/AO.25.000431

Usinger, R. L., & Matsuda, R. (1959). Classification of the Aradidae (Hemiptera – Heteroptera). British Museum of Natural History, London: vii +1-410.

Vereecke, G., Xu, X., Tsai, W. K., Yang, H., Armini, S., Delande, T., … De Gendt, S. (2014). Partial Wetting of Aqueous Solutions on High Aspect Ratio Nanopillars with Hydrophilic Surface Finish. *ECS Journal of Solid State Science and Technology*, *3*(1), N3095–N3100. https://doi.org/10.1149/2.013401jss

Vericat, C., Vela, M. E., Benitez, G., Carro, P., & Salvarezza, R. C. (2010). Self-assembled monolayers of thiols and dithiols on gold: new challenges for a well-known system. *Chemical Society Reviews*, *39*(5), 1805. https://doi.org/10.1039/b907301a

Wang, J., Chen, Z., Mauk, M., Hong, K.-S., Li, M., Yang, S., & Bau, H. H. (2005). Self-Actuated, Thermo-Responsive Hydrogel Valves for Lab on a Chip. *Biomedical Microdevices*, *7*(4), 313–322. https://doi.org/10.1007/s10544-005-6073-z

Washburn, E. W. (1921). The Dynamics of Capillary Flow. *Physical Review*, *17*(3), 273–283. https://doi.org/10.1103/PhysRev.17.273

Wenzel, R. N. (1936). RESISTANCE OF SOLID SURFACES TO WETTING BY WATER. *Industrial & Engineering Chemistry*, *28*(8), 988–994. https://doi.org/10.1021/ie50320a024

White, B., Sarkar, A., & Kietzig, A.-M. (2013). Fog-harvesting inspired by the Stenocara beetle—An analysis of drop collection and removal from biomimetic samples with wetting contrast. *Applied Surface Science*, *284*, 826–836. https://doi.org/10.1016/j.apsusc.2013.08.017

Wigglesworth, V. B. (1957). The physiology of insect cuticle. *Annual Review of Entomology*, *2*(1), 37–54.

Zhu, X., Loo, H.-E., & Bai, R. (2013). A novel membrane showing both hydrophilic and oleophobic surface properties and its non-fouling performances for potential water treatment applications. *Journal of Membrane Science*, *436*, 47–56. https://doi.org/10.1016/j.memsci.2013.02.019

9. Appendix

Table 4: Overview of identified substances in GC-MS. *Table as presented in Reiswich (2013)*

Verbindung	Stoff-gruppe	Ketten-länge	Dysodius lunatus		Dysodius magnus	
			Retentions zeit	Peak-fläche	Retentions zeit	Peak-fläche
dodecanoic acid	Fettsäure	C12:0	17,30	34,63		
hexadecandioic acid-bis-(2-methylpropyl)-ester	Fettsäure	C16:0			17,49	293,67
tetradec-x-enoic acid	Fettsäure	C14:1			22,39	6,23
tetradecanoic acid	Fettsäure	C14:0	22,85	161,84	22,98	57,85
hexadec-x-enoic acid	Fettsäure	C16:1	27,31	2.005 ,69	27,43	1325,5 0
hexadec-x-enoic acid	Fettsäure	C16:1			27,56	8,59
hexadecanoic acid	Fettsäure	C16:0	28,53	11.10 5,79	28,29	1293,1 2
octadeca-x,x-dienoic acid	Fettsäure	C18:2			31,86	17,31
octadec-x-enoic acid	Fettsäure	C18:1	32,33	7.757 ,90	32,37	4889,8 8
octadecanoic acid	Fettsäure	C18:0	33,31	5.787 ,88	33,13	451,55
not identified	not identified		34,22	120,1 6	34,03	8,27
hexadecandioic acid-bis-octyl-ester	Fettsäure	C16:0			35,72	19,20
n-tetracosane (interner Standard)	n-alkane	C24:0	36,70	2.420 ,00		
not identified	not identified		37,15	609,9 8	37,24	82,86
eicosanoic acid	Fettsäure	C20:0	37,53	175,3 0	37,65	16,62

hexadec-x-enoic acid-glycerol-ester	Mono-glycerid	C16:1			40,89	18,32
hexadecanoic acid-glycerol-ester	Mono-glycerid	C16:0	41,38	38,89	41,56	26,11
docosanoic acid	Fettsäure	C22:0	41,90	121,51	42,05	12,57
octadec-x-enoic acid-glycerol ester	Mono-glycerid	C18:1	44,12	21,01	44,31	16,94
octadec-x-enoic acid-glycerol ester	Mono-glycerid	C18:1	44,82	124,80		
octadecanoic acid-glycerol ester	Mono-glycerid	C18:0			44,95	51,68
nonacosanal	Aldehyd	C29:0			45,88	149,82
tetracosanoic acid	Fettsäure	C24:0	46,21	56,21		
bis-hexadecanoic acid-glycerol-ester	DI-glycerid	C16:0, C16:0	65,40	59,80	65,99	70,20
bis-hexadecanoic acid-glycerol-ester	DI-glycerid	C16:0, C16:0	66,18	129,61	66,44	86,63
hexadec-x-enoic acid-, octadec-x-enoic acid-glycerol-ester	DI-glycerid	C16:1, C18:1	68,05	59,87	68,23	49,97
hexadecanoic acid-, octadec-x-enoic acid-glycerol-ester	DI-glycerid	C16:0, C18:1	68,44	140,41	68,58	165,08
hexadecanoic acid-, octadec-x-enoic acid-glycerol-ester glycerol-ester	DI-glycerid	C16:0, C18:1 or C16:1, C18:0	68,86	112,66	69,07	162,99
hecadecanoic acid-, octadecanoic acid-glycerol-ester	DI-glycerid	C16:0, C18:0	69,27	57,46	69,52	98,34
bis-octadec-x-enoic acid-glycerol-ester	DI-glycerid	C18:1, C18:1	70,88	97,42	71,10	87,69
bis-octadec-x-enoic acid-glycerol-ester	DI-glycerid	C18:1, C18:1	71,39	124,62		

octadecanoic acid-, octadec-x-enoic acid-glycerol-ester	DI-glycerid	C18:0, C18:1	71,82	46,31	71,58	134,66
octadecanoic acid-, octadec-x-enoic acid-glycerol-ester	DI-glycerid	C18:0, C18:1			72,03	67,75
bis-octadecanoic acid-glycerol-ester	DI-glycerid	C18:0, C18:0	72,26	25,52	72,46	31,41
triacyl-glycerol-ester	Tri-glycerid	CXX:X			77,90	9,56
triacyl-glycerol-ester	Tri-glycerid	CXX:X	80,48	27,16	80,68	19,51
triacyl-glycerol-ester	Tri-glycerid	CXX:X	83,48	22,20		
triacyl-glycerol-ester	Tri-glycerid	CXX:X	84,00	52,71		
triacyl-glycerol-ester	Tri-glycerid	CXX:X	84,35	71,81	84,32	201,24
triacyl-glycerol-ester	Tri-glycerid	CXX:X	86,43	462,87		
triacyl-glycerol-ester	Tri-glycerid	CXX:X	86,73	190,68	86,72	1273,19
triacyl-glycerol-ester	Tri-glycerid	CXX:X	88,45	371,70		
triacyl-glycerol-ester	Tri-glycerid	CXX:X	88,74	388,10	88,75	1070,14
triacyl-glycerol-ester	Tri-glycerid	CXX:X	89,00	250,10	89,03	752,03
triacyl-glycerol-ester	Tri-glycerid	CXX:X	90,37	130,08	90,60	182,75
triacyl-glycerol-ester	Tri-glycerid	CXX:X	90,93	379,22	90,85	255,07
triacyl-glycerol-ester	Tri-glycerid	CXX:X	91,12	109,94	91,11	231,82
triacyl-glycerol-ester	Tri-glycerid	CXX:X			93,30	22,077

10. Acknowledgements

I would like to offer my special thanks and gratitude to the advisors of this work, Prof. Dr. Werner Baumgartner and Prof. Dr. Peter Bräunig, for the continuous support, the help and advises, and overall the chance, to make this work happen in the first place.

My special thanks also go to Prof. Dr. Ernst Heiss, for the provision of sample material and the superb counseling in all questions concerning the biological aspect of this work.

I would also like to thank all colleagues of the former Institute of Neurobiomimetics at the RWTH Aachen, as well as the staff at Institute for Biomedical Mechatronics, JKU Linz, for their support and help in various aspects of life and work. Particularly my thanks go to Dr. Philipp Comanns, Dr. Anna-Christin Joel, Agnes Weth and Msc. Cristina Plamadeala.

Furthermore, I thank Prof. Dr. Johannes Heitz and Dr. Oskar Armbruster for support with the physical experiments, Dr. Michael Riedel and Prof. Dr. Markus Himmelsbach for help and support with the chemical analysis, Dipl. Ing. Kai Wienands and Dipl. Ing. Arch. Holger Mescheder for the laser ablation, and Dr. Gerda Buchberger for various contributions towards this work.

Last but not least, my very special thanks goes to my parents, family and Dariya Baiko, for their continuous support in life, endurance and patience.

Thank you all so much!